PHASE-FIELD FRACTURE MODELING AND NUMERICAL SOLVER ACCELERATION

WEI WANG

PhD

The Hong Kong Polytechnic University

2026

The Hong Kong Polytechnic University

Department of Mechanical Engineering

Phase-Field Fracture Modeling And Numerical Solver Acceleration

Wei Wang

A thesis submitted in partial fulfillment of the requirements for the degree of Doctor of Philosophy

August 2025

CERTIFICATE OF ORIGINALITY

I hereby declare that this thesis is my own work and that, to the best of my knowledge and belief, it reproduces no material previously published or written, nor material that has been accepted for the award of any other degree or diploma, except where due acknowledgement has been made in the text.

_____(Signature)

WANG Wei (Name of Student)

Abstract

In this thesis, we develop two phase-field fracture models (PFFMs) to investigate: (1) the mechanical failure mechanisms in all-solid-state batteries (ASSBs) using Landau-Ginzburg framework, and (2) the fracture behavior of ion-exchange (IOX)-strengthened cover glass using a variational framework. Although the phase-field (PF) method mitigates the nonlinearity of crack propagation by introducing a diffusive interface and is compatible with finite element (FE) solver, the standalone FE fracture simulations remain computationally intensive. To overcome this limitation, we propose a numerical solver acceleration, particularly through AI-accelerated FE framework, to enhance computational efficiency. This approach offers a promising route for efficiently solving highly nonlinear PFFMs in large scales and in multi-physical fields, eventually achieving quantitative analysis to further guide experiments.

ASSBs are anticipated to achieve exceptional energy density and enhanced safety, enabled by the direct use of lithium metal anodes and the suppression of dendrites through solid-state electrolytes (SSEs). However, recent experimental studies have revealed discharging-induced void formation at lithium/SSE (Li/SSE) interfaces and charging-induced cracks within SSEs, both of which facilitate lithium penetration, finally resulting in mechanical failure of cell. To address these challenges, we develop a high-fidelity mechano-electrochemical model for ASSBs, particularly focusing on the coupled kinetics of void and crack evolution. This model demonstrates that void growth results from lithium stripping, driven by the disparate interfacial and bulk diffusivity of lithium. This process results in nonuniform Li^+ distribution during electroplating, subsequently localized interfacial damage zone, SSE cracking, and ultimately, lithium plating within cracks. Our findings indicate that while high stack pressures reduce void size, they do not prevent cracking; in contrast, optimized lateral compressive stresses can effectively suppress SSE fracture and inhibit dendrite formation.

Ion-exchange (IOX)-strengthened cover glass has become ubiquitous in portable electronics due to its exceptional fracture resistance. However, establishing a quantitative

relationship between residual stress profiles and fracture strength remains elusive, as the experimental data are highly scattered due to the uncertainties in surface flaws severity. To address this challenge, we develop a variational PFFM to systematically investigate the fracture mechanisms and the stress-shielding effects of surface compressive stress (CS) on pre-existing surface flaws. Our study specifically evaluates the strengthening effectiveness of different combinations of surface CS and depth of layer (DOL) under compression, employing both ring-on-ring (ROR) and ball-drop (BD) test. Simulations reveal that surface CS plays a more dominant role in crack inhibition for ROR test; while for BD scenarios, DOL emerges as the more critical parameter. These insights are illustrated through comprehensive fracture strength contour maps and BD height analyses.

Numerical solvers for partial differential equations (PDEs) often face a trade-off between computational efficiency and accuracy. Neural operators (NOs) offer a promising avenue to accelerate simulations, but they are hindered by several challenges: the need for large training datasets, error accumulation in dynamic settings, and poor generalization in multi-physics scenarios. To tackle these problems, a novel hybrid framework is proposed, which integrates physics-informed deep operator network (PI-DeepONet) with finite element method (FEM) via domain decomposition. The core innovation lies in efficient coupling FEM and DeepONet subdomains using a Schwarz alternating method, expecting to solve complex and nonlinear regions by a pre-trained DeepONet, while the remainder is handled by FEM. The Newmark-Beta time-stepping scheme is embedded directly into the DeepONet architecture, substantially reducing long-term error propagation. Furthermore, an adaptive subdomain evolution strategy enables the machine learning (ML)-resolved region to expand dynamically, capturing emerging fine-scale features. The framework's efficacy has been rigorously validated across a range of solid mechanics problems—spanning static, quasi-static, and dynamic regimes for either linear elasticity or hyper-elasticity—demonstrating accelerated convergence rates (up to 20% improvement over traditional FE coupling approaches) while preserving solution fidelity with error margins consistently below 3%. The validation in mechanics shows the potential of this framework to further achieve high-fidelity multi-physical simulations.

Publications arising from the thesis

Published papers:

[1] **Wei Wang**, Jiaxuan Wang, Chen Lin, and Haihui Ruan. *Modeling of Void-Mediated Cracking and Lithium Penetration in All-Solid-State Batteries*. Advanced Functional Materials, 2023.

[2] **Wei Wang**, Jiaxuan Wang, Junjun Xu, Jianbiao Wang, Haihui Ruan. *Fracture of ion-exchange-strengthened thin cover glass investigated using a phase-field model*. Journal of the American Ceramic Society, 2025.

[3] **Wei Wang**, Maryam Hakimzadeh, Haihui Ruan, Somdatta Goswami. *Time-Marching Neural Operator–FE Coupling: AI-Accelerated Physics Modeling*. Computer Methods in Applied Mechanics and Engineering, 2025

[4] Awais Akhtar, **Wei Wang**, Haihui Ruan. *A study of Ru–Cr protective coatings for precision glass molding.* Applied Surface Science, 2024

[5] Yi Yang, **Wei Wang**, Haihui Ruan. *Evolution of Holes and Cracks in Pre-Carbonized Glassy Carbon.* Materials, 2024

Submitted paper:

[6] **Wei Wang**, Tang Paai Wong, Haihui Ruan. Somdatta Goswami. *Causality-Respecting Adaptive Refinement for PINNs: Enabling Precise Interface Evolution in Phase Field Modeling.* Engineering Applications of Artificial Intelligence (under first review), 2025

[7] Yutong Liu*, Wenhua Zuo*, **Wei Wang***, Cong Lin, Qingsong Weng, Yinggang Zhu, Xianghui Xiao, Ke Du, Haihui Ruan, Gui-Liang Xu, Khalil Amine, Guohua Chen, Qiang Liu. *Dynamic delocalization of stress in brittle positive electrode materials by shape-memory polymers*. Nature Nanotechnology (in press), 2025 (* Co-first authors)

Acknowledgement

My four-year PhD journey at The Hong Kong Polytechnic University has been one of the most transformative and unforgettable experiences of my life.

First and foremost, I wish to express my deepest gratitude to my supervisor, Prof. Ruan Haihui, for his invaluable guidance, unwavering support, and profound wisdom. His dedication to nurturing my scientific growth, along with his inspiring life lessons, has left an indelible mark on my academic and personal development.

I am also profoundly grateful to Prof. Somdatta Goswami for the extraordinary opportunity to work in her research group at Johns Hopkins University. My visit there was both intellectually enriching and personally rewarding, introducing me to the exciting field of AI for science and helping shape my career trajectory.

My sincere thanks go to all my colleagues and collaborators whose camaraderie and support made this journey possible. In particular, I appreciate the stimulating discussions and shared experiences with my research group members: Mr. Jiaxuan Wang, Dr. Jinan Liu, Dr. Yi Yang, Dr. Awais Akhtar, Dr. Yiqiang Fu, Mr. Yanpei Dang, Miss Junju Xu, Mr. Yuzhou Zhang, Mr. Chiyu Zeng, Mr. Zhanchen Zhu, Dr. Lufeng Xue, Dr. Jie Li, Mr. Zhao Xu, and Mr. Yifei Wu. I am also deeply grateful to Dr. Yutong Liu for her exceptional experimental expertise in battery research and her generosity in sharing knowledge. Additionally, I extend my appreciation to the members of Prof. Goswami's group, particularly Dr. Maryam Hakimzadeh and Mr. Dibakar Roy Sarkar, for their support and collaboration.

Finally, words cannot fully express my gratitude to my family and my beloved soulmate, Miss Jiayi Shi, for their unconditional love, patience, and encouragement throughout this challenging yet rewarding journey. Their unwavering belief in me has been my greatest source of strength.

Table of Contents

List of Figure Captions

List of Table Captions

Nomenclature

A_c	creep parameter
a_{TS}	activity for the transition state
a_x	acceleration in x-direction
a_y	acceleration in y-direction
B	scalar in initial magnitude of strain history field
$\mathcal{B}$	spatial differential operators for boundary
α	asymmetry parameter
β	Newmark parameters
$\mathbf{c}$	series of concentrations in investigated system
c_{Li}	concentration of lithium
c_{Li^+}	concentration of lithium ions
c_{e^-}	concentration of electron
c_i^{ref}	saturated concentration of species $*$ in corresponding phase i
c_{v_1}	concentration of vacancies in solid-state electrolyte

c_{v_2}	concentration of vacancies at Li/void surface
$\overline{c_*}$	dimensionless concentration of species $*$
$\mathbf{C}$	right Cauchy-Green deformation tensor
D_{Li^+}	diffusion coefficient of Li^+ in investigated system
$D_{Li^+}^{Li}$	diffusion coefficient of Li^+ in lithium
$D_{Li^+}^{SSE}$	diffusion coefficient of Li^+ in solid-state electrolyte
$D_{Li^+}^{13}$	diffusion coefficient of Li^+ in the interface between lithium and void
$\mathbf{D}$	stiffness matrix
$\mathbf{D}_{\mathrm{Li}}$	stiffness matrix of lithium electrode
$\mathbf{D}_{\mathrm{SSE}}$	stiffness matrix of solid-state electrolyte
$\mathbf{D}_{\mathrm{void}}$	stiffness matrix of void
$d(\mathbf{x}, \Gamma)$	closest distance from point x to the discontinuity Γ
δ	interfacial thickness
δ_i	interfacial thickness of phase *i*
Δt	time increment
E	Young's modulus
$\boldsymbol{\varepsilon}$	total strain tensor
$\boldsymbol{\varepsilon}^{\mathrm{e}}$	elastic strain tensor
$\boldsymbol{\varepsilon}^{\mathrm{mis}}$	chemical strain tensor from mismatch
$\varepsilon^{\mathrm{mis}}$	chemical strain value from mismatch
ε^0	vacuum permittivity

ε_{r}	relative permittivity of the investigated system
ε_0	residual strain caused by ion-exchange strengthening
ε_1	first principal strain
ε_2	second principal strain
ε_3	third principal strain
$\varepsilon_{\mathrm{a}}^{\mathrm{e}}$	principal elastic strain
$\varepsilon_{\mathrm{r}}^{\mathrm{Li}}$	relative permittivity of lithium electrode
$\varepsilon_{\mathrm{r}}^{\mathrm{SSE}}$	relative permittivity of solid-state electrolyte
$\varepsilon_{\mathrm{r}}^{\mathrm{void}}$	relative permittivity of void
$\boldsymbol{\varepsilon}_{+}^{\mathrm{e}}$	tensile elastic strain tensors
$\boldsymbol{\varepsilon}_{-}^{\mathrm{e}}$	compressive elastic strain tensors
$\mathbf{f}$	body force
f	free energy density
f_d	driving force function
f_{chem}	chemical potential energy density
f_{elec}	electric potential energy density
f_{int}	interface energy density
f_{mech}	mechanical energy density
F	Faraday constant
$\mathcal{F}$	free energy of system
$\mathbf{F}$	external force vector

$\mathbf{F}_{\mathrm{g}}$	total deformation gradient
$\mathbf{F}^{\mathrm{e}}$	elastic deformation gradient
$\mathbf{F}^{\mathrm{r}}$	residual deformation gradient caused by ion-exchange strengthening
G_c	critical energy release rate
$G_{\boldsymbol{\theta}_1}^{u_x}$	neural operator for x-displacement
$G_{\boldsymbol{\theta}_2}^{u_y}$	neural operator for y-displacement
Γ	crack path
$\Gamma_{\mathrm{I}}^{\mathrm{in}}$	inner boundary of subdomain I
$\Gamma_{\mathrm{I}}^{out}$	outer boundary of subdomain I
$\Gamma_{II}^{\mathrm{in}}$	inner boundary of subdomain II
$\Gamma_{\mathrm{II}}^{out}$	outer boundary of subdomain II
$\Gamma_{inner}^{\mathrm{in},3}$	inner boundary of subdomain III in neural operator region expansion
$\Gamma_{inner}^{\mathrm{in},2}$	inner boundary of subdomain II in neural operator region expansion
g	degradation function in Landau-Ginzburg-based PFFM
$\mathrm{g_b}$	boundary condition function
g_{d}	double well function
g_k	degradation function in Griffth-energy-generalized PFFM
γ	Newmark parameters
γ_ϕ	interfacial energy in conventional phase field model
$\gamma(\phi)$	function of scaling factor for crack energy density

H	history strain field
H_i	height of energy barrier for phase *i*
H_ε	Heaviside function
H_0	initial magnitude of strain history field
$\mathbf{I}$	identity matrix
$\mathbf{I}_1$	first invariant of right Cauchy-Green deformation tensor
J	volume change factor
K	gradient-energy coefficient
K_i	gradient-energy coefficient of phase *i*
$\mathbf{K}$	global stiffness matrix
k	small and positive parameter in degradation function
k_0	kinetics constant
ξ	strain energy
ξ_{cr}	critical strain energy for crack
L	Lagrangian energy functional
L_{cr}	crack propagation rate in solid-state electrolyte
L_{k_i}	coefficient to scale the contribution of reaction kinetics to the phase
L_{s_i}	coefficient to scale the contribution of the interfacial energy to the phase
$\mathcal{L}_{res}$	residual loss function
$\mathcal{L}_{\mathrm{bcs}}$,	boundary loss function
l_0	a parameter controlling the thickness of the diffusive interface

$\Lambda_{c/d}$	dimensionless reaction driving force for charge or discharge
λ_0	Lamé's first parameter
M_ϕ	atomic mobility
$\mathbf{M}$	mass matrix
μ_0	Lamé's second parameter
$\mu_{\mathrm{TS}}^{\mathrm{ex}}$	excessive electrochemical potential for transition state
μ_1^{ex}	excessive electrochemical potential for initial states
μ_2^{ex}	excessive electrochemical potential for final states
$\widetilde{\mu_1^{\mathrm{ex}}}$	effective excessive electrochemical potential for initial states
$\widetilde{\mu_2^{\mathrm{ex}}}$	effective excessive electrochemical potential for final states
μ_*^{ex}	excessive electrochemical potential for species $*$
μ_i^{int}	interfacial potentials for phase *i*
$\mu_{e^-}^0$	standard chemical potential of electron
μ_{Li}^0	standard chemical potential of lithium
$\mu_{Li^+}^0$	standard chemical potential of lithium ion
$\mathcal{N}$	spatial differential operators for collocation points
$\mathcal{N}_1$	spatial differential operators for collocation points in x-direction
$\mathcal{N}_2$	spatial differential operators for collocation points in y-direction
N_1^r	number of collocation points
N_1^b	number of boundary points
$\mathbf{n}$	normal vector

$\mathbf{n}_a$	direction vector of principal elastic strain
$\boldsymbol{\nu}$	Poisson's ratio
$\mathbf{p}$	series of order parameters in investigated system
p_i	order parameter of phase *i* in multi-phases phase field model
$\mathbf{P}_1$	first Piola-Kirchhoff stress tensor
Ω	computational domain
Ω_I	subdomain I
Ω_{II}	subdomain II
Ω_o	overlapping region
Ω_I^p	subdomain I in neural operator region expansion
Ω_{II}^p	subdomain II in neural operator region expansion
Ω_{III}^p	subdomain III in neural operator region expansion
Ω_o^p	overlapping region in neural operator region expansion
ϕ	order parameter for phase field model
φ_{Li}	electric potential in lithium electrode
$\varphi_{Li/SSE}$	electric potential in Li and solid-state electrolyte interface
φ_{SSE}	electric potential in solid-state electrolyte
ψ_{tot}	total potential energy
ψ_e	elastic energy density
ψ_e^+	positive component of elastic energy density
ψ_e^-	negative component of elastic energy density

R	molar gas constant
$\mathcal{S}$	Banach space for output functions
s	auxiliary scalar
r_s	reaction rates
$r_{1\to2}$	forward reaction rate
$r_{2\to1}$	backward reaction rate
ρ	density
$\boldsymbol{\rho}_r$	Relaxation parameter
ρ_{Li^+}	volumetric charge density of lithium ions
$\boldsymbol{\sigma}$	stress tensor
σ_m	von Mises stress
σ_{ref}	reference stress
σ_I	first principal stress
$\mathbf{t}$	traction
T	temperature
$\boldsymbol{\theta}$	tunable parameters
$\boldsymbol{\theta}_1$	tunable parameters for x-displacement
$\boldsymbol{\theta}_2$	tunable parameters for y-displacement
$\boldsymbol{\theta}^*$	optimal parameters
$\boldsymbol{\Theta}$	finite-dimensional parameter space
u_x	x-displacement

u_y	y-displacement
$\mathbf{u}$	displacement field vector
$\dot{\mathbf{u}}$	velocity vector
$\ddot{\mathbf{u}}$	acceleration vector
$\mathcal{U}$	Banach space for input functions
$\vec{\boldsymbol{V}}_{\text{advective}}$	advective velocity
v_x	velocity in x-direction
v_y	velocity in y-direction
W_ϕ	energetic barrier height of two phases

Chapter 1 Introduction

1.1 Background

Throughout human history, fracture has remained one of the most prevalent failure modes in engineering structures and materials. In modern manufacturing, while technological advancements have enabled the development of novel materials and designs, they have simultaneously introduced new and unpredictable fracture phenomena [1].

Though the material fracture can be found ubiquitously, the experimental study presents significant challenges across both temporal and spatial dimensions. Temporally, crack initiation and propagation occur at nanosecond (~ns) timescales, while spatially, fracture constitutes a multiscale problem spanning from atomic-level (~nm) initiation to macroscopic (~m) propagation [2]. These extreme spatiotemporal resolution requirements, combined with the high costs of experimentation, make direct observation of fracture processes particularly challenging. Furthermore, the inherent multiscale nature of fracture and the unavoidable presence of randomly distributed microdefects introduce substantial uncertainty and compromise experimental repeatability, thereby limiting the reliability of experimental findings. Consequently, the development of highly accurate and computationally efficient simulation methods has become essential for quantitative analysis of fracture mechanisms and prevention of material and system failures.

Fracture mechanics, as a fundamental branch within solid mechanics, has been theoretically studied for over a century, marking the beginning with the formulation of Griffith's linear elastic fracture mechanics theory in 1921 [3]. The inherent strong discontinuity and high nonlinearity of fracture processes pose great challenge in numerical simulation. Furthermore, in realistic scenarios, the fracture process is significantly influenced by various environmental factors, such as the Oxidation Assisted Cracking (OAC) [4, 5], Hydrogen Induced Cracking (HIC) [4, 5], and stress corrosion cracking (SCC) [6, 7], exhibiting the exponential growth of non-linearity in these multi-physical fracture

systems. In fact, the corresponding partial differential equations (PDEs) to elaborate the cracking mechanism in these systems can be derived without great efforts. However, combined with the strong discontinuity, these multi-physical fracture problems present the strenuosity in both mathematical description and computation: How to describe the multi-physics induced cracking process within a sing PDE? And how to solve the governing PDEs accurately and efficiently?

It is found that the Phase-Field (PF) is an ideal framework to answer these questions. By introducing a diffusive interface to quantitatively characterize interfacial evolution in multiphase and multi-physics systems, the PF approach effectively regularizes the strong discontinuity, thereby simplifying the mathematical formulation. Treating the crack region as a specific phase, the PF method demonstrates remarkable capability in simulating crack propagation while naturally incorporating various environmental factors.

Therefore, the phase field fracture models (PFFMs) are implemented in this thesis to investigate the fracture mechanisms in industrial realities. A particularly critical research focus is the solid-state electrolyte (SSE) cracking during electrochemical cycling in all-solid-state batteries (ASSBs) [8], which is the key issue to hinder their way to commercialization. We develop a mechano-electrochemical PFFM to quantitatively predict crack propagation and demonstrate that surface strengthening offers an effective solution to this challenge.

Among various surface strengthening techniques for inorganic nonmetallic materials, ion-exchange (IOX) strengthening has emerged as a well-established and widely implemented methodology [9]. The IOX process shows considerable promise for enhancing SSE fracture resistance through the introduction of beneficial surface compressive stresses. Despite its widespread industrial application in glass manufacturing, quantitative tools for characterizing its fracture behavior under different compressive stress (CS) profiles remain underdeveloped. To address this gap, we propose a novel PFFM incorporating residual stresses, validated through standardized experimental tests, to systematically investigate IOX-strengthened glass.

While PFFMs can be readily implemented within commercial finite element (FE) software, their computational efficiency and accuracy remain constrained by two fundamental limitations: (1) the stress singularity at crack tips necessitates prohibitively fine meshes, and (2) extreme loading conditions often induce mesh distortion, leading to solution inaccuracies or complete simulation failure. Mesh-free methods could be more suitable for cracking simulation. However, conventional mesh-free methods, for instance peri-dynamics [10], demands substantial computational efforts.

Many scientific machine learning (SciML) methods, which can also be regarded as mesh-free methods in solving PDEs, have been utilized in solving fracture mechanical problems. Among them, Deep Operator Neural Network (DeepONet) is recognized as the most promising method due to its generalized prediction ability and fast inference after pretraining. However, in large scale simulation, the standalone DeepONet requires huge amount of computing resources for pretraining and introduces great inaccuracy, especially in dynamic regime. To overcome the limitations and leverage the advantages of FE and DeepONet, this thesis includes an AI-accelerated computational framework that synergistically combines FE analysis with physics-informed DeepONet (PI-DeepONet). Through domain decomposition, our approach selectively replaces only the highly nonlinear regions in traditional FEM with PI-DeepONet, while retaining the FEM solver in the remaining domains. This strategy effectively exploits DeepONet's nonlinear mapping capabilities while avoiding large-scale implementation challenge, resulting in a more robust, scalable, and computationally efficient simulation methodology. Another key advantage of SciML lies in its ability to directly incorporate scarce experimental data, effectively bridging the gap between physical experiments and numerical simulations. The working flowchart of this thesis from experimental observation to AI-accelerated framework is summarized in Fig. 1.1.

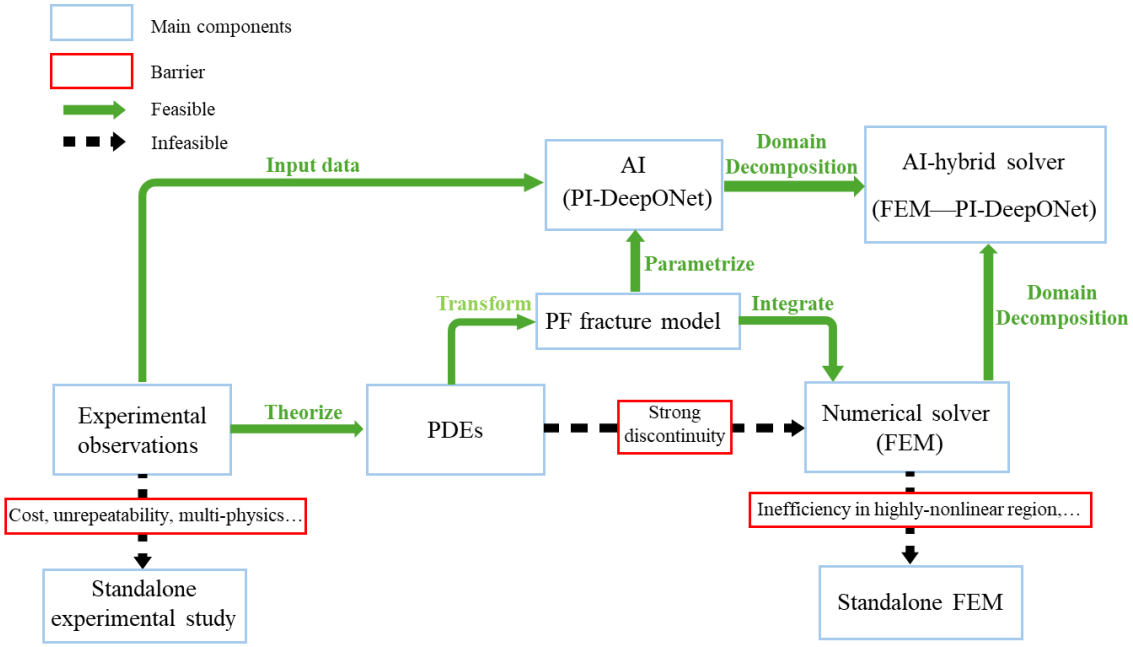

Figure 1.1 Working flowchart of this thesis.

1.2 Objectives and Content outline

The primary research objectives of this doctoral thesis are delineated as follows:

(1) Establish a mechano-electrochemical PFFM within Landau-Ginzburg framework to investigate the SSE cracking during electrochemical cycling, unveiling the void-mediated fracture mechanism.

(2) Establish a residual-stress-existing PFFM within variational framework to study the IOX-strengthened glass fracture, thereby deepening the understanding of its fracture mechanism and enabling optimization of residual stress distribution through critical parameter analysis.

(3) Establish an AI-accelerated framework by coupling the FE and PI-DeepONet, significantly enhancing simulation efficiency and robustness while establishing a platform for future PFFM integration.

The thesis is organized as follows:

- **Chapter 2** presents a comprehensive review of the PF models from the conventional PF model to the Landau-Ginzburg-based and Griffth-theory-

generalized PFFM, the applications in SSE cracking and IOX strengthening glass, and the state-of-the-art AI-accelerated methods.

- **Chapter 3** details the methodological framework for Landau-Ginzburg-based PFFM in SSE cracking, the Griffth-theory-generalized PFFM in IOX-strengthened glass, and the FE-neural operator (NO) coupling framework via domain-decomposition.

- **Chapter 4** implements the Landau-Ginzburg-based PFFM to develop a mechano-electrochemical model for all-solid-state lithium metal batteries (ASSLMBs), which reproduces the void expansion in stripping, crack initiation and propagation in SSE along with lithium penetration and finally unveils the critical role of void in ASSLMBs' mechanical failure.

- **Chapter 5** implements the Griffth-theory-generalized PFFM to investigate the IOX-strengthened thin glass, illustrates the crack initiation and propagation with different compressive stress (CS) profiles, and finally determines the most optimal CS profile for fracture resistance and impact resistance, respectively.

- **Chapter 6** implements the FE-NO coupling framework with domain decomposition to solve the mechanical problems for linear elasticity under static loading, hyper-elasticity under quasi-static loading, and elasto-dynamic, demonstrating the promising future of AI-accelerated in efficiently and robustly solving highly non-linear problems.

Chapter 2 Literature review

2.1 Phase-field models

2.1.1 Conventional PF method

The PF method was originally developed for first-order phase transition description by Langer in 1986 [11], addressing the fundamental challenge of tracking moving solid-liquid interfaces. To distinguish the different phases and identify the interfacial regions, the order parameter was first introduced by Landau and Khalatnikov [12]. For instance, in solidification [13, 14], the order parameter ϕ varies continuously from 0 (liquid phase) to 1 (solid phase), with intermediate values ($0 < \phi < 1$) representing phase interface.

The theoretical framework begins with the formulation of the system's free energy $\mathcal{F}$ in terms of order parameter ϕ within domain Ω:

$$\mathcal{F}(\phi) = \int_{\Omega} f(\phi) + \frac{K}{2}(\nabla\phi)^2 + \frac{W_{\phi}}{2} g_{\mathrm{d}}(\phi)\,\mathrm{d}\omega \tag{2.1}$$

Thus, this free energy functional can be divided into three distinct contributions in order: bulk free energy density *f*, the gradient energy term, and the double-well potential. Here, *K* denotes the gradient-energy coefficient, W_{ϕ} represents the energetic barrier height between two phases, and $g_{\mathrm{d}}(\phi) = (1-\phi)^2\phi^2$ vanishes at ϕ=0 and ϕ=1.

The bulk free energy density consists of the volumetric contribution of free energy and the driving force for phase transition at the interface. Thus it does not contribute to the interfacial energy at equilibrium between coexisting phases. In contrast, as demonstrated by Cahn and Hillard 1958 [15], the gradient energy term is directly associated with the interfacial energy. Regarding the expression $g_{\mathrm{d}}(\phi)$, the double well potential remains strictly positive within the interface region ($0 < \phi < 1$). So, both the gradient term and double-well potential contribute to interfacial energy γ_{ϕ}, whose one-dimensional expression is given by:

$$\gamma_{\phi} = \int_{-\infty}^{+\infty} \left[\frac{K}{2} \left(\frac{\mathrm{d}\phi}{\mathrm{d}x} \right)^2 + \frac{W_{\phi}}{2} (1-\phi)^2 \phi^2 \right] \mathrm{d}x \tag{2.2}$$

The order parameter profile at equilibrium in one dimension can consequently be derived [16, 17]:

$$\phi = \frac{1}{2} \left[1 - \tanh \left(\frac{x}{2\delta} \right) \right] \tag{2.3}$$

The corresponding order parameter profile is shown in Figure 2.1. Notably, the PF model yields a diffusive interface with a fixed width $\delta = \sqrt{\frac{K}{W_{\phi}}}$.

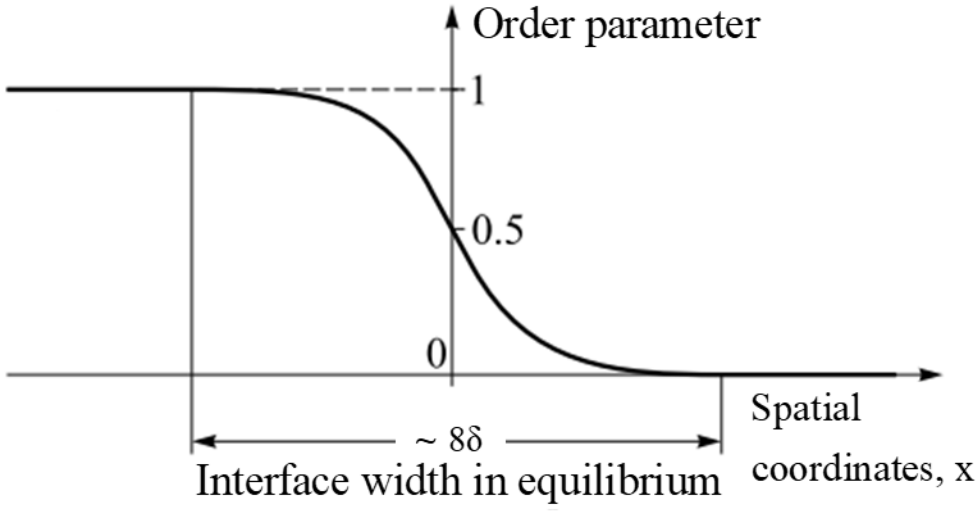

Figure 2.1 Order parameter profile at equilibrium of coexisting phases in one dimension [17].

Though the fixed-width expression of order parameter in Eq. 2.3 is derived without considering driving forces, this characteristic fixed-width interface represents the most fundamental and universal feature of PF model in both equilibrium and non-equilibrium systems [16, 18]. Specifically, the order parameter exhibits a smooth transition from 0 to 1 across an interface of constant thickness, as illustrated in Fig. 2.2. By replacing the sharp interface between two phases with a diffusive fixed-width interface, the PF method eliminates the strong discontinuity, thereby mitigating computational difficulty. Unlike

computationally intensive sharp-interface models that rely on explicit tracking methodologies, the PF method with diffusive interface captures interfacial morphology evolution without requiring additional assumptions [17]. Owing to these significant strengths, the PF method becomes a natural choice to investigate the interfacial variations, and it has been seamlessly extended in multi-phases and multi-physics systems [19].

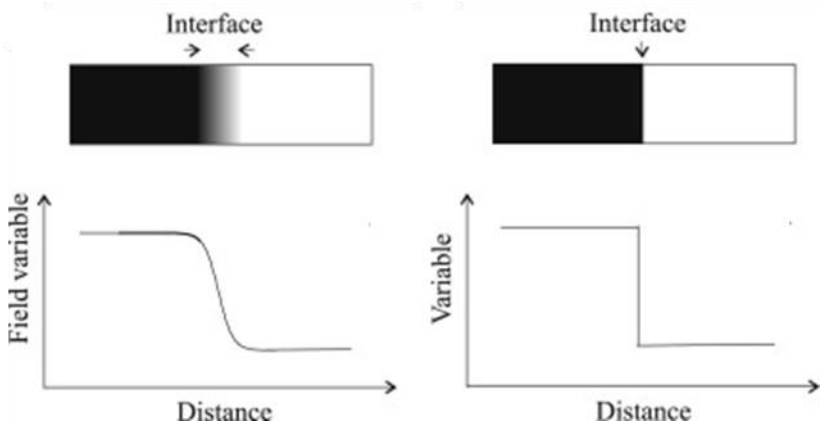

Figure 2.2 Diffuse interface (left column) and sharp interface (right column) [18].

By utilizing free energy in Eq. 2.1, two fundamental equations in PF models — Cahn-Hillard (CH) and Allen-Cahn (AC) equations, can be derived to describe the phase evolution with interfacial variations. The equations read:

$$\text{CH equation: } \frac{\partial \phi}{\partial t} = \nabla \cdot \left(M_\phi \nabla \frac{\delta \mathcal{F}}{\delta \phi} \right) \tag{2.4}$$

$$\text{AC equation: } \frac{\partial \phi}{\partial t} = -M_\phi \frac{\delta \mathcal{F}}{\delta \phi} \tag{2.5}$$

with the mobility M_ϕ being a presumed constant. The CH equation is to describe the evolution of conserved order parameters in phase separation process; a typical example is the spinodal decomposition of alloys [20-22], as shown in Figure 2.3. Because of the conservation property, CH equation has been extensively used in the 'reaction-diffusion' systems, achieving notable success in biological problems, such as tumor growth dynamics [23, 24], cell mobility [25], and cellular aggregation [26].

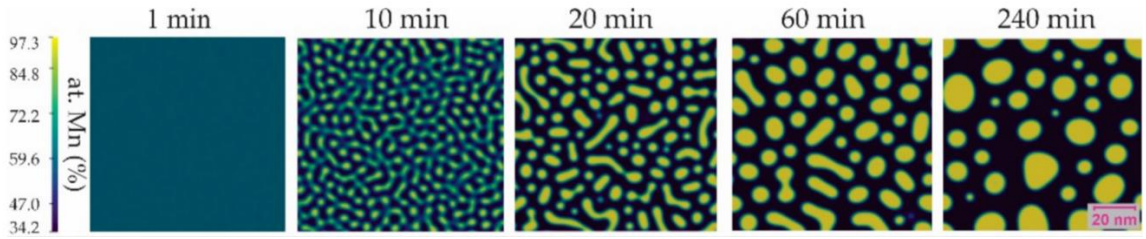

Figure 2.3 Spinodal decomposition of Mn-30 at. %Cu alloy at 300 ℃ from 1 min to 240 min. [27]

The AC equation, also known as time-dependent Ginzburg-Landau equation, describes the non-conserved order parameter, which was first utilized in a superconductivity theory [28]. The specific formulation in Eq. 2.5 was later established within phase-field theory proposed by Allen and Cahn in 1977 [29]. This equation has proven particularly effective for modeling order-disorder transitions in material systems. The AC framework is subsequently extended to multi-phase systems by Fan and Chen [19] establishing its utility for studying polycrystalline metal microstructure evolution [30]. The equation's versatility is evidenced by its successful application to diverse materials phenomena, including: precipitation [31, 32], grain growth [19, 33], and martensitic transformation [34-36]. The PF simulation of martensitic transformation is shown in Figure 2.4.

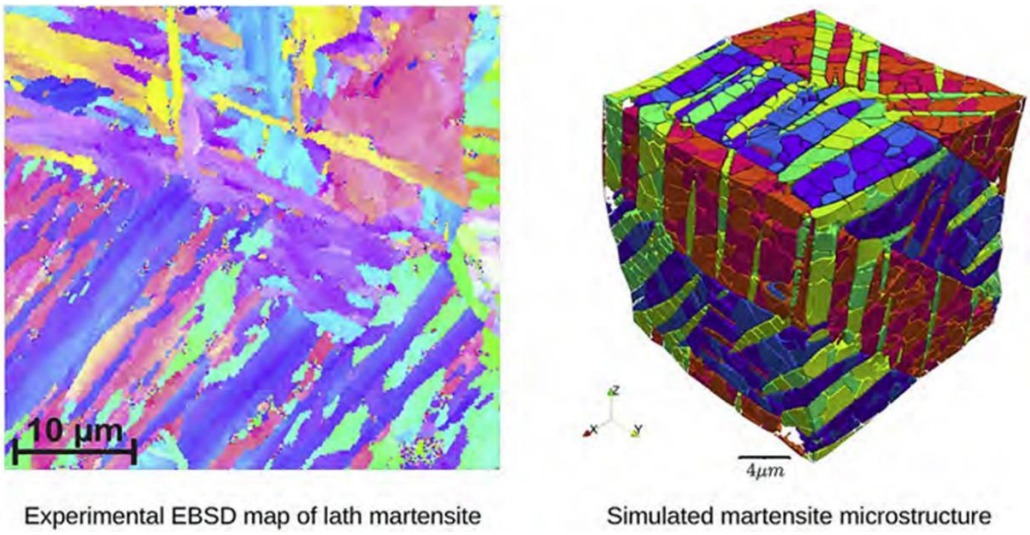

Figure 2.4 Martensitic microstructures in low-carbon steels: (left) EBSD orientation maps of a steel containing 0.3 wt%C and (right) phase-field simulated microstructure with color map showing the 24 Kurdjumov-Sachs orientation variants [36].

In PF modeling, the CH and AC equations are often coupled to concurrently describe the evolution of conserved and non-conserved order parameters within a unified theoretical framework, enabling comprehensive simulation of complex interactions between different physical quantities.

Over decades of development, PF modeling has emerged as a fundamental computational framework for investigating multi-physics phenomena [37, 38], with particularly successful applications in mechano-electrochemical systems. In these systems, coupled PF models have been effectively employed to study various corrosion mechanisms [39-41], demonstrating the PF method's capability to capture the intricate interplay between mechanical deformation, electrochemical reactions, and microstructural evolution.

2.1.2 PF fracture models

PF methods have achieved remarkable success not only in material science but also in computational mechanics, particularly in fracture mechanics [42, 43]. By treating cracks as a specific phase, the PF approach enables the simulation of fracture phenomena through a diffusive crack representation, thereby overcoming the fundamental challenges associated with modeling discontinuities in conventional fracture mechanics. This

innovative approach has led to the ongoing development of various PFFMs designed to address diverse fracture problems [44-47]. PFFMs simulate crack initiation, propagation, and branching through the minimization of a system's free energy, expressed as an energy functional. Based on their free energy formulations, PFFMs can be classified into two primary categories: 1. Landau-Ginzburg-based PFFM; 2. Griffth-theory-generalized PFFM.

To overcome the difficulty in describing the singularity and discontinuity of cracks, the continuum two-field fracture model was first proposed by Aranson *et al.* [48]. In this continuum model, the order parameter is governed by pure dissipative dynamics derived from the 'free energy' type functional, namely the Landau-Ginzburg type evolution. This model successfully reproduced crack propagation and energy dissipation; however, it failed to relieve the bulk strain and thus caused a logarithmic dependence of the crack opening on the system size [42]. Additionally, discrepancies were observed between numerical results and experimental observations. Inspired by solidification PF model [13, 49], a PPFM based on the two-minimum Landau-Ginzburg equation is proposed by Karma *et al.* [42], referred to as Landau-Ginzburg-based PFFM in this thesis. Without any additional prerequisites, the characteristic crack branching instability is achieved by using this Landau-Ginzburg-based PFFM, as shown in Fig. 2.5 [43].

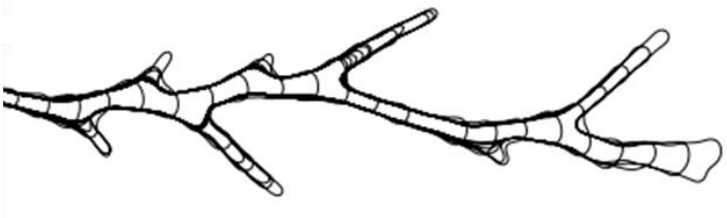

Figure 2.5 Contour of order parameter $\phi = 0.5$ Crack branching[42].

Consistency with the conventional PF formulation enables seamless integration of diverse energy into the total free energy functional of the system under investigation. This characteristic allows the free energy functional to comprehensively describe order parameter evolution under the influence of multi-physical driving forces. Consequently, Landau-Ginzburg-based PFFMs provide a robust framework for addressing multi-physics fracture phenomena, particularly material degradation under environmental attack, as

reported in ref. [39, 50-54].

SCC is a typical multi-physical cracking problem, which involves complex coupling between mechanical and electrochemical factors, as illustrated in Figure 2.6. Kovacevic *et al.* [44] developed a mechano-electrochemical PFFM, whose fracture term adheres to Landau-Ginzburg-based PFFM. Similar formulation of PFFM is also reported in ref. [45], in which the HIC is quantitatively analyzed within the same PF framework.

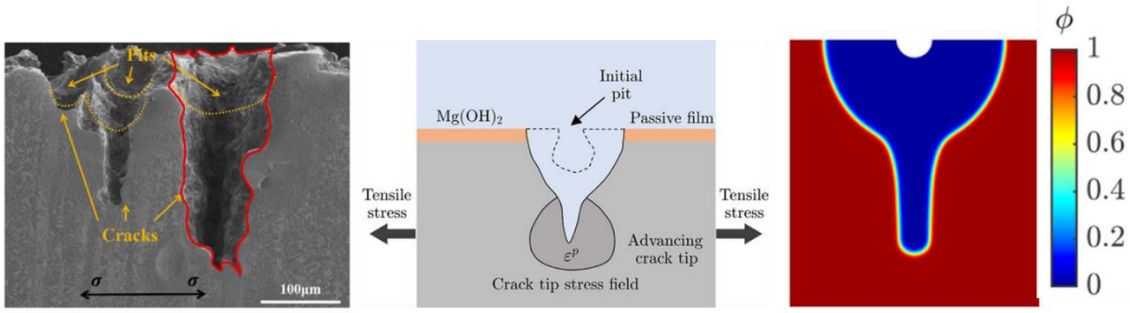

Figure 2.6 Experimental observation of SCC [55], schematic of SCC, and Landau-Ginzburg-based PFFM result [44].

Despite the fact that the Landau-Ginzburg-based PFFM has been widely adopted, it has certain limitations from mechanical perspective. Specifically, the length scale of a crack is not introduced to regularize a diffusive crack, resulting in the omission of fracture energy in the total free energy [56]. Additionally, the mechanical energy evolution violates the physical laws; that is, the energy dissipation fluctuates with continuous crack growth instead of increasing monotonically [57, 58]. To address these issues, Griffith-theory-generalized PFFMs were developed to extend classical Griffith fracture theory through the introduction of a length scale parameter for crack regularization [59, 60]. During crack growth, these models ensure the strain energy decreases, fracture energy increases, and the sum of these two energies continuously declines.

The theoretical foundation stems from Francfort and Marigo's variational formulation of brittle fracture [61], which explicitly incorporates Griffith's fracture energy G_c to quantify crack initiation and propagation. Introducing an auxiliary scalar s continuously transiting between s =1 (intact material) and s =0 (full damaged material),

Bourdin *et al*.[62] developed a regularized version of variational formulation. The fracture energy term in total free energy is no longer strongly discontinuous; instead, there exists a transition zone between the fully damaged and intact regions, of whose length scale is controlled by parameter Υ . When $\Upsilon \to 0$, the regularized approach can be recovered to the original discontinuous variational approach in the sense of Γ-convergence[63].

By implementing the variational free energy proposed in ref. [62], Kuhn and Muller [64] considered the cracking phenomenon as a phase transition and consequently derived the Landau-Ginzburg-type evolution to describe the cracking process. However, due to the lack of distinction between compression and tension in fracture mechanics, some unrealistic crack patterns are obtained [62, 64]. Amor *et al*. resolved these issues by decomposing the elastic energy into volumetric and deviatoric components, ensuring that crack occurs exclusively under tension [65].

The aforementioned PFFMs incorporating Griffith fracture energy G_c maintain their evolution equations within the Landau-Ginzburg framework, reflecting the enduring influence of conventional PF paradigms. A groundbreaking work by Miehe *et al*.[59, 60] developed a thermodynamically consistent PFFM grounded exclusively in the continuum mechanics and Griffith fracture theory [3]. In this Griffith-theory-generalized PFFM, the order parameter ϕ (with $\phi = 1\text{-}s$) possesses a clear physical interpretation for crack width regulation, rather than merely smearing out discontinuous crack path (detailed mathematical expression in **Chapter 3.2)**. The sketch of a discrete fracture and the PF representation in one dimension are shown in Fig. 2.7. with $\phi(x)$ depending on the distance from crack center.

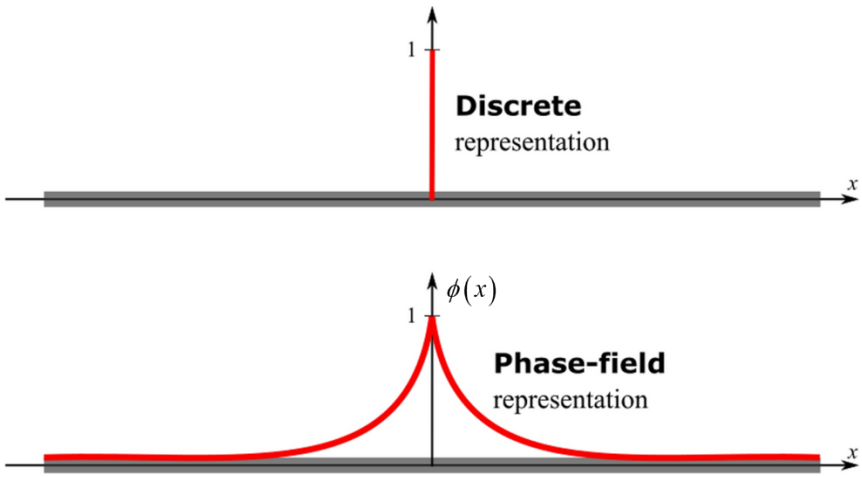

Figure 2.7 Sketch of a discrete fracture (top) and the PF representation (bottom) [66].

In their work [59, 60], the elastic energy is decomposed using the spectral decomposition of strain tensor to simplify the calculations in PFFM; that is only principal strains and their directions are involved. Given this simplification, Miehe's model brings about a highly non-linear stress-strain relationship [56]; the model's expression is explicitly illustrated in ref. [67], necessitating sophisticated algorithms for fourth-order isotropic tensor operations [68]. The model's validity has been confirmed through fundamental benchmark tests in purely mechanical systems [59, 60].

Subsequent extensions have successfully addressed various multi-physics fracture phenomena, including: HIC [69, 70], SCC [71, 72], and electrode cracking [73, 74]. Compared to Landau-Ginzburg-based PFFM, a significant strength of Griffith-theory-generalized PFFM is the straightforward implementation in three-dimensional simulations, as shown in Fig. 2.8. Furthermore, the crack initiation, growth and coalescence can be automatically determined through energy minimization. The complex crack interactions, merging and branching of multiple cracks, are observed in dynamic mode of Griffith-theory-generalized PFFM without additional efforts or presumption [57].

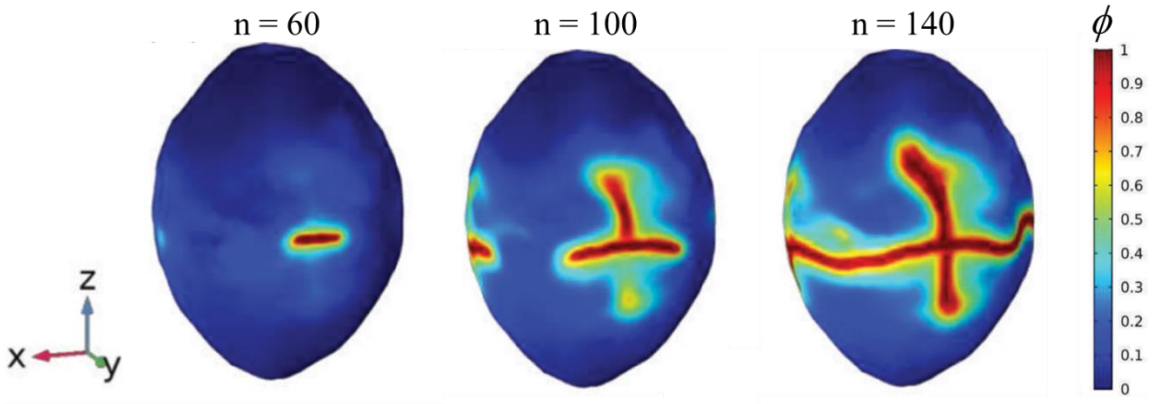

Figure 2.8 3D realistic lithium electrode particle: evolution of the fracture order parameter ϕ contours for n cycles [75].

Given the complex multi-physics coupling inherent in ASSLMBs, we employ a Landau-Ginzburg-based PFFM to investigate solid-state electrolyte fracture during electrochemical cycling. For the analysis of IOX-strengthened thin glass, we utilize a Griffith-theory-generalized PFFM. The prior research of these two cracking phenomena is systematically reviewed in the following two subsections, respectively.

2.2 Solid-State Electrolyte (SSE) Cracking

ASSLMBs represent a promising next-generation energy storage technology, offering superior energy density and enhanced safety through the implementation of metallic lithium anodes and non-flammable SSEs [76, 77]. Early optimism stemmed from the Monroe-Newman conception [78] that SSEs with shear modulus twice that of lithium could effectively suppress dendrite formation. This led to the expectation that developing inorganic SSEs with ionic conductivity comparable to liquid electrolytes would enable practical ASSLMB applications. However, despite significant advancements in synthesizing highly conductive inorganic SSEs over the past decade, persistent lithium dendrite penetration through SSEs continues to cause short-circuit failures. Hence, the endeavor on lithium metal batteries (LMBs) returns to the lithium-dendrite problem. Unlike conventional LMBs with liquid electrolyte, the mechanical failure mechanisms in ASSLMBs are particularly counterintuitive, especially in systems satisfying the Monroe-

Newman criterion.

How can soft lithium dendrites penetrate hard SSEs? Experiments revealed several facts: (i) Li/SSE interface generally exhibit high impedance [79], (ii) current density cannot exceed a critical value [80, 81], and (iii) lithium dendrites are observed to grow within SSE cracks [81]. Based on these findings, several hypotheses have been proposed: (1) the asperity contact between Li and SSE could increase the interfacial impedance and bring down the critical current density (CCD) [80, 82], (2) the formation of solid electrolyte interface (SEI) between Li and SSE could bring about cracks and dendrites, (3) the Li^+ reduction could occur inside SSE [83], and (4) the void formation in a stripping process could result in SSE cracks and Li dendrites in the subsequent plating process [81, 84].

Asperity contact can be attenuated by polishing SSE surfaces and applying a stack pressure [85, 86]. Given lithium's yield strength range of 0.57-1.26 MPa [87], a stack pressure of approximately 1 MPa should theoretically suffice to maximize interfacial contact. Higher stack pressure leads to hydrostatic stress due to friction [88] and is unnecessary; even worse, it may accelerate SSE mechanical degradation [89, 90]. When properly optimized, stack pressure can bring about enhanced interfacial conductivity [90], microcracks healing in SSE [91], and extended cycle life (> 200 electroplating-stripping cycles) before mechanical failure [89]. However, the choice of stack pressure to avoid mechanical failure of cells ranges from 0.1 MPa to 100 MPa [86, 92]. Many reported stack pressure substantially exceed lithium's yield strength, which is intended to force the flow of lithium to mitigate the contact loss caused by void formation [93], that is, the initial Li-SSE contact is not root cause of mechanical failure.

SEI is also an important factor that may either promote or prevent mechanical failure. While SEI effects in liquid electrolyte systems are well-characterized [94], their role in SSE-based cells remains ambiguous. Cheng *et al.* [95] investigated a LiPON-based cell and revealed the formation of a dense passive SEI that prevented dendrite formation. Sebastian et al. [96] compared $Li_{10}GeP_2S_{12}$ and $Li_{0.5}La_{0.5}TiO_3$ and revealed that the formation of electronically conductive Li-Ge alloy and titanates may promote dendrite

formation. However, SEI-induced mechanical failure is unverified due to the lack of *in situ* evidence. For example, the passive SEI of Li_6PS_5Cl, similar to the SEI of LiPON [95, 96], cannot prevent SSE cracking and dendrite penetration [84], which is distinct from what was hypothesized in [95].

Through a series of *in situ* experiments, Bruce and his collaborators [81, 84] unveils a mechanical failure mechanism distinct from previously proposed concepts. Their work [81] revealed that void formation during lithium stripping precedes subsequent dendritic growth during plating. Utilizing *in situ* X-ray computed tomography (XCT), Ning *et al.* [84] later observed spallation and cracks in an SSE (Li_6PS_5Cl) after plating above CCD. More importantly, they found lithium in the spalled zone but not in the tips of cracks in the early state of failure, i.e., cracks run faster than dendrites. Note that this mechanical failure process indicates that vacancies and voids, which are inevitable in stripping-plating cycles, are the root cause of mechanical failure. The question then becomes how to theorize this mechanism, which could ultimately bring about a computational tool to predict and optimize cell performances.

The complex multi-phase nature of ASSLMBs, with their migrating interfaces, makes PFM particularly suitable for capturing the coupled mechano-electrochemical processes. Yuan *et al.* [52] pioneered a mechano-electrochemical PFFM and introduced the Faraday stress [97] to describe cracking. Such stress assumes that a crack tip is always filled with lithium during plating, leading to ultrahigh stresses (several GPa) at dendrite/SSE interface when squeezing additional lithium. Later, Yuan *et al.* [98] involved the effects of stack pressure and grain boundaries in their PFM to simulate intergranular and intragranular crack propagations, as well as lithium plating in grain boundaries and cracks. However, these models assume direct SSE-to-lithium phase transformation, which contrasts with the crack-outrunning phenomenon observed experimentally [84]. Zhao *et al.* [99] developed a PFM to describe void evolution during stripping, revealing significant current density concentration at Li-void-SSE triple-phase boundaries. However, the subsequent SSE cracking caused by this concentrated current density, as observed in [81, 84], has not been modeled.

In this thesis, we developed a novel mechano-electrochemical multiple-phase PFFM that explicitly incorporates with the key ingredients of void formation [81, 100] and crack propagation [84, 101]. Using this model, several experimental findings can be vividly reproduced enabling further study of parametric effects, in particular those causing different CCD. Furthermore, it provides a platform for evaluating potential solutions to SSE cracking and dendrite penetration challenges.

2.3 Fracture of Ion-Exchange (IOX)-strengthened glass

The proliferation of portable electronics with touch screens has made thin cover glass an essential component, providing both transparency and mechanical protection. While the theoretical strength of glass reaches up to 16 GPa due to its strong ionic and covalent bonding [102], its practical strength varies in a range of 10-100 times lower due to the presence of Griffith flaws[103], particularly surface defects introduced during manufacturing and handling processes [104]. To alleviate the impact of surface flaws, the IOX technology, started in the early 20th century and industrialized after Kistler [105] as well as Acloque and Tochon [106] in 1962, is employed to strengthen thin glass. This strengthening effect stems from inducing CS of several hundred MPa in the vicinity of glass surfaces [107] by replacing smaller host ions with larger foreign ions [108]. For example, an alkali-aluminosilicate glass immersed in a KNO_3 melt to exchange K^+ and Na^+ can produce a surface bi-axial CS of 500-900 MPa [109]. It was demonstrated theoretically [110] and experimentally [111] that this level of CS can make glass insensitive to surface flaws, rendering an improved fracture strength.

IOX strengthening has been widely used in the glass industry for decades [112, 113] and has achieved great commercial success [114]. However, it is still obscure how to design IOX that can meet the increasingly stringent requirements of cover glass. For example, it is unclear how the key indicators of an IOX process, namely surface CS and DOL under compression, can be related to fracture strengths measured in various quasistatic loading experiments and the impact velocity in BD experiments, let alone that experimental data in these experiments are significantly scattered. This knowledge gap forces manufacturers

to rely on empirical trial-and-error approaches for each IOX strengthening cover glass product.

Numerous experimental investigations have been conducted to elucidate how surface CS and DOL alter the fracture process of thin glass. These studies have led to diverse understandings regarding the effects of surface CS and DOL. Based on ROR experiments, Egboiyi and Sain [104] concluded that increasing surface CS was more effective than increasing DOL in inhibiting a shallow crack, and vice versa for a deep crack. Morris *et al.* [115] also observed the suppression of shallow cracks during Vickers indentation when the indentation depths were less than DOL. In contrast, Li *et al.* [116] observed radial cracks initiated from a shallow crack caused by a cube-corner indenter and found that cracks initiated in an post-IOX glass more easily than in the pre-IOX glass samples. Green *et al.* [117] asserted that the CS at the tip of the surface flaws was the most effective factor in hindering crack propagation instead of surface CS or DOL. These different views demonstrate the uncertainty of the glass fracture process under residual stresses, especially given that the distribution and severity of surface defects in a glass sample are generally unknown. IOX can reduce the sensitivity of glass to surface flaws but cannot completely desensitize surface flaws. As a result, the strengths of post-IOX glass samples are still widely distributed [108, 118, 119], and experimental investigations of glass fracture in a residual-stress field are limited by these uncertainties. Therefore, computational models of glass fracture are necessary to reveal the details of the fracture process in post-IOX glass.

The fracture behavior of brittle materials has been extensively investigated over several decades[120, 121], leading to the development of various numerical approaches, including the extended finite element method [122, 123], peri-dynamics [10, 124], molecular dynamics [125, 126], and Griffith-theory-generalized PFFM [59, 60]. Among these, PFFM stands out as a variational approach that operates within a continuous framework, replacing sharp cracks with a diffusive representation to circumvent the mathematical and computational challenges posed by discontinuities [62]. The variational structure of PFFM enables its seamless integration with multi-physics phenomena, such as

electrochemical processes in solid-state batteries [51, 52, 99] or SCC [127]. Furthermore, PFFM relies solely on energy minimization, eliminating the need for predefined crack paths. So that the description of crack initiation, extension, branching, and multiplication can be reproduced in the same theoretical framework without additional effort in defining crack propagation paths or other strenuous strategies [57]. Given these advantages, PFFM is particularly well-suited for quantitatively analyzing the fracture behavior of IOX-strengthened glass. To our knowledge, Egboiyi *et al.* [118] pioneered the application of PFFM to simulate ROR experiments for post-IOX glass sheets with pre-existing cracks. Their model successfully predicted damage profiles and the influence of crack depth on fracture strength. However, their analysis was restricted to small-strain theory, despite experimental [128] and computational [108] evidence that thin glass undergoes large deformation in ROR experiments.

In this thesis, we implemented Griffith-theory-generalized PFFM within a large deformation framework to investigate both pre-IOX and post-IOX glass fracture with an emphasis on the impact of CS distribution and DOL. We first calibrated our model against experimental results, followed by a systematic examination of surface flaw effects in IOX-treated glass. Finally, we present contour maps that quantitatively relate surface CS and DOL to fracture strength, as measured by ROR and BD experiments. These findings provide critical insights for optimizing IOX strengthening processes in industrial applications.

2.4 AI-accelerated Solutions

Both Landau-Ginzburg-based PFFM and Griffith-theory-generalized PFFM are formulated by establishing PDEs, for instance, the AC and CH equations given by Eqs. 2.4-2.5. PDEs are foundational for modeling a wide range of scientific and engineering phenomena. However, obtaining analytical solutions to these equations is often infeasible, especially for complex or nonlinear systems. As a result, numerical solvers have become indispensable tools. Achieving high accuracy with these solvers can be computationally expensive, particularly when applied to multiscale and multi-physics systems. The

accuracy of numerical methods is strongly influenced by mesh resolution — denser meshes yield higher accuracy but incur significantly higher computational costs. Moreover, many scientific and engineering applications — such as design optimization, sensitivity analysis, and uncertainty quantification — require repeated solutions of these equations for different parameter settings, further compounding the computational burden.

Surrogate models have gained significant attention for their ability to emulate high-fidelity simulations at a fraction of the computational cost [129-132]. In the rapidly growing field of SciML, deep neural networks (DNNs) are increasingly used as emulators to analyze, solve, and optimize systems governed by PDEs [133-135]. These models are typically trained on a finite set of labeled data, generated from expensive traditional solvers such as finite difference methods, FEM, or computational fluid dynamics methods. Once trained, these models offer fast and accurate predictions under varying initial conditions, boundary conditions, system parameters, and geometric configurations.

Among these surrogate approaches, neural operators, which learn mappings between infinite-dimensional function spaces, have emerged as a powerful class of emulators [136-139]. However, neural operators often suffer from limited generalization capabilities unless they are trained as heavily overparameterized networks [140-142]. High-dimensional systems require models with large trainable parameters to capture the underlying physics, which can reduce their robustness and scalability. Additionally, these models struggle with multiscale, multi-physics problems, where capturing complex interactions across spatial and temporal scales is critical. They also tend to accumulate errors over long-time integrations, making them less reliable for dynamic systems [143-146].

While both traditional numerical solvers and DNN-based surrogate models offer unique strengths, they each face fundamental limitations in scalability, reliability, and generalization for large-scale, multi-physics problems. To overcome these challenges, domain decomposition methods (hereafter referred to as DDM), long used to build parallel, scalable solvers for PDEs-offer a promising framework [147-151]. Non-overlapping

substructuring methods such as FETI (Finite Element Tearing and Interconnecting) [152, 153], BDDC (Balancing Domain Decomposition by Constraints) [154], and their boundary-element coupled variants (BETI) [155, 156] have long provided scalable parallel solvers for PDEs. These methods "tear" the global mesh into independent subdomains and enforce continuity via Lagrange multipliers or primal constraints, yielding parallelizable reduced interface systems. More recently, hybrid schemes that combine traditional FE discretization with neural-network surrogates have emerged [146, 157-161]. For instance, FEMIN [159] replaces large regions of finite element crash simulation meshes with neural networks that predict interface forces based on kinematic data, thereby accelerating vehicle crash simulations; DNNMG [160] uses neural networks to predict fine-scale corrections to coarse finite element solutions, speeding up nonlinear FE calculations; and I-FENN [161] introduces a framework that embeds physics-informed neural networks directly into the finite element stiffness function to solve non-local damage mechanics problems at the computational cost of local damage approach. These approaches typically replace or augment parts of the FE solving with learned components, achieving orders-of-magnitude speedups in certain regimes.

In this work, we present a DDM-based hybrid solver that combines traditional numerical methods with physics informed operator learning-based surrogates to accelerate simulations while preserving accuracy. While DDMs have been extensively employed in SciML for data parallelism, model parallelism, and pipeline optimization, our work introduces a novel framework that uniquely integrates pre-trained physics-informed neural operators with numerical solvers, enabling seamless spatial coupling rather than merely decomposing computational tasks. The core idea is to identify subdomains that are computationally demanding, due to fine-scale features or non-linearities, and approximate them using a DeepONet-based neural operator. The remaining regions, which can be efficiently handled with coarser resolution, are solved using a standard numerical method. The two solvers communicate via an overlapping interface using a Schwarz-type coupling scheme to ensure consistency and continuity [162-164]. We first demonstrate the effectiveness of this hybrid framework on a linear elastic system under static loading, followed by a more complex quasi-static hyper-elastic problem. To handle dynamic

systems, we incorporate a numerical time integrator-specifically the Newmark-Beta method into the neural operator architecture [165, 166]. This integration significantly mitigates error accumulation in longtime simulations, a known limitation of purely data-driven models. Finally, we introduce an adaptive subdomain evolution strategy, where the ML-based subdomain dynamically expands to capture emerging fine-scale features such as stress concentrations, reducing the portion of the domain requiring costly numerical solutions. This not only improves computational efficiency but also opens the door to more autonomous and scalable multiscale simulation pipelines. Key innovations of our framework include:

- Adaptive Coupling: A Schwarz alternating method facilitates efficient information exchange between FE and neural operator subdomains through overlapping interfaces, maintaining solution continuity while balancing accuracy and efficiency.

- Temporal Integration: A Newmark-Beta time-stepping scheme embedded within the neural operator to significantly reduce the long-time error accumulation in dynamic systems, addressing a key limitation of traditional data-driven ML approaches.

- Dynamic Subdomain Optimization: An adaptive algorithm allows the neural operator region to grow in response to evolving fine-scale features (e.g., stress localization), reducing dependence on dense mesh refinements and enhancing overall performance.

Chapter 3 Methodology

3.1 Landau-Ginzburg-based Phase-Field Fracture Model

The total Helmholtz free energy for $\mathcal{F}$ the mechano-electrochemical system can be expressed as:

$$\mathcal{F} = \int_{\Omega} f \mathrm{d}\omega = \int_{\Omega} f_{\mathrm{mech}} + f_{\mathrm{chem}} + f_{\mathrm{int}} + f_{\mathrm{elec}} \mathrm{d}\omega \tag{3.1}$$

where Ω is the system domain, f represents the free energy density, f_{mech} f_{chem} f_{int} and f_{elec} denote the mechanical energy density, chemical potential energy density, interface energy density, and electric energy density, respectively. And the order parameters **p** and concentrations **c** are two sets of variables given by:

$$\mathbf{p} = \{p_1, p_2, p_3\} = \left\{ \frac{c_{\mathrm{Li}}}{c_1^{\mathrm{ref}}}, \frac{c_{\mathrm{Li}^+}}{c_2^{\mathrm{ref}}}, \frac{c_{\mathrm{v}_2}}{c_3^{\mathrm{ref}}} \right\} \tag{3.2}$$

$$\mathbf{c} = \left\{ c_{Li}, c_{Li^+}, c_{v_1}, c_{v_2}, c_{e^-} \right\} \tag{3.3}$$

note that p_1, p_2 and p_3, representing lithium, SSE, and void (or crack), respectively, can be equal to $\overline{c_*} = \frac{c_*}{c_i^{\mathrm{ref}}}$ with $* \in \{\mathrm{Li}, \mathrm{Li}^+, v_2\}$ where c_i^{ref} denotes the saturated concentration of the species * in the corresponding phase i. This treatment relates the order parameters **p** with the concentrations of the main reactive species in the diffusion-reaction system. Hence, the change of order parameters, rendering interface migration in the PFM, can be related to the corresponding kinetic equations governing chemical reactions. In Eq. (3.3), we consider two kinds of vacancies, i.e., v_1 and v_2, respectively. The former is vacancies in SSE which can merge to nucleate voids or diffuse into voids to make them grow. The latter only occurs in Li/void interface that makes voids grow or shrink (e.g., through Li creep). Hereunder, we write out the expressions for each energy density contribution.

The electric potential energy density can be expressed as:

$$f_{\text{elec}} = F\left(\varphi_{\text{SSE}} c_{\text{Li}^+} - \varphi_{\text{Li}} c_{e^-} + \varphi_{\text{Li/SSE}} c_{v_1}\right) \tag{3.4}$$

where F, φ_{SSE}, φ_{Li}, and $\varphi_{\text{Li/SSE}}$ are the Faraday constant, electric potential in SSE, in Li electrode, and that in Li/SSE interface, respectively. For the vacancies in metal, previous studies [167-170] point out that the charge on metal surface can influence the chemical potential of vacancies. Thus, the charged vacancies constitute a part of f_{elec}. Because the reactions referring to vacancies occur only in the Li/SSE interface, the relevant electric potential energy density is proportional to $\varphi_{\text{Li/SSE}}$.

The interfacial energy density expressed as:

$$f_{\text{int}} = \sum_{i}^{n=3}\left(\frac{K_i}{2}\left|\nabla p_i\right|^2\right) \tag{3.5}$$

where K_i are the gradient-energy coefficient of phase *i*. The chemical potential energy density can be expressed as:

$$\begin{aligned} f_{\text{chem}} = &\sum_{i}^{n=3}\left(H_i p_i^2\left(1-p_i\right)^2\right) + c_{\text{Li}^+}\left(\mu^0_{\text{Li}^+} - RT\right) + c_{\text{Li}^+} RT \ln\left(\overline{c_{\text{Li}^+}}\right) + c_{\text{Li}}\mu^0_{\text{Li}} + c_{v_2}\mu^0_{v_2} \\ &+ c_{\text{Li}} RT \ln\left(\overline{c_{\text{Li}}}\right) + c_{e^-}\left(\mu^0_{e^-} - RT\right) + c_{e^-} RT \ln\left(\overline{c_{e^-}}\right) + c_{v_1}\left(\mu^0_{v_1} - RT\right) + c_{v_1} RT \ln\left(\overline{c_{v_1}}\right) \end{aligned} \tag{3.6}$$

where the first term is the well-known double-well function to ensure the existence stability for the phase. H_i is the height of the energy barrier for each phase, R molar gas constant, T temperature, and μ^0_* the standard chemical potential. The mechanical energy density is the strain energy considering crack propagation, which, according to Alain [42, 43, 171], is expressed as:

$$f_{\text{mech}}\left(\mathbf{p}\right) = g\left(p_3\right)\left(\xi - \xi_{\text{cr}}\right) + \xi_{\text{cr}} \tag{3.7}$$

$$\xi = \frac{1}{2}\left[\boldsymbol{\varepsilon}^{\mathrm{e}}(\mathbf{p})\left(\mathbf{D}(\mathbf{p})\boldsymbol{\varepsilon}^{\mathrm{e}}(\mathbf{p})\right)\right] \tag{3.8}$$

where $\mathbf{D} = P(p_1)\mathbf{D}_{\mathrm{Li}} + P(p_2)\mathbf{D}_{\mathrm{SSE}} + P(p_3)\mathbf{D}_{\mathrm{void}}$ is the stiffness matrix involving three phases in which the subscripts "Li", "SSE" and "void" indicate the three phases, $P(x) = x^3\left(10 - 15x + 6x^2\right)$ the interpolation function frequently used in PFMs [172, 173] , and $\boldsymbol{\varepsilon}^{\mathrm{e}}$ the elastic strain. The function $g(.)$ is defined as [42]: $g(x) = (1-x)^3(1+3x)$. In an inorganic SSE, we assume volumetric chemical strains $\boldsymbol{\varepsilon}^{\mathrm{mis}}$ due to the interstitial insertion or depletion of Li^+[174], along with the partial molar volume Ω^{SSE}, i.e.,

$$\boldsymbol{\varepsilon}^{\mathrm{mis}} = \varepsilon^{\mathrm{mis}}\mathbf{I} = \Omega^{SSE}\left(c_{\mathrm{Li}^+} - c^0_{\mathrm{Li}^+}\right)\mathbf{I} \tag{3.9}$$

Note that the concept of chemical strain $\boldsymbol{\varepsilon}^{\mathrm{mis}}$ has been widely used in mechano-electrochemical models [173-175], For example, Wan and Ciucci [174] described $\boldsymbol{\varepsilon}^{\mathrm{mis}}$ induced by Li^+ transport in LiPON, and Zuo and Zhao [175] simulated the cracking of an electrode caused by $\boldsymbol{\varepsilon}^{\mathrm{mis}}$. In addition, in solid oxide fuel cells, such a chemical strain, caused by oxygen insertion and depletion, has been experimentally measured [176]. Following these works, we introduce Eq. 3.9 to describe the mechanical response of an SSE in conducting Li^+.

The total strain tensor $\boldsymbol{\varepsilon}$ is obtained from a displacement field $\mathbf{u}$ as:

$$\boldsymbol{\varepsilon} = \frac{\left(\nabla\mathbf{u} + (\nabla\mathbf{u})^{\mathrm{T}}\right)}{2} \tag{3.10}$$

In lithium, the creep mainly affects its deformation [82], so the creep strain tensor $\boldsymbol{\varepsilon}^{\mathrm{cr}}$ is involved, i.e., $\boldsymbol{\varepsilon}^{\mathrm{e}} = \boldsymbol{\varepsilon} - \boldsymbol{\varepsilon}^{\mathrm{cr}} - \boldsymbol{\varepsilon}^{\mathrm{mis}}$. The variation of $\boldsymbol{\varepsilon}^{\mathrm{cr}}$ under a stress tensor $\boldsymbol{\sigma}$ is governed by a power law [177-180]:

$$\frac{\partial \boldsymbol{\varepsilon}^{\mathrm{cr}}}{\partial t} = A_c \left(\frac{\sigma_{\mathrm{m}}}{\sigma_{\mathrm{ref}}} \right)^n \frac{3}{2} \frac{\mathrm{dev}(\boldsymbol{\sigma})}{\sigma_{\mathrm{m}}} \tag{3.11}$$

where A_c, σ_m, σ_{ref}, and n are the creep parameters, von Mises stress, reference stress, power-law-creep exponent, respectively, and dev($\boldsymbol{\sigma}$) indicates the deviatoric part of the stress tensor.

In ASSLMBs, we consider the following electrochemical reactions for a stripping process:

$$\mathrm{Li} \rightarrow \mathrm{Li}^+ + v_1 + \mathrm{e}^- \tag{3.12}$$

$$\mathrm{Li} \rightarrow \mathrm{Li}^+ + v_2 + \mathrm{e}^- \tag{3.13}$$

where v_1 and v_2 represent vacancies appear in the Li/SSE interfaces and the Li/Void interfaces, respectively. Correspondingly, the electrochemical reactions for plating are expressed as:

$$\mathrm{Li}^+ + \mathrm{e}^- + v_1 \rightarrow \mathrm{Li} \tag{3.14}$$

$$\mathrm{Li}^+ + \mathrm{e}^- + v_2 \rightarrow \mathrm{Li} \tag{3.15}$$

For stripping and plating, the reaction rates r_s and r_p are, respectively, given by:

$$r_s = -\frac{\partial c_{\mathrm{Li}}}{\partial t} = -c_1^{\mathrm{ref}} \frac{\partial p_1}{\partial t} = \frac{\partial c_{\mathrm{Li}^+}}{\partial t} = c_2^{\mathrm{ref}} \frac{\partial p_2}{\partial t} \tag{3.16}$$

$$r_p = \frac{\partial c_{\mathrm{Li}}}{\partial t} = c_1^{\mathrm{ref}} \frac{\partial p_1}{\partial t} = -\frac{\partial c_{\mathrm{Li}^+}}{\partial t} = -c_2^{\mathrm{ref}} \frac{\partial p_2}{\partial t} \tag{3.17}$$

Note that the reaction rates for stripping and plating only differ in the sign of convention; hereunder we only give expression of r_s. Stripping is a kinetic process containing both forward and backward reactions. The net reaction rate is expressed as:

$$r_s = r_{1\to 2} - r_{1\leftarrow 2} = k_0\left(\exp\left(-\frac{\left(\mu_{\mathrm{TS}}^{\mathrm{ex}} - \mu_1^{\mathrm{ex}}\right)}{RT}\right) - \exp\left(-\frac{\left(\mu_{\mathrm{TS}}^{\mathrm{ex}} - \mu_2^{\mathrm{ex}}\right)}{RT}\right)\right) \tag{3.18}$$

where $r_{1\to 2}$ and $r_{1\leftarrow 2}$ are the forward and backward reaction rates respectively, $\mu_{\mathrm{TS}}^{\mathrm{ex}}$, μ_1^{ex}, and μ_2^{ex} are the excessive electrochemical potentials for the transition, initial, and final states, respectively, and k_0 the kinetics constant. Eq. 3.18 is a modified form of the Butler-Volmer equation, which has been widely adopted in phase-field modeling in the studies of corrosions and oxidations [39, 177, 181].

The electrochemical potential, rationalized to be the functional derivatives of Helmholtz free energy with respect to the corresponding concentration, are expressed as:

$$\mu_1 = \frac{\delta \mathcal{F}}{\delta c_{\mathrm{Li}}} = \mu_1^{\mathrm{int}} + \frac{1}{2c_1^{\mathrm{ref}}} g\left(p_3\right)\left[\boldsymbol{\varepsilon}^{\mathrm{el}}\left(\frac{\mathrm{d}\mathbf{D}}{\mathrm{d}p_1}\boldsymbol{\varepsilon}^{\mathrm{el}}\right)\right] + \mu_{\mathrm{Li}}^0 \tag{3.19}$$

$$\begin{aligned}\mu_2 &= \frac{\delta \mathcal{F}}{\delta c_{\mathrm{Li}^+}} + \frac{\delta \mathcal{F}}{\delta c_{e^-}} + \frac{\delta \mathcal{F}}{\delta c_{v_1}} + \frac{\delta \mathcal{F}}{\delta c_{v_2}} \\ &= RT\ln\left(c_{e^-}c_{\mathrm{Li}^+}c_{v_1}\right) + \mu_2^{\mathrm{int}} - F\left(\varphi_{\mathrm{Li}} - \varphi_{\mathrm{SSE}} + \varphi_{\mathrm{Li/SSE}}\right) \\ &\quad + \mu_3^{\mathrm{int}} - g\left(p_3\right)\Omega^{\mathrm{SSE}}\mathrm{tr}\left(\boldsymbol{\sigma}\right) + \frac{1}{c_3^{\mathrm{ref}}}\frac{\mathrm{d}g\left(p_3\right)}{\mathrm{d}p_3}\left(\xi - \xi_{\mathrm{cr}}\right) + \mu_{\mathrm{Li}^+}^0 + \mu_{e^-}^0 + \mu_{v_1}^0\end{aligned} \tag{3.20}$$

where $\mu_i^{\mathrm{int}} = \frac{1}{c_i^{\mathrm{ref}}}\left(H_i p_i\left(1-p_i\right)\left(1-2p_i\right) - K_i\nabla^2 p_i\right)$ are the interfacial potentials with the subscript i representing phase 1, 2, and 3. According to Bazant *et al*. [182], the transition electrochemical potential can be expressed as a composition of excessive electrochemical potentials $\mu_1^{\mathrm{ex}}$and μ_2^{ex}:

$$\mu_{\mathrm{TS}} = \alpha\mu_1^{\mathrm{ex}} + \left(1-\alpha\right)\mu_2^{\mathrm{ex}} + RT\ln\left(a_{\mathrm{TS}}\right) \tag{3.21}$$

where α is the asymmetry parameter, a_{TS} the activity for the transition state, and the excessive electrochemical potentials can be defined as [182]:

$$\mu_*^{\mathrm{ex}} = \frac{\delta \int_S f - f_{\mathrm{chem}} - f_{\mathrm{int}} \mathrm{d}\omega}{\delta c_*} \tag{3.22}$$

Therefore, for initial and final states the excessive electrochemical potentials are respectively:

$$\mu_1^{\mathrm{ex}} = g\left(p_3\right) \frac{1}{2c_{\mathrm{Li}}^{\mathrm{ref}}} \left[\boldsymbol{\varepsilon}^{\mathrm{el}} \left(\frac{\mathrm{d}\mathbf{D}}{\mathrm{d}p_1} \boldsymbol{\varepsilon}^{\mathrm{el}} \right) \right] + \mu_{\mathrm{Li}}^0 \tag{3.23}$$

$$\mu_2^{\mathrm{ex}} = \mu_2^{\mathrm{electrochem}} + \mu_2^{\mathrm{elastic}} + \mu_2^{\mathrm{fracture}} \tag{3.24}$$

and these three terms can be expressed as:

$$\begin{aligned}
\mu_2^{\mathrm{electrochem}} &= -F\left(\varphi_{\mathrm{Li}} - \varphi_{\mathrm{SSE}} + \varphi_{\mathrm{Li/SSE}} \quad\right) + \mu_{\mathrm{Li}^+}^0 + \mu_{e^-}^0 + \mu_{v_{\mathrm{I}}}^0 \\
\mu_2^{\mathrm{elastic}} &= -g\left(p_3\right) \Omega^{\mathrm{SSE}} \mathrm{tr}\left(\boldsymbol{\sigma}\right) \\
\mu_2^{\mathrm{fracture}} &= \frac{1}{c_2^{\mathrm{ref}}} \frac{\mathrm{d}g\left(p_3\right)}{\mathrm{d}p_3} \left(\xi - \xi_{\mathrm{cr}}\right)
\end{aligned}$$

Substituting Eqs. 3.19, 3.20, 3.23, 3.24 into equation 3.18, assuming $RT >> \mu_{\mathrm{i}}^{\mathrm{int}}$ [173] and $RT >> \mu_2^{\mathrm{fracture}}$, and applying the Taylor expansion, the net reaction rate can be deduced as:

$$\begin{aligned}
r = & \frac{k_0}{a_{\mathrm{TS}} RT} \mu_1^{\mathrm{int}} \exp\left(\frac{\left(1-\alpha\right)\left(\mu_1^{\mathrm{ex}} - \mu_2^{\mathrm{ex}}\right)}{RT} \right) \\
& - \frac{k_0}{a_{\mathrm{TS}} RT} \left(\mu_2^{\mathrm{int}} + \mu_3^{\mathrm{int}}\right) \left(\overline{c_{e^-}}\, \overline{c_{\mathrm{Li}^+}}\, \overline{c_{v_{\mathrm{I}}}} \right) \exp\left(\frac{\alpha\left(\mu_2^{\mathrm{ex}} - \mu_1^{\mathrm{ex}}\right)}{RT} \right) \\
& + \frac{k_0}{a_{\mathrm{TS}}} \left(\exp\left(\frac{\left(1-\alpha\right)\left(\mu_1^{\mathrm{ex}} - \mu_2^{\mathrm{ex}}\right)}{RT} \right) - \left(\overline{c_{e^-}}\, \overline{c_{\mathrm{Li}^+}}\, \overline{c_{v_{\mathrm{I}}}} \right) \exp\left(\frac{\alpha\left(\mu_2^{\mathrm{ex}} - \mu_1^{\mathrm{ex}}\right)}{RT} \right) \right) \\
& - \frac{k_0}{c_3^{\mathrm{ref}} a_{\mathrm{TS}} RT} \left(\left(1-\alpha\right) + \alpha \left(\overline{c_{e^-}}\, \overline{c_{\mathrm{Li}^+}}\, \overline{c_{v_{\mathrm{I}}}} \right) \right) h_{23} H\left(\sigma_{\mathrm{I}}\right) \Psi\left(\xi\right) \frac{dg\left(p_3\right)}{dp_3} \left(\xi - \xi_{\mathrm{cr}}\right)
\end{aligned} \tag{3.25}$$

where $\mu_1^{\text{ex}} = \mu_1^{\text{ex}}$ and $\mu_2^{\text{ex}} = \mu_2^{\text{electrochem}} + \mu_2^{\text{elastic}}$.

Note that the fourth term on the right-hand side of Eq. 3.25 is the contribution of cracks, that is, the phase-field model based on the thermodynamics framework naturally brings in the effect of Griffith (surface) energy on the chemical process. Considering that a brittle SSE cracks under tensile stress, we require that the maximum principal stress σ_{I} must be positive to open cracks and that when the strain energy is larger than a critical value, cracks can propagate. Hence, we introduce a function $h_{23}H\left(\sigma_{\text{I}}\right)\Psi\left(\xi\right)$ in Eq. 3.25, where $H\left(\sigma_{\text{I}}\right)$ and $\Psi\left(\xi\right)$ are defined as:

$$H\left(\sigma_{\text{I}}\right) = \begin{cases} 1 & \text{if } \sigma_{\text{I}} > 0 \\ 0 & \text{if } \sigma_{\text{I}} \le 0 \end{cases} \text{ and } \Psi\left(\xi\right) = \frac{\tanh\left(\xi - \xi_{\text{cr}}\right) + 1}{2}$$

respectively. Note that cracks cannot be self-healed, that is, p_3 can only increase in SSE. This feature is realized by incorporating $\Psi\left(\xi\right)$.

Note that an advective term $\nabla\left(p_1\vec{V}_{\text{advective}}\right)$ is introduced into Eq. 3.26 governing the evolution of p_1. It accounts for the rigid-body motions [183, 184] as the centroid of the Li anode should move towards or away from the SSE during stripping or plating under a stack pressure. In addition, the creep of Li also leads to such a motion.

The Allen-Cahn equations [185] for the order parameters p_1 and p_2 are expressed as:

$$\begin{aligned} -\left.\frac{\partial p_1}{\partial t}\right|_{\text{d}} = \left.\frac{\partial p_1}{\partial t}\right|_{c} &= L_{s_1}\left(H_1 p_1\left(1-p_1\right)\left(1-2p_1\right) - K_1\nabla^2 p_1\right) - L_{s_2}\left(H_2 p_2\left(1-p_2\right)\left(1-2p_2\right) - K_2\nabla^2 p_2\right) \\ &- L_{s_3}\left(H_3 p_3\left(1-p_3\right)\left(1-2p_3\right) - K_3\nabla^2 p_3\right) + L_{k_1}h_{12}\left(\exp\left(\frac{\left(1-\alpha\right)\Lambda_{\text{c/d}}}{RT}\right) - \left(\overline{c_{e^-}}\,\overline{c_{\text{Li}^+}}\,\overline{c_{v_1}}\right)\exp\left(\frac{-\alpha\Lambda_{\text{c/d}}}{RT}\right)\right) \\ &+ L_{k_3}h_{13}\left(\exp\left(\frac{\left(1-\alpha\right)\Lambda_{\text{c/d}}}{RT}\right) - \left(\overline{c_{e^-}}\,\overline{c_{\text{Li}^+}}\,\overline{c_{v_1}}\right)\exp\left(\frac{-\alpha\Lambda_{\text{c/d}}}{RT}\right)\right) + \nabla\left(p_1\vec{V}_{\text{advective}}\right) \end{aligned} \tag{3.26}$$

$$\left.\frac{\partial p_2}{\partial t}\right|_{\mathrm{d}} = -\left.\frac{\partial p_2}{\partial t}\right|_{c} = L_{s_1}\left(H_1 p_1\left(1-p_1\right)\left(1-2p_1\right)-K_1\nabla^2 p_1\right)-L_{s_2}\left(H_2 p_2\left(1-p_2\right)\left(1-2p_2\right)-K_2\nabla^2 p_2\right)$$
$$-L_{s_3}\left(H_3 p_3\left(1-p_3\right)\left(1-2p_3\right)-K_3\nabla^2 p_3\right)+L_{k_2}h_{12}\left(\exp\left(\frac{\left(1-\alpha\right)\Lambda_{\mathrm{c/d}}}{RT}\right)-\left(\overline{c_{e^-}}\,\overline{c_{\mathrm{Li}^+}}\,\overline{c_{v_1}}\right)\exp\left(\frac{-\alpha\Lambda_{\mathrm{c/d}}}{RT}\right)\right) \quad (3.27)$$
$$-L_{\mathrm{cr}}h_{23}H\left(\sigma_{\mathrm{I}}\right)\frac{dg\left(p_3\right)}{dp_3}\Psi\left(\xi\right)\left(\xi-\xi_{\mathrm{cr}}\right)$$

where L_{s_i} is the coefficient to scale the contribution of the interfacial energy to the phase migration for phase *i*, $L_{k_i}$is the coefficient to scale the contribution of reaction kinetics to the phase migration for phase *i*, L_{cr} is to regulate crack propagation rate in SSE, $\mathrm{h_{ij}} = \frac{4\mathrm{p_i p_j}}{\sum_{\mathrm{i}} \mathrm{p_i^2}}$ [186, 187] is to constrain the reaction in the interface of phase p_i and p_j, and $\Lambda_{\mathrm{c/d}}$ denotes the dimensionless reaction driving force for charge or discharge. These scaling terms are expressed as:

$$L_{s_1} = \frac{k^0}{a_{\mathrm{TS}}RT\left(c_1^{\mathrm{ref}}\right)^2}\exp\left(\frac{\left(1-\alpha\right)\left(\mu_1^{\mathrm{ex}}-\mu_2^{\mathrm{ex}}\right)}{RT}\right)$$

$$L_{s_2} = \frac{k^0}{a_{\mathrm{TS}}RT\left(c_1^{\mathrm{ref}}\right)^2}\left(\overline{c_{e^-}}\,\overline{c_{\mathrm{Li}^+}}\,\overline{c_{v_1}}\right)\exp\left(\frac{\alpha\left(\mu_2^{\mathrm{ex}}-\mu_1^{\mathrm{ex}}\right)}{RT}\right)$$

$$L_{s_3} = \frac{k^0}{a_{\mathrm{TS}}RT\left(c_3^{\mathrm{ref}}\right)^2}\left(\overline{c_{e^-}}\,\overline{c_{\mathrm{Li}^+}}\,\overline{c_{v_1}}\right)\exp\left(\frac{\alpha\left(\mu_2^{\mathrm{ex}}-\mu_1^{\mathrm{ex}}\right)}{RT}\right)$$

$$L_{k_1} = L_{k_2} = \frac{k^0}{a_{\mathrm{TS}}c_1^{\mathrm{ref}}}$$

$$L_{\mathrm{cr}} = \frac{k_0}{c_3^{\mathrm{ref}}a_{\mathrm{TS}}RT}\left(\left(1-\alpha\right)+\alpha\left(\overline{c_{e^-}}\,\overline{c_{\mathrm{Li}^+}}\,\overline{c_{v_1}}\right)\right)$$

$$\Lambda_{\mathrm{d}} = -\Lambda_{\mathrm{c}} = \frac{\left(\mu_1^{\mathrm{ex}} - \mu_2^{\mathrm{ex}}\right)}{RT}$$

Noted that $L_\eta = L_{k_1} = L_{k_2}$. Assuming $RT \gg \mu_1^{\mathrm{ex}} - \mu_2^{\mathrm{ex}}$ and thus $exp\left(\frac{(1-\alpha)(\mu_1^{\mathrm{ex}} - \mu_2^{\mathrm{ex}})}{RT}\right) \approx 1$, we have $L_s = \frac{L_\eta}{c_1^{ref} RT}$ and determine L_η based on experimental results (i.e., Fig. 4.1(b)).

The lithium ions' transport in the cell is described by the Nernst-Planck equation:

$$\frac{\partial c_{\mathrm{Li}^+}}{\partial t} = \nabla \cdot \left[D_{\mathrm{Li}^+} \nabla c_{\mathrm{Li}^+} + \frac{D_{\mathrm{Li}^+} F}{RT} c_{\mathrm{Li}^+} \left(\nabla \varphi\right) \right] - c_{\mathrm{Li}}^{\mathrm{ref}} \frac{\partial p_1}{\partial t} \tag{3.28}$$

where $D_{\mathrm{Li}^+} = P\left(p_1\right) D_{\mathrm{Li}^+}^{\mathrm{Li}} + P\left(p_2\right) D_{\mathrm{Li}^+}^{\mathrm{SSE}} + h_{13} D_{\mathrm{Li}^+}^{13}$ is the diffusivity of Li^+, in which $D_{\mathrm{Li}^+}^{\mathrm{Li}}$, $D_{\mathrm{Li}^+}^{\mathrm{SSE}}$ and $D_{\mathrm{Li}^+}^{13}$ represent the diffusion coefficient of Li^+ in lithium (p_1), SSE (p_2) and the interface between lithium electrode (p_1) and void (p_3), respectively.

The governing equation for the electric potential is the Gauss's law:

$$\nabla \cdot \left(-\varepsilon_{\mathrm{r}} \varepsilon^0 \nabla \varphi\right) = P\left(p_2\right) \rho_{\mathrm{Li}^+} \tag{3.29}$$

where $\varepsilon_{\mathrm{r}} = P\left(p_1\right) \varepsilon_{\mathrm{r}}^{\mathrm{Li}} + P\left(p_2\right) \varepsilon_{\mathrm{r}}^{\mathrm{SSE}} + P\left(p_3\right) \varepsilon_{\mathrm{r}}^{\mathrm{void}}$, ε^0 is the vacuum permittivity, ε_r is the relative permittivity, ρ_{Li^+} represents the volumetric charge density of lithium ions. Eq. (3.29) is the Poisson equation with a nonzero charge on the right-hand side, that is, we allow accumulation of charges due to a nonuniform ion transport. In doing so, the depletion/accumulation of Li^+ caused by electrochemical reactions can occur. Note that such a treatment is generally adopted in the models of ASSLMBs (e.g. [98, 174]).

Considering in a quasi-static regime, Newton's second law can be expressed as:

$$\nabla \cdot \boldsymbol{\sigma} = 0 \tag{3.30}$$

where σ represents the stress tensor.

To solve this multi-physical cracking problem, Eqs. (3.26-3.30) are coded in a finite-element solver (COMSOL Multiphysics). The parameters used in the numerical simulation are listed in **Table 3.1**.

Table 3.1 Parameters used in the simulation of ASSLMBs.

H, the height of the model	100 μm
W, the width of the model	50 μm
R, ideal gas constant	8.314 J/(K•mol)
T, absolute temperature	298 K
D_{Li+}^{Li}, diffusion coefficient for Li^+ in Li	1×10^{-10} cm^2/s
$D_{Li+}^{Li_5PS_6Cl}$, diffusion coefficient for Li^+ in Li_5PS_6Cl	5×10^{-6} cm^2/s [188]
D_{Li+}^{13}, diffusion coefficient for Li^+ in Li/void interface	5×10^{-5} cm^2/s
σ_{Li+}^{Li}, ion conductivity for Li^+ in Li	10^{-4} mS/cm
$\sigma_{Li+}^{Li_5PS_6Cl}$, ion conductivity for Li^+ in Li_5PS_6Cl	0.12 mS/cm
σ_{Li+}^{13}, ion conductivity for Li^+ in Li/void interface	1.2 mS/cm
ε_r^{Li}, relative permittivity of lithium metal	1×10^{12} [189]
$\varepsilon_r^{Li_5PS_6Cl}$, relative permittivity of Li_5PS_6Cl	2.5×10^{9} [189]
ε_r^{13}, relative permittivity of void	1
E_{Li}, Young's modulus for lithium metal	7.82 GPa [179]

$E_{Li_5PS_6Cl}$, Young's modulus for lithium metal	22.1 GPa [190]
ν, Poisson's ratio	0.37 [190]
L_{s_i}, coefficients to scale the contributions of the interfacial energy	5.28×10^{-9} m•s/kg
$L_{k_1}= L_{k_2}= L_{k_3}/100$, coefficients to scale the contributions of the kinetics	1 1/s
L_{cr}, coefficients to scale the contributions of cracks	0.01 1/(s•Pa)
α, asymmetry factor	0.5
γ_i, interfacial energy density	0.6 J/m^2 [181]
δ_i, interfacial thickness	4 μm
F, Faraday's constant	96483 C/mol
c_1^{ref}, reference concentration for phase 1(lithium metal)	76400 mol/m^3 [191]
c_2^{ref}, reference concentration for phase 2 (Li_5PS_6Cl)	24146 mol/m^3 [192]
A_c, creep parameter	6.81×10^{-4} 1/s [178]
n, power law creep exponent	6.56 [178]
σ_{ref}, reference stress	1 MPa [178]

3.2 Griffith-theory-generalized Phase-Field Fracture Model

We consider an arbitrary elastic body $\Omega \subset \mathbb{R}^d$($d$ is dimension) with the boundary $\partial\Omega$ and a set of discrete internal discontinuity denoted by Γ. The total potential energy ψ_{tot}

can be expressed in terms of the elastic energy density ψ_e, fracture energy and energy due to body force **f** and traction **t**, *i.e.*,

$$\psi_{tot} = \int_\Omega \psi_e \left(\boldsymbol{\varepsilon}^e(\mathbf{u}), \Gamma\right) \mathrm{d}V + \int_\Gamma G_c \mathrm{d}A - \int_\Omega \mathbf{f} \bullet \mathbf{u} \mathrm{d}V - \int_{\partial\Omega} \mathbf{t} \bullet \mathbf{u} \mathrm{d}A \tag{3.31}$$

where $\boldsymbol{\varepsilon}^e$, **u,** and G_c are elastic strain tensor, displacement vector, and critical fracture energy density, respectively. We then define a crack phase field $\phi \in [0,1]$ with $\phi = 1$ denoting cracked zones, $\phi = 0$ for intact zones, and $\phi \in (0,1)$ the diffusive interfaces between cracks and the elastic body. Miege *et al.* [60] introduced the crack energy density function for diffusive cracks (i.e., $\phi \in [0,1]$), given by:

$$\gamma\left(\phi, \nabla\phi\right) = \frac{1}{2l_0}\phi^2 + \frac{l_0}{2}\left|\nabla\phi\right|^2 \tag{3.32}$$

where l_0 is a parameter controlling the thickness of the diffusive interface. In limiting case of sharp crack topology, $l_0 \to 0$ [193]. Thus, the energy release caused by fracture is approximated as [70]:

$$\int_\Gamma G_c \mathrm{d}A \approx \int_\Omega G_c \gamma\left(\phi, \nabla\phi\right) \mathrm{d}V \tag{3.33}$$

A thin glass sheet in ROR test undergoes large deformation. Hence, the finite strain theory is employed and the total deformation gradient tensor $\mathbf{F}_g$ can be decomposed into elastic deformation gradient $\mathbf{F}^e$ and residual deformation gradient $\mathbf{F}^r$ caused by IOX [75] which is simplified to be the deformation gradient caused by volume change. Therefore, we have the relations below:

$$\mathbf{F}_g = \mathbf{F}^e \cdot \mathbf{F}^r \tag{3.34}$$

$$\mathbf{F}^r = \left(\varepsilon_0\left(\mathrm{D}\right) + 1\right)\mathbf{I} \tag{3.35.a}$$

where $\varepsilon_0(\mathrm{D}) = \begin{cases} \varepsilon_0 & \mathrm{D} \le \mathrm{DOL} \\ 0 & \text{otherwise} \end{cases}$ and D denotes the depth of the glass.

$$\boldsymbol{\varepsilon}^{\mathrm{r}} = \frac{1}{2}\left(\left(\mathbf{F}^{\mathrm{r}}\right)^{\mathrm{T}} \cdot \mathbf{F}^{\mathrm{r}} - \mathbf{I}\right) \tag{3.35.b}$$

$$\boldsymbol{\varepsilon}^{\mathrm{tot}} = \left(\mathbf{F}^{\mathrm{r}}\right)^{\mathrm{T}} \cdot \boldsymbol{\varepsilon}^{\mathrm{e}} \cdot \mathbf{F}^{\mathrm{r}} + \boldsymbol{\varepsilon}^{\mathrm{r}} \tag{3.35.c}$$

We assume that glass cracking is only caused by tension. Hence, the elastic strain energy is decomposed into tensile and compressive parts following the treatments suggested in ref. [59]. To decompose the elastic strain energy, the elastic strain tensor $\boldsymbol{\varepsilon}^{\mathrm{e}}$ is decomposed as:

$$\begin{cases} \boldsymbol{\varepsilon}_{+}^{\mathrm{e}} = \sum_{a=1}^{d} \left\langle \varepsilon_a^{\mathrm{e}} \right\rangle_{+} \mathbf{n}_a \otimes \mathbf{n}_a \\ \boldsymbol{\varepsilon}_{-}^{\mathrm{e}} = \sum_{a=1}^{d} \left\langle \varepsilon_a^{\mathrm{e}} \right\rangle_{-} \mathbf{n}_a \otimes \mathbf{n}_a \end{cases} \tag{3.36}$$

where $\boldsymbol{\varepsilon}_{+}^{\mathrm{e}}$ and $\boldsymbol{\varepsilon}_{-}^{\mathrm{e}}$ are the tensile and compressive elastic strain tensors, respectively; $\varepsilon_{\mathrm{a}}^{\mathrm{e}}$ and $\mathbf{n}_{\mathrm{a}}$ indicate a principal elastic strain and its direction vector. The operators $\langle\cdot\rangle_{+}$ and $\langle\cdot\rangle_{-}$ are defined as: $\langle\cdot\rangle_{+} = \frac{\cdot + |\cdot|}{2}$ and $\langle\cdot\rangle_{-} = \frac{\cdot - |\cdot|}{2}$.

With Eq. (6), the strain energy density can be decomposed into two parts:

$$\psi_{\mathrm{e}}\left(\boldsymbol{\varepsilon}^{\mathrm{e}}(\mathbf{u})\right) = \psi_{\mathrm{e}}^{+}\left(\boldsymbol{\varepsilon}^{\mathrm{e}}(\mathbf{u})\right) + \psi_{\mathrm{e}}^{-}\left(\boldsymbol{\varepsilon}^{\mathrm{e}}(\mathbf{u})\right) \tag{3.37}$$

with

$$\begin{cases} \psi_{\mathrm{e}}^{+} = \frac{1}{2}\lambda_0 \left\langle \mathrm{tr}\left(\boldsymbol{\varepsilon}^{\mathrm{e}}\right)\right\rangle_{+}^{2} + \mu_0 \mathrm{tr}\left(\boldsymbol{\varepsilon}_{+}^{\mathrm{e}} \cdot \boldsymbol{\varepsilon}_{+}^{\mathrm{e}}\right) \\ \psi_{\mathrm{e}}^{-} = \frac{1}{2}\lambda_0 \left\langle \mathrm{tr}\left(\boldsymbol{\varepsilon}^{\mathrm{e}}\right)\right\rangle_{-}^{2} + \mu_0 \mathrm{tr}\left(\boldsymbol{\varepsilon}_{-}^{\mathrm{e}} \cdot \boldsymbol{\varepsilon}_{-}^{\mathrm{e}}\right) \end{cases} \tag{3.38}$$

where the λ_0 and μ_0 are Lamé constants.

In cracked regions, stiffness is reduced with ϕ. This is described by a so-called degradation function g(ϕ), given by [57]:

$$g_k(\phi) = (1-k)(1-\phi)^2 + k \tag{3.39}$$

where k is a sufficiently small and positive parameter to ensure that the numerical scheme can be stable (i.e., stiffness tensors in the body Ω are all positive-definite). In this work, k=1×10^{-5} is adopted.

With the above treatments, the strain energy density can be expressed as:

$$\psi_{\mathrm{e}}\left(\boldsymbol{\varepsilon}^{\mathrm{e}}(\mathbf{u}),\phi\right) = g_k(\phi)\psi_{\mathrm{e}}^{+}\left(\boldsymbol{\varepsilon}^{\mathrm{e}}(\mathbf{u})\right) + \psi_{\mathrm{e}}^{-}\left(\boldsymbol{\varepsilon}^{\mathrm{e}}(\mathbf{u})\right) \tag{3.40}$$

Using Eqs. (3.31, 3.33, and 3.40), the total Lagrangian energy functional can be formulated as:

$$\begin{aligned} L = {} & \frac{1}{2}\int_{\Omega}\rho\dot{\mathbf{u}}:\dot{\mathbf{u}}\mathrm{d}V - \int_{\Omega}G_c\gamma(\phi,\nabla\phi)\,\mathrm{d}V - \int_{\Omega}g(\phi)\psi_e^{+}\left(\boldsymbol{\varepsilon}^{e}(\mathbf{u})\right) + \psi_e^{-}\left(\boldsymbol{\varepsilon}^{e}(\mathbf{u})\right)\mathrm{d}V \\ & + \int_{\Omega}\mathbf{f}\cdot\mathbf{u}\,\mathrm{d}V + \int_{\partial\Omega}\mathbf{t}\cdot\mathbf{u}\,\mathrm{d}A \end{aligned} \tag{3.41}$$

where ρ is the density of glass.

Letting the functional derivatives of L with respect to $\mathbf{u}$ and ϕ be zero (minimizing the Lagrange), the corresponding equations of motion are given by:

$$\begin{cases} \nabla\boldsymbol{\sigma} + \mathbf{b} = \rho\ddot{\mathbf{u}} \quad \text{in } \Omega \\ \left[\dfrac{2l_0(1-k)\psi_{\mathrm{e}}^{+}}{G_c} + 1\right]\phi - l_0^2\nabla^2\phi = \dfrac{2l_0(1-k)\psi_{\mathrm{e}}^{+}}{G_c} \quad \text{in } \Omega \\ \boldsymbol{\sigma}\cdot\mathbf{n} = \mathbf{t} \quad \text{on } \partial\Omega \\ \nabla\phi\cdot\mathbf{n} = 0 \quad \text{on } \partial\Omega \end{cases} \tag{3.42}$$

where $\boldsymbol{\sigma} = g_k(\phi)\dfrac{\partial \psi_{\mathrm{e}}^{+}}{\partial \boldsymbol{\varepsilon}^{\mathrm{e}}} + \dfrac{\partial \psi_{\mathrm{e}}^{-}}{\partial \boldsymbol{\varepsilon}^{\mathrm{e}}}$, and $\mathbf{n}$ is the outward normal vector on the boundaries, $\partial\Omega$.

An irreversible condition is needed to ensure the crack cannot be self-healed. Therefore, we define a history strain field H being the maximum of the strain energy ψ_{e}^{+} [194, 195], given by:

$$H(x,t) = \max_{s\in[0,t]}\left\{\psi_e^{+}(x,s)\right\} \tag{3.43}$$

which replaces ψ_{e}^{+} in Eq. (3.42) and recast it as:

$$\begin{cases} \nabla\boldsymbol{\sigma} + \mathbf{b} = \rho\ddot{\mathbf{u}} \quad \text{in } \Omega \\ \left[\dfrac{2l_0(1-k)H}{G_c} + 1\right]\phi - l_0^2\nabla^2\phi = \dfrac{2l_0(1-k)H}{G_c} \quad \text{in } \Omega \\ \boldsymbol{\sigma}\cdot\mathbf{n} = \mathbf{t} \quad \text{on } \partial\Omega \\ \nabla\phi\cdot\mathbf{n} = 0 \quad \text{on } \partial\Omega \end{cases} \tag{3.44}$$

With Eq. (3.36), the stress tensor $\boldsymbol{\sigma}$ can be derived as:

$$\boldsymbol{\sigma} = \frac{\partial \psi_{\mathrm{e}}}{\partial \boldsymbol{\varepsilon}^{\mathrm{e}}} = \left[(1-k)\left(1-\phi^2\right)+k\right]\left[\lambda_0\left\langle \mathrm{tr}(\boldsymbol{\varepsilon})\right\rangle_{+}\mathbf{I} + 2\mu_0\boldsymbol{\varepsilon}_{+}^{\mathrm{e}}\right] + \lambda_0\left\langle \mathrm{tr}(\boldsymbol{\varepsilon})\right\rangle_{-}\mathbf{I} + 2\mu_0\boldsymbol{\varepsilon}_{-}^{\mathrm{e}} \tag{3.45}$$

and the stiffness matrix (fourth-order tensor) $\mathbf{D}$ is obtained as[67, 196]:

$$\begin{aligned} \mathbf{D} = \frac{\partial \boldsymbol{\sigma}}{\partial \boldsymbol{\varepsilon}^{\mathrm{e}}} = \lambda_0\left\{\left[(1-k)\left(1-\phi^2\right)+k\right]H_{\varepsilon}\left\langle \mathrm{tr}(\boldsymbol{\varepsilon})\right\rangle + H_{\varepsilon}\left\langle -\mathrm{tr}(\boldsymbol{\varepsilon})\right\rangle\right\}\mathbf{J} \\ + 2\mu_0\left[(1-k)\left(1-\phi^2\right)+k\right]\frac{\partial \boldsymbol{\varepsilon}_{+}^{\mathrm{e}}}{\partial \boldsymbol{\varepsilon}^{\mathrm{e}}} + 2\mu_0\frac{\partial \boldsymbol{\varepsilon}_{-}^{\mathrm{e}}}{\partial \boldsymbol{\varepsilon}^{\mathrm{e}}} \end{aligned} \tag{3.46}$$

where $H_{\varepsilon}\langle\cdot\rangle$ is the Heaviside function with $H_{\varepsilon}\langle x\rangle = 1$ when $x > 0$ and $H_{\varepsilon}\langle x\rangle = 0$ when $x \le 0$, and $\mathbf{J}$ is a fourth order tensor defined in ref. [67]. To let $\mathbf{D}$ be well-defined, we follow ref. [68] to modify the principal strains as follows in numerical realization:

$$\begin{cases} \varepsilon_1 = \varepsilon_1(1+\delta) & \text{if } \varepsilon_1 = \varepsilon_2 \\ \varepsilon_3 = \varepsilon_3(1-\delta) & \text{if } \varepsilon_2 = \varepsilon_3 \end{cases} \tag{3.47}$$

with $\delta = 1\times10^{-9}$ in this work.

To investigate cases with initial cracks Γ and avoid the self-healing of these cracks, the initial magnitude of strain history field $H_0(\mathbf{x}) = H(\mathbf{x}, 0)$ may be predefined as:

$$H_0(x) = B\begin{cases} \dfrac{G_c}{4l_0}\left(1-\dfrac{d(\mathbf{x},\Gamma)}{l_0}\right) & d(\mathbf{x},\Gamma) \le l_0 \\ 0 & d(\mathbf{x},\Gamma) > l_0 \end{cases} \tag{3.48}$$

where $d(\mathbf{x}, \Gamma)$ is the closest distance from point $\mathbf{x}$ to the discontinuity Γ and B is a scalar [194] from 0 to 1000, and correspondingly, $H_0(\mathbf{x})$ ranges from 0 to 1.

To solve this initial-boundary value problem, Eqs. 3.43, 3.44, 3.46 are coded in COMSOL Multiphysics. The parameters used in the numerical simulation are listed in **Table 3.2**.

Table 3.2 Parameters used in the simulation of IOX glass.

E, Young's modulus	68 GPa[197]
ν, Poisson's ratio	0.22 [198]
G_c, critical energy release rate	30 J/m^2
l_0, the length scale parameter	1 μm
ρ, density	2.5 g/cm^3[199]

3.3 FEM-NO coupling framework

This work focuses on solid mechanics problems under static, quasi-static, and dynamic loading conditions. The governing equations for momentum equilibrium over a computational domain Ω are given by:

$$\text{Static or quasi-static: } \nabla \bullet \boldsymbol{\sigma} + \mathbf{f} = 0 \tag{3.49}$$

$$\text{Dynamic: } \nabla \bullet \boldsymbol{\sigma} + \mathbf{f} = \rho \ddot{\mathbf{u}} \tag{3.50}$$

where $\boldsymbol{\sigma}$, $\mathbf{f}$, $\mathbf{u}$ and ρ denote the stress tensor, body force, displacement vector, and density, respectively. To develop a physics-informed coupling framework, we integrate neural operators — specifically DeepONet — with an FE solver. All FE simulations are carried out using FEniCSx [200], an open-source Python-based FE platform. The FE models utilize triangular meshes generated via Gmsh [201], and implement a first order continuous Galerkin formulation [202] from **Chapter 6.1-6.4**.

DeepONet is employed to learn nonlinear operators that map between infinite-dimensional function spaces defined over a bounded open set $\Omega^* \subset \mathbb{R}^D$, given a set of input-output function pairs. Let $\mathcal{U}$ and $\mathcal{S}$ be Banach spaces defined as:

$$\mathcal{U} = \left\{ \Omega^*; h : \chi \to \mathbb{R}^{d_x} \right\}, \quad \chi \subseteq \mathbb{R}^{d_h} \tag{3.51}$$

$$\mathcal{S} = \left\{ \Omega^*; s : \mathcal{Y} \to \mathbb{R}^{d_x} \right\}, \quad \mathcal{Y} \subseteq \mathbb{R}^{d_s} \tag{3.52}$$

where $\mathcal{U}$ and $\mathcal{S}$ denote the spaces of input and output functions, respectively. The goal is to approximate a nonlinear operator G: $\mathcal{U} \to \mathcal{S}$ via a parametric mapping:

$$G\colon \mathcal{U} \times \boldsymbol{\Theta} \to \mathcal{S} \quad \text{or} \quad G_{\boldsymbol{\theta}}\colon \mathcal{U} \to \mathcal{S},\ \boldsymbol{\theta} \in \boldsymbol{\Theta}, \tag{3.53}$$

where $\boldsymbol{\Theta}$ is a finite-dimensional parameter space and $\boldsymbol{\theta}$ represents the tunable parameters (weights and biases) of the neural network.

To construct a physics-informed DeepONet (PI-DeepONet), we embed the governing Eqs. (3.49) and (3.50) into the learning process to build static and dynamic surrogate models. In PI-DeepONet, physical systems governed by PDEs are described through multiple components: the PDE solution, forcing terms, and initial and boundary conditions. By minimizing a composite loss function incorporating these components, we learn the optimal parameters $\boldsymbol{\theta}^*$ to predict functions in $\mathcal{S}$, conditioned on variations in $\mathcal{U}$. This capability to learn function mappings governed by PDEs makes PI-DeepONe a powerful tool for building high-fidelity surrogate models.

We develop three distinct PI-DeepONet architectures — summarized in **Table 3.3** — to handle static, quasi-static and dynamic regimes, as detailed in **Chapter 3.3.1** and **3.3.2**. The developed surrogate models are designed to be embedded into traditional numerical solvers using a DDM approach, as illustrated in **Chapter 3.3.3**.

3.3.1 PI-DeepONet for static and quasi-static loading

In static or quasi-static cases, the governing equations are time independent, meaning there is no inertia term, as shown in Eq. 3.49. We consider two material models in this context: linear elasticity for small deformations and hyperelasticity for scenarios involving large deformations.

For linear elasticity with infinitesimal strains, the strain tensor is expressed as:

$$\boldsymbol{\varepsilon} = \frac{1}{2}\left(\nabla \mathbf{u} + \left(\nabla \mathbf{u}\right)^T\right) \tag{3.54}$$

with the corresponding stress given by:

$$\boldsymbol{\sigma} = \lambda_0 \mathrm{tr}\left(\boldsymbol{\varepsilon}\right)\mathbf{I} + 2\mu_0 \boldsymbol{\varepsilon} \tag{3.55}$$

Substituting Eqs. 3.54 and 3.55 into Eq. 1, we obtain the standard FE formulation [203]:

$$\mathbf{K}\mathbf{u} = \mathbf{F} \tag{3.56}$$

where **K** and **F** are the global stiffness matrix and external force vector.

For hyperelasticity, we must account for large deformations within the framework of continuum mechanics. In this case, the stress term in Eq. 3.49 is replaced by the first Piola-Kirchhoff stress tensor, $\mathbf{P_1}$, which normalizes forces in the current configuration over areas in the reference configuration. The key kinematic quantities are defined as follows:

$$\mathbf{F}_g = \mathbf{I} + \nabla \mathbf{u}, \tag{3.57}$$

$$\mathbf{C} = \mathbf{F}_g^T \mathbf{F}_g, \tag{3.58}$$

$$\mathbf{I}_1 = \mathrm{tr}(\mathbf{C}), \tag{3.59}$$

$$J = \det \mathbf{F}_g \tag{3.60}$$

where $\mathbf{F}_g$ represents the deformation gradient tensor, **C** is the right Cauchy-Green deformation tensor, $\mathbf{I}_1$ denotes the first invariant of **C**, and J is the volume change factor (determinant of $\mathbf{F}_g$). In this work, we utilize the Neo-Hookean hyperelastic model with the strain energy density function expressed as:

$$\boldsymbol{\psi} = \frac{1}{2}\mu_0 \left(\mathbf{I}_1 - 3\right) + \frac{\lambda_0}{2} \ln\left(J^2\right) - \mu_0 \ln\left(J\right) \tag{3.61}$$

The first Piola-Kirchhoff stress tensor is then derived through:

$$\mathbf{P}_1 = \frac{\partial \boldsymbol{\psi}}{\partial \mathbf{F}_g} \tag{3.62}$$

For both linear elasticity and hyperelasticity in static or quasi-static conditions, we implement the conventional PI-DeepONet architecture as outlined in **Table 3.3**. This structure comprises two fully connected neural networks (FNNs): one functioning as the branch network and the other as the trunk network [137], as illustrated in Fig. 3.1(a). For static and quasi-static loading scenarios, only the 'Branch1' network is utilized, while the 'Branch2' network shown in Fig. 3.1(a) is exclusively used for dynamic models. In the

branch network (labeled 'Branch1' in Fig. 3.1(a)), we use the Dirichlet boundary condition $\mathbf{u}_{|\partial\Omega}$ as input functions from the space $\mathcal{U}$. To ensure robust generalization capabilities, these input functions are generated using the Gaussian Random Field (GRF) approach [136]. The trunk network (labeled Trunk in Fig. 3.1(a)) takes spatial coordinates $\mathbf{x} \in \mathbb{R}^d$ as inputs, where d represents the spatial dimensionality of the model.

By minimizing loss functions derived from the PDE residual loss and boundary conditions, we determine the optimal parameters to establish accurate NOs for static problems, which we refer to as static PI-DeepONet. The specific PDEs and boundary conditions for linear elasticity and hyperelasticity are presented in **Chapter 6.1** and **6.2**, respectively. The training methodology for static PI-DeepONet in both linear elasticity and hyperelasticity contexts will be detailed in **Chapter 3.3.2**.

3.3.2 PI-DeepONet for dynamic loading

PI-DeepONet can be extended beyond static problems to model time-dependent behaviors in structural dynamics by introducing time discretization in the trunk network. However, this approach has demonstrated the accumulation of errors for the problem over long time horizons [143]. To resolve the error accumulation issue, we propose a time-marching framework, which is inspired by the Newmark-Beta method [204] (hereafter referred to as the Newmark method for brevity), a widely-used time-discretization scheme in FE analysis. This hybridization leads to a time-advancing surrogate model that leverages concepts from numerical analysis, enabling the prediction of dynamic responses such as displacement, velocity, and acceleration fields across space and time. In this section, we formulate this dynamic PI-DeepONet, drawing on principles from FE solvers and convolutional architectures to encode spatial information efficiently.

Neglecting damping, the semi-discrete elastodynamic equations over a computational domain Ω are expressed using the Newmark method as:

$$\dot{\mathbf{u}}^n = \dot{\mathbf{u}}^{n-1} + \left(1-\gamma\right)\Delta t\ddot{\mathbf{u}}^{n-1} + \gamma\Delta t\ddot{\mathbf{u}}^n \tag{3.63}$$

$$\mathbf{u}^n = \mathbf{u}^{n-1} + \Delta t \dot{\mathbf{u}}^{n-1} + \frac{\Delta t^2}{2}\left((1-2\beta)\ddot{\mathbf{u}}^{n-1} + 2\beta\ddot{\mathbf{u}}^n\right) \tag{3.64}$$

$$\mathbf{M}\ddot{\mathbf{u}}^n + \mathbf{K}\mathbf{u}^n = \mathbf{F}^n \tag{3.65}$$

where $n-1$ and n indicate the previous and current time steps, respectively; $\mathbf{u}$, $\dot{\mathbf{u}}$, and $\ddot{\mathbf{u}}$ are the displacement, velocity, and acceleration vectors; Δt is the time increment; $\mathbf{M}$ is the mass matrix; and γ, β are Newmark parameters with typical values in the range $\gamma \in [0,1]$, $\beta \in [0,\frac{1}{2}]$. To simplify, we use $\gamma = \beta = \frac{1}{2}$, resulting in:

$$\dot{\mathbf{u}}^n = \dot{\mathbf{u}}^{n-1} + \frac{\Delta t}{2}\left(\ddot{\mathbf{u}}^{n-1} + \ddot{\mathbf{u}}^n\right) \tag{3.66}$$

$$\mathbf{u}^n = \mathbf{u}^{n-1} + \Delta t \dot{\mathbf{u}}^{n-1} + \frac{\Delta t^2}{2}\ddot{\mathbf{u}}^n \tag{3.67}$$

From Eq. 3.67, we can isolate acceleration, $\ddot{\mathbf{u}}^n$ as:

$$\ddot{\mathbf{u}}^n = \frac{2}{\Delta t^2}\left(\mathbf{u}^n - \mathbf{u}^{n-1}\right) - \frac{2}{\Delta t}\dot{\mathbf{u}}^{n-1} \tag{3.68}$$

Substituting this into Eq. 3.65 (assuming zero external force) yields:

$$\left(\mathbf{M}\frac{2}{\Delta t^2} + \mathbf{K}\right)\mathbf{u}^n - \mathbf{M}\frac{2}{\Delta t^2}\mathbf{u}^{n-1} - \frac{2}{\Delta t}\dot{\mathbf{u}}^{n-1} = \mathbf{0} \tag{3.69}$$

Here, the term $\left(M\frac{2}{\Delta t^2} + K\right)$ is recognized as the effective stiffness matrix.

In standard FE methods, Eq. 3.69 is solved for displacement $\mathbf{u}^n$, with velocity and acceleration subsequently updated via Eq. 3.66 and 3.68. Instead, we embed this equation into the DeepONet architecture to form a time-marching PI-DeepONet. This modified architecture introduces a second branch network ('Branch2' as shown in Fig. 3.1(a)), in addition to Branch1. Branch2 encodes prior-step displacement $\mathbf{u}^{n-1}$ and velocity $\dot{u}^{n-1}$ across the domain Ω. To extract domain-wide features efficiently, multi-channel

CNNs are used in Branch2, as shown in Fig. 3.1(a). CNNs not only reduce computational cost compared to FNNs, but also naturally align with the local interaction principles of the FE method-i.e., only neighboring nodes significantly affect computations at a given node. We combine outputs from both branches (Branch1 FNNs and Branch2 CNN + FNNs) with the trunk network to form two operators, $G_{\boldsymbol{\theta}_1}^{u_x}$ and $G_{\boldsymbol{\theta}_2}^{u_y}$, for displacements in x- and y-direction. It is noted that $G_{\boldsymbol{\theta}_1}^{u_x}$ and $G_{\boldsymbol{\theta}_2}^{u_y}$, employ identical DeepONet structures but are parameterized by separate weights and bias ($\boldsymbol{\theta}_1 \neq \boldsymbol{\theta}_2$), allowing them to predict distinct u_x and u_y. The network is trained by minimizing the residual and boundary losses, $\mathcal{L}_{res}$ and $\mathcal{L}_{\mathrm{bcs}}$, to accurately learn displacement fields at each time step without needing to include time in the trunk network.

A schematic of this architecture and the prediction workflow with numerical solvers is shown in Fig. 3.1(b). The trained PI-DeepONet receives inputs from the previous time step (red-dashed box) and current boundary displacements obtained from numerical solver (green-dashed box) to predict the full-field displacement (orange-dashed box). Using Newmark integration (green arrow), the velocity and acceleration are then inferred (purple-dashed box), enabling recursive forward prediction. This work is the first to incorporate classical time-advancing schemes into DeepONet, offering a novel route for hybrid time-marching surrogate modeling. Moreover, this framework can be extended to other time-integration methods such as the generalized-α method [205] or Runge-Kutta schemes [206]. The concept can also be adapted to construct fully data-driven, time-advancing DeepONet.

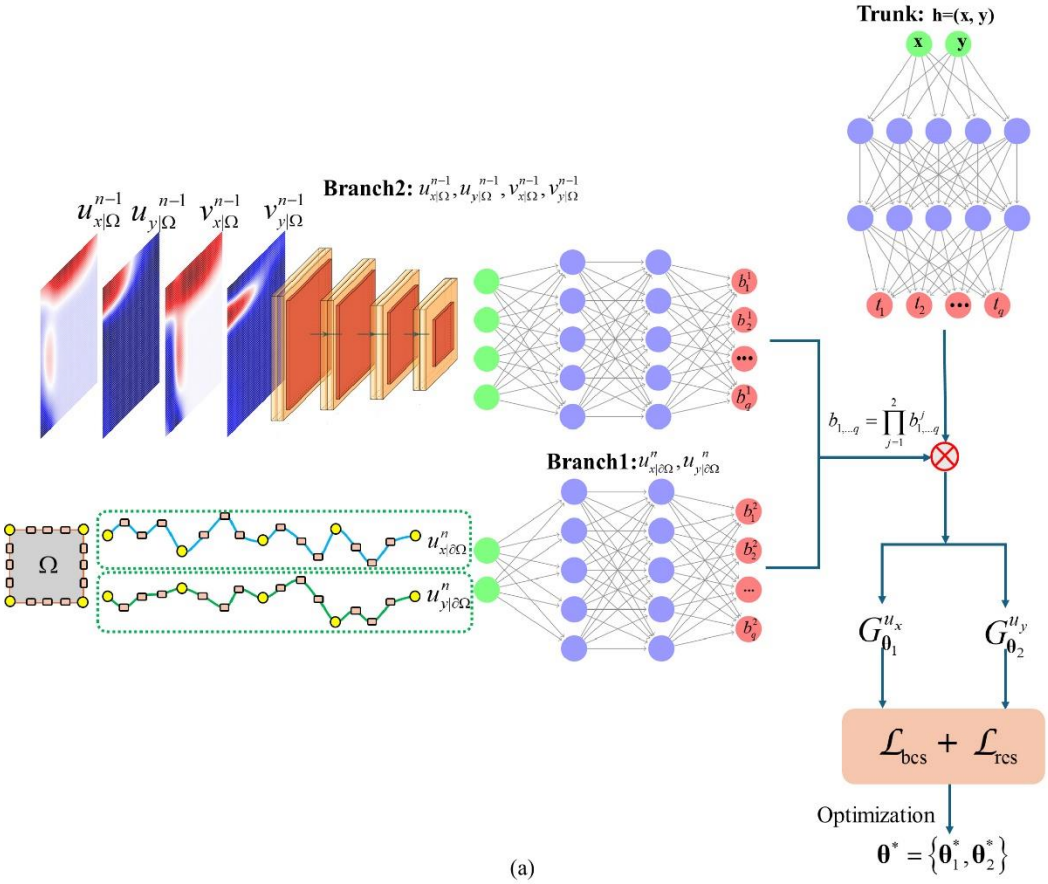

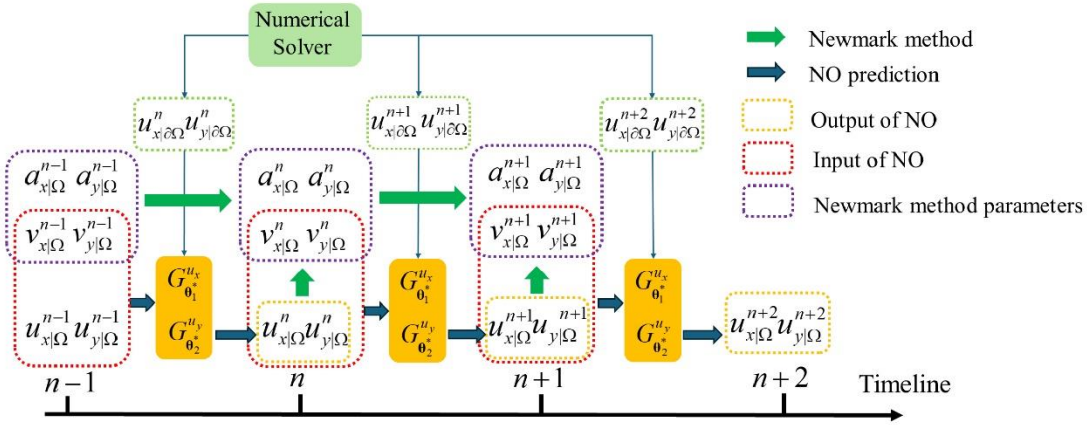

Figure 3.1:Time-advancing DeepONet: (a) The DeepONet structure: Branch1 is the branch network with input functions of the Dirichlet boundary condition ($u^{n}_{x|\partial\Omega}$, $u^{n}_{y|\partial\Omega}$) from square edges at time step n; Branch2 for input functions of the displacement and velocity ($u^{n-1}_{x|\Omega}$, $u^{n-1}_{y|\Omega}$, $v^{n-1}_{x|\Omega}$, $v^{n-1}_{y|\Omega}$) over the entire domain Ω at time step $n-1$; Each branch net returns features embedding $\left[b^i_1, b^i_2, \ldots, b^i_q\right]^T \in \mathbb{R}^q$ with $i = 1,2$ as output, and their dot product obtains $[b_1, b_2, \ldots, b_q]^T$; Trunk denotes the trunk networks taking the spatial coordinates $(x,y) \in \Omega$ as input, returning $[t_1, t_2, \ldots, t_q]^T \in \mathbb{R}^q$ as output. Two identical sets of branch and trunk networks are

merged via two element-wise dot products to output two solution operators $G_{\boldsymbol{\theta}_1}^{u_x}$ and $G_{\boldsymbol{\theta}_2}^{u_y}$, predicting $u_{x|\Omega}^n$ and $u_{y|\Omega}^n$. Given the PDEs and boundary conditions, the residual loss ($\mathcal{L}_{res}$) and boundary conditions loss ($\mathcal{L}_{bcs}$) are defined. The optimal parameters $\boldsymbol{\theta}^*$ are obtained by minimizing the addition of these two loss functions; (b) Flowchart of integrating time-advancing DeepONet and Numerical solver in structural dynamics: the green arrow denotes the Newmark method predicting process, blue arrow indicates NO prediction, the orange-dashed and red-dashed box denote the output and input of NO, and purple-dashed box shows the parameters needed for Newmark method.

From a mathematical standpoint, both static and dynamic PI-DeepONet frameworks reduce to boundary value problems (BVPs) across spatial domains:

$$\mathcal{N}\left[s(\mathbf{x})\right](\mathbf{x}) = f_d(\mathbf{x}),\ s \in \mathcal{S},\ \mathbf{x} \in \Omega \tag{3.70}$$

$$\mathcal{B}\left[h(\mathbf{x})\right](\mathbf{x}) = \mathrm{g}_b(\mathbf{x}),\ h \in \mathcal{U},\ \mathbf{x} \in \partial\Omega \tag{3.71}$$

where $\mathcal{N}$ and $\mathcal{B}$ are spatial differential operators, $f_d : \Omega \rightarrow \mathbb{R}^d$ is the driving force, $g_b : \partial\Omega \rightarrow \mathbb{R}^d$ is the boundary condition with the dimension d. In this work, the driving force (i.e., body force) is not considered, all the boundary conditions are Dirichlet boundary conditions, and the mechanical system is 2 dimensional. Thus, the $G(h,\boldsymbol{\theta})$ can be represented as:

$$G(h,\boldsymbol{\theta}) = \left\{G(u_x,\boldsymbol{\theta}_1), G(u_y,\boldsymbol{\theta}_2)\right\} \tag{3.72}$$

where u_x and u_y are x-displacement and y-displacement with $h = (u_x, u_y)$. For simplification, $G(u_x,\boldsymbol{\theta}_1)$ and $G(u_y,\boldsymbol{\theta}_2)$ are denoted as $G_{\boldsymbol{\theta}_1}^{u_x}$ and $G_{\boldsymbol{\theta}_2}^{u_y}$. Consequently, Eq. 3.70 and Eq. 3.71 are expressed as:

$$\mathcal{N}_1\left(G_{\boldsymbol{\theta}_1}^{u_x}, G_{\boldsymbol{\theta}_2}^{u_y}\right)(\mathbf{x}) = 0,\ \mathbf{x} \in \Omega,\ \boldsymbol{\theta} = \left\{\boldsymbol{\theta}_1, \boldsymbol{\theta}_2\right\} \in \boldsymbol{\Theta} \tag{3.73}$$

$$\mathcal{N}_2\left(G_{\boldsymbol{\theta}_1}^{u_x}, G_{\boldsymbol{\theta}_2}^{u_y}\right)(\mathbf{x}) = 0,\ \mathbf{x} \in \Omega,\ \boldsymbol{\theta} = \left\{\boldsymbol{\theta}_1, \boldsymbol{\theta}_2\right\} \in \boldsymbol{\Theta} \tag{3.74}$$

$$G_{\boldsymbol{\theta}_1}^{u_x}(\mathbf{x}) = s_1(\mathbf{x}),\ \mathbf{x} \in \partial\Omega,\ s = \left\{s_1, s_2\right\} \in \mathcal{S} \tag{3.75}$$

$$G_{\boldsymbol{\theta}_2}^{u_y}(\mathbf{x}) = s_2(\mathbf{x}),\ \mathbf{x} \in \partial\Omega,\ s = \left\{s_1, s_2\right\} \in \mathcal{S} \tag{3.76}$$

where $\mathcal{N}_1$ and $\mathcal{N}_2$ are the spatial differential operators in *x* and *y*-directions, respectively.

It is noteworthy that Eq. 3.73-3.76 are the loss functions of the PI-DeepONet and can be defined as:

$$\begin{aligned}\mathcal{L}(\theta) &= \mathcal{L}_{res}(\theta) + \mathcal{L}_{bcs}(\theta) \\ &= \frac{1}{N_1^r}\sum_{i=1}^{N_1^r}\left(\mathcal{N}_1(G_{\theta_1}^{u_x}, G_{\theta_2}^{u_y})(\mathbf{x}_r^i)\right)^2 + \frac{1}{N_2^r}\sum_{i=1}^{N_2^r}\left(\mathcal{N}_2(G_{\theta_1}^{u_x}, G_{\theta_2}^{u_y})(\mathbf{x}_r^i)\right)^2 \\ &+ \frac{1}{N_1^b}\sum_{i=1}^{N_1^b}\left(G_{\theta_1}^{u_x}(\mathbf{x}_b^i) - s(\mathbf{x}_b^i)\right)^2 + \frac{1}{N_2^b}\sum_{i=1}^{N_2^b}\left(G_{\theta_2}^{u_y}(\mathbf{x}_b^i) - s(\mathbf{x}_b^i)\right)^2,\end{aligned} \tag{3.77}$$

$$\text{for } \{\mathbf{x}_r^i\}_{i=0}^{N_1^r} \subsetneq \Omega, \{\mathbf{x}_b^i\}_{i=0}^{N_1^b} \subsetneq \partial\Omega, N_1^r = N_2^r, N_1^b = N_2^b$$

where $\mathcal{L}_{res}$ and $\mathcal{L}_{bcs}$ are residual loss derived from Eqs. 3.73-3.74 and boundary condition loss derived from Eqs. 3.75-3.76; N_1^r, N_2^r, N_1^b and N_2^b denote the number of collocation points and boundary points. By minimizing the loss function, the $\boldsymbol{\theta}^* = \{\boldsymbol{\theta}_1^*, \boldsymbol{\theta}_2^*\}$ optimal parameter can be obtained as:

$$\boldsymbol{\theta}^* = \arg\min_{\boldsymbol{\theta}}(\mathcal{L}) \tag{3.78}$$

3.3.3 DDM and coupling strategy

We introduce a hybrid computational framework that couples a traditional FE solver with a PI-DeepONet to enable efficient and accurate simulations of complex physical phenomena. The coupling is achieved via a DDM approach based on the Schwarz alternating method, which facilitates iterative information exchange across overlapping subdomains in static and dynamic settings [146, 207]. To the best of our knowledge, this is the first study to demonstrate the integration of a PI-DeepONet with an FE solver, forming a cohesive FE–Neural Operator (FE–NO) architecture capable of simulating dynamic physical systems. While we present the methodology in a two-dimensional (2D) context, the approach is readily extendable to three dimensions.

The computational domain $\Omega \subset \mathbb{R}^2$ is decomposed into two overlapping subdomains, Ω_I and Ω_{II}, such that $\Omega = \Omega_I \cup \Omega_{II}$ and the overlapping region is defined as $\Omega_o = \Omega_I \cap \Omega_{II}$. Figure 3.2 illustrates the decomposition, where Ω_I (gray + orange) is governed by the FE model, and Ω_{II} (green + orange) is modeled by the PI-DeepONet.

We denote the interface boundary between subdomains as Γ_{II}^{in} (blue line), the external boundary of Ω_{II} as Γ_{II}^{out} (red line), and the external boundary of Ω_I as Γ_I^{out} (yellow line).

Two configurations are considered in this work: Figure 3.2(a) corresponds to the static and quasi-static settings involving linear elastic and hyperelastic materials, where Ω_{II} is circular. Figure 3.2(b) depicts the dynamic setting involving elastodynamics, with a square-shaped Ω_{II}. Importantly, this framework allows Ω_{II} to assume arbitrary geometry, even in cases where the interface Γ_I^{in} lacks smoothness (i.e., $\Gamma_I^{in} \notin C^1(\mathbb{R})$ as shown in the dynamic case.

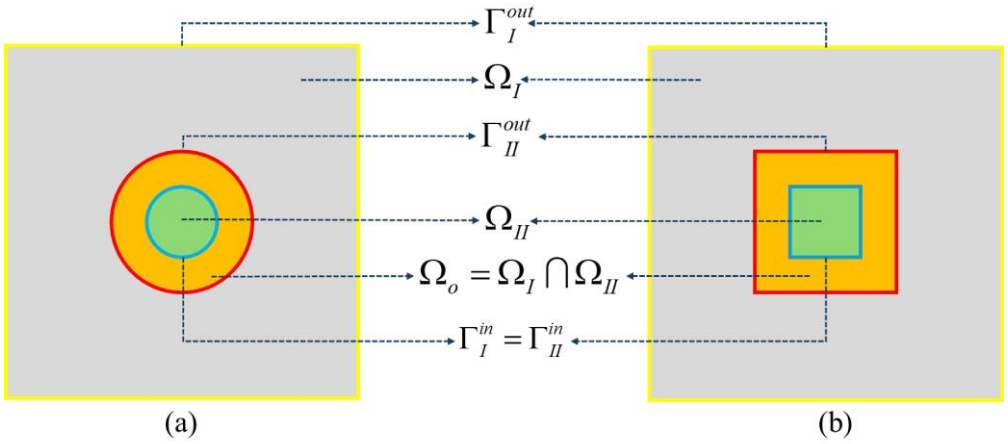

Figure 3.2 Schematics of DDM: Ω_I denotes the gray region and orange region, Ω_{II} denotes the green region and the orange region, (Ω_o) is the overlapping region in orange. Γ_I^{out} (yellow lines) and Γ_{II}^{out} (red lines) denote the outer boundary of Ω_I and Ω_{II}, respectively. $\Gamma_{II}^{out} = \Gamma_{II}^{in}$ (blue lines) is the inner boundary lines for both Ω_I and Ω_{II}.

The algorithm of the Schwarz alternating method at the overlapping boundary in quasistatic or dynamic mode is illustrated in Algorithm 1. The core of the coupling strategy

lies in the Schwarz alternating method, outlined in Algorithm 1. At each iteration, the FE and NO models alternately solve their respective subdomains. Each solver uses the most recent interface data from the other, which ensures consistency and continuity across the overlapping region. Relaxation parameter (denoted as $\boldsymbol{\rho}_r$) is introduced at the interface to stabilize the iteration and accelerate convergence.

Algorithm 1: Schwarz alternating method at overlapping boundary in the coupling framework

Initialization: Set $\mathbf{u}_{NO}^{0} = \mathbf{0}$ in Ω_{II} and $\mathbf{u}_{FE}^{0} = \mathbf{0}$ in Ω_{I};
Main loop:
for $n = 0 : n_{max} - 1$ **do**:
  Set $j = 0$, and ϵ a critical value
  while $j \geq 0$ **do**:
    $j = j + 1$
    Model FE:
      1. Receive the interface information $\mathbf{u}_{|\Gamma_I^{in}}^{n,j-1}$ from Model NO and $\mathbf{u}_{|\Gamma_I^{out}}^{n,j-1}$ from the external sources.
      2. Solve $u_{|\Omega_I}^{n,j}$ based on the boundary conditions.
      3. Obtain the $\mathbf{u}^{n,j}$ at Γ_{II}^{out} and pass it to Model NO.
    Model NO:
      1. Receive the interface information $\mathbf{u}_{|\Gamma_{II}^{out}}^{n,j}$ from Model FE.
      2. Solve $\mathbf{u}_{|\Omega_{II}}^{n,j}$ based on the boundary conditions and obtain $\mathbf{u}_{|\Gamma_{II}^{in}}^{n,j}$.
      3. Calculate the relaxation formula: $\tilde{\mathbf{u}}_{|\Gamma_{II}^{in}}^{n,j} = (1 - \boldsymbol{\rho}_r)\mathbf{u}_{|\Gamma_{II}^{in}}^{n,j} + \boldsymbol{\rho}_r \mathbf{u}_{|\Gamma_I^{in}}^{n,j}$; and pass it back to Model FE.
    If $\|\mathbf{u}_{|\Omega_I}^{n,j} - \mathbf{u}_{|\Omega_I}^{n,j-1}\|_{L^2} + \|\mathbf{u}_{|\Omega_{II}}^{n,j} - \mathbf{u}_{|\Omega_{II}}^{n,j-1}\|_{L^2} < \epsilon$, **end while**
  End for

In static problems, time stepping is unnecessary and only the inner iteration loop is executed. The convergence criterion is defined by the L^2 norm of successive iterates:

$$L^2 \text{ error} = \left\|\mathbf{u}_{|\Omega_I}^{n,j} - \mathbf{u}_{|\Omega_I}^{n,j-1}\right\|_{L^2} + \left\|\mathbf{u}_{|\Omega_{II}}^{n,j} - \mathbf{u}_{|\Omega_{II}}^{n,j-1}\right\|_{L^2} \tag{3.79}$$

Once convergence is achieved, the solutions are assembled for each subdomain at time step n, as:

$$\mathbf{u}_{|\Omega_I}^{n} := \mathbf{u}_{|\Omega_I}^{n,j} \tag{3.80}$$

$$\mathbf{u}^{n}_{|\Omega_{II}} \coloneqq \mathbf{u}^{n,j}_{|\Omega_{II}} \tag{3.81}$$

This results in a global solution $\mathbf{u}^{n}_{|\Omega}$over the entire domain. The Schwarz method, long used in classical DDM for PDEs [208], proves equally effective in this hybrid FE–NO context.

3.3.4 Expansion of ML-subdomain in dynamic simulations

A key objective of the FE–NO coupling framework is to accelerate the simulation of complex mechanical systems, particularly under dynamic loading conditions. In many such problems, the regions requiring the most computational effort evolve spatially and temporally throughout the simulation. For example, during crack propagation, the highest stress and computational intensity is localized near the moving crack front. As the crack advances or branches, the surrogate model must adapt accordingly to maintain efficiency and accuracy. In such cases, one needs to either shift the ML-subdomain to the desired location or to adaptively expand its size.

To address this challenge, we propose a strategy for ML-subdomain expansion, which enables the PI-DeepONet to follow and encapsulate the most demanding computational regions during the simulation. This is achieved by expanding or repositioning the PI-DeepONet subdomain dynamically, replacing the original region with a larger or differently located one as needed. Initially, only a small region-typically centered in the domain-is modeled by the PI-DeepONet, as shown in Fig. 3.2. After a certain number of time steps, this region may be expanded to include more area of interest, such as a propagating crack tip. As illustrated in Fig. 3.3, two DeepONet subdomains are combined to form a larger surrogate domain. To efficiently train the PI-DeepONet for the expanded subdomain, we apply transfer learning [208] by fine-tuning only the trunk network of the original PI-DeepONet while keeping the branch network fixed (frozen). These DeepONet models are used in parallel to model the extended region. This dynamic strategy maintains high accuracy while reducing the burden on the FE solver, which continues to handle the remainder of the computational domain.

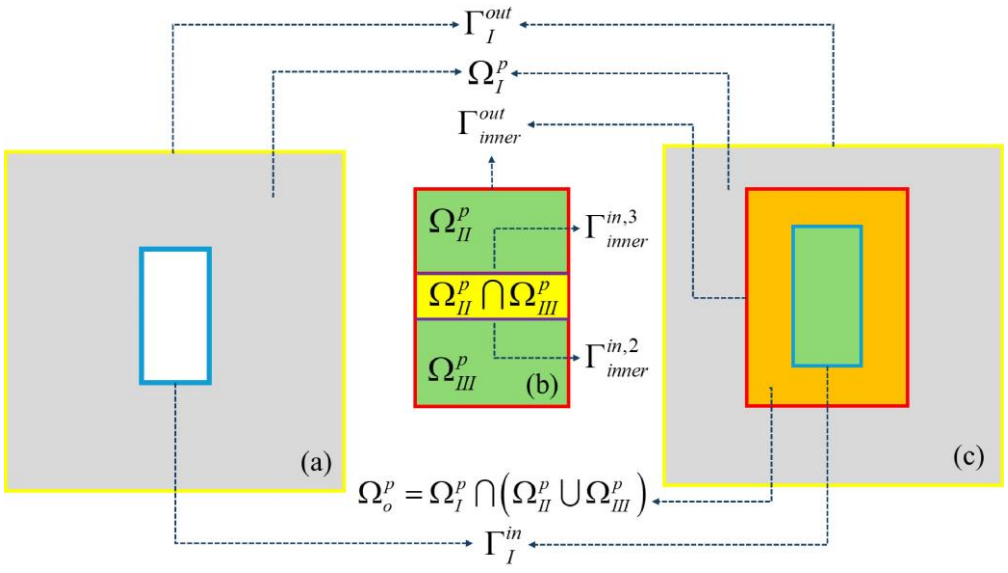

Figure 3.3 Schematic of adaptive DeepONet subdomain expansion: (a) Ω_I^p is the FE domain (gray region) with a central hole representing the initial DeepONet region. (b) Two PI-DeepONet regions Ω_{II}^p and Ω_{III}^p (green squares) are activated and combined to cover a larger area. The yellow area represents their overlap. (c) The full domain showing the overlapping region (orange) between the FE domain Ω_I^p and the union of the expanded DeepONet domains.

The underlying algorithm follows a similar structure to the Schwarz alternating method introduced earlier (Algorithm 1), with the main difference being the multiple DeepONet regions that must be synchronized. These DeepONet models are treated as a combined surrogate system, exchanging information with each other and with the FE solver. The modified Schwarz algorithm is outlined in Algorithm 2, where the inner iteration handles FE–NO coupling and an additional layer handles synchronization between the two NO regions.

Algorithm 2: Schwarz alternating method for multi-region DeepONet coupling

Initialization: Set $\mathbf{u}^0_{NO1} = \mathbf{0}$ in Ω^p_{II}, $\mathbf{u}^0_{NO2} = \mathbf{0}$ in Ω^p_{III}, and $\mathbf{u}^0_{FE} = \mathbf{0}$ in Ω^p_I
Main loop:
for $n = 0 : n_{max} - 1$ **do**:
  Set $j = 0$, $k = 0$, ϵ and ϵ' the critical values
  while $j \geq 0$ **do**:
    $j = j + 1$
    Model FE:
      1. Receive the interface information $\mathbf{u}^{n,j-1}_{|\Gamma^{in}_I}$ from Model combined NOs and $\mathbf{u}^{n,j-1}_{|\Gamma^{out}_I}$ from the external sources.
      2. Solve $\mathbf{u}^{n,j}_{|\Omega^p_I}$ based on the boundary conditions.
      3. Obtain the $\mathbf{u}^{n,j}$ at Γ^{out}_{inner} and pass it to Model combined NOs.
    Model combined NOs:
      while $k \geq 0$ **do**:
        $k = k + 1$
        Model NO1:
          If $n = 0, j = 0, k = 0$ **do**:
            1. Receive the boundary conditions of Model NO1 from interface information $\mathbf{u}^{n,j}_{|\Gamma^{out}_{inner}}$ obtained in Model FE; and assume $\mathbf{u}^{n,j,k}_{|\Gamma^{in,1}_{inner}} = \mathbf{0}$.
          Else do:
            1. Receive the boundary conditions of Model NO1 from interface information $\mathbf{u}^{n,j}_{|\Gamma^{out}_{inner}}$ and $\mathbf{u}^{n,j,k-1}_{|\Gamma^{in,1}_{inner}}$ obtained in Model FE and Model NO2, respectively.
            2. Solve $\mathbf{u}^{n,j,k}_{|\Omega^p_{II}}$ based on the boundary conditions and obtain $\mathbf{u}^{n,j,k}_{|\Gamma^{in,2}_{inner}}$ and pass it to Model NO2.
        Model NO2:
          1. Receive the interface information $\mathbf{u}^{n,j}_{|\Gamma^{out}_{innner}}$ from Model FE and $\mathbf{u}^{n,j,k}_{|\Gamma^{in,2}_{inner}}$ from Model NO1
          2. Solve $\mathbf{u}^{n,j,k+1}_{|\Omega^p_{III}}$ based on the boundary conditions, then obtain $\mathbf{u}^{n,j,k+1}_{|\Gamma^{in,1}_{inner}}$, and pass it to Model NO2.
        If $\|\mathbf{u}^{n,j,k}_{|\Omega_{II}} - \mathbf{u}^{n,j,k-1}_{|\Omega_{II}}\|_{L^2} + \|\mathbf{u}^{n,j,k}_{|\Omega_{III}} - \mathbf{u}^{n,j,k-1}_{|\Omega^p_{III}}\|_{L^2} < \epsilon'$, **end while**, obtain the boundary conditions $\mathbf{u}^{n,j}_{|\Gamma^{in}_I}$ and pass it to Model FE.
    If $\|\mathbf{u}^{n,j,k}_{|\Omega_I} - \mathbf{u}^{n,j-1,k}_{|\Omega_I}\|_{L^2} + \|\mathbf{u}^{n,j,k}_{|\Omega_{II}\cup\Omega_{III}} - \mathbf{u}^{n,j-1,k}_{|\Omega_{II}\cup\Omega_{III}}\|_{L^2} < \epsilon$, **end while**
  End for

To ensure consistency between the FE and ML subdomains and among the ML subdomains themselves, we define two L^2-based convergence metrics:

$L^2_{p_1}$ measures convergence between the DeepONet subdomains:

$$L_{p_1}^2 = \left\| \mathbf{u}_{|\Omega_{II}}^{n,j,k} - \mathbf{u}_{|\Omega_{II}}^{n,j,k-1} \right\|_{L^2} + \left\| \mathbf{u}_{|\Omega_{III}}^{n,j,k} - \mathbf{u}_{|\Omega_{III}}^{n,j,k-1} \right\|_{L^2} \tag{3.82}$$

$L_{p_2}^2$ evaluates convergence between the combined DeepONet region and the FE domain:

$$L_{p_2}^2 = \left\| \mathbf{u}_{|\Omega_I}^{n,j,k} - \mathbf{u}_{|\Omega_I}^{n,j-1,k} \right\|_{L^2} + \left\| \mathbf{u}_{|\Omega_{II} \cup \Omega_{III}}^{n,j,k} - \mathbf{u}_{|\Omega_{II} \cup \Omega_{III}}^{n,j-1,k} \right\|_{L^2} \tag{3.83}$$

Convergence is achieved when both $L_{p_1}^2 < \epsilon$ and $L_{p_2}^2 < \epsilon$. The final solution at time step *n* across all three subdomains is then defined as:

$$\mathbf{u}_{|\Omega_I}^{n} := \mathbf{u}_{|\Omega_I}^{n,j,k} \tag{3.84}$$

$$\mathbf{u}_{|\Omega_{II}}^{n} := \mathbf{u}_{|\Omega_{II}}^{n,j,k} \tag{3.85}$$

$$\mathbf{u}_{|\Omega_{III}}^{n} := \mathbf{u}_{|\Omega_{III}}^{n,j,k} \tag{3.86}$$

The global solution $\mathbf{u}_{|\Omega}^{n}$ is assembled by stitching together these subdomain solutions. In this work, we manually expanded the ML subdomain to demonstrate the feasibility of adaptive surrogate integration. In future work, we aim to develop a fully automated scheme that dynamically expands the ML subdomain based on parametric thresholds derived from physical or error-based indicators. Furthermore, we demonstrate the method using two DeepONet subdomains; however, the strategy naturally extends to more regions. By incrementally activating and repositioning DeepONet subdomains during simulation, the surrogate model can continuously track and adapt to evolving regions of interest. Additionally, due to the interchangeable roles of the FE and DeepONet solvers, the PI-DeepONet region can be translated across the domain as needed, allowing dynamic redistribution of computational resources. This adaptive strategy offers a powerful way to accelerate large-scale simulations without sacrificing accuracy-enabling simultaneous model refinement and physical prediction throughout the simulation.

Table 3.3 PI-DeepONet architectures for different material models.

Model	Branch Net	Trunk Net	Activation
Linear Elastic	[200 ×2, 100 ×4, 800]	[2, 100×4, 800]	tanh
Hyper-elastic	[200 ×2, 100 ×4, 800]	[2, 100×4, 800]	tanh
Elasto-dynamic	CNN + [82^2×4, 256, 800] and [82×4×2, 100 × 4, 800]	[2, 100×4, 800]	tanh

Chapter 4 Void-Mediated Cracking and Lithium Penetration in ASSLMBs

4.1 Modelling and validation

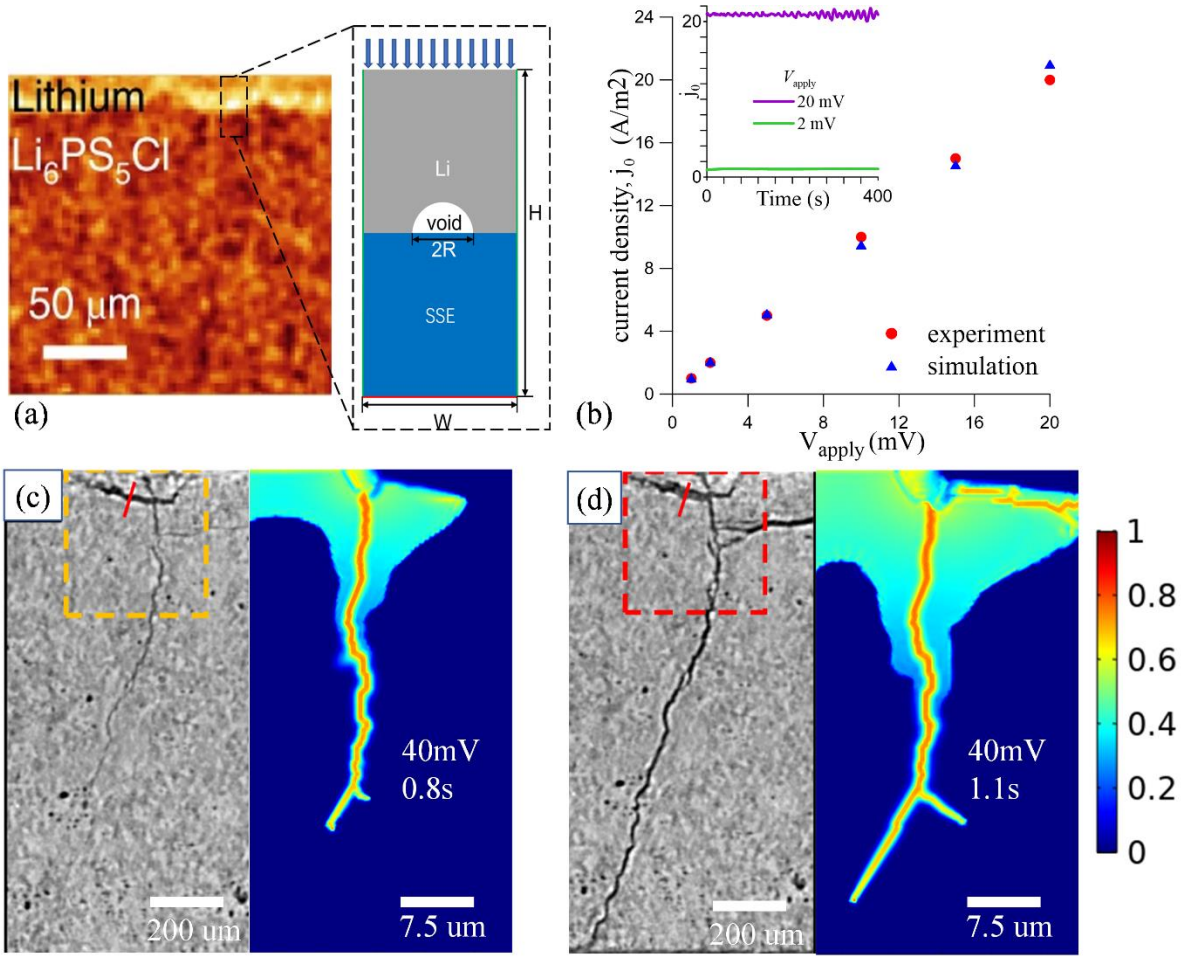

Figure 4.1 Numerical model and experimental verification: (a) left: the voids in Li/Li_6PS_5Cl interface obtained in Bruce's experiments [81]; right: The schematic for the model, blue arrows represent the stack pressure, the red line denotes the fixed boundary, and the green lines for periodic boundary, the radius of semicircle region for void is R, in discharging case and stack pressure at 5MPa and 10MPa, R=5 um, in charging case, R=10 μm; (b) current density, j_0 versus applied voltage V_{apply} for experiment and simulation respectively, and the inset figure shows j_0 versus time for applied voltage at 20 mV and 2 mV; left figures in (c) (d) are the cracks after plating observed by Ning *et al.* [84], right figures in (c)(d) are the cracks obtained in our simulations.

We consider a multiphase system comprising lithium metal (p_1), SSE (p_2), and voids (p_3), where p_i represents the corresponding phase-field order parameter. The constraint $p_1 + p_2 + p_3 = 1$ holds at every material point, allowing for complete characterization of pure phases, lithium ($p_1 = 1$), SSE ($p_2 = 1$), void ($p_3 = 1$), as well as interfacial regions ($0 < p_i < 1$). In the case of a three-phase mixture, besides interfaces, it can also be a damaged area in SSE with some microcracks partially filled with lithium or a lithium zone that has been partially stripped, leaving vacancies. To quantitatively describe the evolution of this complex microstructure in this multiphase system, we assumed diffusive interfaces instead of sharp interface to evade mathematical difficulties in dealing with discontinuities [175]. Within a PF framework, the diffusive interface thickness remains constant and is determined by the gradient energy density and a double-well potential, as expressed in Eq. 2.3.

In the concerned electrochemical system, there are two categories of phase transformations. First, the electro-stripping or plating of lithium leads to the migration of Li-SSE interfaces, which is described by the competitive processes of electron loss and gain; this can be described using the Butler-Volmer (BV) equation [173, 181]. Second, cracking leads to separation of material, which can be regarded as the enlargement of the void phase. This is a one-way process; that is, a cracked SSE cannot be self-healed in a mechano-electrochemical process. To enforce the thermodynamic irreversibility of fracture in this mechano-electrochemical system, a special Heaviside-like continuous function $H(\sigma_I)$ is introduced in the equation governing crack propagation. Since voids or cracks are designated by p_3, the employment of $\Psi(\xi)$ is to ensure monotonic increase of p_3 in SSE.

The derivation of the governing equations is detailed in **Chapter 3.1** and consists of four components: (i) generalized AC equations derived from the BV equation [181] with an advective term dealing with rigid body motion [183], (ii) Nernst-Planck equations describing ion transport, (iii) equilibrium equations governing mechanical deformation, and (iv) Alain's fracture term in PFFM [209], which activates crack propagation when the strain energy exceeds a critical threshold under tensile stresses. This coupled formulation

provides a comprehensive framework for simulating the complex interplay between electrochemical processes and mechanical degradation in ASSBs.

Let us exhibit some of the results based on the numerical model shown in Fig. 4.1(a). This numerical model represents a small area near a Li/SSE interface referring to the experimental result presented in [81], which is captured on the left in Fig. 4.1(a). The model dimensions are 50 μm in width (W) and 100 μm in height (H), containing a semicircular void (radius R = 5 μm) in the lithium anode. A uniform stack pressure of 1 MPa is applied, as indicated by the blue arrows. The bottom (red line) of the SSE model is mechanically fixed (no vertical displacement) and set with a constant Li^+ concentration to absorb or provide the flux of lithium ions during discharging or charging, respectively. The latter setting is to ensure the bulk electroneutrality of the SSE. The two sides (green lines) are periodic boundaries. It is noted that the problem has been simplified to be two-dimensional (2D), representing a cuboid with thickness several times larger than the width, thus satisfying the plane-strain assumption in solid mechanics. This simplification can stand considering that the actual ASSLMB system is much larger than the numerical model. On the other hand, the 2D model can reveal most of experimental phenomena, and thus, suffice to study parametric effects.

Model calibration was performed through current-voltage characteristic matching, as shown in Fig. 4.1(b). After removing the void and adjusting parameters within experimentally reported ranges [81], the simulated charging behavior agreed well with experimental measurements. The inset in Fig. 4.1(b) demonstrates two simulation results of the time-dependent current densities under applied voltages of 2 and 20 mV, demonstrating stable current densities in the absence of mechanical failure. After calibration (calibrated parameters are listed in **Appendix A.2**), the semicircular void is introduced in the lithium and applied voltage V is gradually increased. Notably, charging and discharging voltage merely differ in sign, and our description in this section focuses solely on the magnitude of V. In charging, at V = 40 mV (corresponding to the applied current density of 40 A/m^2 based on current density-applied voltage relation shown in Fig. 4.1(b)), two successive cracking morphologies of SSE at the simulation time of 0.8s and

1.1s are captured by the numerical model, as shown in Fig. 4.1(c, d), respectively. It is found that the SSE is damaged (*i.e.*, with nonzero p_3) initially near the interface, then fractured with a main crack propagating toward to the cathode and a transverse crack parallel to the Li/SSE interface as shown in Fig. 4.1(d). These two typical cracks are both caused by the non-uniform ion transport near three-phase points, leading to large stresses over there. These results are consistent with the *in situ* experimental observations from [81], which are shown on the left-hand side of each simulated result for direct comparison. These results let us have the confidence to further investigate the mechanical failure mechanism of ASSLMBs and suggest methods to improve the stability of SSE.

4.2 Voids induced by stripping

The simulation results confirm that stripping-induced voids (Fig. 4.1(a)) constitute the fundamental cause of SSE cracking during high-voltage or high-current charging. While the origin of these voids and the effectiveness of stack pressure remain subjects of debate [93, 210, 211], our phase-field model provides new insights into these phenomena. It has been argued that the transport of lithium along free surfaces can be faster than that in the bulk [97], causing void growth in stripping. The model incorporates a diffusivity ratio (DR) between lithium transport at free surfaces (Li/void interfaces) and within the bulk anode, enabling detailed investigation of void evolution during stripping. In particular, it also allows the quantitative examination of how stack pressure can affect the voids.

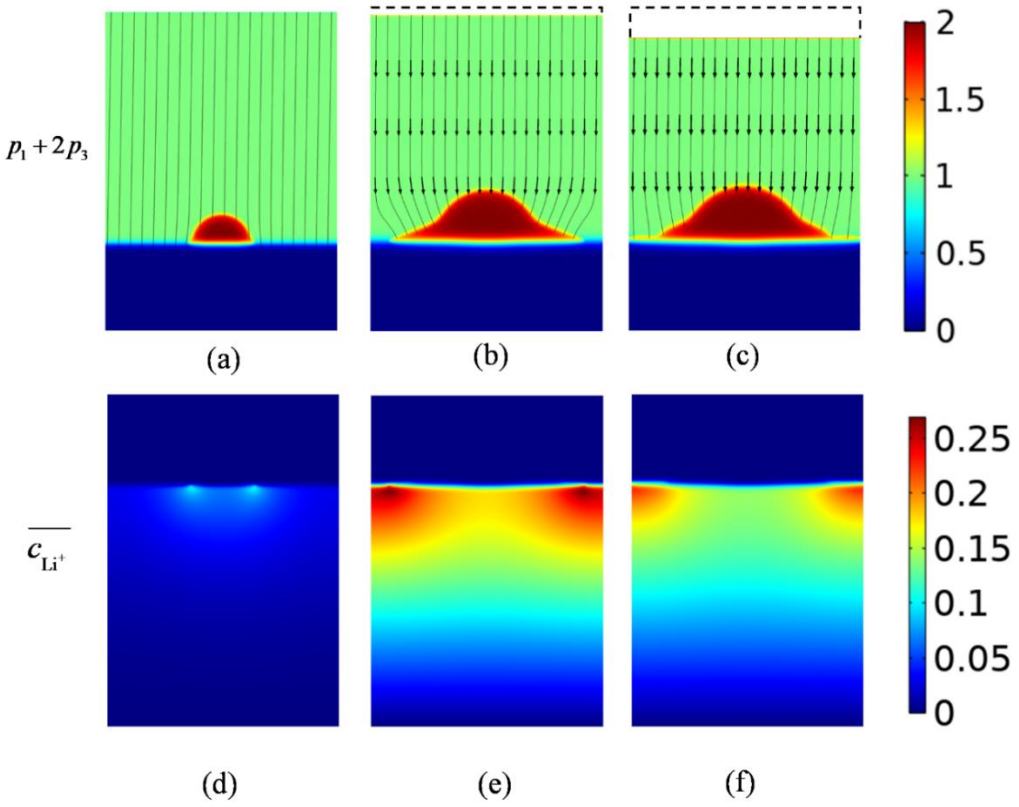

Figure 4.2 Void's evolution in discharge process with stack pressure at 1MPa: (a)(b)(c) and (d)(e)(f) are the morphology and lithium ions concentration respectively at 1s 5s and 7s.

Figure 4.2 presents the void evolution during stripping under a potential of 40 mV and stack pressure of 1 MPa, assuming an initial semicircular void (R = 5 μm) and DR = 100. It is noted that the results demonstrate void growth during stripping, with lithium creep under stack pressure deforming the void into a "straw hat" morphology, consistent with previous findings [99]. The streamlines in the upper panel of Figs. 4.2(a-c) indicate the displacement of lithium under the stack pressure, which tends to fill the void. The expediated surface diffusion and creep under stack pressure are the competing mechanisms, achieving a dynamic equilibrium that stabilizes the void size after initial growth. It is evidenced by the unchanged geometry between the 5th and 7th seconds in Fig. 4.2.

The stabilized void size depends critically on DR, stack pressure, and the initial size. Our analysis shows that DR > 1 inevitably leads to transient void growth during stripping (see Fig. A.3 in **Appendix A.3** for cases of DR = 5, 10, 50); while even DR = 1 cannot completely eliminate preexisting voids under stack pressure. Voids initially form at

the Li/SSE interface either as inherent defects or through accumulation during stripping processes, with subsequent coalescence leading to larger void structures. Therefore, in experiments voids of different sizes were observed. This mechanism explains the experimental observation of voids with varying dimensions. When subjected to substantial stack pressures (1 MPa), the voids develop a characteristic straw-hat morphology. The merging of these deformed voids likely accounts for the flattened, oval-shaped voids of significant size documented in reference [81]. In experimental settings, researchers have employed elevated stack pressures to leverage lithium's viscoplastic creep behavior at room temperature, aiming to minimize void formation and enhance Li-SSE contact. However, such high pressures merely modify void geometry through flattening rather than complete elimination. Furthermore, this approach may inadvertently increase susceptibility to cracking. A detailed examination of these critical issues will be presented in subsequent sections.

Figures 4.2(d-f) show the Li+ concentration distribution at 1, 5, and 7 seconds, revealing maximum concentration at the three-phase points due to enhanced Li^+ transport and electrochemical reactivity at Li/void interfaces. These excess Li^+ ions, existing as interstitials in the SSE lattice [212, 213], induce the local chemical expansion [177] and high strain energy in the SSE. Interestingly, the strain energy density is not the highest in the region next to the three-phase point, though Li^+ concentration maximizes there. Instead, the highest strain energy density occurs in the middle between the two three-phase points. During stripping, the local chemical expansion leads to compressive stresses from the constraint of surrounding SSE; hence, the crack of SSE is absent in stripping, aligning with the experimental results in Ref. [84]. Conversely, the plating process reverses these effects, creating tensile stresses ($\sigma_I > 0$) at void/SSE interfaces that ultimately lead to crack nucleation.

4.3 Embryo and extension of cracks in plating

The numerical simulations corroborate experimental observations that crack initiation and propagation precede lithium dendrite formation, as demonstrated in Fig.

4.3(h). During charging, lithium-ion depletion near void edges generates substantial tensile stresses at the void/SSE interface, ultimately inducing crack formation. Subsequent lithium deposition occurs on crack surfaces, with high stack pressures further squeezing lithium into cracks.

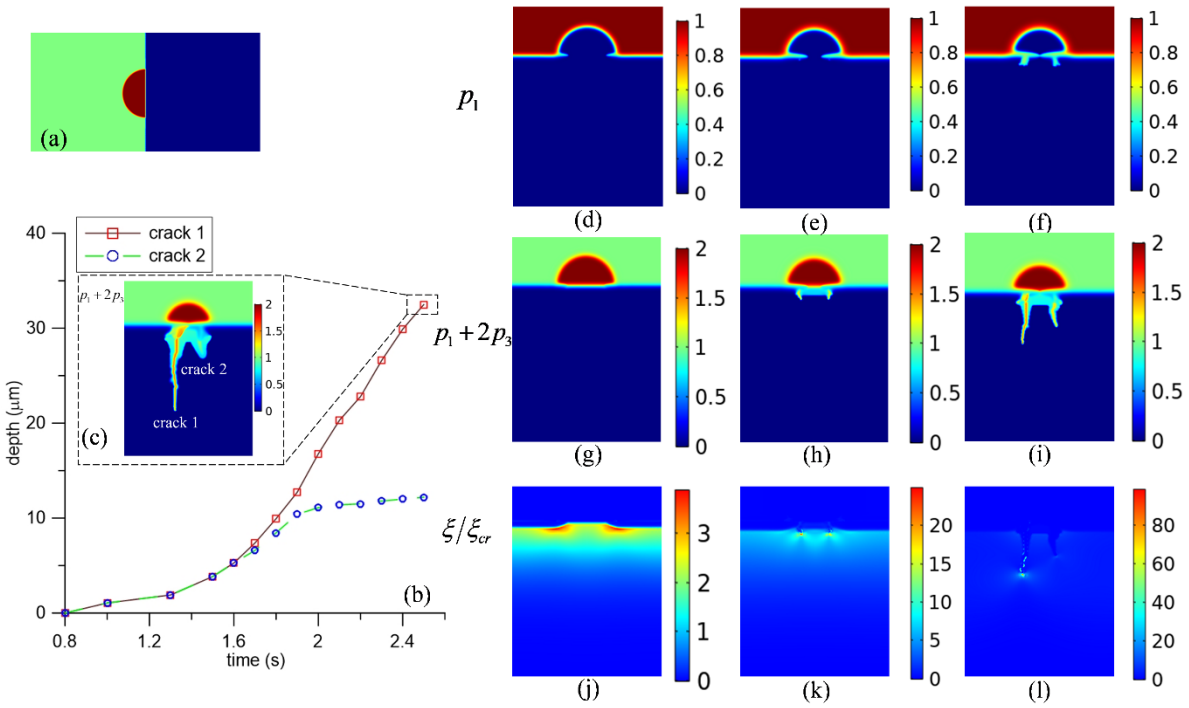

Figure 4.3 Cracks and dendrites' formation and evolution in charge process with stack pressure at 1 MPa: (a) the initial morphology at 0s of cell; (b) the relation between the crack length in SSE (Li_6PS_5Cl) versus time for crack 1 and crack 2 at 2.5s noted in inset figure, respectively; (d)(e)(f) are the order parameters (p_1); (g)(h)(i) are the order parameter of lithium (p_1+2p_3), (j)(k)(l) are the dimensionless strain energy distribution (ξ/ξ_{cr}) at 0.8s and 1.5s and 2s.

We first consider the stack pressure of 1 MPa, applied a charging voltage of 40 mV, and critical strain energy ξ_{cr} = 6 MJ/m^3 (corresponding to the mode-I fracture toughness K_{Ic} = 0.22 MPa·m$^{0.5}$, cf. **Appendix A.1** Fig. A.1 for the correspondence) with the initial morphology (void radius R = 10 μm) shown in Fig. 4.3(a). The cracking depth versus time are depicted in Fig. 4.3(b) with the final cracked SSE morphology in the inset Figure 4.3(c). As shown in Fig. 4.3(b), the competition of two cracks nucleated from the two three-phase points, where only one develops into the dominant crack propagating toward the bottom (or cathode), as its advancement effectively releases strain energy and suppresses the

competing crack to further propagate. These asymmetric cracks generation results from the use of triangular meshes, introducing inherent asymmetry and minor geometric imperfections. These initial irregularities, combined with the inherent instability of the cracking process, result in slight differences in early crack growth. Given the unfair strain energy release feature, only one crack unceasingly propagates.

The evolutions of order parameters p_1 (lithium), p_1+2p_3 (lithium and void), and dimensionless strain energy are presented in Fig. 4.3(d-l). In the simulation, lithium plating is manifested by the migration of three-phase points where lithium ions can be reduced, and empty spaces are available to accommodate newly formed lithium metal. Fig. 4.3(d) and (g) show that the deposition near the three-phase point is much faster than that in other areas, leading to partially closure of the initial semicircular or straw-hat-shaped void in Fig. 4.3(d, e), aligning with the mechanism reported in Ref. [81]. Fig. 4.3(g-i) shows a void-closing process, which is similar to those demonstrated in [99]. Concomitantly, cracks are formed, and lithium preferentially grows on crack surfaces [214], as shown in Fig. 4.3(f).

During the electroplating process, lithium ions depletion near three-phase points arises from the high rates of ion transport and reduction (deposition), leading to a tendency of local contraction that is constrained by surrounding media (SSE). Therefore, tensile stresses are generated near three-phase points, as presented in Fig. 4.3(j-l). Notably, at 0.8 s, the local strain energy ξ is almost four times ξ_{cr} (Fig. 4.3(j)), causing damaged zones (i.e., $p_3 > 0$) near the Li/SSE interface. Before the propagation of main cracks, the SSE near the interface has been spalled, and lithium deposits in this spalled zone. Crack formation induces stress concentration at tips, further elevating strain energy (Figures 4.3(k, l)) and driving crack advancement. Continued plating expands the spalled zone, with lithium growth progressing through both spalled regions and crack, found in Fig. 4.3(f, i).

4.4 Critical current density (CCD)

The CCD of our simulation model was determined by systematically increasing the applied current (or equivalently the voltage, based on their relationship established in Figure 4.1(b) for non-failure cases). The detailed methodology for current density

application is provided in **Appendix A.2**. Figure 4.4(a) presents the temporal evolution of voltage under various current densities ranging from 15 to 25 A/m², revealing three distinct response regimes: (i) at current densities between 15-17 A/m², the voltage initially rises before gradually decreasing, with complete void occlusion occurring without crack formation, as shown in Fig. 4.4(b); (ii) in the 17-22 A/m² range, the voltage exhibits a steeper initial increase followed by sustained oscillations at high levels, accompanied by slow crack propagation, as shown in Fig. 4.4(c); (iii) above 22 A/m², the voltage increases monotonically with rapid, catastrophic crack growth. It should be noted that the CCD of our simulation model is identified between 17-18 A/m², as crack initiation occurs within this range. Though crack propagation is slow in this range of current density, repeated cycling, in particular plating, ultimately leads to mechanical failure of cell. Notably, when the current density is below CCD, the SSE remains intact, and voids can be fully closed. When the applied current density is slightly larger than CCD, although the void can also be quickly closed, the accompanying crack formation degrades local Li/SSE contact, manifesting as voltage oscillations. When the applied current density is even larger, the crack propagation is accelerated, driving continuous voltage rise until complete mechanical failure.

A 0.6V increase in voltage during plating is observed by Porz *et al*. [97] at a cracked area of their SSE. To probe such a local area, the researchers employed a brass tip electrode. If a whole macroscopic cell is concerned, the overpotential is much lower (e.g., 0.05 V as reported in [81]). This difference arises from the strong nonuniformity in electric field near a cracked area, caused by the microscale contact loss. Fig. 4.4 shows that the increase in overpotential can be as high as 1.8 V if a transient local (50 μm in width) potential is probed.

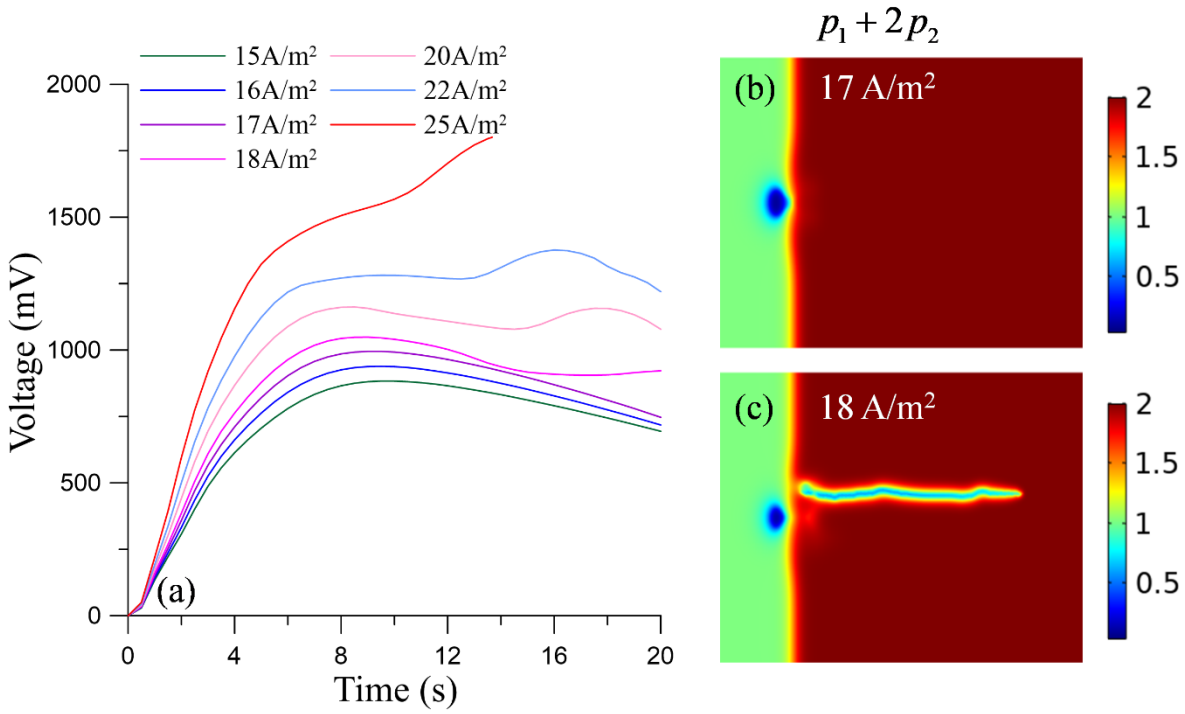

Figure 4.4 Analysis of critical current density (CCD): (a) the voltage (V) versus time (s) at constant current density ranging from 15 to 25A/m^2, (b)(c) are the morphology (p_1+$2p_2$) for the current density at 17A/m^2 and 18A/m^2 at 20s, respectively.

The simulations reveal a remarkable sensitivity of crack propagation behavior to the applied current density, with just a 1 A/m² difference producing the distinct outcomes shown in Figures 4.4(b) and 4.4(c). This demonstrates the critical nature of the mechanical failure threshold. Notably, crack initiation occurs in subsurface layers rather than at the SSE surface (Figure 4.4(c)), attributable to partial stress relief at the surface, i.e., the surface is not under tension along the normal direction or under compressive stress due to stack pressure. Experimental observations confirm that current densities exceeding the CCD produce unstable voltage responses. The elevated voltages during charging stem from reduced contact area caused by cracking. Interestingly, when operating slightly above the CCD threshold (before catastrophic mechanical failure occurs), lithium plating within cracks can temporarily increase contact area, potentially leading to gradual voltage reduction over multiple cycles. After several stripping and plating cycles, in final cycle the starting voltage in charging will become very large then quickly decrease to 0 due to the short circuit, as revealed experimentally in ref. [81]. This phenomenon, accurately captured

by our simulations, elucidates the mechanism behind accelerated battery degradation under high charging currents. Extreme current densities (e.g., 25 A/m² in our model) produce continuously rising plating voltages, as shown in Fig. 4.4(a), consistent with Porz *et al.*'s experimental findings [97]. Thus, the different voltage profiles in the two experiments [81, 97] fundamentally arise from the dynamic competition between two opposing processes: crack propagation (increasing the contact loss) and lithium penetration (reducing the contact loss)

4.5 Effect of stack pressure

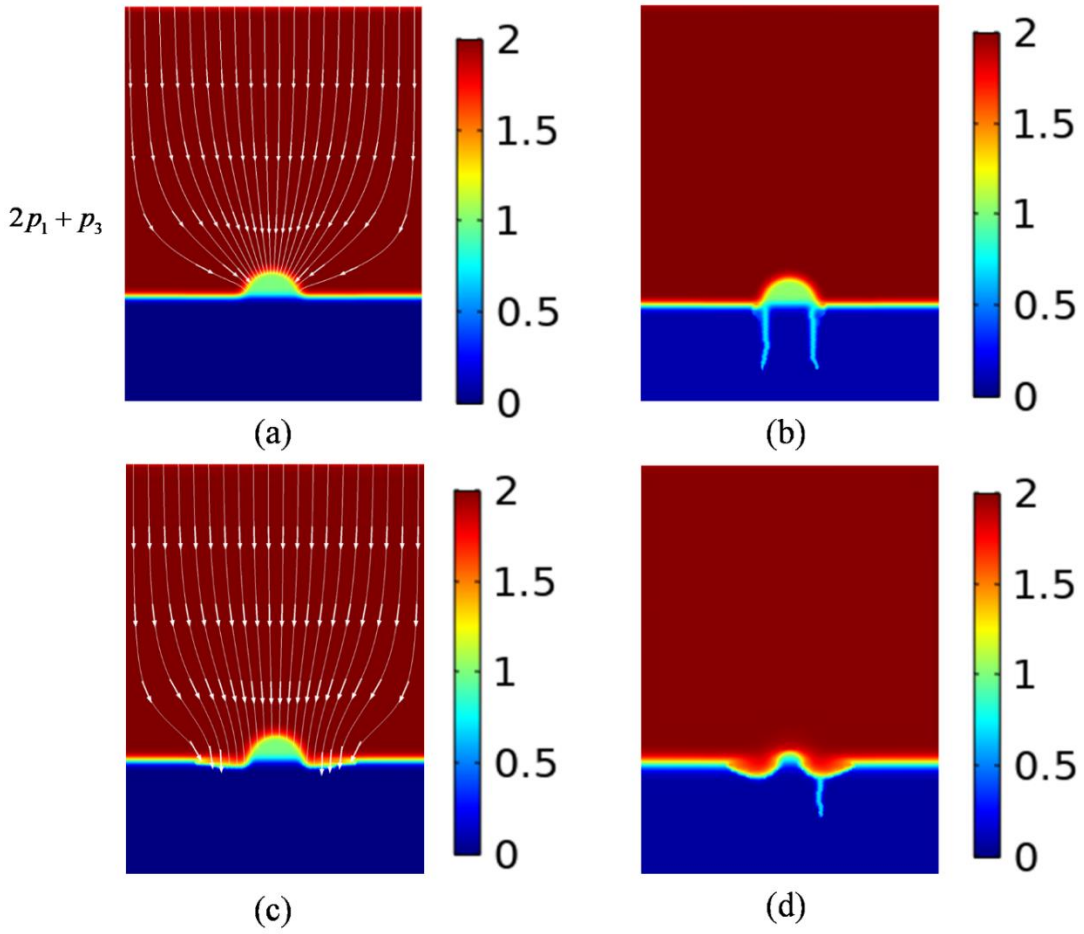

Figure 4.5 Cell performance with stack pressure at 5 MPa and 10 MPa: (a)(b) are the morphology with and without the consideration of electrochemical reaction at 5 MPa at 0.6 s and 0.5 s, respectively. (c)(d) are at

10MPa respectively at 0.8 s and 0.31 s. The radius of the void is 5 μm for these four models.

The above sections discussed the evolutions of void, crack, and lithium dendrite. In this section, we concentrate on the methods to prevent the ASSLMBs from cracking based on the preceding mechanical failure analysis. We first examine the most popular approach: applying stack pressure. As elucidated in **Chapter 4.2**, moderate stack pressures can stabilize void size and minimize contact loss. To investigate this further, we increased the pressure to 5 MPa and 10 MPa while monitoring dendrite and crack development, maintaining an initial void radius of 5 μm. The simulations revealed that higher pressures do reduce void dimensions, but with significant trade-offs.

Fig. 4.5(a) and (c) present purely mechanical simulations excluding electrochemical processes, i.e., we only consider lithium creep and SSE crack based on the multiphase PF model. The velocity streamlines and arrows demonstrate that lithium can creep and reduce the void. It can be found that under 5 MPa stack pressure, the lithium creep effectively reduces the semicircular void to straw hat shape, as shown in Fig. 4.5(a). In the 10 MPa case, damage to the SSE and insertion of lithium are observed, indicating that extreme stack pressure can directly induce SSE damage due to the stress concentration at the boundary of voids. This phenomenon suggests that such an extreme stack pressure could be harmful to a SSE, aligning with experimental observation of Doux *et al*. [89], that is, applying a high stack pressure on a sintered SSE with inevitable porosity and low fracture toughness can cause a mechanically induced short-circuit. Fig. 4.5(b) and (d) show that simulation results incorporating electrochemical processes under high stack pressure. Under 5 MPa, the occurrence of the cracks precedes the closure of the void, and mechanical insertion of lithium is facilitated by the high pressure. Under 10 MPa, the void can be closed but the SSE has already been damaged. The mechanical force pushes lithium dendrites into the SSE, resulting in further SSE cracking. In both scenarios, synergistic acceleration occurs between lithium creep and crack propagation, hastening mechanical failure of cell.

These results challenge the perceived benefits of using high stack pressure to improve cell performance; in fact, it could even accelerate cell's mechanical failure. The

generally accepted view is that stack pressure is a necessary condition to have a stable cell. Some studies advocate high pressures for dendrite suppression [85, 215], while others warn of catastrophic mechanical failure [90, 91]; therefore, many researchers attempted to estimate a specific ideal stack pressure for each ASSLMB cell [89]. However, our simulations suggest that no matter how large the stack pressure is, cracks and dendrites appear in an SSE if the applied current density is larger than a finite CCD, because crack formation is independent on stack pressure and may even be accelerated by a high stack pressure. Then why a high stack pressure can indeed render the high recyclability of some cells [215]?

4.6 Effect of lateral pressure

While a high stack pressure is often applied to enhance Li/SSE contact and, hopefully, stabilize stripping-plating cycles, the lateral constraint on the SSE caused by high vertical pressure is often overlooked. Fig. 4.6(a) is a schematic of a typical ASSLMB testing assembly, in which the cell is sleeved and compressed between two flat punches. In such an assembly, the interaction between the SSE and the side wall of the sleeve is important, as the side constraint can impose lateral pressures on the SSE. Such a lateral pressure is proportional to stack pressure due to Poisson's effect. Under a high stack pressure, the lateral pressure is already remarkable. In addition, clamping the SSE in the sleeve can lead to an even higher lateral pressure. Here, our simulations specifically investigate these underappreciated lateral stress effects.

The model configuration applies 1 MPa vertical stack pressure combined with 3 GPa lateral pressure, as shown in Fig. 4.6(b). While this compressive stress is high, it is noted that engineering ceramics can generally withstand a compressive stress in the range of 1-5 GPa [216]. Remarkably, the applied charging voltage is 40 mV, which, without lateral pressure, should induce cracks as shown in Fig. 4.3. However, the high lateral pressure prevents the SSE from cracking; the corresponding morphology at 5 s is shown in Fig. 4.6(c). Under such lateral pressure, even at applied current density (40 A/m^2) far

exceeding the CCD (17 A/m^2), cracking and lithium penetration can be inhibited, and the void is ultimately closed.

The cell's morphological evolution is illustrated in Fig. 4.6(d, e, f) at 1.5, 2.5, and 5s, respectively. Compared with Fig. 4.3(c, d, e), the common point is that the lithium deposits faster near the three-phase point and the void tends to be occluded by the lithium deposition. However, the discrepancy between the cases with and without lateral pressure is obvious. For example, both Fig. 4.3(c) and Fig. 4.6(e) are the results at 1.5s; the former exhibits spallation and crack nucleation, whereas the latter has a much smaller spallation zone which does not further transform into cracks. Figures 4.6(g, h, i) demonstrate the distribution of dimensionless strain energy (ξ/ξ_{cr}) at 1.5, 2.5 and 5s. Although the spallation occurs in the SSE near the Li/SSE interface, compared with Fig. 4.3(j, k, l), the strain energy is much smaller and ξ/ξ_{cr} is below 1 near the void/SSE interface because the lateral compressive stress compensates for the tension induced by the chemical eigenstrain associated with the depletion of Li^+ during plating.

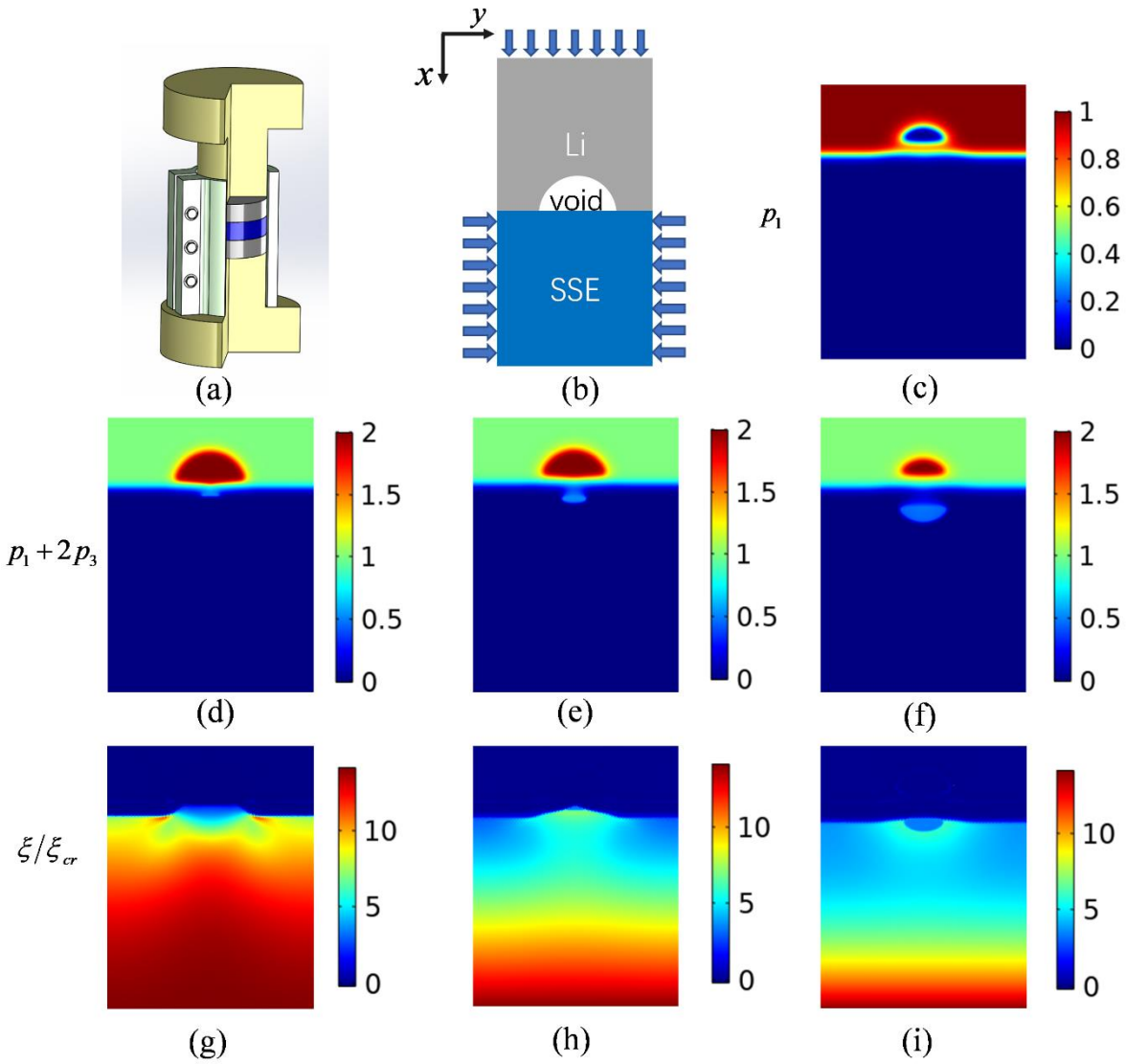

Figure 4.6 Inhibition of cracks by applying lateral stress: (a) Possible set for the ASSLIBs cell; (b) schematic for our model, the lateral stress is added, and the others are the same as Fig. 4.1(a); (c) lithium's morphology. (d)(e)(f) and (g)(h)(i) are respectively the morphology and dimensionless strain energy (ξ/ξ_{cr}) with 3GPa lateral stress at 1.5s,2.5s, and 5s.

The preceding analysis, combined with the discussion on stack pressure in **Chapter 4.5**, demonstrates that lateral pressure application can significantly improve cell stability. This finding clarifies why certain studies report enhanced performance under high stack pressures—such conditions inherently induce beneficial lateral constraints. This concept aligns with Ban *et al.* [217], who proposed stabilizing cells through compressive residual

stresses at the Li/SSE interface. Additionally, Xu *et al.* [93] developed a 3D-micropatterned SSE to maintain interfacial integrity and suppress crack formation, further underscoring the critical role of lateral compressive stresses in preventing mechanical failure mechanisms.

4.7 Stability map

After demonstrating the significant effect of lateral pressure, additional simulations were conducted to construct a stability map for the simulated ASSLMB considering the combined effect of lateral compressive stress σ_{22} and critical strain energy ξ_{cr} on the cell performance. Note that the critical strain energy is determined by the toughness of SSE (i.e., the fracture resistance of SSE), such that higher ξ_{cr} is more desirable. However, as an inherent materials parameter, ξ_{cr} depends merely on chemical bonding and can be substantially affected by unavoidable microdefects in sintering inorganic SSEs, making it difficult to improve ξ_{cr} for an SSE. In various SSEs, ξ_{cr} ranges from 1.8×10^6 to 1.6×10^8 J/m^3, corresponding to fracture toughness K_{Ic} values between 0.1 and 1 MPa·m$^{0.5}$ (cf. **Appendix A.1**). In contrast, lateral or residual compressive stresses offer a more practical means of performance enhancement, as they can be readily adjusted over a wide range. To generalize our findings across SSEs with varying Young's modulus (E) and ξ_{cr} we introduce two dimensionless parameters: ξ_{cr}/E (normalized critical strain energy) and $-\sigma_{22}/E$ (normalized lateral stress). Figure 4.7 presents stability boundaries derived from these parameters, with each boundary representing conditions under which crack formation and lithium penetration are suppressed, as exemplified in Figure 4.6. It should be noted that the partial molar volume Ω^{SSE} determines the magnitude of eigenstrain in charging and discharging, with lager Ω^{SSE} values shifting the stability boundary toward upright corner as shown in Fig. 4.7. Overall, superior cell performance is achieved at higher lateral stress and higher critical strain energy, with stable operation occurring in the regions above the plotted curves.

The stability boundaries clearly indicate the important role of high toughness. With a small Ω^{SSE} (e.g., 13.4 cm^3/mol), an SSE with high toughness ($10^3\xi_{cr}/E$ >0.54) can already achieve stable performance even without lateral stress. This suggests that increasing the fracture toughness of SSE can circumvent mechanical failure of cells. However, increasing fracture toughness meanwhile meeting the electrochemical needs, such as a high ionic conductivity and chemical stability, is difficult and probably unviable based on the existing SSEs. Instead, the application of lateral or residual compressive stresses is a more viable approach.

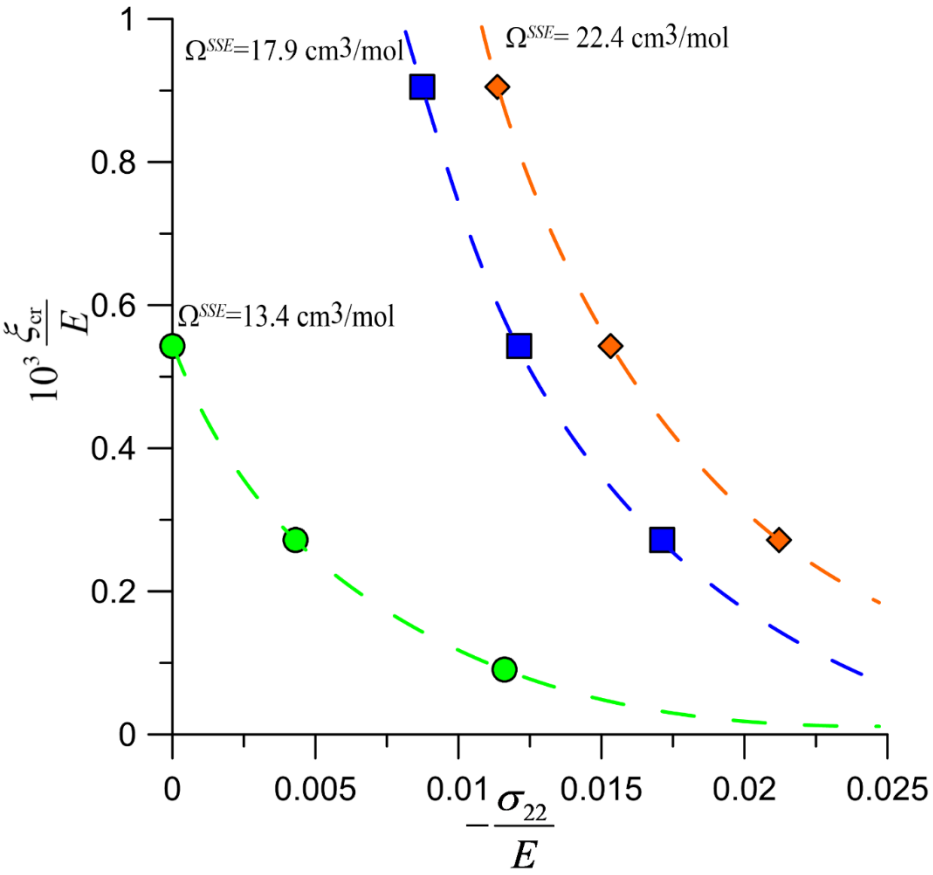

Figure 4.7 The map for cell design to eliminate crack: the map of $10^3\xi_{cr}/E$ versus $-\sigma_{22}/E$ for three different partial molar volume in SSE 13.4 cm^3/mol, 17.9 cm^3/mol and 22.4 cm^3/mol.

The preceding analysis demonstrates that lateral compression effectively suppresses SSE cracking and lithium penetration. Such compressive stress can be localized specifically at the SSE surface layer in contact with lithium [217], where crack initiation

typically occurs. For instance, in multilayer ASSLMB configurations [218], a 200-nm LiPON protective layer has proven effective in preventing lithium penetration. Studies by Cheng *et al.* [95] found that the SEI of LiPON was a dense amorphous matrix embedded with the decomposition products of LiPON (Li_2O, Li_3N and Li_3PO_4). These crystalline inclusions may induce residual compressive stress in the SEI, which can stabilize cell performance. Similarly, Ye and Xin took the advantage of Ge reduction from LGPS decomposition [96]—as it induces local compressive stress—to create an multilayer ASSLMB with a long life (10^4 cycles) and high current density (86 A/m^2) [219]. These experimental results demonstrate the stabilizing effect of lateral compression in SSE surface in contact with lithium. Furthermore, ion-exchange technology—well-established for surface strengthening in glass and ceramics [109, 111]—could potentially be adapted to induce similar compressive residual stresses in SSE surfaces [220], offering another promising approach to performance enhancement.

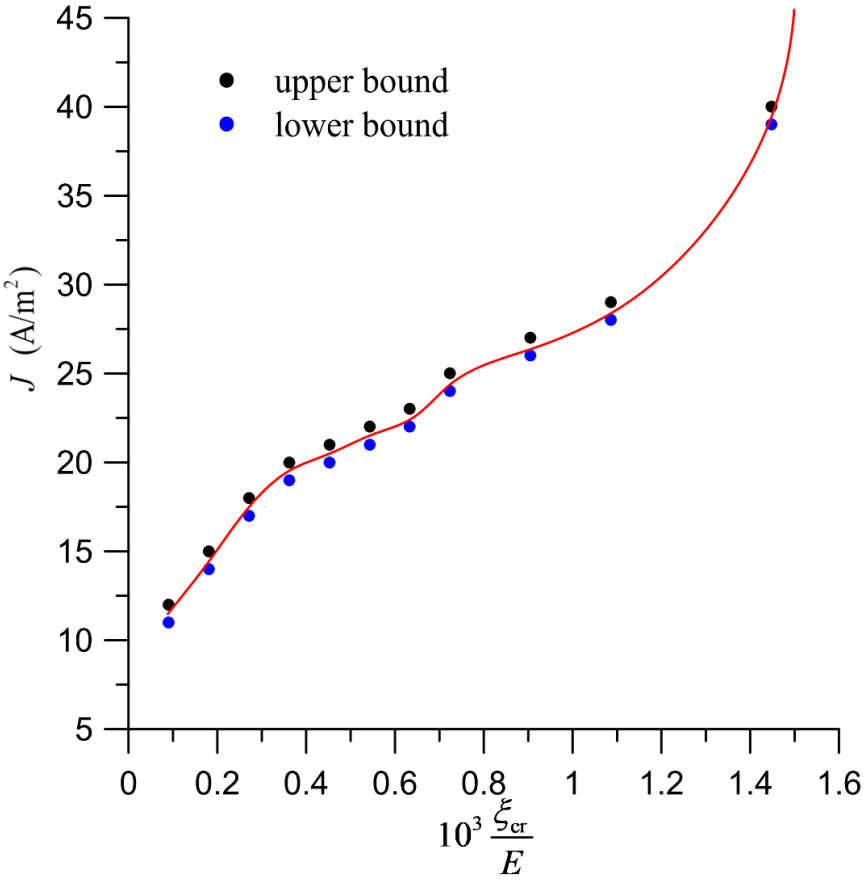

Figure 4.8 The stability map for fracture toughness and corresponding CCD: the map of applied current density J versus $10^3\xi_{cr}/E$ for partial molar volume 22.4 cm^3/mol in SSE, where blue dot and black dot represent the upper bound and lower bound of CCD at corresponding $10^3\xi_{cr}/E$.

Another question is how the fracture toughness affects the CCD of ASSLMBs, which is critical in the development of the manufacturing technology of SSEs. To quantify this dependence, we employed our computational model to establish the correlation between CCD and the dimensionless parameter ξ_{cr}/E. Through systematic simulations, we determined upper and lower bounds for CCD—defined as the current densities (differing by 1 A/m^2) that respectively induce or prevent crack formation—while maintaining Ω^{SSE} =22.4 cm^3/mol, as illustrated in Fig. 4.8. It is noted that the trend of CCD in Figure 4.8 exhibits an increase in the range of $0.3<10^3\xi_{cr}/E<1$, then a reduced rate of increase when $10^3\xi_{cr}/E>1$, and approaches infinity when $10^3\xi_{cr}/E>1.6$. Such a nonlinear increase in CCD stems primarily from the nonlinearity of the BV equation, which causes a significant (exponential) increase in Li^+ concentration when the CCD is high. Notably, infinite CCD

is achieved when $10^3 \xi_{cr}/E \approx 1.6$, a threshold corresponds to a fracture toughness K_{IC} of ~1.1 MPa.m$^{1/2}$ for an oxide-based SSE with E ~70 GPa. It should be noted that this is not a stringent requirement of K_{IC} as many engineering ceramics exceed this toughness requirement [221].

4.8 Summary

A multiphase Landau-Ginzburg-based PFFM has been established to elucidate the mechanical failure mechanism of ASSLMBs. This model reveals the critical role of voids in initiating crack formation and dendritic growth. Key insights derived from the model include the following: (1) During discharging, vacancy accumulation at the Li/SSE interface leads to void nucleation. Subsequent void growth and size are governed by the ratio of surface and bulk diffusivities of lithium, as well as lithium creep under applied stack pressure. (2) The presence of voids induces nonuniform distribution of Li^+ in the SSE surface near the void during a charging process, resulting in localized stress concentrations that promote crack propagation and lithium dendrite formation. While elevated stack pressure mitigates void size, it simultaneously exacerbates crack initiation and lithium penetration during charging. (3) The analysis demonstrates that lateral stress can effectively suppress crack propagation within the SSE. Based on these findings, a stability map correlating lateral pressure and SSE fracture toughness is proposed to guide material design.

This model is established based on experiments with inorganic SSEs. To extend it to other battery systems, modifications are needed. For example, the linear stress-strain relation may be changed to a non-linear (e.g., viscoelastic) constitutive model for polymer electrolytes, and the linear law of ion transport, *i.e.*, the Nernst-Planck equation, may also be modified to study the nonlinearity caused by cooperative segmental motion in polymers [222]. Additionally, size effects are also worth investigating. For example, there are experimental results showing the increase in yield strength when lithium samples are at micro- or nanoscale [223]. Hence, lithium dendrites could be harder than bulk lithium, which requires a high-order theory, such as the strain-gradient plasticity [224], to describe.

This work proposed one possible mechanical failure mechanism of ASSLMBs. In fact, this failure is largely influenced by synergistic effects of multiple factors. For example, the lithium insertion in SSE crack. In experiments, the cracks are only partially filled with lithium dendrite. Thus, lithium insertion cannot directly lead to cracking. However, after the crack generation, lithium metal can be inserted into the crack by stack pressure, which accelerates the crack propagation. Therefore, the relevant mechanical failure mechanisms should be carefully considered, eventually bringing about a generalized mechanism capable of exploring various SSE cracking phenomena.

Chapter 5 Fracture of IOX-strengthened thin cover glass

In investigation of SSE cracking, it is found that the lateral compressive stresses at the SSE surface in contact with lithium can effectively inhibit the SSE cracking. Instead of externally applying compressive loadings as illustrated in Fig. 4.6(b), a more feasible way for brittle materials resisting cracking is to introduce the surface compressive residual stresses through IOX [220, 225] or ion implantation [226, 227]. Among these methods, IOX strengthening has emerged as particularly promising for SSE applications [220], given its widespread industrial use in glass strengthening and its potential for precise engineering of residual stress profiles.

Despite the proven effectiveness of IOX strengthening in industrial applications, quantitative analysis of its mechanical benefits remains scarce. In this chapter, we address this gap by developing a PFFM for IOX-glass. While our previous Landau-Ginzburg-based PFFM successfully described SSE cracking in mechano-electrochemical environments, it lacked proper consideration of fracture energy and transition between fracture energy and strain energy during crack propagation.

To overcome these limitations, we implement a Griffith-theory-generalized PFFM within a finite deformation framework. This enhanced formulation properly accounts for the energy transition from strain energy to fracture energy during crack propagation. The model is rigorously calibrated against standard mechanical tests, that is, ROR tests. The four-point bending and tensile tests exhibit significantly scattered fracture strength data, resulting from the pronounced influence of flaws at the glass edges. Thus, they are excluded from the standard tests in our work. The ROR tests establish a robust foundation for quantitative analysis of fracture processes in IOX-strengthened brittle materials. This approach enables precise evaluation of how engineered residual stress profiles could influence fracture resistance in SSEs.

5.1 Crack initiation and formation in pre-IOX and post-IOX glass

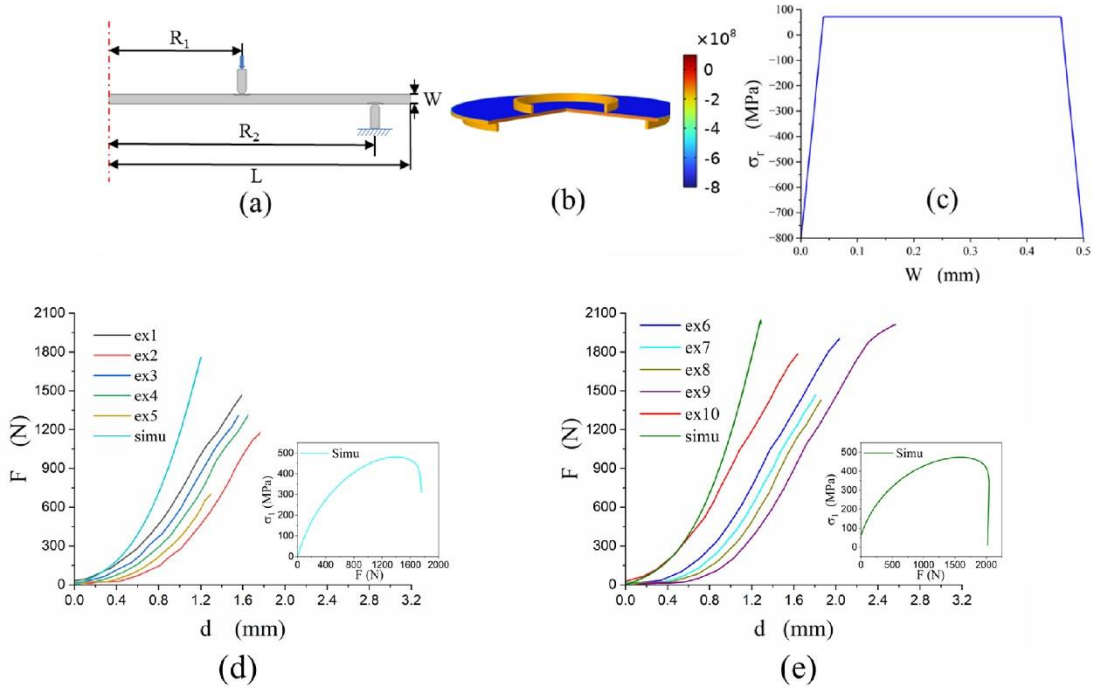

Figure 5.1 Model establishment and calibration: (a) cross section of a ROR test schematic, dot dash line represents central axis of symmetry, R_1 = 7.5mm and R_2 = 15mm denote radius of small ring and large supporting ring, L=17mm and W=0.5mm indicate the length and width of glass sample; (b) 3D sectional view of an post-IOX glass in ROR test with radial stress σ_r; (c) CS profile, the distribution of σ_r along post-IOX glass depth (D) before loading; (d) and (e) are curves of load force (F) versus displacement (d) of loading ring d in experiments (ex 1-10) and in simulation (simu) for pre-IOX and post-IOX glass, respectively, and the inset figures are the corresponding simulation results for the first principal stress (σ_1) versus F at the fracture origin.

The numerical model for ROR experiments, depicted in Figure 5.1(a), maintains dimensional and boundary condition consistency with the experimental setup described in **Appendix B**. Figure 5.1(b) presents a 3D sectional view of a post-IOX glass in ROR test with σ_r distribution, exhibiting characteristic CS distribution with a maximum at glass surface. The presumed σ_r profile (i.e., CS profile) is demonstrated in Fig. 5.1(c), featuring an 800 MPa surface CS that transitions linearly to a 62.7 MPa tensile stress at DOL= 40μm, with this linear profile serving as the baseline assumption unless otherwise noted. By applying the Griffith-theory-generalized PFFM, as illustrated in **Chapter 3.2**, the resulting

load(F)-deflection(d) curves for glass samples pre and post IOX can be obtained in Fig. 5.1 (d) and (e), respectively. Due to the large deformation, the F-d curves obtained in experiments and simulations are curved instead of linear. The inset figures in Fig. 5.1(d) and (e) are the first principal stress (σ_1) versus load force (F) curves at the fracture origins in Fig. 5.2 (a) and (b), showing the non-linearity of F and σ_1.

It is found that the fracture strengths of glass, as measured by the breaking loads in ROR experiments, are scattered over a wide range. The glass samples could have been severely flawed, rendering very low fracture strength even post IOX-strengthened, such as ex5 in Fig. 5.1(d) and ex8 and ex9 in Fig. 5.1(e). If we only consider the least flawed glass samples with the highest fracture strength before and after IOX, that is, ex1 and ex9, whose improvement of fracture strength due to IOX is from 1466N to 2010N, i.e., 37.1%. In simulations, without consideration about any surface flaws, the enhancement is only from 1752N (pre-IOX) to 2040 N (post-IOX), i.e., 15.3%, as shown by the 'simu' curves in Fig. 5.1(d, e). This strengthening effect after IOX is only half of the experimental result, suggesting the critical importance of incorporating realistic surface flaws in numerical models to accurately capture IOX strengthening effects.

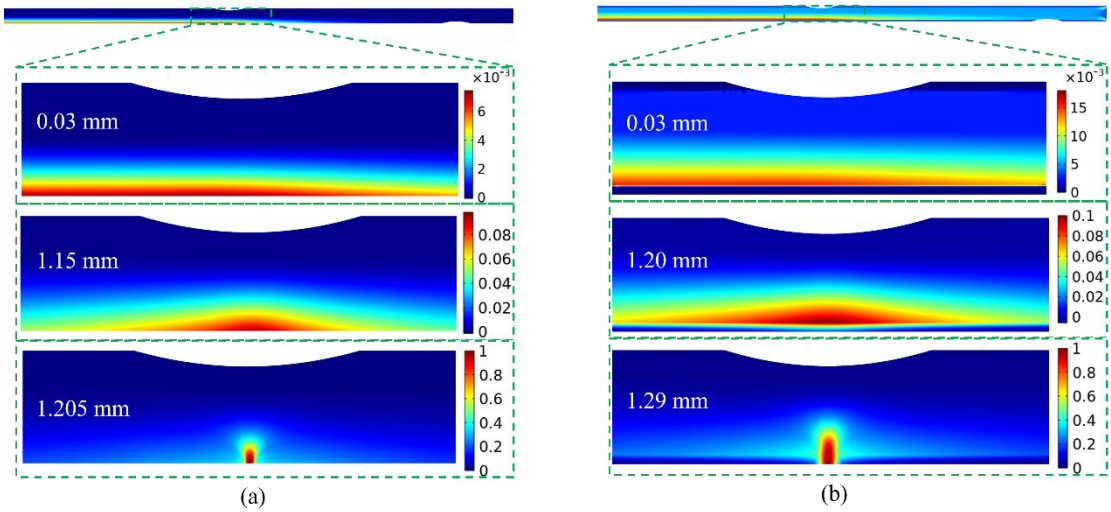

Figure 5.2 Crack initiation and formation in: (a) pre-IOX glass and (b) post-IOX glass.

Prior to incorporating surface flaws in our computational model, we first examine

the fracture mechanisms in both intact glass pre-IOX (Fig. 5.2(a)) and post-IOX (Fig. 5.2(b)). Under bending loads, membrane forces induce maximum tensile stresses in the bottom surface region beneath the loading ring [128], making this area most susceptible to crack initiation. Note that the value of the order parameter ϕ represents the severity of damage, ranging from $\phi = 0$ (intact) to $\phi = 1$ (crack), with $0 < \phi < 1$ indicating flaws or microcracks. The simulated cracking process in pre-IOX glass, as shown in Fig. 5.2(a), demonstrates that damage initiates uniformly along the bottom surface at displacement d = 0.03 mm, then concentrates at the lower surface area underneath the smaller loading ring, and eventually develops into a crack. For the post-IOX glass, as shown in Fig. 5.2(b), the damage initiates at the depth of DOL, then also concentrates in an area under the smaller loading ring (still at the depth of DOL), and eventually spreads to the glass surface, leading to a crack. It is noted that the crack in the post-IOX glass is initiated at DOL rather than glass surface; hence, surface flaws can be shielded to a certain extent. To quantitatively investigate the influence of surface flaws, an initial surface flaw or crack are introduced in our numerical model.

5.2 Inhibition effect of IOX for a pre-existing surface flaw

In this subsection, the numerical model incorporates a predefined flaw ($\phi = 0.3$) with dimensions of 1 μm in width and 20 μm in depth, located 7.3 mm from the glass center as shown in Fig. 5.3(a). Note that because the numerical model is axisymmetric, the predefined surface flaw represents a ring of defects (i.e., microcracks). Under ROR testing conditions, the combination of high membrane stresses is expected to transform this artificial flaw into a crack.

Figure 5.3(b) presents a comparative analysis of F-d curves responses for three cases: the pre-IOX glass models with and without the flaw, and the post-IOX glass model with the flaw. With the flaw, IOX results in a 62.7% improvement of fracture strength (from 1254N to 2020N), closely matching experimental measurements ex4 (1307N) and ex5 (2010N), as shown in Fig. 5.1(d, e). This agreement suggests that the predefined surface flaw may represent the experimental scenario to some extent. It is noted that the difference

in fracture strength for post-IOX with and without the flaw is insignificant (15.3 %), while a substantial difference (39.7%) can be found between the pre-IOX glass with and without the flaw. This confirms that implementing IOX strengthening makes the glass insensitive to the surface flaw, bringing about the flaw-tolerant cover glass products for potable electronics. However, this enhancement is not always true if the depth and intensity (i.e., ϕ) of the flaw are varied.

The distinct fracture processes of the flawed glass before and after IOX are shown in Fig. 5.3(c) and (d), respectively. In Fig. 5.3(c), for a pre-IOX glass, the pre-defined flaw evolves into a crack at an upper-ring displacement of d = 1.035mm. Conversely, IOX-treated glass maintains the initial flaw severity (ϕ = 0.3) at the same loading displacement, as shown in Fig. 5.3(d) for the post-IOX glass. It is noted that flaws still initiate at DOL and eventually the crack is generated from the DOL rather than the pre-defined flaw region, aligning with the fracture process the unflawed post-IOX glass in Figure 5.2(b). Hence, they give rise to a similar magnitude of fracture strength. The distributions of radial stress σ_r at the same deflection (d = 1.035 mm) for the flawed glass pre and post IOX are exhibited in Fig. 5.3(e) and (f), respectively. Figure 5.3(e) shows stress concentration at the tip of the predefined flaw. While under the same loading condition, no stress concentration or tensile stress can be found in Figure 5.3(f), demonstrating the prohibitive effect of the compressive residual stress in the DOL layer.

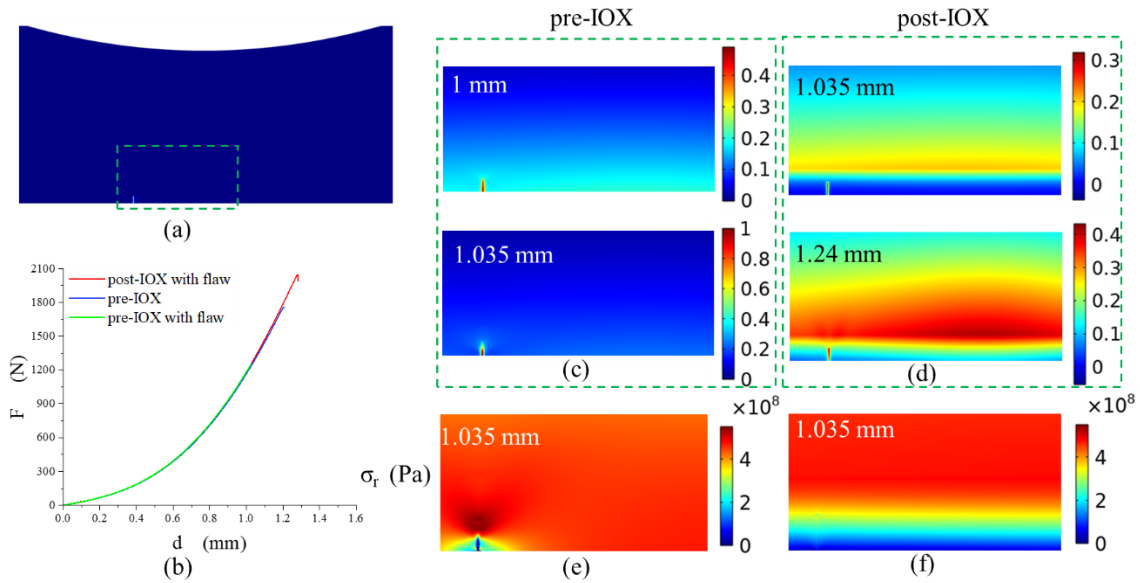

Figure 5.3 Inhibition effect of IOX for pre-existing flaw: (a) initial damage zone (1μm×20μm) in post-IOX and pre-IOX glass at a radius of 7.3 mm from the center of glass with $\phi = 0.3$; (b) F-d curves for post-IOX glass with flaw, pre-IOX glass with flaw and pre-IOX intact glass; Morphological evolution (enlarged view of green box in (c)) of (d) pre-IOX glass and (d) post-IOX glass. (e)(f) are radial stress σ_r in pre-IOX glass and post-IOX glass, respectively.

5.3 Inhibition effect of IOX for a pre-existing surface crack

What would happen if the surface flaw were changed to a pre-existing crack? In this chapter, a pre-defined circumferential notch (1 μm width × 4 μm depth) is introduced at the previously studied location (7.3 mm from the glass center). This geometric discontinuity serves as a stress concentrator, inducing crack initiation at the notch tip in both pre-IOX and post-IOX glass. As demonstrated in Figure 5.4(a), the fracture strength of the post-IOX glass is 3 times higher than that of pre-IOX glass. This substantial improvement significantly exceeds the strengthening effect observed in specimens containing milder flaws ($\phi = 0.3$), rendering the remarkable efficacy of IOX treatment in mitigating the detrimental effects of severe surface defects.

Figures 5.4(b) and (c) illustrate σ_r distribution at the moment just before crack extension, i.e., at d = 0.74 mm and 1.245 mm for the pre-IOX and post-IOX glass, respectively. It is noted that the pre-IOX glass exhibits highly localized tensile stresses (>500 MPa) concentrated at the notch tip, while the IOX-strengthened glass shows a

broader stress distribution due to the combined effects of greater deflection and residual tensile stresses. This observation aligns with experimental findings [228], where the residual tensile stress in the core layers (known as central tension, CT) induced by IOX treatment governs fracture fragment size — higher CT values producing smaller fragments and consequently safer fracture behavior [119]. We then set the numerical scheme to capture the dynamic process of cracking.

The dynamic fracture processes reveal fundamentally different crack propagation mechanisms between the pre and post IOX glass. For the pre-IOX glass shown in Fig. 5.4(d), the crack propagates straight upwards at 7 ns after fracture initiates, then widens and continues to propagate upwards at 17 ns, and finally slightly branches at 25 ns. The fracture pattern obtained in an experiment shows that the crack in pre-IOX glass occurs in the vicinity of two rings, with slight fragmentation especially at the ring under the smaller loading ring. In contrast, a more complex fracture process is exhibited in Fig. 5.4(e) for the post-IOX glass: the crack also propagates straightly in the first 3 ns, then widens, and another two cracks initiate from DOL at 9 ns; these three cracks propagate and start to branch at 20 ns. The initial crack branches at DOL, connecting with the other two cracks, meanwhile the latter two cracks' branches spread to the bottom of the initial crack to break the glass into small pieces. The simulated crack multiplication and fragmentation patterns show excellent agreement with experimental observations in Figure 5.3(e), demonstrating how IOX treatment promotes the formation of numerous small cracks and fragments. This fragmentation of glass is always accompanied by the tiny-rounded-cornered glass pieces, bringing about the safety of post-IOX glass fracture.

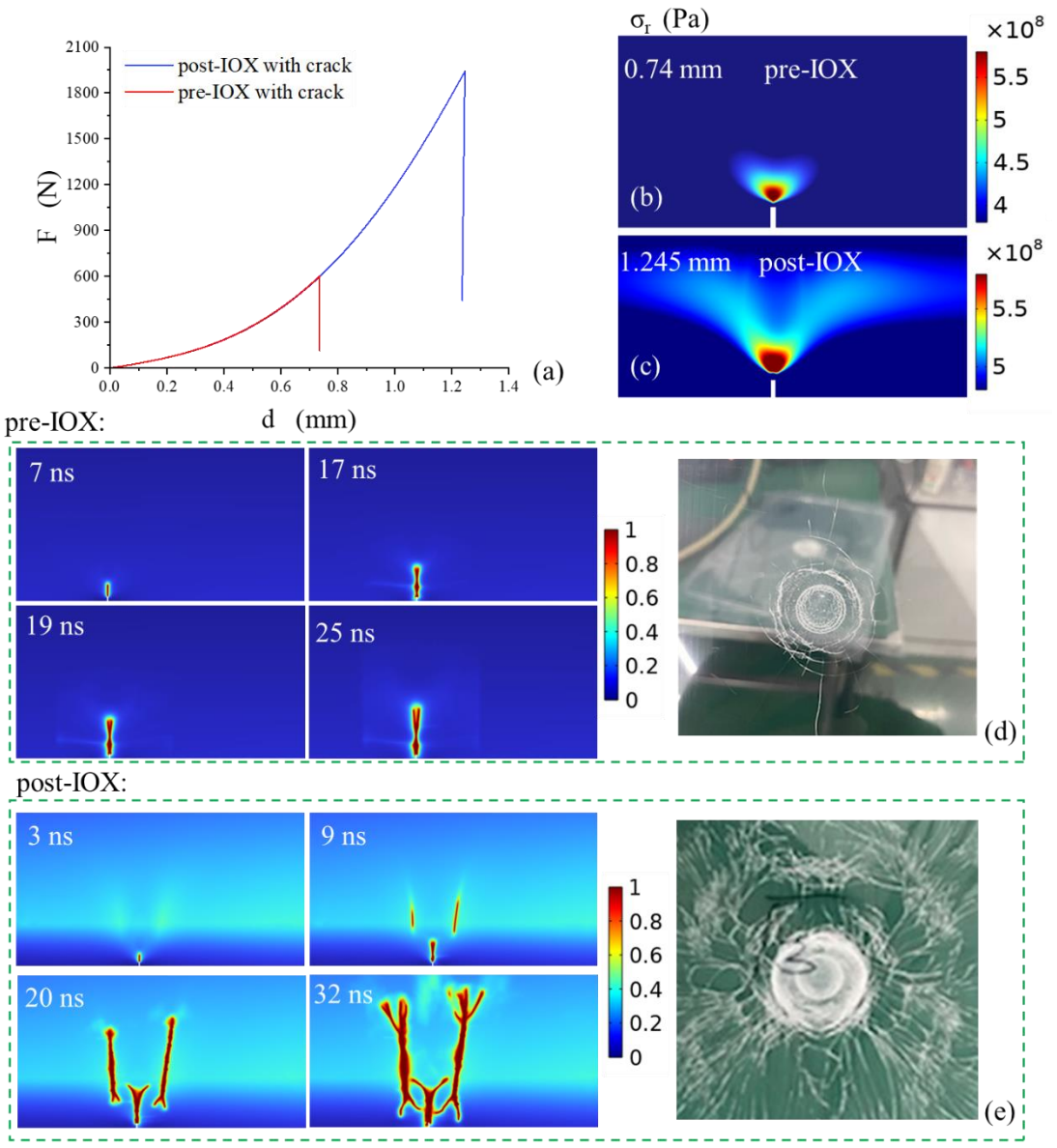

Figure 5.4 Inhibition effect of IOX for pre-existing crack: (a) F-d curves for post-IOX glass with notch, pre-IOX glass with notch (notch size 1μm×4μm). (b) (c) are σ_r distribution in pre-IOX glass at d=0.74mm and post-IOX glass at d=1.245mm, i.e., 0ns for each case. The morphological evolution in simulation and the fracture pattern in experiments for (d) pre-IOX and (e) post-IOX.

5.4 Effects of initial flaw intensity and depth

After demonstrating the effectiveness of IOX in inhibiting a pre-existing flaw and crack, we summarize how the flaw intensity ϕ and depth L_1 influence the fracture strength in Fig. 5.5. For a mild damage intensity (e.g., $\phi = 0.3$), the fracture strength of the post-IOX glass maintains at 2020N when $L_1 \leq 20$ μm, rendering a plateau zone that demonstrates

the remarkable insensitivity of IOX-strengthened glass to mild and shallow defects. This behavior correlates with the stress distribution patterns shown in Fig. 5.3(d, f), where pre-existing flaws remain stable rather than developing stress concentrations at the flaw tip. An approximately linear decline is observed when 25 μm $\leq L_1 \leq$ 45 μm; then the decreasing rate gradually weakens when 45 μm $< L_1 <$ 90 μm, and finally levels off at 1425N when $L_1 \geqslant$ 90 μm. For a more severe damage density ϕ = 0.6, a similar trend can be observed, but the fracture strength stabilizes at lower value of 759N when $L_1 \geqslant$ 90 μm. Pre-existing cracks show fundamentally distinct behavior, with catastrophic linear strength reduction to 935N as depth increases to 30 μm.

The results shown in Fig. 5.5 demonstrate that surface flaws can be effectively inhibited by the IOX-induced residual stress fields, and they can also explain why some post-IOX glass samples do not exhibit a significant strengthening effect, i.e., the fracture strength can be similar to that of pre-IOX glass, for example, “ex8” shown in Fig. 5.1(e). When surface imperfections remain as microcracks with limited severity (characterized by a flaw intensity factor ϕ = 0.3), post-IOX glass exhibits fracture strengths ranging from 1425N to 2020N in ROR experiments, consistent with experimental measurements shown in Fig. 5.1(e). However, the presence of more severe defects, particularly pre-existing notches or cracks exceeding 10 μm in depth, leads to dramatic strength reduction. This sensitivity to defect severity represents a fundamental challenge for industrial implementation of IOX strengthening, directly impacting production yields. In engineering practice, engineers may find that the post-IOX glass treatment needs to be ground and polished to remove a surface layer of several micrometers to improve the yield. This practice can be well explained by the results in Fig. 5.5.

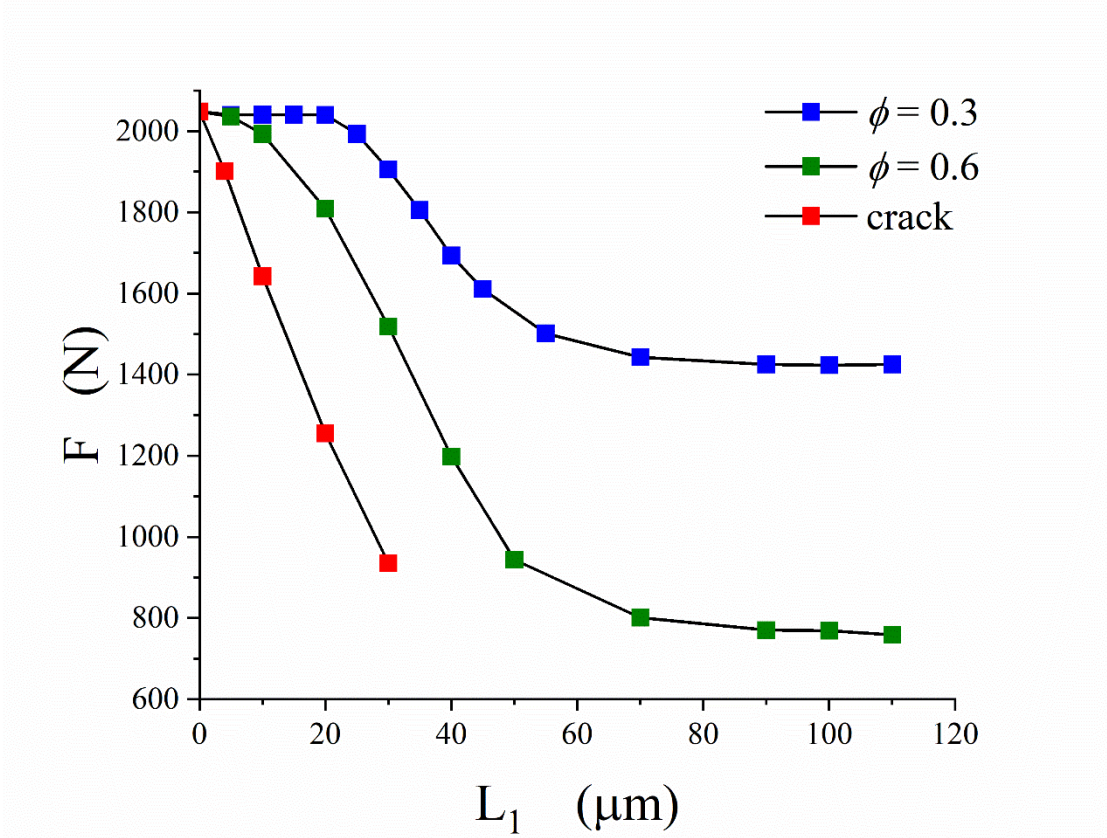

Figure 5.5 Fracture load force F (N) versus depth (L_1) of pre-existing damage zone ($\phi = 0.3$ and $\phi = 0.6$) and pre-existing crack.

5.5 Influence of CS profile on fracture strength

The effectiveness of IOX in glass is proven and discussed in the above subchapters, based on a traditional binary-ion IOX that possesses a residual-stress profile as shown Fig. 5.1(c). This subchapter systematically examines alternative stress distributions in post-IOX glass. Through comparative evaluation of various strengthening configurations, we quantitatively assess the influence of surface CS, DOL, and the other parameters on mechanical performance.

Green *et al.*[117] proposed a quadric CS profile to replace the traditional linear CS profile. It is believed that maximizing CS at the crack tips should be the most effective in inhibiting crack propagation. Following their approach, a quadric CS profile as shown in Fig. 5.6(a) was set in the numerical model, with peak compressive stress occurring at a depth of 10 μm. Figure 5.6(b) compares the F-d curves of an intact glass and a post-IOX

glass with 10 μm surface notch, exhibiting only a slight decrease (5%) of fracture strength caused by the notch. The numerical models allow a more detailed investigation of the initial crack pattern. For the intact post-IOX glass, cracks (the regions with $\phi \approx 1$) initiate at depths greater than the DOL, as shown in Fig. 5.6(c). The corresponding σ_r distribution indicates that the internal crack tends to propagate to the lower surface because the highest tensile stresses are at DOL and the lower layers, as depicted in Fig. 5.6(d). For glass with a pre-existing crack (i.e., the 10 μm notch), it is found that the pre-existing crack does not propagate; instead, another two cracks are initiated at DOL, as shown in Fig. 5.6(e). The corresponding σ_r distribution in Fig. 5.6(f) suggests that the two internal cracks are propagating downwards to connect with the notch. The excellent performance of quadric CS profile supports the argument of Green *et al.* [117]. However, in applications, the depths of surface damage are unknown, and the quadratic CS profile is difficult to control. Hence, we simplified CS profiles to be piecewise linear to clarify the most critical factors.

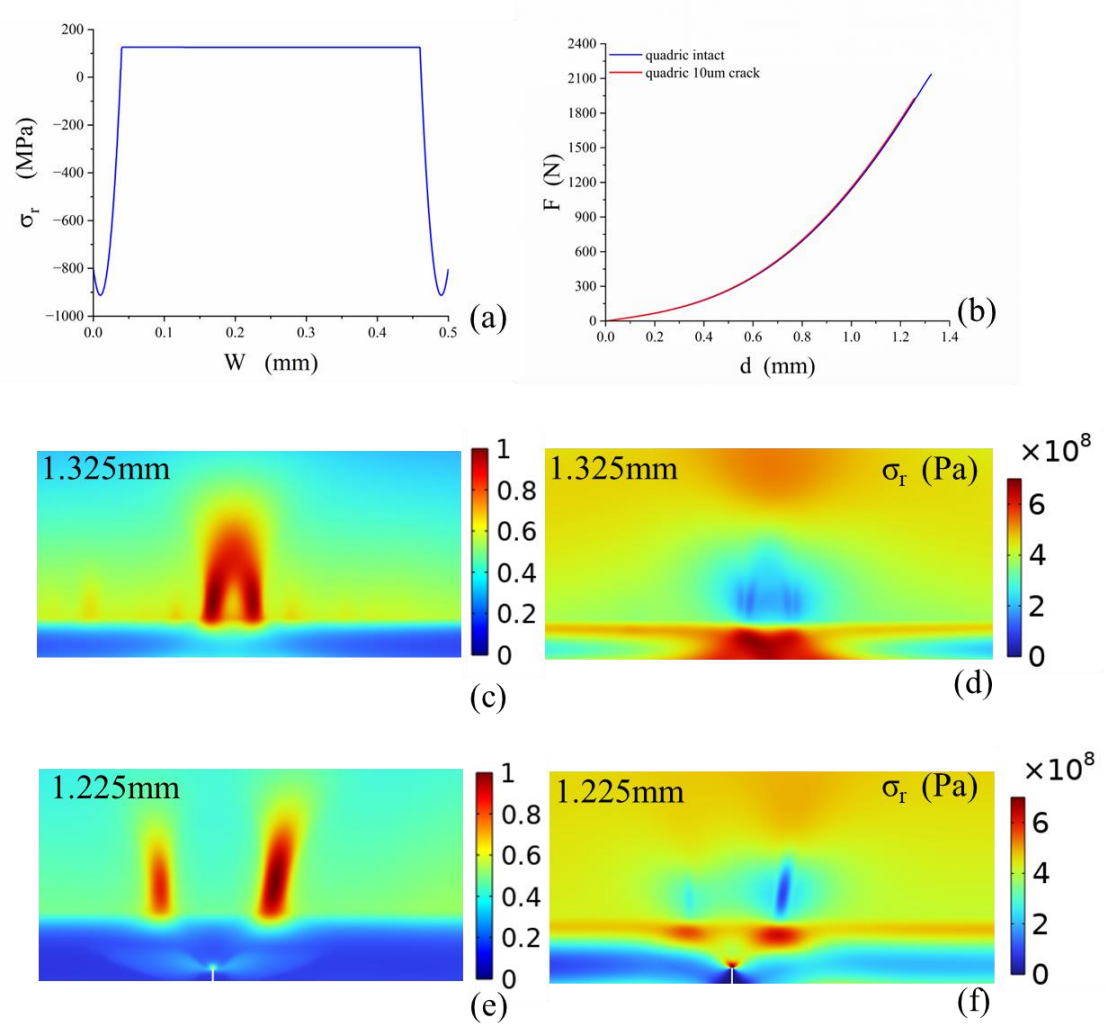

Figure 5.6 Quadric post-IOX glass fracture: (a) distribution of σ_r within quadric post-IOX glass width, (b) F-d curves for intact post-IOX glass and a post-IOX glass with 10μm pre-existing crack; (c) crack morphology of intact quadric post-IOX glass at d=1.325 mm, and its corresponding σ_r in (d); (e) and (f) for quadric post-IOX glass with a10μm pre-existing crack.

We first assumed several linear CS profiles with similar "compressed area" (i.e., surface CS × DOL), and the resulting F-d curves are shown in Fig. 5.7(a-c) for an intact glass, a flawed glass with $\phi = 0.3$ and $L_1 = 10$ μm, and a cracked glass with a 10 μm notch, respectively. The CS values in these figures denote the highest surface CS. It is noted that in Fig. 5.7(a) and (b), the fracture strengths are almost identical and all above 2000N. These results illustrate that the post-IOX glass with similar "compressed area" can achieve a similar fracture strength if flaws are mild. For the notched glass, the three different CS profiles lead to three different fracture strengths, and the profile with the highest surface

CS results in the highest fracture strength. Hence, to inhibit surface cracks, larger surface CS is more effective. But is the CS at crack tip still more important? In Fig. 5.7(d, e), we compare four CS profiles and their corresponding F-d curves. Profiles 1-3 have the same CS at the crack tip, i.e., 10 μm, but different surface CS and DOL, which are to compare with the best case—"surface CS = 1455 MPa, and DOL = 20 μm"—shown in Fig. 5.7(c). The corresponding F-d curves for glasses with a 10 μm crack, as shown in Fig. 5.7(e), depict the differences in fracture strength. The CS at crack tip may not be as important as presumed by Green et al. [117]. Instead, the high surface CS is the more important factor. If the surface CS is reduced, a larger DOL is needed to compensate for the loss in surface CS, as indicated by the result of Profile 3 in Fig. 5.7. These results suggest that the combined effect of surface CS and DOL determines the fracture strength in ROR experiments for cracked glass.

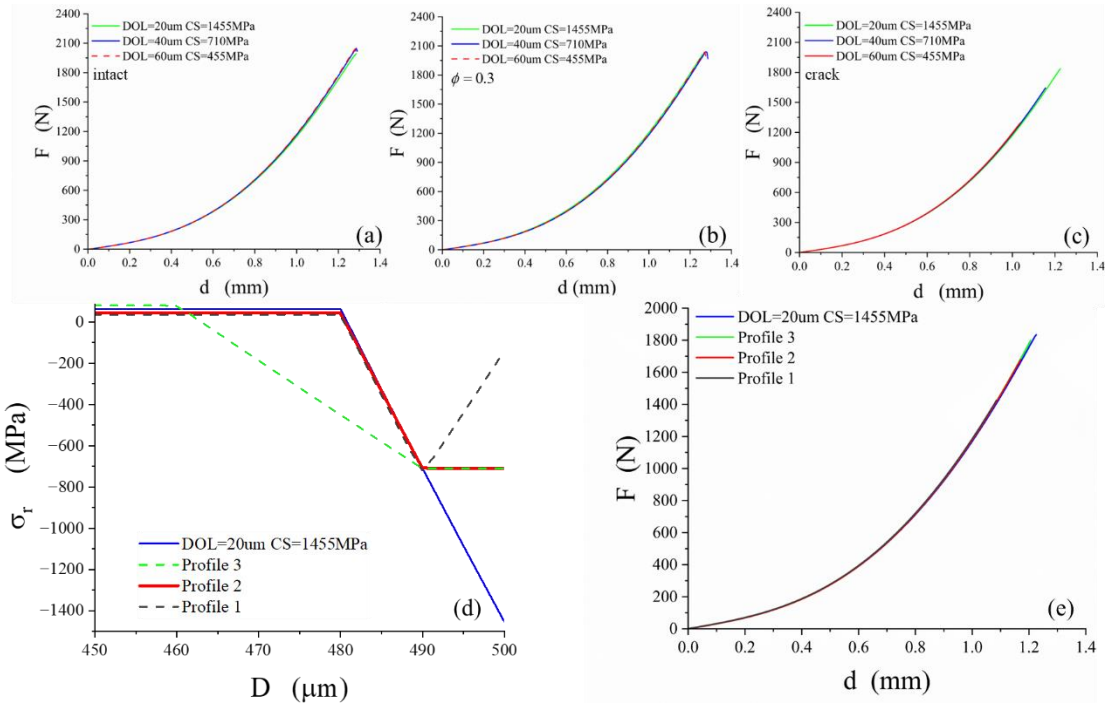

Figure 5.7 Influence of CS and DOL in post-IOX glass fracture: (a)(b)(c) are F-d curves for intact post-IOX glass, post-IOX glass with a pre-existing 10μm flaw, and crack, respectively; (d) is the CS profile for different profiles from glass depth (D) from 450μm to 500μm, (e) is the corresponding F-d curves.

A contour map of ROR fracture strength affected by surface CS and DOL (with CS decreasing linearly with depth) is shown in Fig. 5.8 for a glass with a crack depth of 10 μm.

For the same fracture strength, a decrease in surface CS must be compensated by an increase in DOL. It is found that the CS is proportional to DOL^{-n} for each fracture strength. And a higher fracture strength corresponds to a higher power n, leading to a larger decrease in CS by increasing DOL to maintain the same fracture strength. As DOL reaches 40 μm, the decline in CS becomes subtle, indicating that the fracture strength is no longer sensitive to the pre-existing crack, i.e., a 40-μm DOL is very effective in inhibiting the effect of a 10-μm pre-existing crack, and further increasing DOL has little additional benefit. In general, achieving a surface CS over 1 GPa is very difficult in an IOX process due to stress relaxation. If the surface CS can be maintained at approximately 800 MPa, increasing DOL can effectively improve the ROR fracture strength. However, it should be noted that achieving a large DOL needs a long time, and this long-time process leads to the surface stress relaxation in post-IOX glass [107], consequently reducing fracture strength. To recapitulate, the ideal CS profile is one with a high surface CS and adequate DOL to desensitize the surface flaw. It is also noted that modern IOX process generally involves three ions, i.e., K-Na-Li IOX, in which Na-Li exchange can produce a large DOL, and K-Na exchange can produce high surface CS in a short time. Hence, the ternary IOX is gradually replacing binary IOX in the industry.

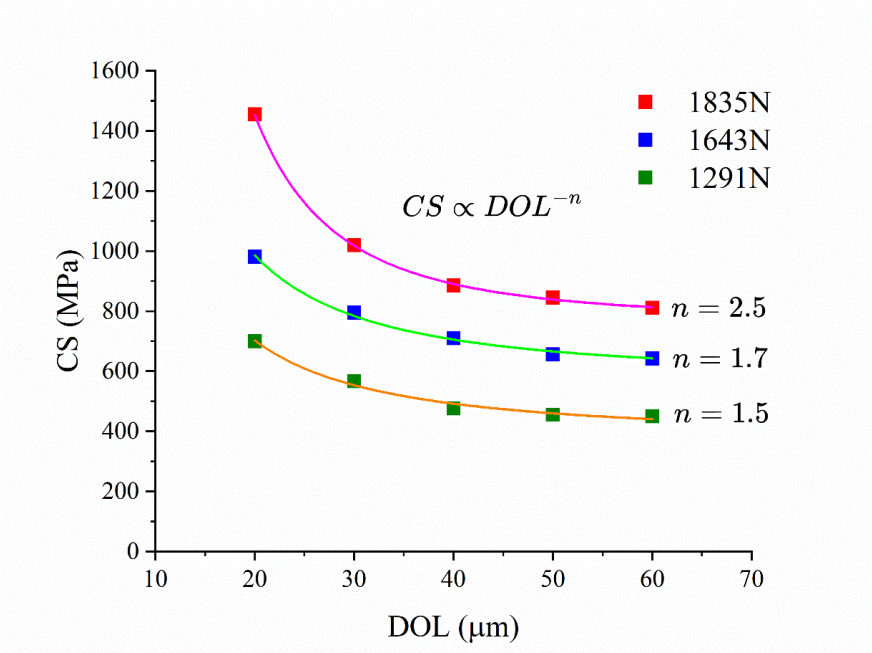

Figure 5.8 Fracture strength map for different post-IOX glasses (i.e., different CS and DOL) with a 10μm pre-existing crack

5.6 The effect of CS profile on impact resistance

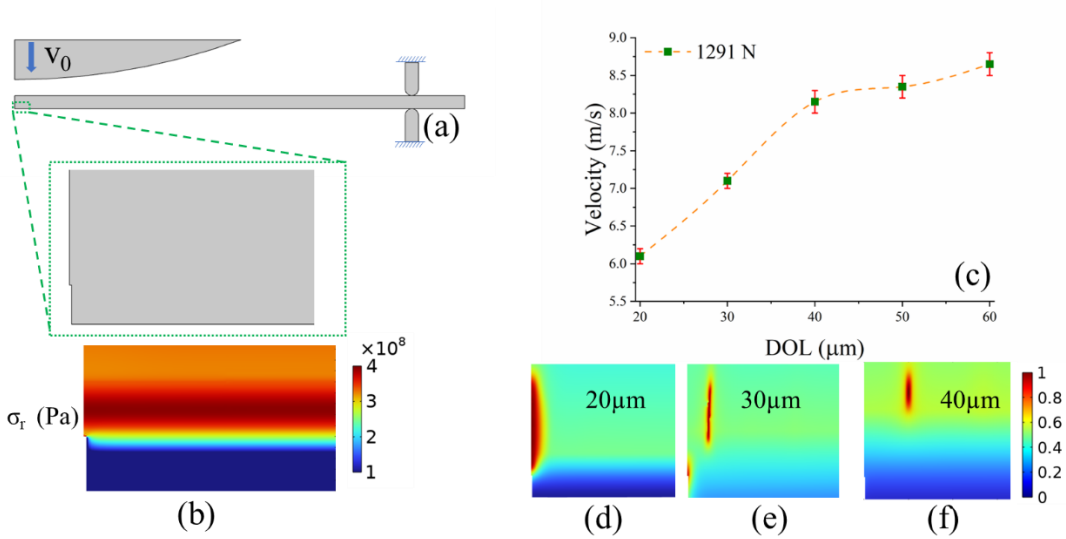

Figure 5.9 Simulation results of BD tests: (a) cross-sectional view of a BD test, the size of glass sample is the same as before with a pre-existing 10μm central crack at the lower surface as shown in the enlarged view, V_0 denotes the initial velocity of the dropping steel ball with a diameter of 50 mm; (b) enlarged view of an post-IOX (DOL = 20 μm) glass just before the fracture occurrence in BD test with radial stress σ_r; (c) the effect of DOL on the critical impact velocity leading to glass fracture if the glass has same ROR fracture strength(i.e., 1291N, cf. Fig. 5.8); (d-f) the distributions of the order parameter (damage intensity factor) ϕ

for DOL= 20, 30 and 40μm, respectively.

ROR is a quasi-static testing method to characterize the fracture strength of glass. In this subchapter, we use numerical simulations to study the dynamic fracture of thin glass in standard BD experiments, in which a thin glass is subjected to the impact of a steel ball with a diameter of 50 mm. We assume a pre-existing crack (with a width of 1 μm and a depth of 10 μm) at the center of the lower surface, as shown in the enlarged view in Fig. 5.9(a). Because the dropping ball impacts the center of the glass, its lower surface experiences a higher tensile stress than the other areas. Figure 5.9(b) shows the distribution of radial stress near the crack when the glass is dynamically deformed by the impact loading and is about to fracture. A tensile stress of 400 MPa at the crack tip is observed.

Figure 5.9(c) shows the critical impact velocities that lead to glass fracture. In this figure, we set the ROR strength constant (1291 N) and vary DOL, corresponding to the lowest curve in Fig. 5.8. This setup is intended to clarify to what extent the ROR strength reflects the impact resistance of cover glass. In Fig. 5.9(c), the data points include an error bar, indicating the possible range of the critical impact velocity with the upper and lower bounds pertaining to the velocities at which fracture does and does not occur in our simulations, respectively. The actual critical BD velocity for glass fracture must fall in this range.

Through simulations of ROR tests, Fig. 5.8 demonstrates that the different combinations of surface CS and DOL can result in constant fracture strength. Intuitively, in BD tests, the critical velocity would also remain constant if the static fracture strength of the glass samples is the same. However, it is surprisingly found that the lower CS combined with a deeper DOL renders the higher critical velocity. This counterintuitive (from an industrial perspective) phenomenon resulted from the different loading types of ROR and BD tests; that is, continuous loading and instantaneous loading, respectively. In ROR test, once the loading-induced strain energy exceeds the critical fracture energy, a crack propagates catastrophically from the pre-existing crack tip. In BD test, because the whole impact process lasts only about 0.2 ms, even when a damage zone starts to develop, it may not evolve into a crack before the ball rebounds. In this case, although the

instantaneous local strain energy (e.g., at the crack tip) may exceed critical fracture energy, the limited loading time and the surrounding compressive stresses can inhibit the extension of the main crack.

Fig. 5.9(d-f) demonstrate the damaged zone when DOL = 20, 30, and 40 μm, respectively. A change of cracking mode along with the increase of DOL is observed, which explains why DOL is more effective than surface CS in resisting dynamic fracture caused by BD. When DOL = 20 μm, the crack extends from the pre-existing crack. When DOL = 40 μm, cracking starts from DOL, where the residual stresses change from compression to tension. For the case of DOL = 30 μm, cracks initiate from both places. It can be concluded that the increase in DOL leads to better inhibitive effect to shield the propagation of dynamic cracks. However, this trend slows down when DOL is larger than 40 μm due to the increase in central tension.

5.7 Summary

A Griffith-theory-generalized PFFM was employed to examine the mechanical behavior of post-IOX glass. This study yields several key findings: (1) crack initiation occurs within the DOL in post-IOX glass, even in the presence of surface flaws. However, this shielding effect diminishes as the severity and depth of surface flaws increase; (2) the PFFM successfully simulates the fragmentation of post-IOX glass ,i.e., multiplication of cracks, unveiling that the CT in layers deeper than the DOL leads to this phenomenon; (3) high surface CS is the dominant factor in suppressing crack formation in ROR experiments, while the DOL plays a more critical role than surface CS in BD impact resistance. Due to stress relaxation during the IOX process, surface CS is typically constrained to values below 1 GPa. Consequently, enhancing the DOL is essential for improving resistance to both static and dynamic loading conditions. To guide material design, a fracture strength contour map is constructed, correlating surface CS and DOL based on simulation results.

Chapter 6 FEM-NO coupling with Domain Decomposition

In the above two chapters, the PDEs are solved by FEM solvers to reproduce the experimental observations and quantitatively investigate the cracking mechanisms. The wealthy information obtained in FEM is at the cost of substantial computation time. For instance, in the previous chapter, the dynamic cracking of IOX-strengthened in 32ns, in Fig. 5.4, requires more than 48 hours computation time on an AMD Ryzen Threadripper PRO 5975WX CPU. Although the PFFM significantly mitigates the discontinuity of a crack path, the fracture process is highly non-linear and very demanding in computational efforts.

It should be emphasized that the high non-linearity is dominated at a crack tip instead of the whole domain. Thus, the extremely fine meshes are required at the crack tip, while coarse meshes are acceptable in other intact domains. Motivated by the non-uniform meshes, the domain decomposition (DD) is consequently considered as a promising method to reduce computational cost: replacing the dense meshes subdomain by high-efficient method, remaining coarse meshes out of the replaced subdomain. As functional non-linear mappings for PDEs solutions, DeepONet is such a highly efficient method, only demanding offline training. In addition, a Physics-informed (PI) method [133] is implemented in DeepONet training, namely, no substantial data are needed to generate for the DeepONet training. A FE–PI-DeepONet framework can potentially be more efficient than conventional approaches (i.e., FEM) to solve mechanical and multiphysical problems with PFFM formulism.

In this chapter, five case studies are presented to demonstrate the robustness and versatility of the proposed FE–PI-DeepONet coupling framework. These cases have different material models, loadings, and mesh distributions, with increasing complexity in physics, coupling strategy, and meshed geometry.

- **Case 1** (**Chapter 6.1**): A linear elastic model under static loading, where displacement responses are mapped from prescribed boundary conditions.

- **Case 2** (**Chapter 6.2**): A hyperelastic model subjected to quasi-static loading, capturing large deformations in nonlinear materials.

- **Case 3** (**Chapter 6.3**): A linear elastic model under dynamic loading, incorporating time-dependent behavior and field evolution.

- **Case 4** (**Chapter 6.4**): A dynamic case that also demonstrates adaptive expansion of the ML-resolved subdomain within the simulation.

- **Case 5** (**Chapter 6.5**): A static case with non-uniform mesh distribution over complex geometry, demonstrating the potential of our coupling framework for multi-scale problems that require adaptive mesh refinement.

In all examples, the PI-DeepONet is coupled with the FE solver across a designated spatial subdomain. Each architecture has a single trunk network, which encodes the spatial coordinates (x,y). For each case, two identical PI-DeepONet are trained independently to predict the u_x- and u_y-displacements, enabling efficient and accurate inference during coupled simulations. The Adam optimizer [229] is used for training, with a learning rate of 10^{-3} for the linear elastic models and 10^{-4} for the hyperelastic model. Once trained, the resulting network parameters θ^* define a displacement-predicting surrogate that integrates seamlessly within the FE–NO framework. The branch network design varies between static/quasi-static and dynamic cases:

- For the *static and quasi-static* cases, the branch network encodes Dirichlet boundary conditions from Γ_{II}^{out} using 200 boundary points and 2 displacement components per point, yielding a total of 400 input features.

- For the *dynamic* cases, the square domain allows for richer input features. The branch network incorporates both field variables (e.g., displacement, velocity) and boundary data.

A CNN or a large fully connected network is used to encode u_x, u_y, v_x, and v_y on an 82 × 82 grid, boundary data are provided separately as input.

Time integration for the dynamic cases (**Chapters 6.3** and **6.4**) is performed using the Newmark method. Nondimensionalized formulae are employed with fixed material properties: density $\rho = 5$, time increment $\Delta t = 1$, Young's modulus $E = 1000$, and Poisson's ratio $v = 0.3$. All governing equations of this work are presented in non-dimensional form, along with their corresponding dimensional parameters, in **Appendix D**. All simulations in **Chapters 6.1 - 6.4** are performed on a square domain of length 2 units. To demonstrate the prediction accuracy of the training of DeepONet, we have provided additional plots in the **Appendix C**.

6.1 Hybrid framework for static loading

In the first example, we consider a linear elastic problem defined on a square domain subject to displacement-controlled loading applied to the top face of the domain. The schematic representation of the decomposed domains for the FE-NO coupling is shown in Fig. 6.1(a), where the inner domain Ω_{II} is a disk with radius 0.35 and the outer domain Ω_I is a square with a circular hole of radius 0.3. The displacement along the bottom face of the domain is fixed, while a constant displacement $u_y = 0.01$ in the y-direction is uniformly imposed on the top face. Figures 6.1(b) and 6.2(b) present the results for displacement in x direction and y direction respectively, obtained by FE simulation on the entire domain. These results serve as the ground truth against which the accuracy of the DDM based approaches is evaluated. Our first task in implementing the proposed spatial coupling framework is to train the PIDeepONet. For this purpose, we generate 1000 boundary conditions as a Gaussian random field with length scale parameters $l_u = l_v = 2$ for displacements u_x and u_y, respectively. By substituting these displacements into the PI-DeepONet operators $G_{\boldsymbol{\theta}_1}^{u_x}$ and $G_{\boldsymbol{\theta}_2}^{u_y}$ in Eq. 3.54, 3.55, and 3.49, and considering the case with no body force ($\mathbf{f} = \mathbf{0}$), the physics-informed neural operator is trained using the following governing equations:

$$\left(\lambda_0+2\mu_0\right)\frac{\partial^2 G_{\boldsymbol{\theta}_1}^{u_x}}{\partial x^2}+\mu_0\frac{\partial^2 G_{\boldsymbol{\theta}_1}^{u_x}}{\partial y^2}+\left(\lambda_0+\mu_0\right)\frac{\partial^2 G_{\boldsymbol{\theta}_2}^{u_y}}{\partial x\partial y}=0,\ \left(x,y\right)\in\Omega_{II} \tag{6.1}$$

$$\left(\lambda_0+2\mu_0\right)\frac{\partial^2 G_{\boldsymbol{\theta}_2}^{u_y}}{\partial y^2}+\mu_0\frac{\partial^2 G_{\boldsymbol{\theta}_2}^{u_y}}{\partial x^2}+\left(\lambda_0+\mu_0\right)\frac{\partial^2 G_{\boldsymbol{\theta}_1}^{u_x}}{\partial x\partial y}=0,\ \left(x,y\right)\in\Omega_{II} \tag{6.2}$$

$$G_{\boldsymbol{\theta}_1}^{u_x}\left(x,y\right)=u_x\left(x,y\right),\ \left(x,y\right)\in\Gamma_{II}^{out} \tag{6.3}$$

$$G_{\boldsymbol{\theta}_2}^{u_y}\left(x,y\right)=u_y\left(x,y\right),\ \left(x,y\right)\in\Gamma_{II}^{out} \tag{6.4}$$

After training this PI-DeepONet for 2×10^6 iterations, the loss plot is obtained as shown in Fig. C.1(a) with the boundary conditions loss ($\mathcal{L}_{bcs}$) and the residual loss ($\mathcal{L}_{res}$), which are based on the Eq.6.3-6.4 and Eq.6.1-6.2, respectively.

To evaluate the performance of the trained DeepONet prior to the coupling process, we test the trained DeepONet with one unseen boundary conditions of Ω_{II}. For example, we apply boundary conditions extracted from the ground truth in Fig. 6.1(b) and 6.2(b).

Comparing the prediction results with ground truth, the absolute error for u_x and u_y are both lower than 1.75×10^{-5}, as shown in Fig. C.1 in **Appendix C**. This indicates that our ML model is trained well for accurate generalization.

The domain Ω_I shown in Fig. 6.1(a) is modeled in FEniCSx with uniform displacement on the top face, fixed bottom face, and responding displacement from Ω_{II} at the interface Γ_I^{in}.The domain Ω_I is discretized into 38,812 elements, with 200 nodes uniformly distributed along the interfaces Γ_{II}^{out} and Γ_{II}^{in} to facilitate information transfer.

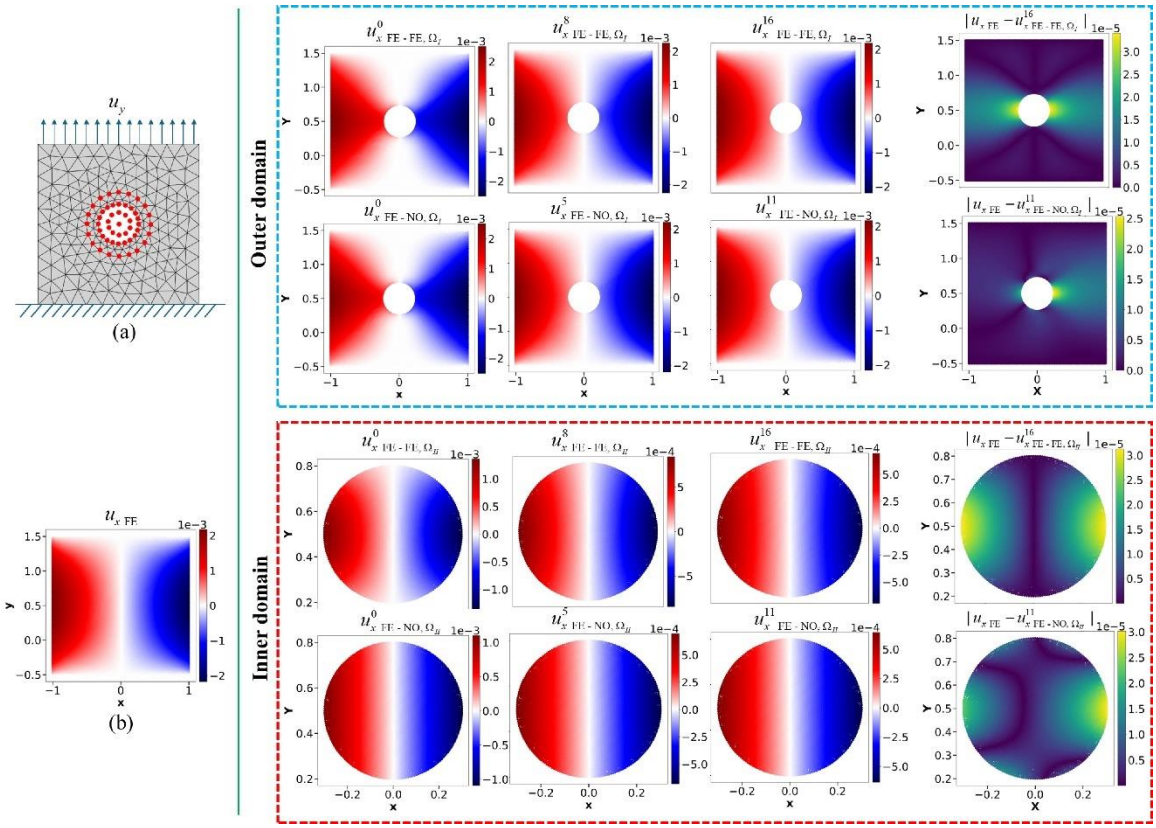

Figure 6.1: Response in x-direction (u_x) of the linear elastic coupling model under static loading conditions: (a) Schematic of decomposed domains for the spatial coupling framework, where the bottom edge has fixed boundary conditions and the top edge is subjected to an applied displacement in the y-direction ($u_y = 0.01$); (b) Ground truth displacement u_x obtained by solving the intact domain using FEniCSx. The blue-dashed box contains: Columns 1-3 showing the evolution of u_x in Ω_I for FE-FE coupling (top row) at iterations $j = 0,8,16$ and FE-NO coupling (bottom row) at iterations $j = 0,5,11$, with column 4 displaying the absolute error between the converged solution ($j = 16$ for FE-FE and $j = 11$ for FE-NO) and the ground truth. The red-dashed box contains: Columns 1-3 showing the evolution of u_x in Ω_{II} for both coupling frameworks at the same iterations, with column 4 similarly displaying the absolute error relative to the ground truth.

We first present our results for the FE-NO coupling before comparing its convergence with the FE-FE coupling approach. The coupling process begins by solving for Ω_I using the FEniCSx solver and transferring the displacement information (u_x and u_y) at Γ_{II}^{out} to the pre-trained PI-DeepONet. The neural operator then predicts the displacements throughout Ω_{II}, providing values for $u_{x|\Gamma_{II}^{in}}$ and $u_{y|\Gamma_{I}^{in}}$ that are passed back to Ω_I. This exchange of information continues until convergence between the solutions of the two subdomains is achieved, as calculated using Eq. 3.79.

For the FE-FE coupling, we follow the same process, except that subdomain Ω_{II} is simulated using the FE solver instead of the PI-DeepONet. In this case, Ω_{II} is discretized into 21,490 elements with 200 nodes on Γ_{II}^{in} and Γ_{II}^{out}. The nodes are positioned at the same coordinates as those in Ω_I to ensure efficient boundary condition exchange. In Figures 6.1 and 6.2, we use the notations $u_{x,FE-FE}^{j}$ and $u_{y,FE-FE}^{j}$ to denote the x and y displacements obtained using the FE-FE coupling at the j-th iteration of the Schwarz coupling strategy. For the FE-NO coupling, we use the same notation with the subscript modified to FE-NO. It should be emphasized that the superscript n in **Chapter 6.2 - Chapter 6.4** indicates the time step.

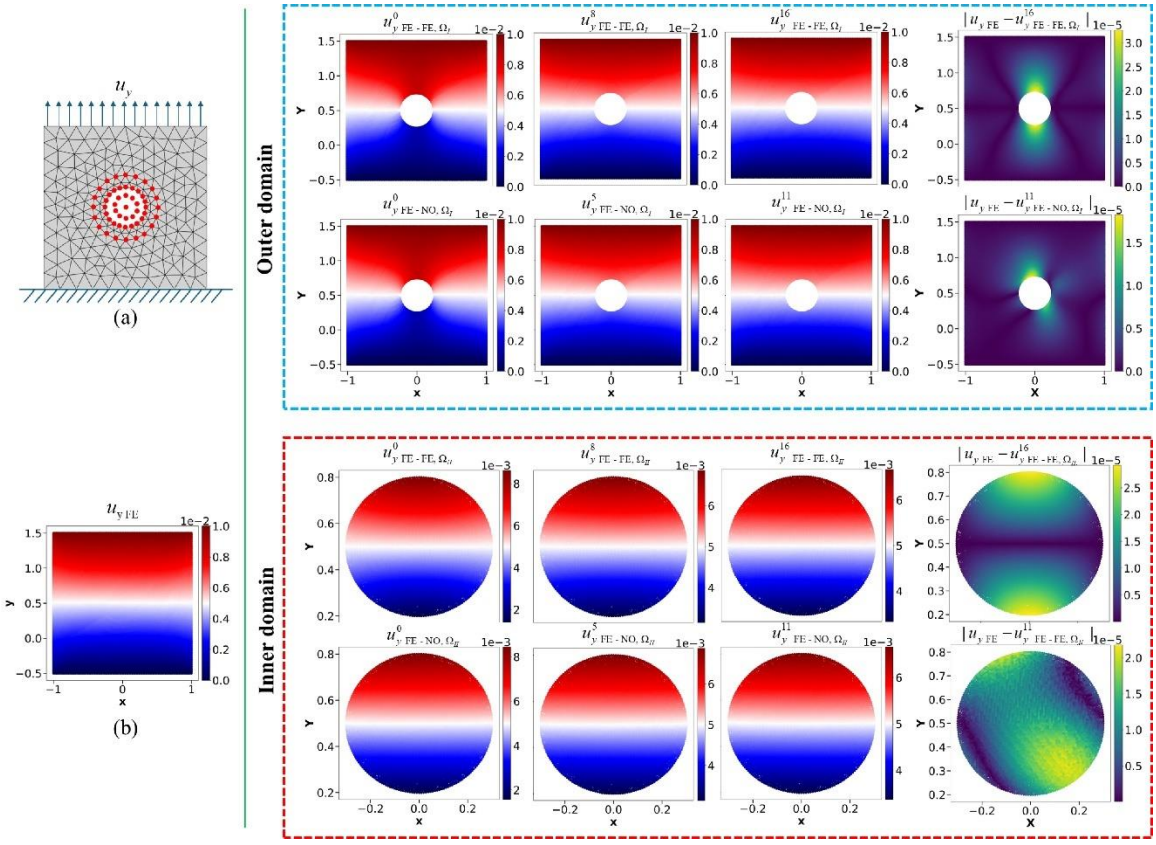

Figure 6.2 Response in y-direction (u_y) of the linear elastic coupling model under static loading conditions: (a) Schematic of decomposed domains for the spatial coupling framework, where the bottom edge has fixed boundary conditions and the top edge is subjected to an applied displacement in the y-direction ($u_y = 0.01$); (b) Ground truth displacement u_y obtained by solving the intact domain using FEniCSx. The blue-dashed box contains: Columns 1-3 showing the evolution of u_y in Ω_I for FE-FE coupling (top row) at iterations $j = 0,8,16$ and FE-NO coupling (bottom row) at iterations $j = 0,5,11$, with column 4 displaying the absolute error between the converged solution ($j = 16$ for FE-FE and $j = 11$ for FE-NO) and the ground truth. The red-dashed box contains: Columns 1-3 showing the evolution of u_y in Ω_{II} for both coupling frameworks at the

same iterations, with column 4 similarly displaying the absolute error relative to the ground truth.

Figure 6.1 presents the *x*-displacement results for FE-FE at inner iterations $j = 0,8,16$ and for FE-NO at $j = 0,5,11$, along with the computed errors at the final iteration for both Ω_I and Ω_{II}. At $j = 0$, both $u^0_{x,FE-FE,\Omega_I}$ and $u^0_{x,FE-NO,\Omega_I}$ exhibit sharp gradients in displacement field near Ω_{II}, which appears as a hole for the FE solver of Ω_I. After 9 iterations ($j = 8$), the sharp gradients in the displacement field in $u^8_{x,FE-FE,\Omega_I}$ are significantly reduced across both domains. A similar mitigation is also observed in $u^5_{x,FE-NO,\Omega_I}$.

After additional iterations, the difference between $u^8_{x,FE-FE,\Omega_I}$ and $u^{16}_{x,FE-FE,\Omega_I}$ becomes nearly indistinguishable, similar to that between $u^5_{x,FE-NO,\Omega_I}$ and $u^{11}_{x,FE-NO,\Omega_I}$.

The final column in Fig. 6.1 shows the absolute error between the FE reference solution u_{FE} and final converged solutions in both domains. For both coupling methods, the largest errors occur near the interface between Ω_I and Ω_{II}. While the FE-NO coupling yields slightly lower errors than the FE-FE coupling, all absolute errors remain within the same order of magnitude 10^{-5}.

Similarly, Fig. 6.2 illustrates the evolution of the *y*-displacement for both coupling frameworks. The absolute error between the final converged solution and ground truth, depicted in the last column of Fig. 6.2, is comparable to that observed for u_x, also on the order of 10^{-5}.

Given the uniaxial loading in the *y*-direction, the u_y displacement is approximately 10 times greater than u_x, the latter arising primarily from the Poisson effect. Consequently, similar absolute error magnitudes translate into different relative errors for u_x (less than 5%) and u_y (less than 0.5%).

Due to symmetry in both loading and geometry, the displacement distribution and the absolute error in the FE-FE coupling exhibit symmetric patterns. The maximum error in $\left|u_{x,FE} - u^{16}_{x,FE-FE}\right|$ appears along the *x*-direction, while for $\left|u_{y,FE} - u^{16}_{y,FE-FE}\right|$, it occurs

along the y-direction. In contrast, the FE-NO coupling introduces asymmetric error distributions, leading to slight asymmetries in the final u_x and u_y fields, as shown in Fig. 6.1 and Fig. 6.2. However, due to the small magnitude of the errors, these asymmetries are not visually noticeable.

Following Algorithm 1, the Schwarz alternating method terminates based on the L^2 error defined in Eq. 3.79. The error profile for the linear elastic material in the static regime is shown in Fig. 6.3. For both coupling approaches, the L^2 error decreases with each iteration, indicating a continuous reduction in the displacement difference between successive iterations. Eventually, the L^2 error falls below the critical threshold $\epsilon = 10^{-3}$, signifying convergence in both domains as defined by Eq. 3.80 and 3.81. With this threshold, absolute errors remain on the order of 10^{-5}, as demonstrated in Fig. 6.1 and Fig. 6.2. While a smaller ϵ would require more iterations, it does not significantly improve the absolute error.

Figure 6.3 presents the error L^2 versus the number of inner iterations for the FE-FE and FE-NO coupling. As shown, the FE-NO solution starts with a higher L^2 error in the initial iteration ($j = 1$), which can be attributed to the limitations of the PI-DeepONet model. Specifically, the model was trained using relatively large length parameters ($l_u = l_v = 2$), while the radius of Ω_{II} is only 0.35. This mismatch hinders the model's ability to accurately capture the complex boundary conditions in this region.

This behavior is evident in Figs. 6.1 and 6.2 at $j = 0$: due to the sharp displacement gradient in Ω_I, the FE-FE coupling yields an arc-shaped displacement distribution, while the FE-NO solution remains nearly uniform.

Since the inner iteration process in linear elasticity serves to smooth sharp displacement gradients, the FE-NO coupling converges faster than the FE-FE approach, requiring five fewer inner iterations to meet the convergence criterion. As a result, the total computation time is reduced from 102 seconds for FE-FE to 80 seconds for FE-NO-yielding a 20% improvement in efficiency for this simple, small-scale linear elastic example.

It should be emphasized that at each iteration of the FE-FE coupling, the inner domain Ω_{II} must be completely recalculated. In contrast, for the FE-NO coupling, $u_{x|\Omega_{II}}$ is obtained through direct evaluation of the neural operator at spatial coordinates (x, y), without requiring additional calculations or training. It is anticipated that highly nonlinear materials and complex geometries would pose greater challenges to the FE solver, making FE-FE significantly more time-consuming than FE-NO in such scenarios.

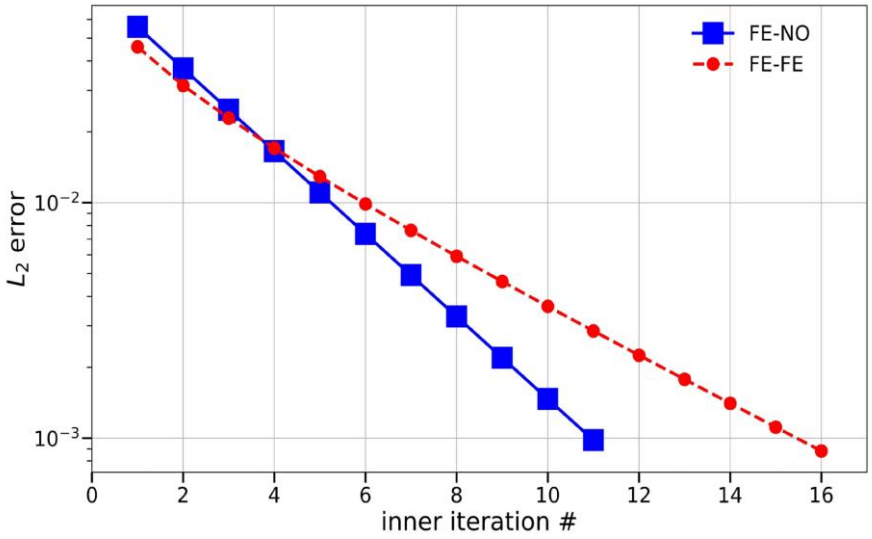

Figure 6.3 L^2 error norm evolution across iterations for the linear elastic model under static loading conditions.

6.2 Hybrid framework for quasi-static loading

In this subsection, a hyperelastic material in a square domain is examined under quasistatic loading. The schematic of the decomposed domains for the FE-NO coupling is similar to that of the previous **Chapter 6.1**, as displayed in Fig. 6.4(a). The discretization in FE analysis is also the same as before; however, the boundary conditions are different. The left and bottom edges are fixed, and the monotonically increasing displacement is uniformly applied on the top ($u_y = 0.05\times(n+1)$) and right ($u_x = 0.05\times(n+1)$) edges at the time step n (with n denoting the quasi-static time step). The ground truth values are computed using FE over the entire domain. The displacement components u_x and u_y in n =

4 are shown in Fig. 6.4(b) and Fig. 6.5(b), respectively. It is worth noting that in this example, the FE solvers employ Newton's nonlinear solver in FEniCSx [230], as each loading step involves solving a nonlinear equation due to the Neo-Hookean material model.

To enable FE-NO coupling, a PI-DeepONet is trained for the hyperelastic system, following the same approach as for the linear elastic case in the static setting. A total of 1000 boundary conditions are sampled from a Gaussian random field with length scale parameters $l_u = l_v = 1$. These are used as input to the DeepONet operators $G_{\theta_1}^{u_x}$ and $G_{\theta_2}^{u_y}$ (see Eq. 3.57–3.62). Substituting these predicted displacements into the constitutive equations yields the first Piola-Kirchhoff stress tensor $\mathbf{P}_1^n$ at time step n under quasi-static conditions. The equilibrium condition in the reference configuration (neglecting body forces) is:

$$\nabla \bullet \mathbf{P}_1^n = 0 \tag{6.5}$$

Substituting the PI-DeepONet predictions into this equation, the governing system for the hyper-elastic model at time step n becomes:

$$\begin{aligned}
&\frac{\partial}{\partial x}\left[\mu_0\left(1+\frac{\partial G_{\boldsymbol{\theta}_1}^{u_x}}{\partial x}\right)+\left(\lambda_0 \log\left(J\left(G_{\boldsymbol{\theta}_1}^{u_x}, G_{\boldsymbol{\theta}_2}^{u_y}\right)\right)-\mu_0\right)\frac{1}{J\left(G_{\boldsymbol{\theta}_1}^{u_x}, G_{\boldsymbol{\theta}_2}^{u_y}\right)}\left(1+\frac{\partial G_{\boldsymbol{\theta}_2}^{u_y}}{\partial y}\right)\right] \\
&+\frac{\partial}{\partial x}\left[\mu_0 \frac{\partial G_{\boldsymbol{\theta}_2}^{u_y}}{\partial x}+\left(\lambda_0 \log\left(J\left(G_{\boldsymbol{\theta}_1}^{u_x}, G_{\boldsymbol{\theta}_2}^{u_y}\right)\right)-\mu_0\right)\frac{1}{J\left(G_{\boldsymbol{\theta}_1}^{u_x}, G_{\boldsymbol{\theta}_2}^{u_y}\right)}\left(-\frac{\partial G_{\boldsymbol{\theta}_2}^{u_y}}{\partial y}\right)\right]=0,\ (x,y)\in\Omega_{II},
\end{aligned} \tag{6.6}$$

$$\begin{aligned}
&\frac{\partial}{\partial x}\left[\mu_0\left(1+\frac{\partial G_{\boldsymbol{\theta}_2}^{u_y}}{\partial y}\right)+\left(\lambda_0 \log\left(J\left(G_{\boldsymbol{\theta}_1}^{u_x}, G_{\boldsymbol{\theta}_2}^{u_y}\right)\right)-\mu_0\right)\frac{1}{J\left(G_{\boldsymbol{\theta}_1}^{u_x}, G_{\boldsymbol{\theta}_2}^{u_y}\right)}\left(1+\frac{\partial G_{\boldsymbol{\theta}_1}^{u_x}}{\partial x}\right)\right] \\
&+\frac{\partial}{\partial x}\left[\mu_0 \frac{\partial G_{\boldsymbol{\theta}_1}^{u_x}}{\partial y}+\left(\lambda_0 \log\left(J\left(G_{\boldsymbol{\theta}_1}^{u_x}, G_{\boldsymbol{\theta}_2}^{u_y}\right)\right)-\mu_0\right)\frac{1}{J\left(G_{\boldsymbol{\theta}_1}^{u_x}, G_{\boldsymbol{\theta}_2}^{u_y}\right)}\left(-\frac{\partial G_{\boldsymbol{\theta}_2}^{u_y}}{\partial x}\right)\right]=0,\ (x,y)\in\Omega_{II},
\end{aligned} \tag{6.7}$$

where the Jacobian determinant J represents the local volume change:

$$J = \left(1 + \frac{\partial G_{\boldsymbol{\theta}_1}^{u_x}}{\partial x}\right)\left(1 + \frac{\partial G_{\boldsymbol{\theta}_2}^{u_y}}{\partial y}\right) - \frac{\partial G_{\boldsymbol{\theta}_1}^{u_x}}{\partial y}\frac{\partial G_{\boldsymbol{\theta}_2}^{u_y}}{\partial x} \tag{6.8}$$

The boundary conditions were imposed as:

$$G_{\boldsymbol{\theta}_1}^{u_x}(x,y) = u_x^n(x,y),\ (x,y) \in \Gamma_{II}^{out} \tag{6.9}$$

$$G_{\boldsymbol{\theta}_2}^{u_y}(x,y) = u_y^n(x,y),\ (x,y) \in \Gamma_{II}^{out} \tag{6.10}$$

The PI-DeepONet described by Eqs. 6.6-6.10 is trained over 2 million iterations to optimize the parameters $\boldsymbol{\theta}^* = \{\boldsymbol{\theta}_1^*, \boldsymbol{\theta}_2^*\}$. Figure C.2(a) shows the loss reduction over iterations, accounting for both the residual and the boundary components. To assess generalization, the trained PI-DeepONet is tested on an unseen boundary condition at time step $n = 4$, corresponding to uniform displacement loading. The ground truth FE solutions $u_{x\,FE,\Omega_{II}}^4$ and $u_{y\,FE,\Omega_{II}}^4$ are compared with PI-DeepONet predictions $u_{x\,NO,\Omega_{II}}^4$ and $u_{y\,NO,\Omega_{II}}^4$. The absolute errors, $\left|u_{x\,FE,\Omega_{II}}^4 - u_{x\,NO,\Omega_{II}}^4\right|$ and $\left|u_{y\,FE,\Omega_{II}}^4 - u_{y\,NO,\Omega_{II}}^4\right|$, are both below 1.2 × 10^{-3}, as presented in Fig. C.2 in **Appendix C**. Given the maximum displacement magnitude of 0.139, the relative error is below 1%, which is acceptable for engineering applications. These results confirm that the PI-DeepONet accurately generalizes to unseen inputs and is well suited for use in FE-NO coupling frameworks.

The FE-NO coupling framework under quasi-static conditions follows the same setup as described in **Chapter 6.1**, with convergence determined by the L^2 error criterion in Eq. 3.79, using $\epsilon = 10^{-3}$. A key difference here is that for each time step, the inner iterations must converge before advancing to the next step. This time-marching scheme and the information exchange procedure are outlined in Algorithm 1. For comparison, the FE-FE coupling uses the same algorithm, with Ω_{II} solved by FE rather than a neural operator. We denote the converged displacements in time step n as $u_{x,FE-FE}^n$ and $u_{y,FE-FE}^n$ for the FE-FE case, and $u_{x,FE-NO}^n$ and $u_{y,FE-NO}^n$ for the FE-NO case.

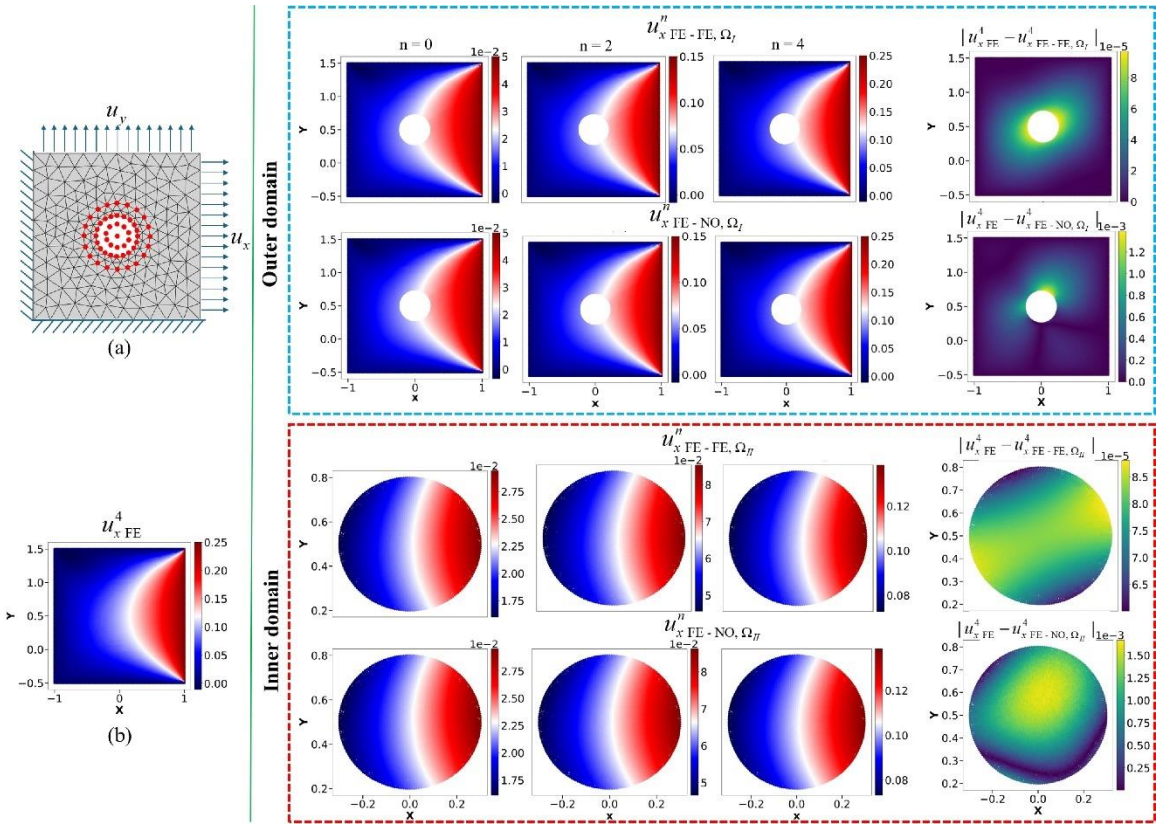

Figure 6.4 Response in x-direction (u_x) of the hyperelastic coupling model under quasi-static loading conditions: (a) Schematics of decomposed domains for spatial coupling framework, where the left and bottom edges have fixed boundary conditions and the top and right edges are subjected to an applied displacement at time step n in y-direction ($u_y = 0.05(n+1)$) and x-direction ($u_x = 0.05(n+1)$); (b) Ground truth displacement u_x at time step $n = 4$ obtained by solving the intact domain using FEniCSx; The blue-dashed box contains: Columns 1-3 showing the evolution of u_x in Ω_I for FE-FE coupling (top row) and FE-NO coupling (bottom row) at time step $n = 0,2,4$, with column 4 displaying the absolute error between the converged solution at time step $n = 4$ and ground truth. The red-dashed box contains: Columns 1-3 showing the evolution of u_x in Ω_{II} for both coupling frameworks at the same time steps, with column 4 displaying the absolute error relative to the ground truth.

The last columns of Fig. 6.4 display the absolute error of the coupling frameworks against the reference solution of FE at n = 4 in both domains. This FE-FE coupling presents a comparable absolute error to that in the linear elastic example, at the same order of magnitude 10^{-5}. Due to the large deformation in the hyperelastic model, the displacement is at magnitude 10^{-1}, and the relative error is below 0.1%. Although the absolute error in FE-NO is an order of magnitude higher than that in FE-FE, it remains negligible in relative terms, below 1% compared to the reference solution of FE.

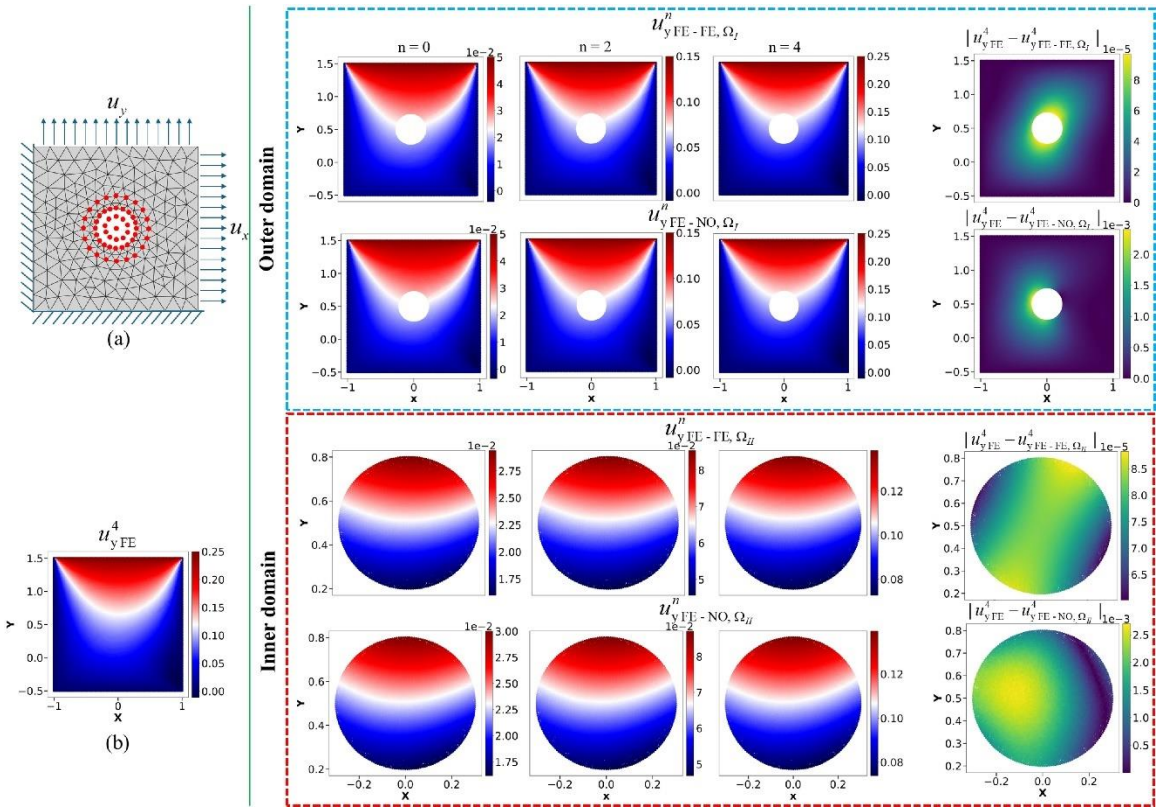

Figure 6.5 Response in y-direction (u_y) of the hyperelastic coupling model under quasi-static loading conditions: (a) Schematics of decomposed domains for spatial coupling framework, where the left and bottom edges have fixed boundary conditions and the top and right edges are subjected to an applied displacement at time step n in y-direction ($u_y = 0.05(n+1)$) and x-direction ($u_x = 0.05(n+1)$); (b) Ground truth displacement u_y at time step $n = 4$ obtained by solving the intact domain using FEniCSx; the blue-dashed box contains: Columns 1-3 showing the evolution of u_y in Ω_I for FE-FE coupling (top row) and FE-NO coupling (bottom row) at time step $n = 0,2,4$, with column 4 displaying the absolute error between the converged solution at time step $n = 4$ and ground truth. The red-dashed box contains: Columns 1-3 showing the evolution of u_y in Ω_{II} for both coupling frameworks at the same time steps, with column 4 displaying the absolute error relative to the ground truth.

Similarly, in Fig. 6.5, the diagonal-symmetric results of u_y with respect to u_x are shown in both domains, resulting from the diagonal symmetry of the loading and fixed boundary conditions. The arc-shaped distribution of u_y can be found in Ω_I and Ω_{II} at $n = 0$, 2, 4 with loading conditions increasing from 0.05 to 0.25. Relative to edge length 2, it can be considered as a large deformation. The absolute errors in y-displacement for FE-FE are almost in the same range as those in x-displacement. Meanwhile, in FE-NO, the absolute error is slightly larger than in u_x.

Except for the NO predictions in Ω_{II}, all absolute errors obtained by the FE solver reach the maximum at the edges of Ω_{II}. The higher errors within Ω_{II} in $\left|u^4_{x\,FE} - u^4_{x\,FE-NO,\,\Omega_{II}}\right|$ and $\left|u^4_{y\,FE} - u^4_{y\,FE-NO,\,\Omega_{II}}\right|$ are probably derived from the intrinsic error of our trained PI-DeepONet. Due to coupling, $\left|u^4_{x\,FE} - u^4_{x\,FE-NO,\,\Omega_{II}}\right|$ and $\left|u^4_{y\,FE} - u^4_{y\,FE-NO,\,\Omega_{II}}\right|$ are slightly higher, while at the same order of magnitude 10^{-3}. Moreover, the large error region (indicated in light yellow) appears along the edges of Ω_{II}, rather than being completely isolated, as observed in $\left|u^4_{x\,FE} - u^4_{x\,FE-NO,\,\Omega_{II}}\right|$ and $\left|u^4_{y\,FE} - u^4_{y\,FE-NO,\,\Omega_{II}}\right|$.

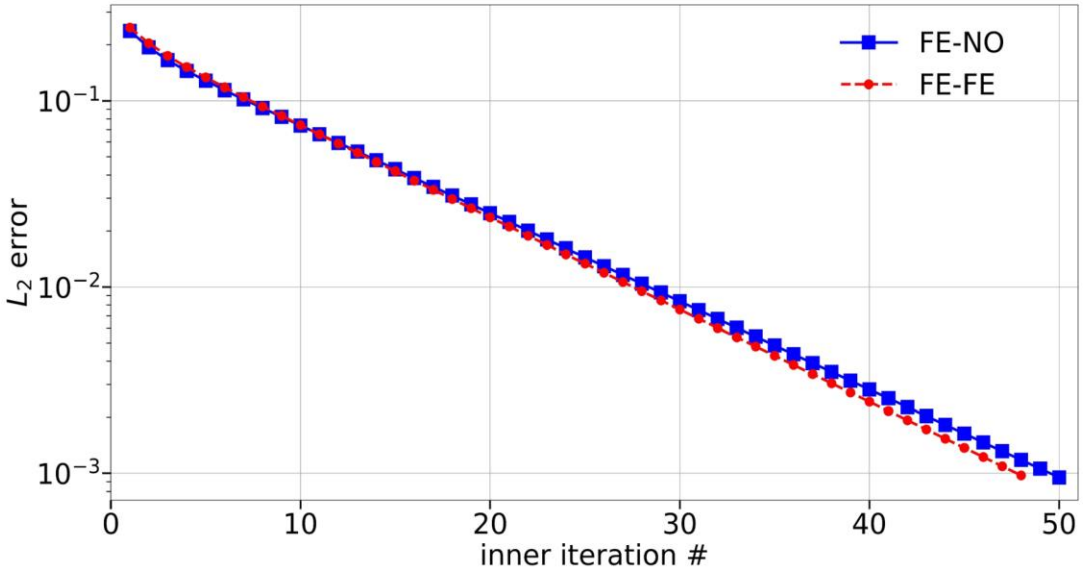

Figure 6.6 L^2 error norm evolution across iterations for the hyper-elastic model under quasi-static loading conditions at time step $n = 4$.

Figure 6.6 presents the L^2 error profiles of FE-FE and FE-NO in the hyperelastic model in quasi-static regime at time step $n = 4$. The L^2 error is defined in Eq. 3.79. As shown in Fig. 6.6, the error L^2 drops below the threshold $\epsilon = 10^{-3}$, indicating convergence of the coupling.

Thus, the displacement over the entire domain is obtained, as illustrated in Eqs. 3.80-3.81. During the first 20 inner iterations, the FE-FE and FE-NO error profiles overlap

closely. As the inner iterations progress, the deviation between them becomes increasingly noticeable. Ultimately, FE-FE reaches the convergence condition at 48 inner iterations, while FE-NO converges at 50 iterations. This indicates the comparable convergence behaviors and the robustness of both coupling frameworks.

However, the computational efficiency in FE-FE and FE-NO is different. As mentioned in the linear elastic model in a static regime, the FE-FE coupling method needs recalculation by the FE solver in Ω_{II} at each inner iteration step. In the hyperelastic model, this process involves the Newton solver, necessitating additional iteration steps to obtain the solution at each inner iteration. In particular, at $n = 4$, the FE-FE approach takes 184.8 seconds for 49 inner iterations, whereas the FE-NO method completes 51 inner iterations in 160.8 seconds. Moreover, once trained, FE-NO leverages the direct evaluation of PI-DeepONet without requiring recalculations or further training.

In addition to computational efficiency, the stability of the FE-FE framework is also challenged by the implementation of the nonlinear FE solver. The nonlinear FE solver is prone to divergence due to various factors, such as large load increments, element distortion, and other highly nonlinear behaviors. In contrast, neural operators are specifically designed for nonlinear mappings in a mesh-free form, offering significant stability in simulating highly nonlinear models.

6.3 Neural operator coupling for dynamic loading

In this elasto-dynamic example, the entire computational domain is a square. As shown in Fig. 6.7(a), the schematic illustrates the DDM used in the FE-NO coupling framework. The outer domain, Ω_I, is a 2×2 square with an embedded 0.6×0.6 square hole, while the inner domain, Ω_{II}, is a square with side length 0.7. The boundary conditions remain consistent with those described in **Chapter 3.2**, except that a constant displacement is applied, with $u_x = 0.01$ and $u_y = 0.01$. Figure 6.7(b) and 6.8(b) show the displacement results for the intact square domain at the final time step $n = 139$, obtained from the FE simulation in the intact domain. These results serve as the ground truth against which the accuracy of DDM-based methods is evaluated.

To establish an elastodynamic FE-NO coupling framework, we begin by implementing the FE-FE coupling approach. The domain is divided into two regions: Ω_I and Ω_{II}. At each time step, data is transferred between the subdomains using the Schwarz alternating method, as outlined in Algorithm 1. The discretization, computation, and information exchange closely follow the FE-FE coupling procedure used in the quasi-static hyperelastic model. The key difference under dynamic loading is the incorporation of the time dependency, which is handled using the Newmark method, as described in Eq. 3.69. The results of the FE-FE coupling under dynamic conditions are shown in Fig. 6.7, 6.8, and 6.10, demonstrating high accuracy and validating the effectiveness of this approach.

For the FE-NO coupling, a pretrained PI-DeepONet is used to transfer displacement information (u_x and u_y) across Γ_{II}^{in} and Γ_{II}^{out} at each time step. Since the system is dynamic and involves both acceleration and velocity, the time dimension must be considered. Therefore, the inner domain's PI-DeepONet is designed as an auto-regressive model. Moreover, to ensure compatibility with the Newmark method used in the FE analysis of the outer domain, the PI-DeepONet must also reflect the underlying time integration scheme. This motivates the development of a time-advancing PI-DeepONet architecture, inspired by the Newmark method, as illustrated in Fig. 3.1(a). In this architecture, the Branch1 network incorporates current time step's boundary conditions, while the Branch2 network uses a convolutional neural network (CNN) to extract velocity and displacement features from the previous time step. The trunk network then predicts the current displacement at spatial coordinates $(x,y) \in \Omega_{II}$.

The time-advancing prediction process is further detailed in the flowchart in Fig. 3.1(b). Functionally, this PI-DeepONet acts as a Newmark-integrated surrogate for the FE solver, allowing consistent prediction of displacements at each time step. Thus, the time-advancing PI-DeepONet and the FE solver are naturally coupled in the time domain. Meanwhile, spatial coupling is achieved via the Schwarz alternating method through boundary data exchange. Importantly, the time-advancing PI-DeepONet is not restricted to single-step predictions; it can sequentially predict multiple future time steps, thereby broadening its applicability to long-term dynamic simulations.

The next step involves training the time-advancing PI-DeepONet. Unlike earlier DeepONet models that rely solely on boundary conditions, the time-advancing variant requires full domain information as input to the branch network. Therefore, constructing a suitable dataset for PI-DeepONet pretraining is essential. This dataset is generated from a square domain solved using a FE solver, as shown in the reference ground truth results in Fig. 6.7(b) and Fig. 6.8(b). To begin, we generate 200 Gaussian random field samples with length scale parameters $l_u = l_v = 0.2$ to replace the constant displacements u_x and u_y. The boundary conditions applied to the intact square are identical to those shown in Fig. 6.7(a), except that the constant values of u_x and u_y are substituted by the generated Gaussian random field data. We employ the Newmark method within the FE solver to simulate the dynamic response of this square domain. For each of the 100 random field samples, we extract the boundary conditions on Γ_{II}^{out}, as well as the domain displacements and velocities (v_x and v_y) within Ω_{II}, across 11 time steps. To train the PI-DeepONet for prediction over 10 specific time steps, we select the corresponding segment of the dataset. The domain displacements and velocities from time steps 0 through 10 are used as inputs to the Branch2 network, while the boundary conditions from time steps 1 through 11 serve as inputs to the Branch1 network. As the domain displacements and velocities are generated from FEM with unstructured girds, the radial basis function interpolation in Scipy library [231] should be utilized to obtain the structured data, which can be used as inputs of CNN.This process yields 1000 total training samples (10 time steps × 100 samples) for the displacement components u_x, u_y, and velocity components v_x, v_y, along with their corresponding boundary values on Γ_{II}^{out}. During training, batches of size 100 are randomly sampled at each step.

The PI-DeepONet is trained using the governing equations in strong form, as defined in Eq. 3.50, by substituting u_x^n and u_y^n into the PI-DeepONet networks $G_{\theta_1}^{u_x}$ and $G_{\theta_2}^{u_y}$, respectively.

The acceleration is computed using Eq. 3.68. The resulting physics-informed residual equations used for training are:

$$\left(\lambda_0+2\mu_0\right)\frac{\partial^2 G_{\boldsymbol{\theta}_1}^{u_x}}{\partial x^2}+\mu_0\frac{\partial^2 G_{\boldsymbol{\theta}_1}^{u_x}}{\partial y^2}+\left(\lambda_0+\mu_0\right)\frac{\partial^2 G_{\boldsymbol{\theta}_2}^{u_y}}{\partial x\partial y}=\frac{-2}{\left(\beta \mathrm{d}t\right)^2}\left(u_x^{n-1}+v_x^{n-1}\mathrm{d}t-G_{\boldsymbol{\theta}_1}^{u_x}\right),\ \left(x,y\right)\in\Omega_{II} \quad (6.11)$$

$$\left(\lambda_0+2\mu_0\right)\frac{\partial^2 G_{\boldsymbol{\theta}_2}^{u_y}}{\partial y^2}+\mu_0\frac{\partial^2 G_{\boldsymbol{\theta}_2}^{u_y}}{\partial x^2}+\left(\lambda_0+\mu_0\right)\frac{\partial^2 G_{\boldsymbol{\theta}_1}^{u_x}}{\partial x\partial y}=\frac{-2}{\left(\beta \mathrm{d}t\right)^2}\left(u_y^{n-1}+v_y^{n-1}\mathrm{d}t-G_{\boldsymbol{\theta}_2}^{u_y}\right),\ \left(x,y\right)\in\Omega_{II} \quad (6.12)$$

$$G_{\boldsymbol{\theta}_1}^{u_x}\left(x,y\right)=u_x^n\left(x,y\right),\ \left(x,y\right)\in\Gamma_{II}^{out} \quad (6.13)$$

$$G_{\boldsymbol{\theta}_2}^{u_y}\left(x,y\right)=u_y^n\left(x,y\right),\ \left(x,y\right)\in\Gamma_{II}^{out} \quad (6.14)$$

It is important to note that the choice of 11 time steps in this study is arbitrary and can be extended to a larger number of steps, depending on the application requirements. After training the PI-DeepONet for 1 million iterations, the corresponding loss history is shown in Fig. C.3(a). In this plot, $\mathcal{L}_{\mathrm{bcs}}$ refers to the boundary condition loss, and $\mathcal{L}_{\mathrm{res}}$ denotes the residual loss, which correspond to Eq. 6.13-6.14 and Eq. 6.11-6.12, respectively. Before proceeding to the coupling process, we evaluate the trained PI-DeepONet using an unseen test case. Specifically, we apply the domain information at the time step n = 112 and the boundary conditions at n = 113, taken from the ground truth solution of an intact square domain under constant dynamic loading simulated using FEniCSx. When comparing the predicted results to the ground truth, the absolute errors in displacement components are found to be $\left|u_{x\,FE,\Omega_{II}}^{113}-u_{x\,NO,\Omega_{II}}^{113}\right|<5\times10^{-5}$ and $\left|u_{y\,FE,\Omega_{II}}^{113}-u_{y\,NO,\Omega_{II}}^{113}\right|<7\times10^{-5}$, which is depicted in Fig. C.3 in **Appendix C**. These results demonstrate that the PI-DeepONet is well-trained and capable of accurate generalization to unseen dynamic conditions.

After training the PI-DeepONet surrogate model, we can couple it with the FE solver over Ω_I. At each time step, the information transfer is carried out following the Algorithm 1. The coupling process for each inner iteration at each time step remains the same as described in **Chapter 3.2**. For the FE-FE coupling, the process remains the same, with the only difference being that Ω_{II} is solved using an FE solver. Instead of repeating the inner iteration process at each time step in the elastodynamic case, we present only the

converged result at every time step, requiring that L^2 error falls below the critical threshold $\epsilon = 10^{-5}$. For elastodynamic results, we use the same notations for converged results $u_{x\,FE-FE}^{n}$, $u_{y\,FE-FE}^{n}$, $u_{x\,FE-NO}^{n}$ and $u_{y\,FE-NO}^{n}$ as in **Chapter 3.2**, with n the superscript indicating the time step.

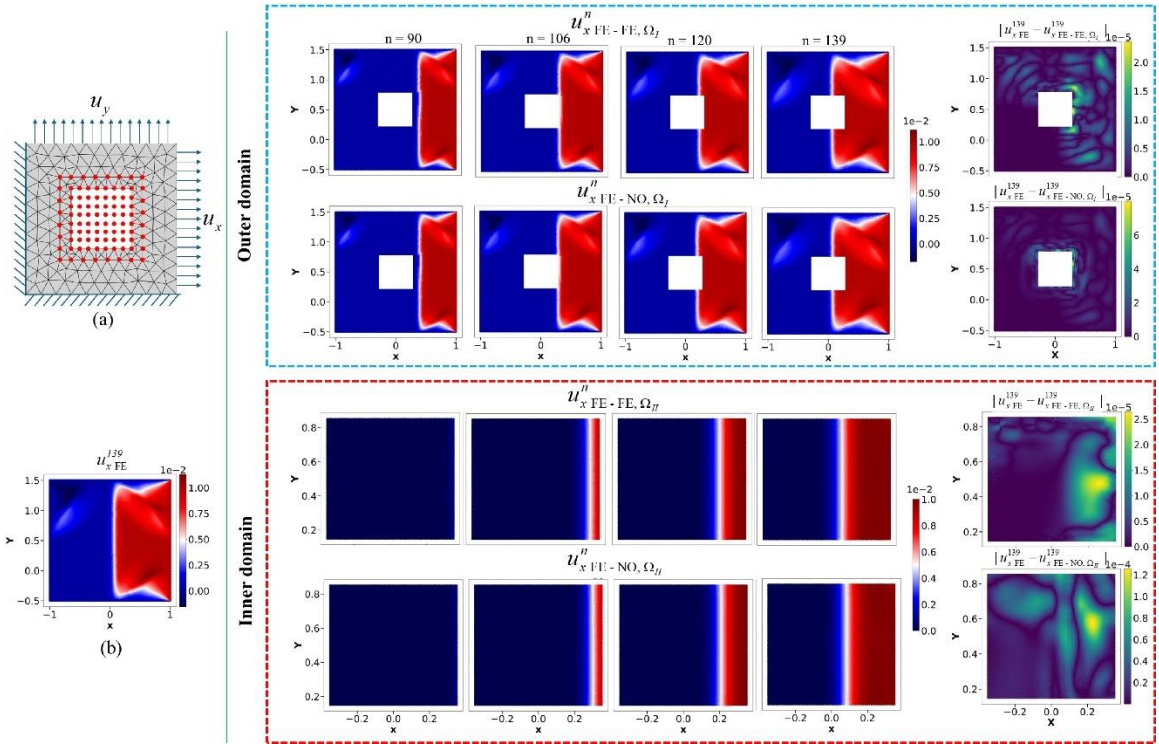

Figure 6.7 Response in x-direction (u_x) of the linear elastic coupling model under dynamic loading conditions: (a) Schematics of decomposed domains for spatial coupling framework, where the left and bottom edges have fixed boundary conditions and the top and right edges are subjected to an applied displacement in y-direction ($u_y = 0.01$) and x-direction ($u_x = 0.01$); (b) Ground truth displacement u_y at time step $n = 139$ obtained by solving the intact domain using FEniCSx; The blue-dashed box contains: Columns 1-4 showing the evolution of u_x in Ω_I for FE-FE coupling (top row) and FE-NO coupling (bottom row) at time step n = 90,106,120,139, with column 5 displaying the absolute error between the converged solution at time step n = 139 and ground truth. The red-dashed box contains: Columns 1-4 showing the evolution of u_x in Ω_{II} for both coupling frameworks at the same time steps, with column 5 displaying the absolute error relative to the ground truth.

Fig. 6.7 shows the evolution of displacement u_x for both coupling frameworks from time step n = 90, 106, 120, 139. Note that the domain information at n = 89 is obtained from the FE-FE coupling framework. Based on the $u_{x\,FE-FE}^{89}$, $u_{y\,FE-FE}^{89}$, $v_{x\,FE-FE}^{89}$ $v_{y\,FE-FE}^{n}$, $u_{x|\Gamma_{II}^{out}}^{90}$ and $u_{y|\Gamma_{II}^{out}}^{90}$, we can calculate and predict domain displacements $u_{x\,\Omega_{II}}^{90}$ and $u_{y\,\Omega_{II}}^{90}$ in

FE-FE and FE-NO, respectively. At n = 90, $u^{90}_{x\,FE-FE,\Omega_I}$ and $u^{90}_{x\,FE-NO,\Omega_I}$ both show that the high displacement values have not reached the domain Ω_{II}.

The entire blue region in $u^{90}_{x\,FE-FE,\Omega_{II}}$ and $u^{90}_{x\,FE-NO,\Omega_{II}}$ confirms that displacements are small in Ω_{II}. Due to the negligible displacement value in Ω_{II}, the inner iteration until time step 90 only requires 5 steps in FE-NO and 6 steps in FE-FE. However, as soon as high displacement values reach Ω_{II}, a higher number of inner iterations (e.g., 9 − 10) are required for convergence.

After 16 time steps (n = 106), it is found in both $u^{90}_{x\,FE-FE,\Omega_I}$ and $u^{106}_{x\,FE-NO,\Omega_I}$ that high displacement values u_x reach the right edge of Γ_I^{in}, and have already occupied the right area of the overlap region (Ω_o).

After another 14 time steps (n = 120), the x-displacement surpasses the Γ_I^{in}, stepping into the center hole of Ω_I. The upper and lower wings of the displacement in $u^{120}_{x\,FE-FE,\Omega_I}$ and $u^{120}_{x\,FE-NO,\Omega_I}$ uniformly propagate, and no reflection or sharp gradients of displacement field can be observed. This indicates the continuity between the two domains and the convergence of the inner iterations.

After an additional 20 time steps (n = 139), the higher values of u_x propagate further toward the left edge of the square.

The absolute error $|u^{139}_{x\,FE} - u^{139}_{x\,FE-FE}|$ in both Ω_I and Ω_{II} is on the order of magnitude 10^{-5}, while $|u^{139}_{x\,FE} - u^{139}_{x\,FE-NO}|$ is slightly higher in both domains. Specifically, the highest value reaches 8×10^{-5} in Ω_I and 1.25×10^{-4} in Ω_{II}. In both coupling frameworks, the highest absolute errors in Ω_I can be found around Γ_I^{in}, especially for FE-NO coupling.

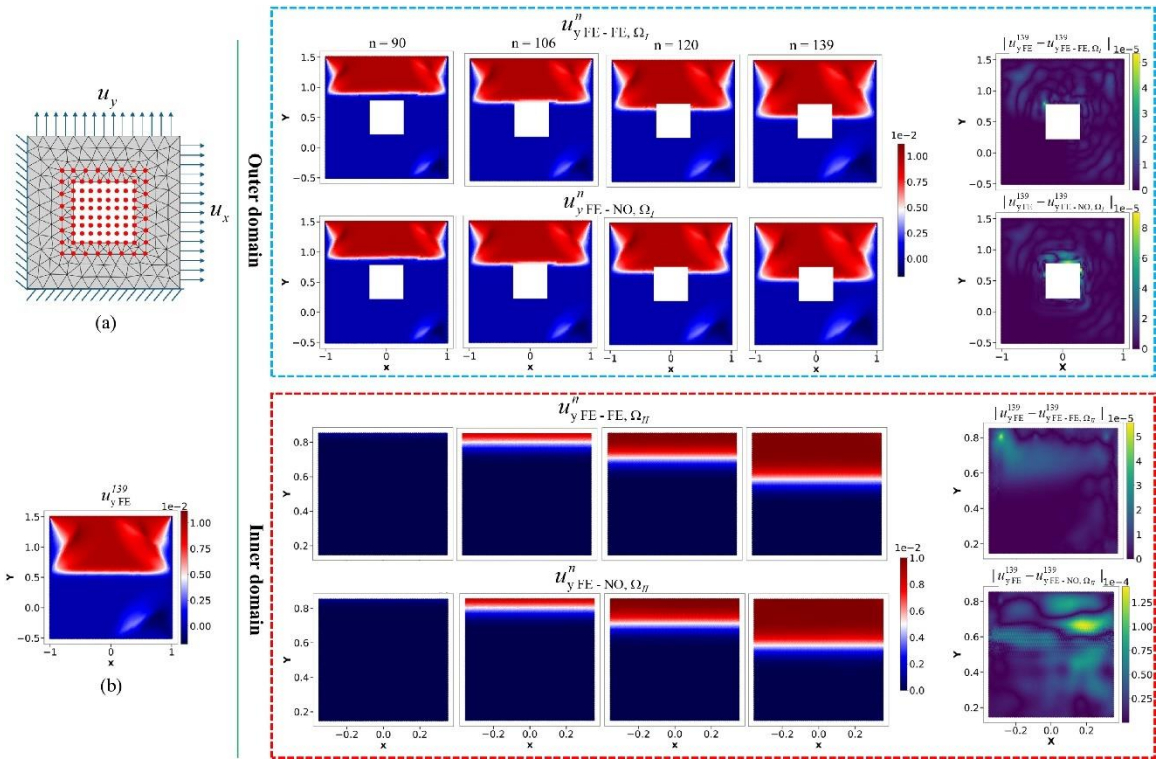

Figure 6.8 Response in y-direction (u_y) of the linear elastic coupling model under dynamic loading conditions: (a) Schematics of decomposed domains for spatial coupling framework, where the left and bottom edges have fixed boundary conditions and the top and right edges are subjected to an applied displacement in y-direction ($u_y = 0.01$) and x-direction ($u_x = 0.01$); (b) Ground truth displacement u_x at time step $n = 139$ obtained by solving the intact domain using FEniCSx; the blue-dashed box contains: Columns 1-4 showing the evolution of u_y in Ω_I for FE-FE coupling (top row) and FE-NO coupling (bottom row) at time step $n = 90, 106, 120, 139$, with column 5 displaying the absolute error between the converged solution at time step $n = 139$ and ground truth. The red-dashed box contains: Columns 1-4 showing the evolution of u_y in Ω_{II} for both coupling frameworks at the same time steps, with column 5 displaying the absolute error relative to the ground truth.

In Fig. 6.8, the evolution of displacement in y direction, u_y, from $n = 90$ to 139 is illustrated. In the first time steps, the red region of displacement uniformly propagates towards the bottom of the domain, then it gradually extends into Ω_{II} and propagates along with the transition interface as shown by a white line. Column 5 of the blue-dashed box and red-dashed box show the $\left|u_{y\,FE}^{139} - u_{y\,FE-FE}^{139}\right|$ and $\left|u_{y\,FE}^{139} - u_{y\,FE-NO}^{139}\right|$. The order magnitude of the absolute error is the same as that in displacement u_x.

Regarding the absolute error in Ω_I, the maximum error occurs in Γ_I^{in}. Similarly, the highest error in $\left|u_{y\,FE}^{139} - u_{y\,FE-FE,\Omega_{II}}^{139}\right|$ is also observed near Γ_I^{in}. In contrast, the maximum error in $\left|u_{y\,FE}^{139} - u_{y\,FE-NO,\Omega_{II}}^{139}\right|$ appears near the transition interface between the blue and red regions. As noted in [132], such relatively sharp interfaces are particularly challenging to accurately approximate in scientific machine learning frameworks.

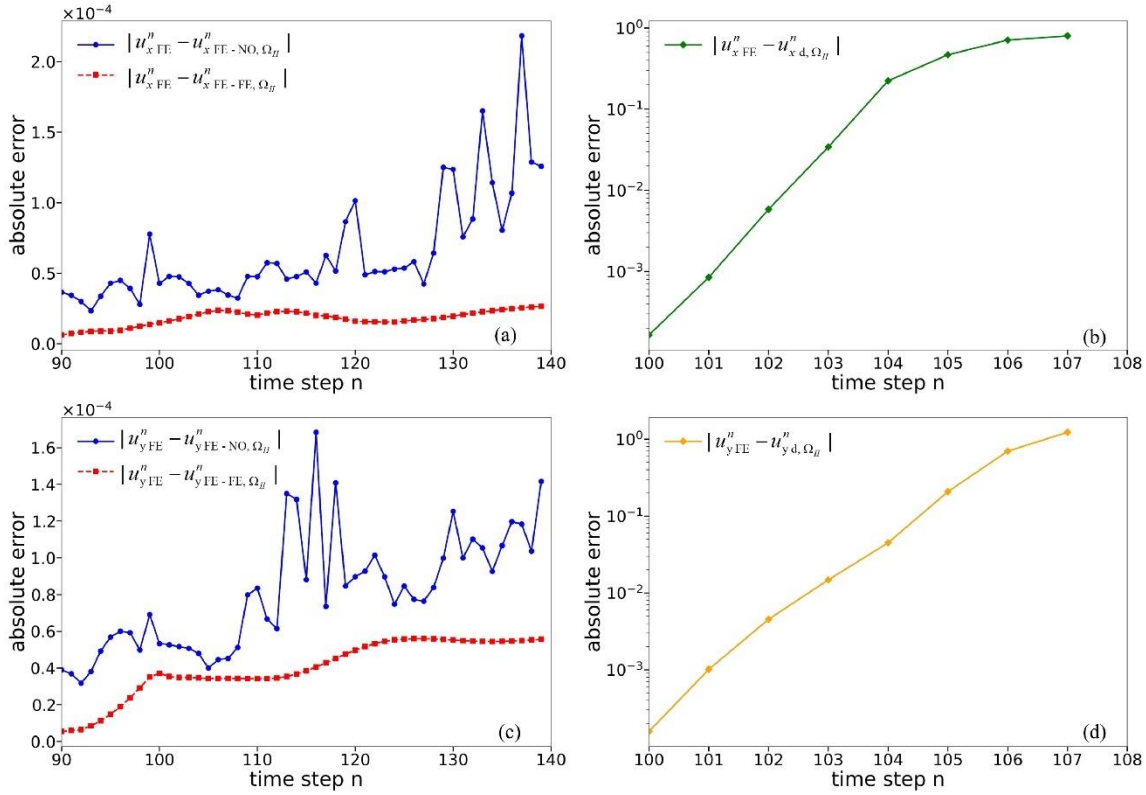

Figure 6.9 The maximum absolute error value in Ω_{II}: (a) absolute error of u_x from time step n = 90 to 139 for FE-NO ($|u_{x\,FE}^n - u_{x\,FE-NO}^n|$) and FE-FE ($|u_{x\,FE}^n - u_{x\,FE-FE}^n|$) coupling (b) absolute error of u_x by auto-regressive data-driven DeepONet. (c) and (d) are for u_y

The detailed evolution of the absolute error for both coupling frameworks is depicted in Fig. 6.9. It is noteworthy that the auto-regressive method is used in both coupling frameworks, meaning that information from the previous time step is used to derive the results for the next time step. As a result, if there is an error in the previous time step, it will be carried over to the next time step's result. This is a commonly observed issue in auto-regressive models within scientific machine learning, where error accumulation often leads to an exponential increase in error, potentially causing it to exceed several

orders of magnitude [143]. In Fig. 6.9(a, c), the absolute errors for both FE-FE and FE-NO have an increased tendency. The $|u^n_{x\,FE} - u^n_{x\,FE-FE}|$ changes smoothly, remaining within a small value range (below 5×10^{-5}), while the $|u^n_{x\,FE} - u^n_{x\,FE-NO}|$ varies more drastically, exhibiting abrupt fluctuations, specifically in the last 10 time steps. Similarly, the $\left|u^n_{y\,FE} - u^n_{y\,FE-FE}\right|$ keeps increasing in smooth manner, and the $\left|u^n_{y\,FE} - u^n_{y\,FE-NO}\right|$ oscillates abruptly.

Notably, in $\left|u^n_{y\,FE} - u^n_{y\,FE-NO}\right|$ from n = 113 to n = 118, the error value jumps steeply, showing three spikes with the highest value 1.68×10^{-4} at n = 116. Despite these error spikes, the absolute error $\left|u^n_{y\,FE} - u^n_{y\,FE-NO}\right|$ self-corrects to lower values (approximately 1.02×10^{-4}) during time steps $n = 119 - 129$, demonstrating the resilience of the framework. This self-heal phenomenon indicates that the auto-regressive error accumulation is not dominant in FE-NO coupling, though it is an auto-regressive surrogate model. We hypothesize that the significant error attenuation is because of the accurate boundary conditions provided by the FE solver in Ω_I.

We compare our model against a purely data-driven DeepONet to demonstrate the substantial accuracy improvements achieved through the incorporation of boundary conditions. This data-driven DeepONet implements the identical dataset utilized in time-advancing PI-DeepONet. The 100 samples of domain information (u_x and u_y) at each time step from n = 99 to 108 (100 × 10 samples in total) are provided as input of the branch network. The corresponding 100 samples for each time step from n = 100 to 109 are set as the output. Notably, the architecture of the data-driven model is identical to the elastodynamic model in **Table 3.3**, except that the Branch1 network responsible for enforcing boundary conditions is removed. We train this data-driven DeepONet to predict the next time step's displacements in x-direction and y-direction. Consequently, we obtain two auto-regressive models for x-displacement and y-displacement, which predict the displacement in Ω_{II} only depending on the domain displacement from the previous time step without boundary conditions. The accurate results for n = 99 are provided by the FE

solver. The data-driven DeepONet predicts the displacements in Ω_{II}, denoted as $u^n_{x_d,\Omega_{II}}$ and $u^n_{y_d,\Omega_{II}}$.

The corresponding absolute error $\left|u^n_{x\,FE} - u^n_{x_d,\Omega_{II}}\right|$ and $\left|u^n_{y\,FE} - u^n_{y_d,\Omega_{II}}\right|$ are shown in Fig. 6.9(b, d). Both exhibit enormous increases of the order of magnitude 10^{-4} to 10^{0}. In the first step at $n = 100$, both absolute errors are smaller than 1×10^{-4} exhibiting the accuracy of the data-driven DeepONet for the trained timestep. However, when this model is used to predict the next 7 steps (i.e., from $n = 100$ to 107), the auto-regressive error accumulates significantly, resulting in an increase of five orders of magnitude. This highlights the superiority of our time-advancing PI-DeepONet over the data-driven DeepONet.

Although the error accumulation in our FE-NO framework seems unavoidable in the current method, the absolute error for u_x and u_y are still lower than 3×10^{-4} after 49 time-steps, while the displacement values of u_x and u_y are at 10^{-2} orders. To restrict the FE-NO error within a bounded threshold, we perform FE-FE coupling for a few timesteps after a few FENO coupling for significantly large timesteps, as a recalibration for the coupling framework. As displayed in Fig. 6.9(a,c), after 139-time steps, the absolute error in FE-FE is still in 10^{-5}, varying continuously and smoothly without any spikes.

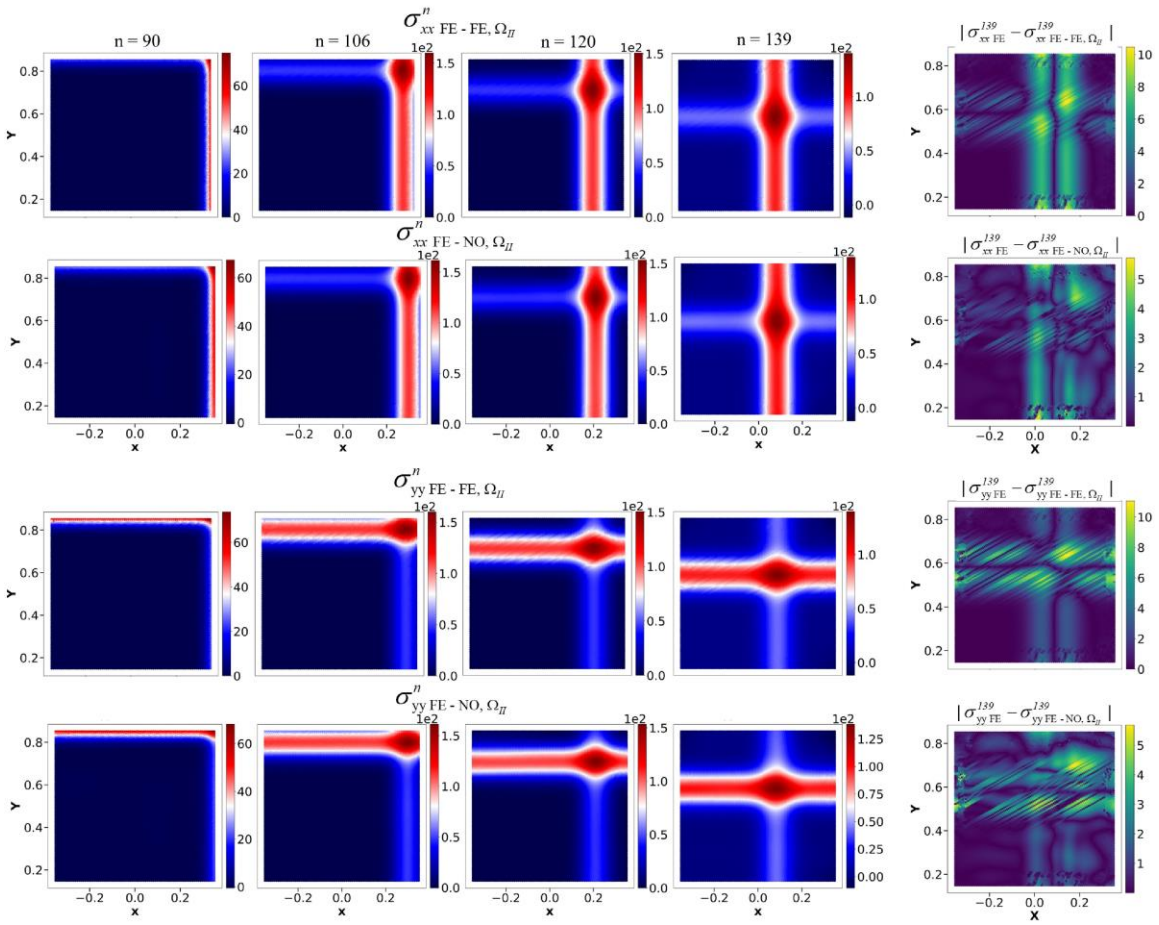

Figure 6.10 Response in x-direction (σ_{xx}) and y-direction (σ_{yy}) of the linear elastic coupling model under dynamic loading in Ω_{II}: First two rows are the evolution of σ_{xx} at $n = 90, 106, 120, 139$, obtained in FE-FE and FE-NO respectively, with column 5 displaying the absolute error between the converged solution at time step $n = 139$ and ground truth. The last two rows are σ_{yy} for both coupling frameworks, with column 5 displaying the absolute error relative to the ground truth.

Figure 6.10 presents the stress fields for the elastodynamic example. The stress distributions in both coupling frameworks (i.e, FE-FE and FE-NO) are consistent with the displacement fields, with σ_{xx} and σ_{yy} propagating toward the left and bottom edges, respectively. The displacements $u^n_{x\,\Omega_{II}}$ and $u^n_{y\,\Omega_{II}}$, shown in Fig. 6.7 and Fig. 6.8 remain nearly constant within the red and blue regions, separated by a single transition interface. As a result, σ_{xx} and σ_{yy} exhibit stripe-like patterns centered around this displacement interface. Due to the Poisson effect, a light blue stripe intersects a red stripe in both σ_{xx} and σ_{yy}, leading to a localized maximum in the intersection region.

Due to the use of the first-order continuous Galerkin method, stress discontinuities appear in the FE-FE coupling results. These are particularly evident in the white regions of $\sigma^{106}_{yy\,FE-FE,\Omega_{II}}$, $\sigma^{120}_{yy\,FE-FE,\Omega_{II}}$ and $\sigma^{139}_{yy\,FE-FE,\Omega_{II}}$. In contrast, FE-NO coupling stress distributions are smoother because of the high-order differentiability. Therefore, in absolute errors, $\left|\sigma^{139}_{xx\,FE} - \sigma^{139}_{xx\,FE-NO,\Omega_{II}}\right|$ and $\left|\sigma^{139}_{yy\,FE} - \sigma^{139}_{yy\,FE-NO,\Omega_{II}}\right|$ are slightly lower than $\left|\sigma^{139}_{xx\,FE} - \sigma^{139}_{xx\,FE-FE,\Omega_{II}}\right|$ and $\left|\sigma^{139}_{yy\,FE} - \sigma^{139}_{yy\,FE-FE,\Omega_{II}}\right|$.

It is worth noting that increasing the element order in finite element methods can mitigate the stress discontinuity issue. However, this comes at the cost of significantly increased computational effort, resulting in reduced efficiency. Instead of compromising between accuracy and efficiency in traditional FE solvers, employing neural operators to solve high-order PDEs presents a promising alternative.

6.4 Expansion of the ML-subdomain

In **Chapter 6.3**, the computational domain was pre-partitioned into two subdomains, Ω_I and Ω_{II}, with Ω_{II} replaced by a DeepONet surrogate. Therefore, during the simulation in **Chapter 6.3**, the DeepONet region remained fixed. However, in realistic multi-scale and dynamic systems, computationally intensive regions often evolve over time. To optimize the performance of our framework in such scenarios, we propose the dynamic expansion of the DeepONet region, which allows the DeepONet domain to expand adaptively in a tile-like manner following Algorithm 2.

In this subsection, we consider the same global computational domain and boundary conditions as in **Chapter 6.3**. As shown in Fig. 3.3, the DeepONet region Ω_{II} is now extended to include two additional square domains, Ω_{II} and Ω_{III}, positioned 0.3 units above and below Ω_{II}, respectively, and having the same length (0.7 units). This configuration results in a larger rectangular surrogate composed of three adjacent DeepONet domains. The outer domain Ω_I is a 2×2 square with a 0.12×0.6 rectangle hole.

To train these two time-advancing PI-DeepONet, we implement the same method as illustrated in previous section. For Ω_{II}, the DeepONet is trained with suitable dataset

extracted from the intact square domain solved by FE solver. For the DeepONet on Ω_{III}, we have implemented a transfer learning strategy [232], leveraging the trained model for Ω_{II}. These two PI-DeepONet can also be trained using Eq. 6.11, 6.12, 6.13 and 6.14. We refer to the DeepONet for Ω_{II} as upper DeepONet, Ω_{III} as lower DeepONet. After training the two PI-DeepONets in the FE-NO coupling framework, we first couple them together. The combined DeepONet model is then treated as a single solver and coupled with the FE solver in Ω_I, as outlined in Algorithm 2. The two different L^2 errors, $L^2{}_{p1}$ and $L^2{}_{p2}$, defined in Eq. 3.82 and Eq. 3.83, should be lower than the critical thresholds $\epsilon = 1 \times 10^{-5}$ and $\epsilon' = 1 \times 10^{-5}$, respectively. In this FE-NO coupling framework, FE is discretized into 47,828 elements, with 162 nodes uniformly distributed along the left and right edges of Γ_{inner}^{out} and 82 nodes on the top and bottom edges.

For FE-NO coupling, we first solve Ω_I using FEniCSx and pass the displacement information at Γ_{inner}^{out} to $\Omega_{II} \cup \Omega_{III}$. Having received the boundary conditions provided from Ω_I and Ω_{III} (at first coupling iteration of $\mathbf{u}_{|\Gamma_{inner_2}^{in}} = \mathbf{0}$, as detailed in Algorithm 2), the upper DeepONet predicts the displacement throughout Ω_{II}, giving the values of $u_{x|\Gamma_{inner_3}^{in}}$ and $u_{x|\Gamma_{inner_3}^{in}}$ that are passed to Ω_{III}. Then, based on the boundary conditions from Ω_I and Ω_{II}, the displacement over Ω_{III} is obtained, which provides the value $u_{x|\Gamma_{inner_2}^{in}}$ and $u_{y|\Gamma_{inner_2}^{in}}$ to Ω_{II}. Information exchange between Ω_{II} and Ω_{III} continues until the iteration converges, as calculated in Eq. 3.82. Then, the $\Omega_{II} \cup \Omega_{\mathrm{III}}$ predicted by the DeepONet passes the $u_{x|\Gamma_{inner}^{out}}$ and $u_{y|\Gamma_{inner}^{out}}$ back to the Ω_I. Consequently, the FE solver updates the displacement in Ω_I, providing the new boundary conditions to $\Omega_{II} \cup \Omega_{III}$. It is important to note that once convergence is achieved for the coupling between Ω_{II} and Ω_{III}, each subsequent update from Ω_I requires only one additional iteration to satisfy the convergence criterion $L_{p_1}^2 < 1 \times 10^{-5}$. Information is continuously transferred between Ω_I and $\Omega_{II} \cup \Omega_{III}$, until the inner iteration convergence condition $L_{p_2}^2 < 1 \times 10^{-5}$ is achieved. Eventually, we can get $\mathbf{u}_{|\Omega}^n$ by composing the subdomains of the results $I - III$. In this example, we use

the same notations as Section 3.3 $u^n_{x\,FE-NO}$ and $u^n_{y\,FE-NO}$ to denote the converged x and y displacement at time step n obtained using FE-NO coupling.

Applying the domain information obtained at n = 139 by FE-FE coupling in previous **Chapter 6.3**, further displacement propagation of the dynamic system is illustrated in Fig. 6.11 – 6.12.

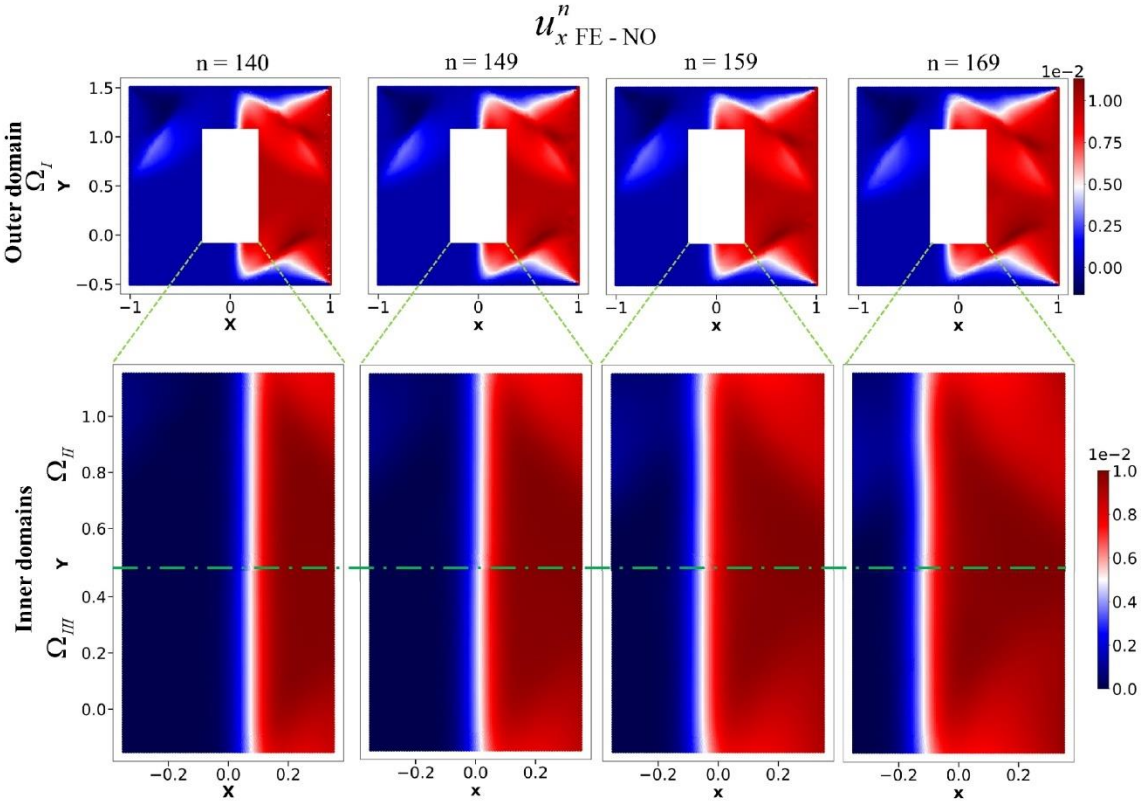

Figure 6.11 Response in x-direction (u_x) of NO replacement for linear elastic FE-NO coupling model under dynamic loading conditions: first row showing the evolution of u_x at time step n = 140,149,159,169 in Ω_I, second row and third row displaying the evolution in Ω_{II} and Ω_{III}, respectively.

Fig. 6.11 illustrates the evolution of $u_{x\,FE-NO}$ in Ω_I, Ω_{II} and Ω_{III} at time step n = 140,149,159,169. At n = 140, the displacement u_x in Ω_I is similar to that in Fig. 6.7, with two triangle wings on the upper and lower regions. In Ω_{II} and Ω_{III}, the almost constant results show up, uniformly distributed red and blue regions along with a transition interface. After 9 time steps (n = 149), the transition interface of displacement u_x almost reaches the central axis (x = 0). The non-uniformity can be observed in the red region of Ω_{II}, where the

right top is slightly lighter than the others. The transition interface is still relatively straight. After another 10 time steps (n = 159), the displacement u_x has already surpassed the central axis (x = 0), and the non-uniformity becomes more pronounced. Moreover, the transition interface is no longer a straight line; instead, it evolves into a curved shape-particularly near the upper end in Ω_{II} and the lower end in Ω_{III}. This phenomenon becomes more pronounced after an additional 10 time steps at n = 169, where the transition interface in $u_{x\,FE-NO,\Omega_{II}}^{169}$ exhibits a more prominent curvature. Additionally, the light red region extends toward the upper-right corner. In Ω_{III}, a similar light red area appears symmetrically in the lower-right corner; however, the transition interface in Ω_{III} is not symmetrically curved.

The difference of the transition interface in Ω_{II} and Ω_{III} originates from the Poisson's effect. The dark blue propagates from the left-top region to the right-bottom region. After red region passing the central axis, the dark blue influences the transition interface. Due to fixed boundary conditions on the left and bottom edges, there is no displacement wave from the left-bottom region. Therefore, the transition interface is not greatly influenced.

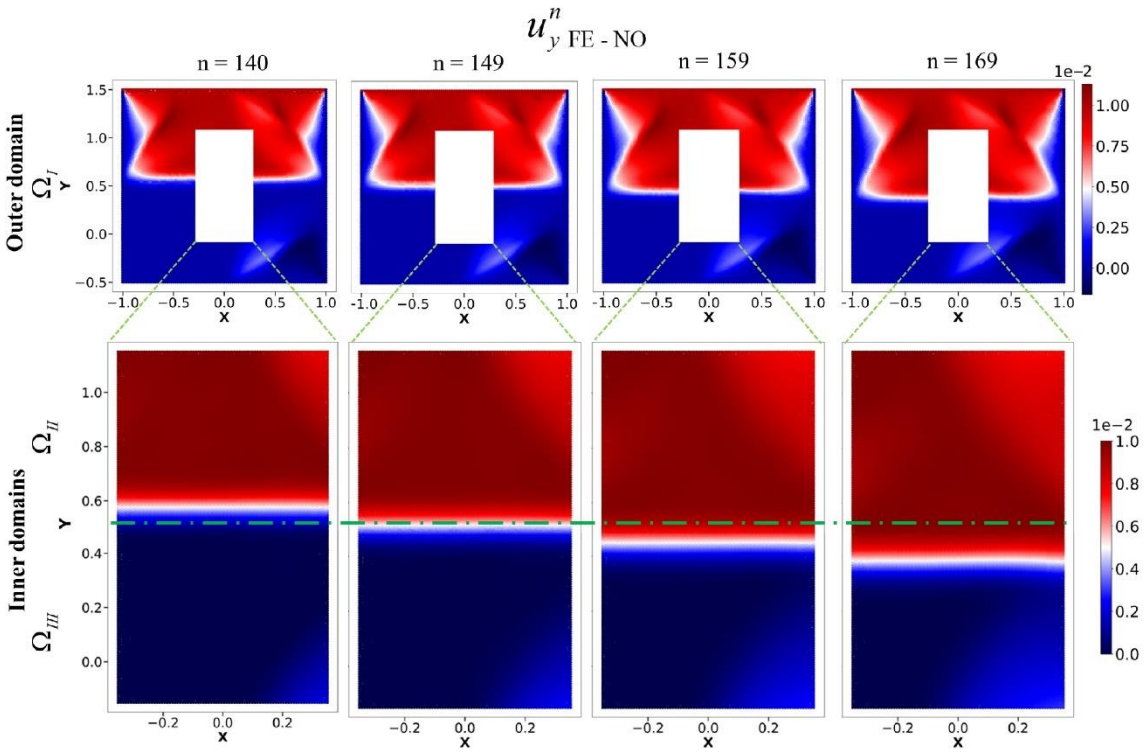

Figure 6.12 Response in y-direction (u_y) of NO replacement for linear elastic FE-NO coupling model under dynamic loading conditions: first row showing the evolution of u_y at time step n = 140,149,159,169 in Ω_I, second row and third row displaying the evolution in Ω_{II} and Ω_{III}, respectively.

The evolution of u_y from n = 140 to 169 is shown in Fig. 6.12, where the non-uniformity becomes clearly noticeable. Despite the non-uniformity and transition interface variance for u_y, the more intriguing process is the displacement propagation from Ω_{II} to Ω_{III}.

At n = 140, the displacement u_y in Ω_{II} is observed to remain nearly constant at approximately 1×10^{-2}. In contrast, the value of $u_{y\,FE-NO,\Omega_{III}}^{140}$ is significantly lower, with a maximum around 3×10^{-3}. The light blue region in the lower-right corner is attributed to the Poisson effect, as previously discussed. After 9 additional time steps (n = 149), the displacement u_y continues to propagate toward the bottom edge, with its maximum value in Ω_{III} reaching 6.7×10^{-3}—more than twice the value observed at n = 140. After another 9 time steps (n = 159), the maximum value reaches 1×10^{-2}, indicating that the uniform displacement field has extended into Ω_{III}. Finally, at n = 169, the minimum of u_y in Ω_{II} is higher than 7.5×10^{-3}, indicating that the transition interface leaves Ω_{II} to Ω_{III}.

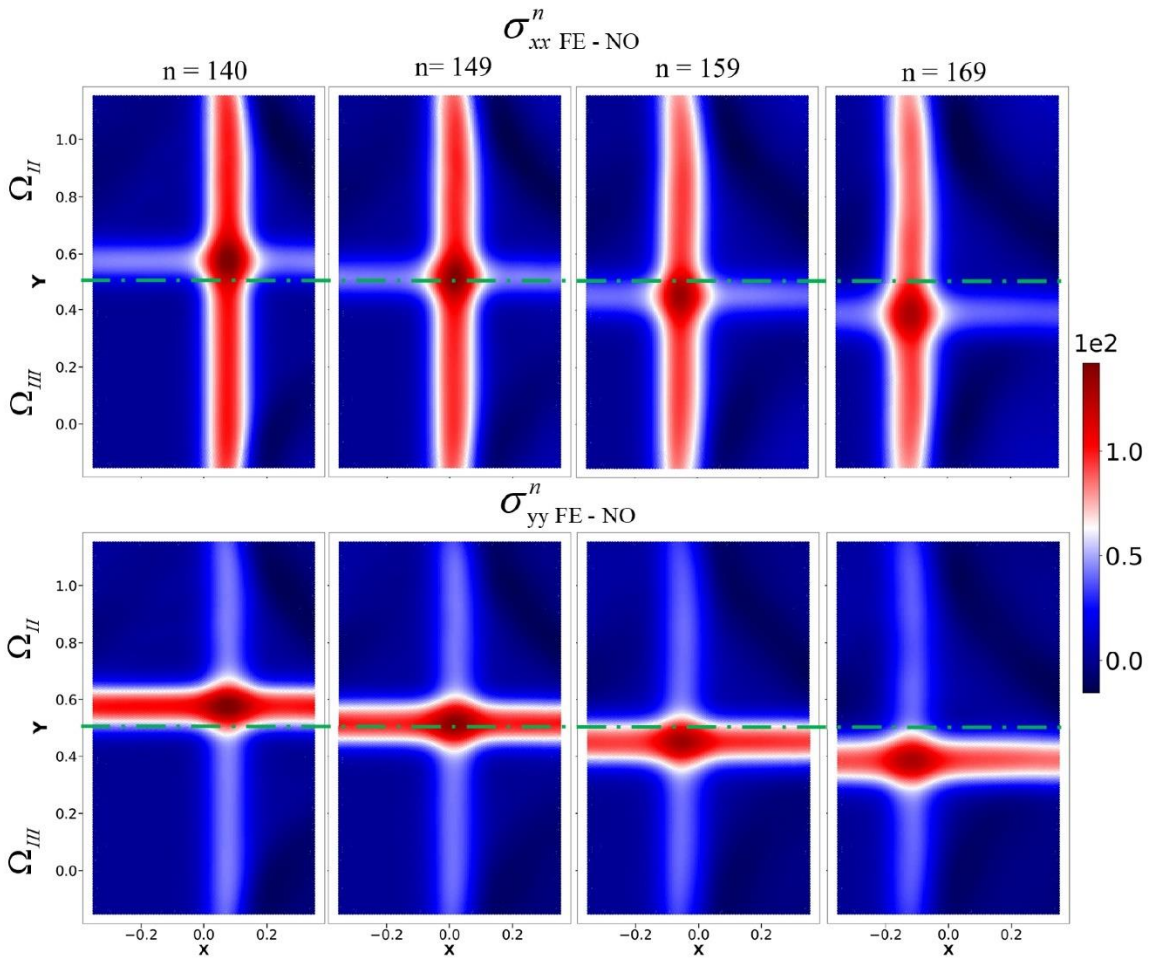

Figure 6.13 Response in x-direction (σ_{xx}) and y-direction (σ_{yy}) of NO replacement for linear elastic coupling model under dynamic loading in Ω_{II}: First two rows are the evolution of σ_{xx} at n = 140,149,159,169 in Ω_{II} and Ω_{III}, respectively, last two rows are σ_{yy} at corresponding time steps in Ω_{II} and Ω_{III}

In Fig. 6.13, the evolution of stress σ_{xx} and σ_{yy} in Ω_{II} and Ω_{III} is depicted. It is evident that the σ_{xx} is not straight at the upper end in Ω_{II} and lower end in Ω_{III}, confirming the curved transition interface obtained in Fig. 6.7. This adaptive ML-subdomain expansion strategy offers a powerful tool for enabling real-time optimization of computational resources. This approach is particularly promising for dynamic multi-physics systems, such as phase-field models [18, 51, 233, 234], which require high-resolution computations near evolving interfaces. For instance, in phase-field fracture mechanics, mesh refinement is necessary at the crack tip, where localized stress singularities demand high resolution, which requires significant increase in computational cost. Therefore, adaptively replacing the crack-tip

region with DeepONet, as proposed in [235], can significantly improve simulation efficiency.

6.5 Neural operator coupling as surrogate of adaptive mesh refinement: An essential key in multiscale modeling

In preceding examples, our framework has been validated using domains with uniform mesh refinement to demonstrate the efficiency of the spatial and temporal coupling. This section extends our investigation to applications with non-uniform mesh density, a critical consideration for multiscale modeling problems. Adaptive mesh refinement (AMR) allows for selectively increasing the resolution in regions exhibiting fine-scale features (smaller length scale), such as stress concentrations near crack tips in fracture mechanics. However, both the identification of regions requiring refinement and the subsequent numerical solution of these densely meshed domains incur substantial computational costs.

Our approach addresses this challenge by strategically replacing computationally intensive fine-mesh regions with neural operator surrogates. The current implementation demonstrates this capability for static loading conditions with predetermined location of the ML subdomain (i.e. we are aware of the locations that require refinement). This represents a foundational step toward our future research objective: developing a fully adaptive framework for static and dynamic problems where the neural operator subdomain automatically expands to encompass evolving regions that would otherwise require progressive mesh refinement.

In this subsection, we examine a linear elastic thick cylinder with an inner radius of 1 and an outer radius of 4 under static loading conditions. A non-uniform mesh with varying mesh densities is used in this example: the coarse-mesh region is modeled using the FE, while the fine-mesh region is modeled using the neural operator. To simplify the analysis, the full cylinder domain is reduced to a quarter-cylinder by imposing roller support boundary conditions along the left and bottom edges. The schematic of the decomposed domains for the FE-NO coupling approach is shown in Figure 6.14(a). The outer cylindrical region, Ω_I, extending from a radius of 1.8 to 4, is discretized and solved

using the FE method, while the inner cylindrical region, Ω_{II}, spanning a radius of 1 to 2, is resolved using the neural operator. A non-uniform, displacement-controlled loading, **u**, is imposed on the inner circular boundary, $\partial\Omega_{II}$, and is defined as:

$$\mathbf{u} = \left(0.01\times x^2, 0.01\times y^2\right),\ \ (x,y) \in \partial\Omega_{II} \tag{6.15}$$

The resulting displacement fields in the x and y directions, obtained from FE analysis over the entire domain, are presented in Figures 6.14(b) and 6.15(b), respectively. For training of the PI-DeepONet operators, $G_{\boldsymbol{\theta}_1}^{u_x}$ and $G_{\boldsymbol{\theta}_2}^{u_y}$, the loss functions $\mathcal{L}_{bcs}$ and $\mathcal{L}_{res}$ are formulated similar to those described in **Chapter 6.1**, following Eq. 6.1–6.3. Due to the roller support boundary conditions imposed along the left and bottom edges, an additional loss function, $\mathcal{L}_{bcs\,fix}$, is introduced to enforce the following constraints:

$$G_{\boldsymbol{\theta}_1}^{u_x}\left(0,y\right) = 0,\ \mathrm{y} \in \partial\Omega_{II} \tag{6.16}$$

$$G_{\boldsymbol{\theta}_2}^{u_y}\left(x,0\right) = 0,\ x \in \partial\Omega_{II} \tag{6.17}$$

The PI-DeepONet was trained for 2×10^6 iterations, with the corresponding loss plot shown in Fig. C.4(a). Here, $\mathcal{L}_{bcs\,fix}$,is the loss function defined by Eq. 6.16–6.17. Notably, $\mathcal{L}_{bcs\,fix}$, can be regarded as a specialized contribution to the broader boundary condition loss $\mathcal{L}_{bcs}$. At each training iteration, 1600 collocation points were randomly sampled across the entire domain to compute the loss functions. This dense sampling strategy ensures that the trained PI-DeepONet achieves sufficient resolution to accurately predict results comparable to those obtained from FE analysis on highly refined meshes.

To evaluate the accuracy of the surrogate model, the trained neural operators were tested under the non-uniform displacement loading **u** specified in Eq. 6.15. The predictions, $u_{x\,NO,\Omega_{II}}$ and $u_{y\,NO,\Omega_{II}}$, were compared against the FE ground truth solutions. The absolute errors were found to be negligible, with magnitudes of 9.5×10^{-5} for $\left|u_{x\,FE,\Omega_{II}} - u_{x\,NO,\Omega_{II}}\right|$ and 8.5×10^{-5} for $\left|u_{y\,FE,\Omega_{II}} - u_{y\,NO,\Omega_{II}}\right|$, as illustrated in the last column of Fig. C.4 in

Appendix C. Given this high level of accuracy, the trained neural operators are deemed suitable for integration within the FE-NO coupling framework.

As a linear elastic system under static loading, the thick cylinder model follows the same computational methodology and governing equations detailed in **Chapter 6.1**. However, the mesh density distribution differs significantly from those used in **Chapter 6.1**, **6.2**, **6.3**, and **6.4**, as a non-uniform mesh is employed in this case, in contrast to the uniform mesh density used in the previous examples. Specifically, Ω_I is discretized with a coarser mesh compared to the meshes used in the earlier sections, while Ω_{II} is resolved with a much finer mesh, as illustrated in Figures 6.14(b) and 6.15(b).

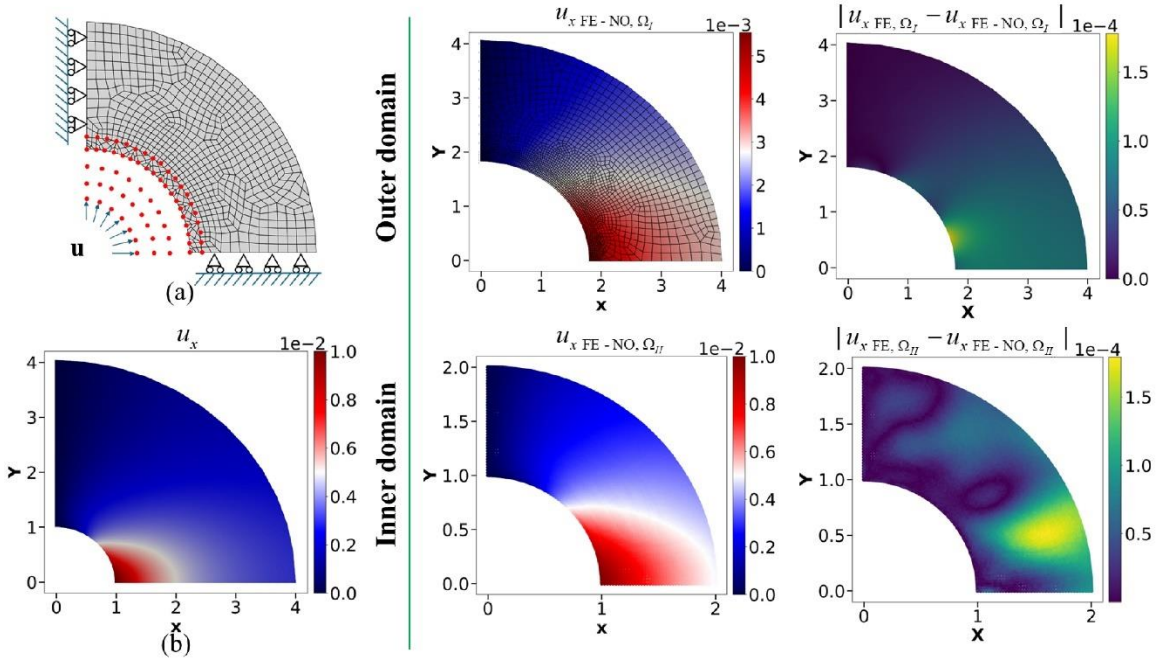

Figure 6.14 Response in x-direction (u_x) of the linear elastic coupling model for thick cylinder: (a) Schematic of decomposed domains for the spatial coupling framework, where the left and bottom edge have support roller boundary conditions and inner circular edge is subjected to an applied displacement $\mathbf{u} = (0.01 \times x^2, 0.01 \times y^2)$; (b) Ground truth displacement u_x obtained by solving the intact domain using FEniCSx. Middle column shows the u_x in Ω_I (first row) and Ω_{II} (second row) for FE-NO coupling at iteration $j = 19$, the last column displays the absolute error relative to the ground truth.

Figure 6.14 (middle column) shows the converged solution of $u_{x\,FE-NO}^{19}$ for both domains Ω_I and Ω_{II} in iteration $j = 19$. The maximum absolute errors, quantified as $\left|u_{x\,FE} - u_{FE-NO,\Omega_I}^{19}\right|$ and $\left|u_{x\,FE} - u_{FE-NO,\Omega_{II}}^{19}\right|$, both peak at approximately 1.7×10^{-4}. This

slightly exceeds the error levels observed in Figure C.4, reflecting the minor accuracy reduction typically introduced by domain decomposition methods (DDM). Moreover, the largest errors are mostly concentrated near the Ω_I–Ω_{II} interface, indicating that the dominant contributions to the total error arise from interface-related discrepancies inherent in DDM.

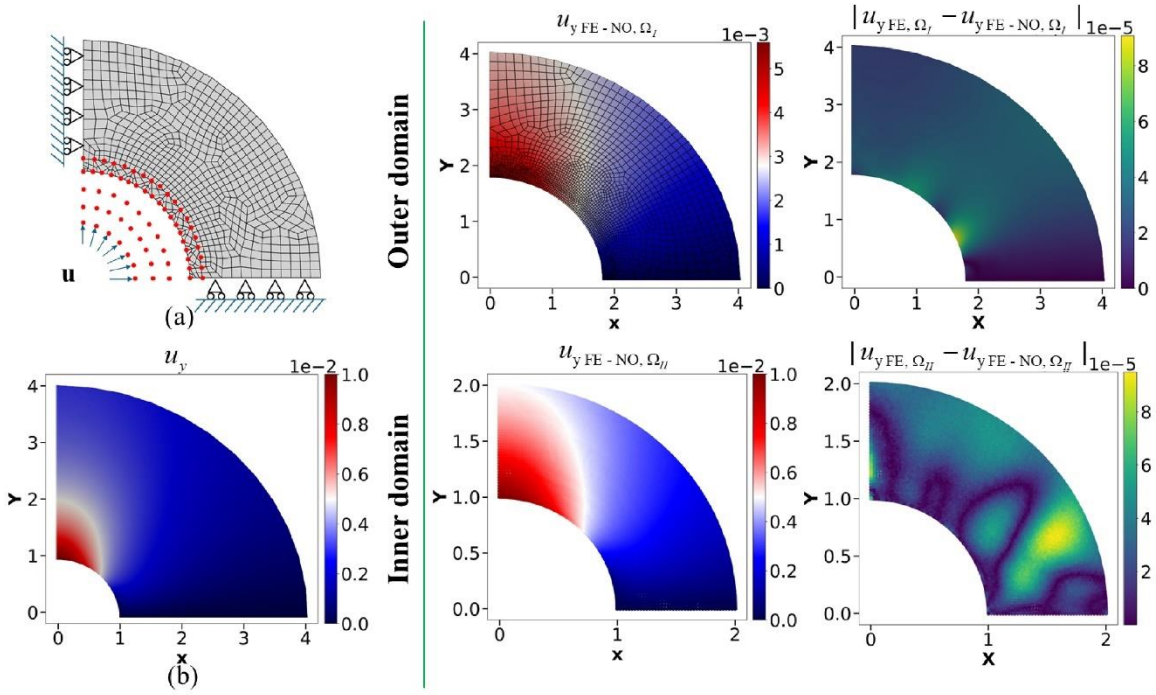

Figure 6.15 Response in y-direction (u_y) of the linear elastic coupling model under static loading conditions: (a) Schematic of decomposed domains for the spatial coupling framework, where the left and bottom edge have support roller boundary conditions and inner circular edge is subjected to an applied displacement $\mathbf{u} = (0.01 \times x^2,\ 0.01 \times y^2)$; (b) Ground truth displacement u_y obtained by solving the intact domain using FEniCSx. Middle column shows the u_y in Ω_I (first row) and Ω_{II} (second row) for FE-NO coupling at iteration $j = 19$, the last column displays the absolute error relative to the ground truth.

Figure 6.15 similarly presents the converged solutions for the vertical displacement components, $u_{y\,FE-NO,\Omega_I}^{19}$ and $u_{y\,FE-NO,\Omega_{II}}^{19}$, in its middle column. The corresponding absolute errors, shown in the last column, demonstrate excellent agreement with the reference solution, with maximum errors of approximately 9×10^{-5}. This level of accuracy is comparable to that achieved by the standalone NO model in Ω_{II} without DDM, as discussed previously. These results confirm that the pre-trained NO successfully captures

the displacement field in Ω_{II}, further validating the effectiveness of our FE-NO coupling approach.

Previous studies [236-238] have consistently demonstrated that accurate simulation of sharp gradients near cylindrical inner boundaries requires substantial mesh refinement. Adaptive refinement techniques enable appropriate variations in discretization density across subdomains [239, 240]. However, these methods involve an iterative computational cycle comprising pre-processing, solution, error estimation, marking, refinement, and resolution steps [237, 241]. This computationally intensive process typically demands multiple iterations before achieving satisfactory accuracy.

The implementation of NOs presents a transformative alternative to conventional refinement methodologies. The example in this subsection indicated that by randomly sampling points throughout the computational domain at each iteration, NOs are capable of predicting solutions on highly dense point grids. They only require that dense coordinates (x,y) be provided as input to the trunk network.

Therefore, here we briefly demonstrated that our method remains robust across varying mesh densities and does not require mesh conformity, unlike traditional numerical solvers. In our future work, we will deploy the proposed method for studying local behaviour like fracture analysis. In our future work, we plan to extend the method to multi-physics couplings and phase-field fracture problems. This extension will draw on prior studies such as [242] and [151]. Unlike those works, which employ physics-informed neural networks (PINNs) as surrogates, our approach uses physics-informed neural operators and handles time-dependent systems using the time-marching scheme introduced in this work. In particular, by incorporating velocity fields into the Branch Net architecture, our framework substantially mitigates autoregressive error accumulation over long time horizons.

6.6 Summary

In this chapter, we introduce a hybrid computational framework that synergistically integrates PI-DeepONet with FE to solve several mechanical problems. We develop two specialized DeepONet architectures: the first is optimized for static and quasi-static problems; the second incorporates an innovative time-marching scheme for dynamic systems, substantially mitigating error propagation prevalent in conventional ML solvers. The framework employs efficient domain decomposition, with inter-subdomain coupling achieved via the Schwarz alternating method across overlapping boundaries. The key contributions of this work are as follows:

1. A spatial coupling framework is proposed, allowing a pre-trained ML model to replace high-resolution discretized regions in numerical solver. The model is trained exclusively on governing physical laws, obviating the need for additional data generation.

2. A traditional time discretization technique, i.e., the Newmark-Beta method, from numerical solvers are embedded into DeepONet structures, resulting in a high-fidelity surrogate model that substantially attenuates error accumulation in dynamic simulations.

3. The ML region expansion is presented to serve as a dynamic subdomain optimization strategy during simulation, enabling computationally efficient and flexible multiscale modeling.

While our current investigations focus on solid mechanics, this coupling framework can readily extend to other physical systems, potentially transforming computational mechanics in terms of efficiency, scale, and generalization capabilities. The rapid inference capabilities of pre-trained DeepONet models, coupled with their ability to capture complex nonlinear mappings, make the FE-NO framework particularly effective for replacing computationally intensive nonlinear components.

The FE-NO coupling framework in this work employs a Dirichlet-Dirichlet information exchange scheme at overlapping boundaries. While this approach, given the architecture of our PI-DeepONet, is straightforward and has demonstrated stability, its primary limitation is low efficiency. Factors such as subdomain partitioning and overlap size can influence this efficiency, yet they cannot overcome the inherent computational bottleneck. Therefore, we continue to explore new information exchange methods, such as, Neumann-Dirichlet, Robin-Neuman, Robin-Robin etc., at non-overlapping boundary condition, outperforming in both efficiency and robustness.

Chapter 7 Conclusions and suggestions for future work

7.1 Conclusions

In this thesis, the mechanical failure mechanisms of ASSLMBs and IOX-strengthened cover glass are studied by establishing a Landau-Ginzburg-based PFFM and a Griffith-theory-generalized PFFM, respectively. These PFFMs can be easily integrated into the FEM. However, the complex multiphysical coupling and highly non-linear features of crack restrict the current PFFMs to limited temporal and spatial scales, resulting in extreme difficulty in quantitative investigations and exact reproduction of experimental observations. An FE—PI-DeepONet coupling framework is subsequently established to reduce computational cost, which has the potential to be an effective method for solving PFFM and multiphysical problems on large scales. The key insights obtained from the two PFFMs and AI-accelerated FE framework are summarized as below.

A multiphase Landau-Ginzburg-based PPFM has been established to elucidate the mechanical failure mechanism of ASSLMBs. This model unveils the role of voids in leading to cracks and dendrites. The key findings are as follows:

(1) The accumulation of vacancies at the Li/SSE interface forms voids during a discharging, and these voids can grow to a size determined by the ratio of surface and bulk diffusivities of lithium, as well as lithium creep under stack pressure.
(2) The presence of voids causes Li^+ ions to distribute nonuniformly within SSE near the void during charging, leading to nonuniform stresses that eventually induce cracks and Li dendrites. Although a high stack pressure can reduce the size of voids, it also accelerates cracking and lithium insertion in a charging process.
(3) The lateral stress can effectively inhibit cracks in SSE, and a stability map in terms of lateral pressure and fracture toughness of SSEs is proposed.

A Griffith-theory-generalized PFFM is implemented to investigate the mechanical performance of post-IOX glass. The main findings are:

(1) In ROR experiments, cracks initiate from DOL in a post-IOX glass even when surface flaws are present, whereas this shielding effect diminishes as the intensity and depth of surface flaws increase.
(2) The fragmentation of post-IOX glass, i.e., multiplication of cracks, can be simulated by Griffith-theory-generalized PFFM, and it is confirmed that the CT in layers deeper than the DOL leads to this phenomenon.
(3) High surface CS is considered to be the most important factor in inhibiting cracking in ROR experiments, while DOL is more important than surface CS in BD experiments. Considering stress relaxation in the IOX process, surface CS is often limited to below 1 GPa; therefore, increasing DOL is important for resisting both static and dynamic loadings, and a contour map of fracture strength relating surface CS and DOL is provided based on simulations.

A hybrid framework that integrates PI-DeepONet with FE solvers is proposed to solve a series of mechanical problems (linear elastic and static cases, hyperelastic and quasi-static cases, and elasto-dynamic cases). We develop two specialized DeepONet architectures tailored to these settings—one for static and quasi-static problems, and another for dynamic problems. The dynamic architecture is further enhanced with an innovative time-marching technique that drastically reduces error accumulation observed in traditional ML solvers. Our framework supports efficient domain decomposition, with inter-domain communication facilitated by the Schwarz alternating method across overlapping boundaries. The primary contributions of this research are threefold:

(1) We propose a spatial coupling framework that enables a pre-trained ML model to replace localized regions requiring high-resolution discretization. The model is trained using the governing physics of the system, eliminating the need for additional data generation.
(2) We incorporate traditional time discretization techniques in numerical solvers specifically, the Newmark-Beta method, into the DeepONet architecture. This integration results in a high-accuracy surrogate operator-learning model with significantly reduced error accumulation in dynamical simulations.

(3) We present a dynamic subdomain optimization strategy that adaptively expands machine learning subdomains during simulation, providing significant flexibility for reducing computational costs

7.2 Suggestions for future work

The Landau-Ginzburg-based PFFM achieved great success in multi-physical problems due to its compatibility with conventional PF framework; however, the fracture energy dissipation fluctuates rather than monotonically increase during cracking. Hence, the Griffith-theory-generalized PFFM is considered a more promising method for investigating fracture problems. Despite the Griffith-theory-generalized has been exploited in multi-physical systems, further development is needed to establish a unified framework for Griffith-theory-generalized PFFM in coupled problems [72]. We plan to leverage this unified framework to develop a new thermodynamically consistent PFFM for the SSE cracking in ASSBs and other multi-physical fracture problems in industrial applications.

It should be noted that Griffith-theory-generalized PFFMs can be readily utilized to solve three-dimensional (3D) cracking problems. However, only a few purely mechanical fracture benchmarks are reported in three dimensions, without considering any other physical field. In addition to the lack of a unified framework, the main barrier of 3D multi-physical fracture simulation stems from the computational inefficiency of current numerical solvers, generally FEM. The high non-linearity at the crack tip requires extremely fine meshes, bringing about formidable computational costs; meanwhile, the multi-physical coupling can exponentially escalate computational difficulty, making 3D multi-physical PFFM impractical. Thus, even though such 3D models can be developed and integrated into FEM, they are limited to small scales. This curse of dimensionality prevents numerical models from precise quantitative analysis.

Therefore, we are planning to further develop the FE-NO coupling framework in three dimensions. To achieve high efficiency, the computationally expensive regions in FEM, such as those requiring extremely fine meshes, can be replaced by NO in this 3D

model. In addition, the NO expansion will also be utilized in 3D FE-NO coupling method, allowing for continuous enhancements in efficiency. Currently, this coupling framework focuses solely on solid mechanics in this thesis; however, it can be readily extended to describe other physical phenomena and is also compatible with PF methods. With its non-linear mapping capability and mesh-free feature, this coupling framework is well-suited for PFFM with coupled problems. Eventually, we aim to build up an AI-accelerated 3D multi-physical PFFM, enabling real-time and full-scale quantification of multi-physical fracture problems.

Appendix A. Supplementary information for SSE cracking

A.1 Correspondence between the phase-field model and fracture mechanics

In the Eqs. 3.26 and 3.27, we introduced the critical strain energy ξ_{cr} that determines whether a crack will nucleate and propagate. This term should be related to the fracture toughness K_{Ic} (i.e., critical stress intensity factor for Mode-I cracks). For SSE with K_{Ic} ranging from 0.1 to 1 MPa·m$^{0.5}$ [243], the corresponding ξ_{cr} is from 1.8×10^{6} to 1.6×10^{8} J/m^3. The relation between ξ_{cr} and K_{Ic} can be determined by simulating a standard fracture mechanics test for a SSE model with a pre-notch [244], as shown in Fig. A.1(a). Under the far-field tensile stresses, the strain energy concentrates near the crack tip is shown in Fig. A.1(b). Applying different stresses, the relation between ξ_{cr} and K_{Ic}^2 can be obtained in Fig. A.1(c), which appears to be linear.

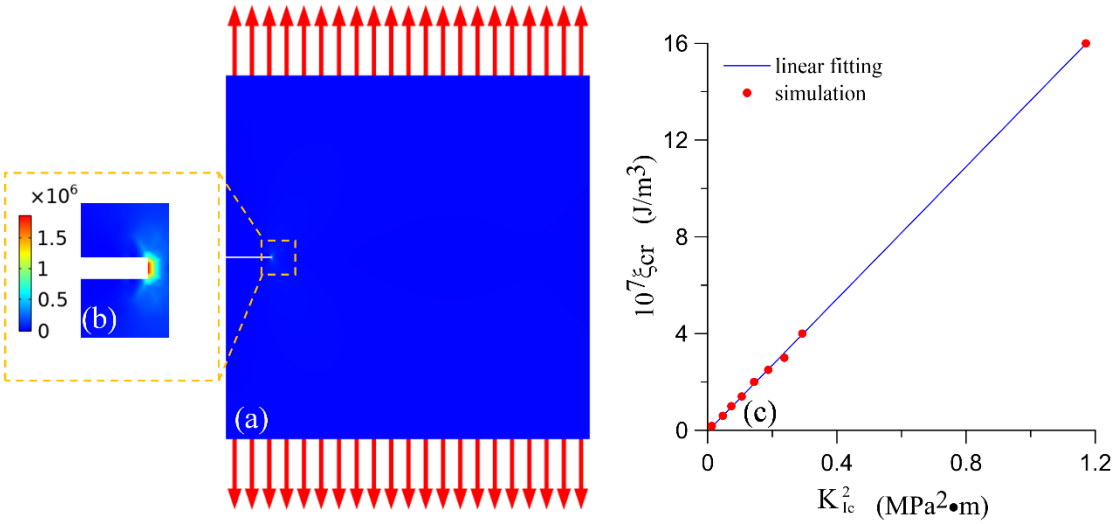

Figure A.1 Relation between ξ_{cr} and K_{Ic}: (a) simulation result of a standard test with a pre-notched specimen under an applied tensile stress of 21 MPa, (b) the enlarged view of strain energy distribution near the crack tip, and (c) the simulated relation between $10^7\xi_{cr}$ and K_{Ic}^2.

In Eq. 3.27, the last term on the right-hand side describes crack propagation, wherein the parameters L_{cr}, Ω^{SSE}, and ξ_{cr} affect crack evolution. Note that $\xi \propto \left(\Omega^{SSE}\right)^2$ and the product $L_{cr}\left(\xi - \xi_{cr}\right)$ determine the crack growth velocity. The determination of these parameters is currently arbitrary. For example, consider two cases:

(I) L_{cr}=0.01 (Pa·s)$^{-1}$, Ω^{SSE} = 0.5 cm^3/mol, and ξ_{cr}=3000 J/m^3, and

(II) L_{cr}=5×10^{-4} (Pa·s)$^{-1}$, Ω^{SSE} = 22.4 cm^3/mol, and ξ_{cr}=6×10^6 J/m^3

For these two cases, one will obtain the same morphology of cracks and distributions of lithium ions in SSE. Moreover, as $\xi_{cr} \propto \left(K_{Ic}\right)^2 \propto \left(\Omega^{SSE}\right)^2$ and $\xi \propto \left(\Omega^{SSE}\right)^2$, the distribution of dimensionless strain energy (ξ/ξ_{cr}) induced by chemical expansion is also identical for both cases. In simulations, a large Ω^{SSE} leads to convergence problems due to the large local strains that distorted meshes. Therefore, we employed the equivalent parameter set with low Ω^{SSE} to conduct simulations for cases with large Ω^{SSE} in order to avoid convergence problems in the numerical solution.

The estimation of Ω^{SSE} is based on the assumption that the lithium concentration in lithium-deficient areas is approximately 5% lower than the nominal value. Hence, the volumetric chemical strains can be expressed as $\boldsymbol{\varepsilon}^{mis} = \varepsilon^{mis}\boldsymbol{I} = \Omega^{SSE}\left(c_{Li^+} - c^0_{Li^+}\right)\boldsymbol{I} = -0.05\Omega^{SSE}c^0_{Li^+}\boldsymbol{I}$. This causes a strain energy: $\xi = \frac{E\left(\varepsilon^{mis}\right)^2}{2} = \frac{E}{2}\left(-0.05\Omega^{SSE}c^0_{Li^+}\right)^2$. Note that the lowest critical strain energy ξ_{cr} is 1.8×10^6 J/m^3. To initiate a crack, $\xi \geq min(\xi_{cr}) = 1.8 \times 10^6$ J/m^3. In this case, $\Omega^{SSE} \geq 10.6$ cm^3/mol. This estimate provides the order of magnitude of Ω^{SSE}. Then, in our simulation, we adjusted Ω^{SSE} in the range of 10-30 cm^3/mol. Higher Ω^{SSE} makes an SSE more easily cracked and leads to a lower CCD. Hence, in principle, Ω^{SSE}can be determined if CCD and K_{IC} are measured.

A.2 Application of constant current density

In the numerical model, it is more convenient to apply the constant voltages at

boundaries. However, in the experimental studies of ASSBs, a constant current density is more commonly applied. The method to implement a constant current density in our PF model is to set a constant ion flux J_0 on the bottom of the model as shown in Fig. 4.1(a). With equations 3.26 and 3.27,

$$J_0 = D_{\mathrm{Li}^+}\nabla c_{\mathrm{Li}^+} + \sigma_{\mathrm{Li}^+}\nabla\varphi \tag{A.1}$$

$$J_0 = -C_0\varepsilon_r\varepsilon_0\sigma_{\mathrm{Li}^+}\nabla\varphi \tag{A.2}$$

where C_0 is a constant to achieve the consistent current-voltage relation between the cases with constant current and with constant voltage.

A.3 Effect of key parameters

Based on the experimental results [81, 84, 101], several assumptions need to be made. First, the relation between current density and applied voltage, as shown in Fig. 4.1(b) requires that the mobility coefficients for Li (L_{k_1}) and SSE (L_{k_2}) are dependent on the applied voltage. To fit the experimental results as shown in Fig. 4.1(b), we assume the following relations between mobility coefficient L_η and voltage:

$$L_\eta = \frac{k_0}{a_{\mathrm{TS}}c_{\mathrm{Li}}^{\mathrm{ref}}} = 4.87\times V_{\mathrm{apply}} - 5.37\times 10^{-4} \tag{A.3}$$

Note that k_0 is the coefficient of reaction kinetics (Eq. 3.18). This extended relation indicates the effect of the applied voltage on the rate of electrodeposition, *i.e.*, it is not just exponentially dependent on the V_{apply}, and the corresponding experimental results and fitted curve are shown in Fig. A.2.

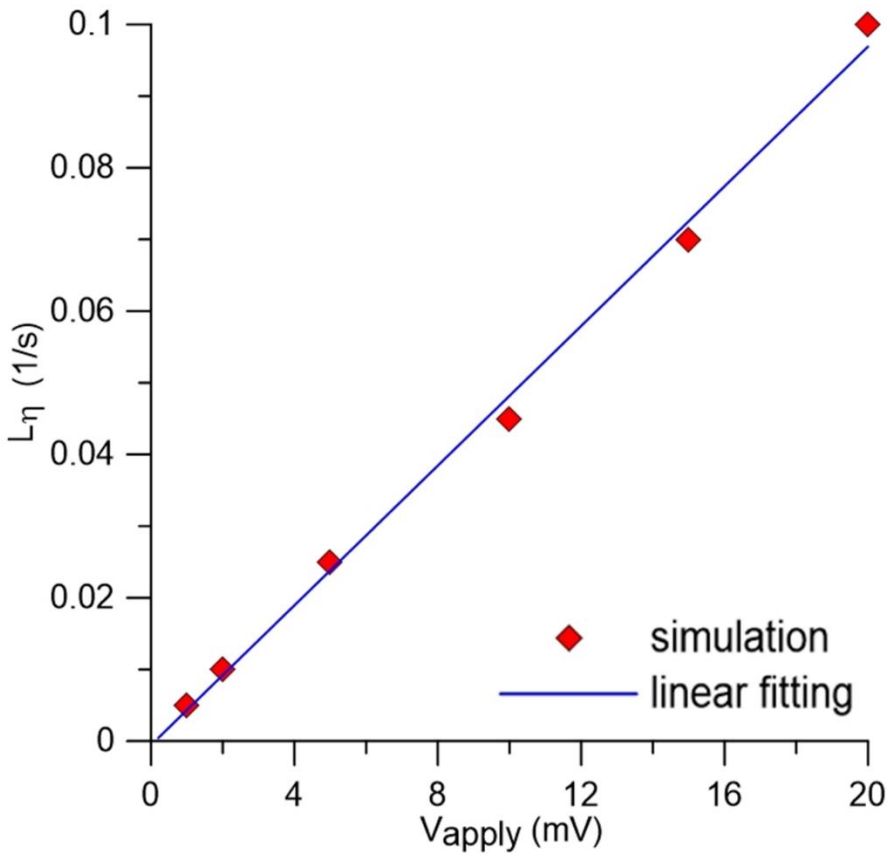

Figure A.2 The simulation results and its fitted line of L_η versus V_{apply}.

Secondly, in ref. [82] it points out that diffusion in pore surfaces is speedier than that in the bulk lithium, therefore, a higher mobility coefficient for the void is used in this model, i.e., $L_{k_3} > L_{k_1} = L_{k_2}$. In this work, we assume that L_{k_3} is 100 times higher than L_η, that is DR = 100, which gives rise to the results shown in Fig. 4.2. And for different DRs, e.g., 5, 10, and 50, the morphology of the maintained void during discharging is shown in Fig. A.3. The voids become oblate because of a stack pressure of 1 MPa. Apparently, DR larger than 1 gives rise to the void growth; however, it can be observed that larger DR leads only to a slightly bigger void, as shown in Fig. 4.1(a). Hence, the magnitude of DR, though arbitrarily determined, does not affect our results of the mechanical failure mechanism.

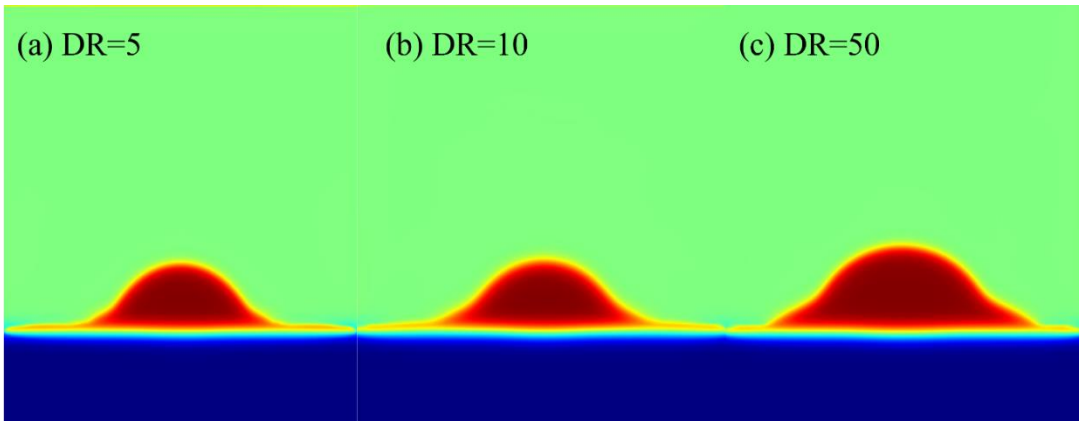

Figure A.3 Void's maintained morphology in discharge process with stack pressure at 1 MPa for DR at (a) 5, (b) 10 and (c) 50.

Appendix B. Experimental method in IOX-strengthened glass

The glass samples used to calibrate our model are sodium-aluminosilicate square sheets with a side length of 100 mm and thickness of 0.5 mm (provided by Biel Crystal (HK) Manufactory Ltd., Hong Kong). The glass samples were immersed in a molten potassium nitrate bath at 420 ℃ for 3 h. The obtained DOL, CS and CT are determined through birefringence stress measurement (FSM-6000LEUV Premium, ORIHARA, Japan). Note that in experiments, we selected five post-IOX glass samples with consistent surface CS (800 MPa) and DOL (40 μm) (scattering within 1%), which led to the residual-stress profile assumed in our numerical model as shown in Fig. 5.1(c).

The fracture strengths of glass samples before and after IOX were investigated through ROR experiments conducted using a universal testing machine (Instron 68TM-10). The fixtures comprised a loading ring and a supporting ring with radii of 7.5 mm and 15 mm, respectively. Both rings had a thickness of 0.5 mm and were rounded with a radius of 0.25 mm. To retain fragments after glass fracture, adhesive tapes were applied to both sides of glass. The resulting load-displacement curves are shown in Fig. 5.1(d, e) for pre and post IOX glass samples, respectively. The curves labeled by “ex1-5” are obtained from five pre-IOX glass samples and “ex6-10” for post-IOX glass samples.

Appendix C. Additional plots for FE-NO coupling framework

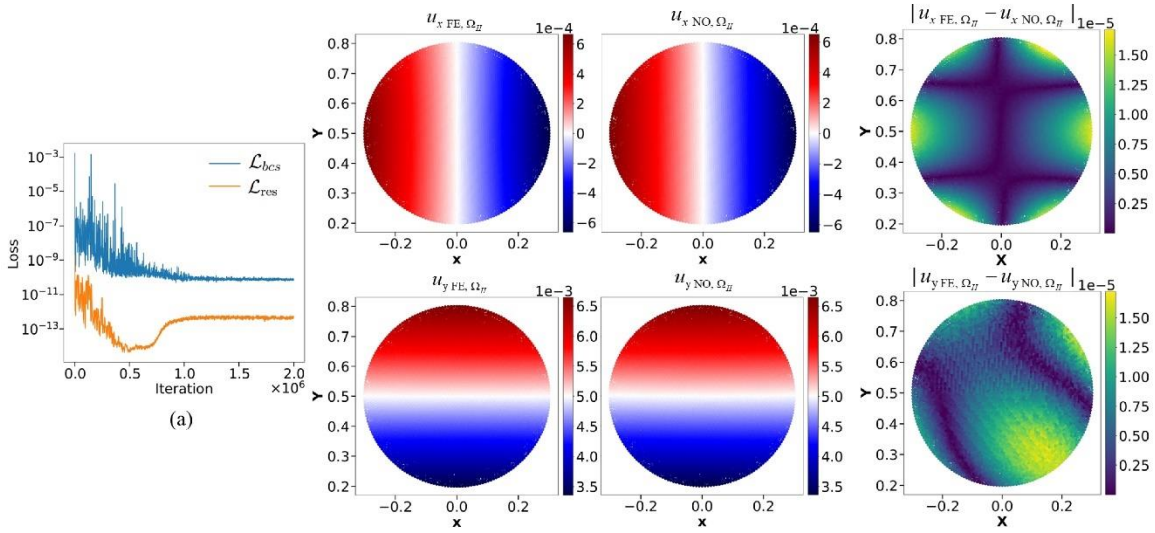

Figure C.1 Linear-elastic DeepONet pretraining: (a) Loss plot of static PI-DeepONet; The $u_{x\,FE,\Omega_{II}}$ and $u_{y\,FE,\Omega_{II}}$ are the ground truth for *x*-displacement and *y*-displacement in Ω_{II}, using FEniCSx; The $u_{x\,NO,\Omega_{II}}$ and $u_{y\,NO,\Omega_{II}}$ are the prediction from static PI-DeepONet, along with the absolute error $|u_{x\,FE,\Omega_{II}} - u_{x\,NO,\Omega_{II}}|$ and $|u_{y\,FE,\Omega_{II}} - u_{y\,NO,\Omega_{II}}|$.

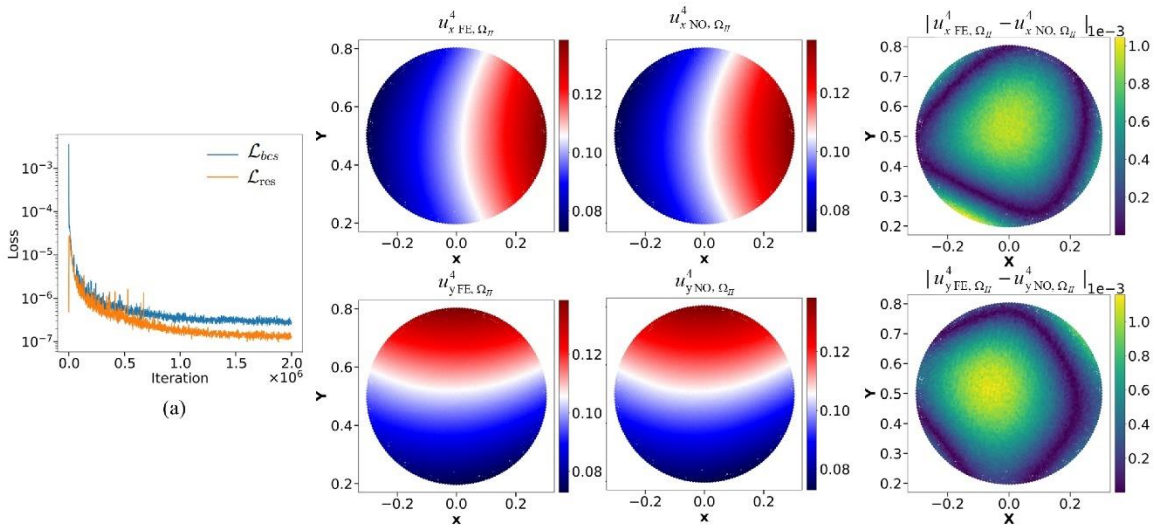

Figure C.2 Hyperelastic DeepONet pretraining: (a) Loss plot of hyperelastic PI-DeepONet; The $u^4_{x\,FE,\Omega_{II}}$ and $u^4_{y\,FE,\Omega_{II}}$ are the ground truth for *x*-displacement and *y*-displacement in Ω_{II}, using FEniCSx; The $u^4_{x\,NO,\Omega_{II}}$ and $u^4_{y\,NO,\Omega_{II}}$ are the prediction from static PI-DeepONet, along with the absolute error

$\left|u^4_{x\,FE} - u^4_{x\,NO,\Omega_{II}}\right|$ and $\left|u^4_{y\,FE} - u^4_{y\,NO,\Omega_{II}}\right|$.

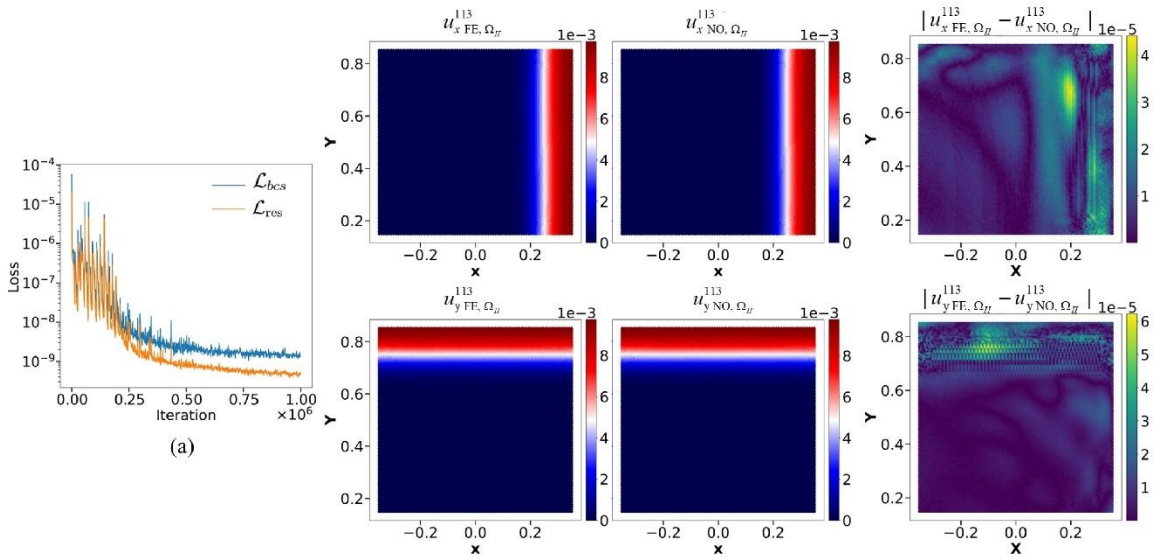

Figure C.3 Elasto-dynamic DeepONet pretraining: (a) Loss plot of time-advancing PI-DeepONet; The $u^{113}_{x\,FE,\Omega_{II}}$ and $u^{113}_{y\,FE,\Omega_{II}}$ are the ground truth for x-displacement and y-displacement in Ω_{II} at time step n = 113, using FEniCSx; The $u^{113}_{x\,NO,\Omega_{II}}$ and $u^{113}_{y\,NO,\Omega_{II}}$ are the prediction from time-advancing PI-DeepONet, along with the absolute error $\left|u^{113}_{x\,FE,\,\Omega_{II}} - u^{113}_{x\,NO,\Omega_{II}}\right|$ and $\left|u^{113}_{y\,FE,\,\Omega_{II}} - u^{113}_{y\,NO,\Omega_{II}}\right|$.

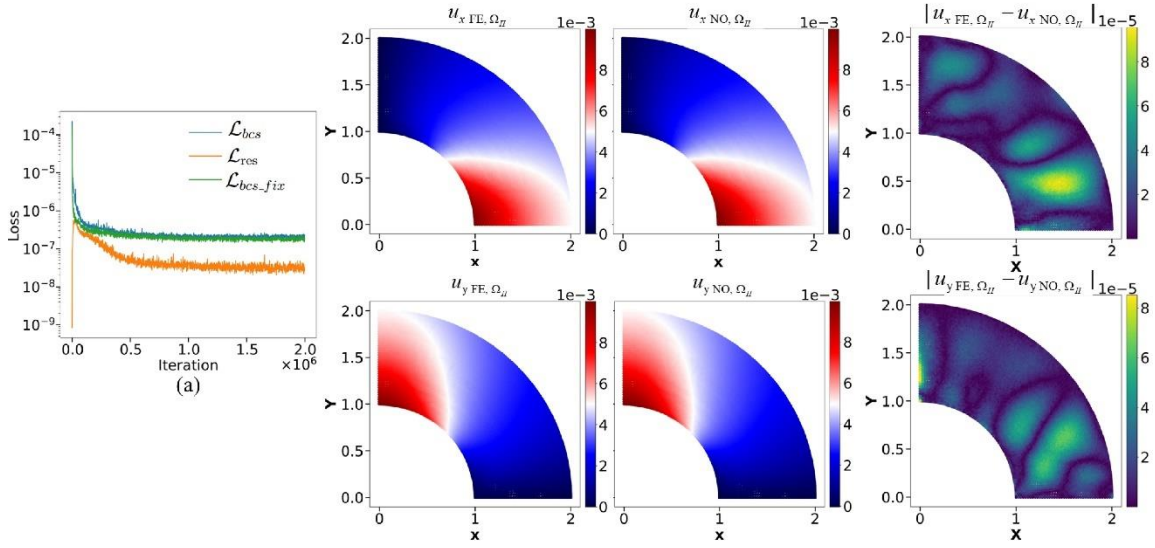

Figure C.4 Linear-elastic thick cylinder DeepONet pretraining:(a) Loss plot of time-advancing PI-DeepONet; The $u_{x\,FE,\Omega_{II}}$ and $u_{y\,FE,\Omega_{II}}$ are the ground truth for x-displacement and y-displacement in Ω_{II} using FEniCSx; The $u_{x\,NO,\Omega_{II}}$ and $u_{y\,NO,\Omega_{II}}$ are the prediction from time-advancing PI-DeepONet, along with the absolute error $\left|u_{x\,FE,\Omega_{II}} - u_{x\,NO,\Omega_{II}}\right|$ and $\left|u_{y\,FE,\Omega_{II}} - u_{y\,NO,\Omega_{II}}\right|$.

Appendix D. Non-dimensionalized Equations

This appendix presents the non-dimensional expression of momentum equilibrium equations in terms of displacement for linear elastic and static case (Eq. 3.49), elasto-dynamic case (Eq. 3.50), and hyper-elastic and quasi-static case (Eq. 6.5), which are directly adopted in numerical implementations.

Substituting Eqs. 3.54 and 3.55 into Eq. 3.49, the non-dimensional equilibrium equation for linear elastic material under static loading (assuming no external force) is derived as:

$$\frac{\lambda_0+\mu_0}{E_{el}L}\nabla^*\left(\nabla^*\bullet\mathbf{u}^*\right)+\frac{\mu_0}{E_{el}L}\nabla^{*2}\mathbf{u}^*=\mathbf{0} \tag{D.1}$$

where * denotes a non-dimensional quantity or operator; L and E_{el} are reference length (1 cm) and reference elastic Young's modulus (2×10^6 Pa), respectively. Similarly, the non-dimensional equilibrium equation under dynamic loading is expressed as:

$$\frac{\lambda_0+\mu_0}{E_{el}L}\nabla^*\left(\nabla^*\bullet\mathbf{u}^*\right)+\frac{\mu_0}{E_{el}L}\nabla^{*2}\mathbf{u}^*=\frac{L^3\rho}{m_0t_0^2}\ddot{\mathbf{u}}^* \tag{D.2}$$

where m_0 and t_0 are reference mass (1 g) and reference time (4×10^{-4} s). For quasi-static loading at time step n (in the absence of external forces), the non-dimensional form of Eq. 6.6 and Eq. 6.7 is given by:

$$\frac{1}{L}\nabla^*\bullet\left[\frac{\mu_0}{E_{hp}}\left(\mathbf{I}+\nabla^*\mathbf{u}^{n*}\right)+\frac{\lambda_0\log J-\mu_0}{E_{hp}J}+\mathrm{Cof}\left(\mathbf{I}+\nabla^*\mathbf{u}^{n*}\right)\right]=\mathbf{0} \tag{D.3}$$

where Cof(·) denotes the cofactor matrix and E_{hp} is the reference Young's modulus (1 Pa) for hyperelastic material.

References:

1. Anderson, T.L. and T.L. Anderson, *Fracture mechanics: fundamentals and applications*. 2005: CRC press.

2. Ravi-Chandar, K., *Dynamic fracture*. 2004: Elsevier.

3. Griffith, A.A., *VI. The phenomena of rupture and flow in solids.* Philosophical Transactions of the Royal Society of London. Series A, Containing Papers of a Mathematical or Physical Character, 1921. **221**(582-593): p. 163-198.

4. Ter-Ovanessian, B., et al., *15 - Oxidation-assisted Cracking*, in *Mechanics - Microstructure - Corrosion Coupling*, C. Blanc and I. Aubert, Editors. 2019, Elsevier. p. 339-358.

5. Lafata, M.A., et al., *Oxidation-Assisted Crack Growth in Single-Crystal Superalloys during Fatigue with Compressive Holds.* Metallurgical and Materials Transactions A, 2018. **49**(1): p. 105-116.

6. Jones, R.H., *Stress-corrosion cracking*, in *Corrosion: fundamentals, testing, and protection*. 2003, ASM international. p. 346-366.

7. Sieradzki, K. and R. Newman, *Stress-corrosion cracking.* Journal of physics and chemistry of solids, 1987. **48**(11): p. 1101-1113.

8. Yoon, K., et al., *Challenges and strategies towards practically feasible solid-state lithium metal batteries.* Advanced Materials, 2022. **34**(4): p. 2104666.

9. Gy, R., *Ion exchange for glass strengthening.* Materials Science and Engineering: B, 2008. **149**(2): p. 159-165.

10. Ha, Y.D. and F. Bobaru, *Characteristics of dynamic brittle fracture captured with peridynamics.* Engineering Fracture Mechanics, 2011. **78**(6): p. 1156-1168.

11. Langer, J.S., *MODELS OF PATTERN FORMATION IN FIRST-ORDER PHASE TRANSITIONS*, in *Directions in Condensed Matter Physics*. 1986. p. 165-186.

12. Landau, L.D., *Collected papers of LD Landau*. 1965: Pergamon.

13. Karma, A., *Phase-field formulation for quantitative modeling of alloy solidification.* Phys Rev Lett, 2001. **87**(11): p. 115701.

14. Steinbach, I., *Phase-field models in materials science.* Modelling and Simulation in Materials Science and Engineering, 2009. **17**(7).

15. Cahn, J.W. and J.E. Hilliard, *Free Energy of a Nonuniform System. I. Interfacial*

Free Energy. The Journal of Chemical Physics, 1958. **28**(2): p. 258-267.

16. Kim, S.G., W.T. Kim, and T. Suzuki, *Phase-field model for binary alloys.* Phys Rev E Stat Phys Plasmas Fluids Relat Interdiscip Topics, 1999. **60**(6 Pt B): p. 7186-97.

17. Galenko, P., *Phase Field Theory in Materials Physics*. 2024: Springer.

18. Moelans, N., B. Blanpain, and P. Wollants, *An introduction to phase-field modeling of microstructure evolution.* Calphad, 2008. **32**(2): p. 268-294.

19. Fan, D. and L.Q. Chen, *Computer simulation of grain growth using a continuum field model.* Acta Materialia, 1997. **45**(2): p. 611-622.

20. Cahn, J.W. and J.E. Hilliard, *Free energy of a nonuniform system. III. Nucleation in a two-component incompressible fluid.* The Journal of chemical physics, 1959. **31**(3): p. 688-699.

21. Zhang, T., J. Zhong, and L. Zhang, *Multi-objective optimization assisting three-dimensional quantitative Cahn-Hilliard simulations of microstructure evolution in Fe-Cr alloys during spinodal decomposition.* Computational Materials Science, 2024. **244**.

22. Lopez-Hirata, V.M., et al., *Thermodynamic and Kinetic Characteristics of Spinodal Decomposition in Ternary Alloys.* Frontiers in Materials, 2022. **9**: p. 901421.

23. Agosti, A., et al., *A Cahn-Hilliard–type equation with application to tumor growth dynamics.* Mathematical Methods in the Applied Sciences, 2017. **40**(18): p. 7598-7626.

24. Garcke, H., B. Kovács, and D. Trautwein, *Viscoelastic Cahn–Hilliard models for tumor growth.* Mathematical Models and Methods in Applied Sciences, 2022. **32**(13): p. 2673-2758.

25. Cucchi, A., A. Mellet, and N. Meunier, *A Cahn--Hilliard Model for Cell Motility.* SIAM Journal on Mathematical Analysis, 2020. **52**(4): p. 3843-3880.

26. Yang, X., V. Mironov, and Q. Wang, *Modeling fusion of cellular aggregates in biofabrication using phase field theories.* Journal of Theoretical Biology, 2012. **303**: p. 110-118.

27. Sigala-García, D.A., et al., *Phase-Field Simulation of Spinodal Decomposition in Mn-Cu Alloys.* Metals, 2022. **12**(7): p. 1220.

28. *73 - ON THE THEORY OF SUPERCONDUCTIVITY*, in *Collected Papers of L.D. Landau*, D. Ter Haar, Editor. 1965, Pergamon. p. 546-568.

29. Cahn, J.W. and S.M. Allen, *A MICROSCOPIC THEORY FOR DOMAIN WALL MOTION AND ITS EXPERIMENTAL VERIFICATION IN Fe-Al ALLOY DOMAIN GROWTH KINETICS.* Le Journal de Physique Colloques, 1977. **38**(C7): p. C7-51-C7-54.

30. Tourret, D., H. Liu, and J. Llorca, *Phase-field modeling of microstructure evolution: Recent applications, perspectives and challenges.* Progress in Materials Science, 2022. **123**.

31. Zhou, N., et al., *Contributions from elastic inhomogeneity and from plasticity to γ′ rafting in single-crystal Ni–Al.* Acta Materialia, 2008. **56**(20): p. 6156-6173.

32. Shi, R. and Y. Wang, *Variant selection during α precipitation in Ti–6Al–4V under the influence of local stress – A simulation study.* Acta Materialia, 2013. **61**(16): p. 6006-6024.

33. Chen, L.Q. and W. Yang, *Computer simulation of the domain dynamics of a quenched system with a large number of nonconserved order parameters: The grain-growth kinetics.* Phys Rev B Condens Matter, 1994. **50**(21): p. 15752-15756.

34. Wang, Y. and A.G. Khachaturyan, *Three-dimensional field model and computer modeling of martensitic transformations.* Acta Materialia, 1997. **45**(2): p. 759-773.

35. Artemev, A., Y. Jin, and A.G. Khachaturyan, *Three-dimensional phase field model of proper martensitic transformation.* Acta Materialia, 2001. **49**(7): p. 1165-1177.

36. Shchyglo, O., et al., *Phase-field simulation of martensite microstructure in low-carbon steel.* Acta Materialia, 2019. **175**: p. 415-425.

37. Lin, C. and H. Ruan, *Mechano-electrochemical modeling of lithium dendrite penetration in a solid-state electrolyte: Mechanism and suppression.* Journal of Energy Storage, 2023. **65**.

38. Lin, C. and H. Ruan, *Multi-phase-field modeling of localized corrosion involving galvanic pitting and mechano-electrochemical coupling.* Corrosion Science, 2020. **177**.

39. Lin, C., H. Ruan, and S.-Q. Shi, *Phase field study of mechanico-electrochemical corrosion.* Electrochimica Acta, 2019. **310**: p. 240-255.

40. Askari, M., P. Broumand, and M. Javidi, *Numerical modeling of stress corrosion cracking in steel structures with phase field method.* Engineering Failure Analysis, 2024. **158**: p. 107921.

41. Mai, W., S. Soghrati, and R.G. Buchheit, *A phase field model for simulating the pitting corrosion.* Corrosion Science, 2016. **110**: p. 157-166.

42. Karma, A., D.A. Kessler, and H. Levine, *Phase-field model of mode III dynamic fracture.* Phys Rev Lett, 2001. **87**(4): p. 045501.

43. Karma, A. and A.E. Lobkovsky, *Unsteady crack motion and branching in a phase-field model of brittle fracture.* Phys Rev Lett, 2004. **92**(24): p. 245510.

44. Kovacevic, S., et al., *Phase-field modeling of pitting and mechanically-assisted corrosion of Mg alloys for biomedical applications.* Acta Biomater, 2023. **164**: p. 641-658.

45. Ansari, T.Q., H. Huang, and S.-Q. Shi, *Phase field modeling for the morphological and microstructural evolution of metallic materials under environmental attack.* npj Computational Materials, 2021. **7**(1).

46. Cui, C., R. Ma, and E. Martínez-Pañeda, *A generalised, multi-phase-field theory for dissolution-driven stress corrosion cracking and hydrogen embrittlement.* Journal of the Mechanics and Physics of Solids, 2022. **166**.

47. Tan, Y., et al., *A phase-field fracture model for piezoelectrics in hydrogen-rich environment.* International Journal of Mechanical Sciences, 2025. **291-292**.

48. Aranson, I.S., V.A. Kalatsky, and V.M. Vinokur, *Continuum field description of crack propagation.* Phys Rev Lett, 2000. **85**(1): p. 118-21.

49. Echebarria, B., et al., *Quantitative phase-field model of alloy solidification.* Phys Rev E Stat Nonlin Soft Matter Phys, 2004. **70**(6 Pt 1): p. 061604.

50. Liang, L., M. Stan, and M. Anitescu, *Phase-field modeling of diffusion-induced crack propagations in electrochemical systems.* Applied Physics Letters, 2014. **105**(16).

51. Wang, W., et al., *Modeling of Void‐Mediated Cracking and Lithium Penetration in All‐Solid‐State Batteries.* Advanced Functional Materials, 2023.

52. Yuan, C., W. Lu, and J. Xu, *Unlocking the Electrochemical–Mechanical Coupling Behaviors of Dendrite Growth and Crack Propagation in All‐Solid‐State Batteries.* Advanced Energy Materials, 2021. **11**(36).

53. Crosby, T. and N.M. Ghoniem, *Multiphysics model of thermomechanical and helium-induced damage of tungsten during plasma heat transients.* Journal of Nuclear Materials, 2013. **442**(1-3): p. S261-S266.

54. Kamikawa, Y., K. Amezawa, and K. Terada, *Chemo-electro-mechanical phase-field simulation of interfacial nanodefects and nanovoids in solid-state batteries.* Communications Materials, 2024. **5**(1).

55. Dai, H., et al., *Pits formation and stress corrosion cracking behavior of Q345R in hydrofluoric acid.* Corrosion Science, 2020. **166**.

56. Zhuang, X., et al., *Phase field modeling and computer implementation: A review.* Engineering Fracture Mechanics, 2022. **262**.

57. Wu, J.-Y., et al., *Phase-field modeling of fracture.* Advances in applied mechanics, 2020. **53**: p. 1-183.

58. Jianying, W., *On the unified phase-field theory for damage and failure in solids and structures: theoretical and numerical aspects.* Chinese Journal of Theoretical and Applied Mechanics, 2021. **53**(2): p. 301-329.

59. Miehe, C., M. Hofacker, and F. Welschinger, *A phase field model for rate-independent crack propagation: Robust algorithmic implementation based on operator splits.* Computer Methods in Applied Mechanics and Engineering, 2010. **199**(45-48): p. 2765-2778.

60. Miehe, C., F. Welschinger, and M. Hofacker, *Thermodynamically consistent phase-field models of fracture: Variational principles and multi-field FE implementations.* International Journal for Numerical Methods in Engineering, 2010. **83**(10): p. 1273-1311.

61. Francfort, G.A. and J.J. Marigo, *Revisiting brittle fracture as an energy minimization problem.* Journal of the Mechanics and Physics of Solids, 1998. **46**(8): p. 1319-1342.

62. Bourdin, B., G.A. Francfort, and J.J. Marigo, *Numerical experiments in revisited brittle fracture.* Journal of the Mechanics and Physics of Solids, 2000. **48**(4): p. 797-826.

63. Braides, A., *A handbook of Γ-convergence*, in *Handbook of Differential Equations: stationary partial differential equations*. 2006, Elsevier. p. 101-213.

64. Kuhn, C. and R. Müller. *A phase field model for fracture*. in *PAMM: proceedings in applied mathematics and mechanics*. 2008. Wiley Online Library.

65. Amor, H., J.-J. Marigo, and C. Maurini, *Regularized formulation of the variational brittle fracture with unilateral contact: Numerical experiments.* Journal of the Mechanics and Physics of Solids, 2009. **57**(8): p. 1209-1229.

66. Clavijo, S.P., et al., *A coupled phase-field and reactive-transport framework for fracture propagation in poroelastic media.* Sci Rep, 2022. **12**(1): p. 17819.

67. Zhou, S., T. Rabczuk, and X. Zhuang, *Phase field modeling of quasi-static and dynamic crack propagation: COMSOL implementation and case studies.* Advances

in Engineering Software, 2018. **122**: p. 31-49.

68. Miehe, C., *Computation of isotropic tensor functions.* Communications in Numerical Methods in Engineering, 1993. **9**(11): p. 889-896.

69. Kristensen, P.K., C.F. Niordson, and E. Martínez-Pañeda, *Applications of phase field fracture in modelling hydrogen assisted failures.* Theoretical and Applied Fracture Mechanics, 2020. **110**: p. 102837.

70. Martínez-Pañeda, E., A. Golahmar, and C.F. Niordson, *A phase field formulation for hydrogen assisted cracking.* Computer Methods in Applied Mechanics and Engineering, 2018. **342**: p. 742-761.

71. Nguyen, T.-T., et al., *A phase field method for modeling stress corrosion crack propagation in a nickel base alloy.* International Journal of Solids and Structures, 2017. **112**: p. 65-82.

72. Navidtehrani, Y., C. Betegón, and E. Martínez-Pañeda, *A generalised framework for phase field-based modelling of coupled problems: Application to thermo-mechanical fracture, hydraulic fracture, hydrogen embrittlement and corrosion.* Engineering Fracture Mechanics, 2025. **326**.

73. Miehe, C., et al., *A phase-field model for chemo-mechanical induced fracture in lithium-ion battery electrode particles.* International Journal for Numerical Methods in Engineering, 2015. **106**(9): p. 683-711.

74. T O'Connor, D., et al., *Phase transformation and fracture in single LixFePO4 cathode particles: a phase-field approach to Li–ion intercalation and fracture.* Modelling and Simulation in Materials Science and Engineering, 2016. **24**(3): p. 035020.

75. Ai, W., B. Wu, and E. Martínez-Pañeda, *A coupled phase field formulation for modelling fatigue cracking in lithium-ion battery electrode particles.* Journal of Power Sources, 2022. **544**.

76. Liu, M., et al., *Quantification of the Li-ion diffusion over an interface coating in all-solid-state batteries via NMR measurements.* Nat Commun, 2021. **12**(1): p. 5943.

77. Doux, J.-M., et al., *Pressure effects on sulfide electrolytes for all solid-state batteries.* Journal of Materials Chemistry A, 2020. **8**(10): p. 5049-5055.

78. Monroe, C. and J. Newman, *The Impact of Elastic Deformation on Deposition Kinetics at Lithium/Polymer Interfaces.* Journal of The Electrochemical Society, 2005. **152**(2).

79. Raj, V., N.P.B. Aetukuri, and J. Nanda, *Solid state lithium metal batteries – Issues and challenges at the lithium-solid electrolyte interface.* Current Opinion in Solid State and Materials Science, 2022. **26**(4).

80. Lu, Y., et al., *Critical Current Density in Solid-State Lithium Metal Batteries: Mechanism, Influences, and Strategies.* Advanced Functional Materials, 2021. **31**(18).

81. Kasemchainan, J., et al., *Critical stripping current leads to dendrite formation on plating in lithium anode solid electrolyte cells.* Nat Mater, 2019. **18**(10): p. 1105-1111.

82. Krauskopf, T., et al., *Toward a Fundamental Understanding of the Lithium Metal Anode in Solid-State Batteries-An Electrochemo-Mechanical Study on the Garnet-Type Solid Electrolyte Li(6.25)Al(0.25)La(3)Zr(2)O(12).* ACS Appl Mater Interfaces, 2019. **11**(15): p. 14463-14477.

83. Aguesse, F., et al., *Investigating the Dendritic Growth during Full Cell Cycling of Garnet Electrolyte in Direct Contact with Li Metal.* ACS Appl Mater Interfaces, 2017. **9**(4): p. 3808-3816.

84. Ning, Z., et al., *Visualizing plating-induced cracking in lithium-anode solid-electrolyte cells.* Nat Mater, 2021. **20**(8): p. 1121-1129.

85. Wang, M.J., R. Choudhury, and J. Sakamoto, *Characterizing the Li-Solid-Electrolyte Interface Dynamics as a Function of Stack Pressure and Current Density.* Joule, 2019. **3**(9): p. 2165-2178.

86. Lee, C., et al., *Stack Pressure Measurements to Probe the Evolution of the Lithium–Solid-State Electrolyte Interface.* ACS Energy Letters, 2021. **6**(9): p. 3261-3269.

87. Fincher, C.D., et al., *Mechanical properties of metallic lithium: from nano to bulk scales.* Acta Materialia, 2020. **186**: p. 215-222.

88. Haslam, C.G., J.B. Wolfenstine, and J. Sakamoto, *The effect of aspect ratio on the mechanical behavior of Li metal in solid-state cells.* Journal of Power Sources, 2022. **520**.

89. Doux, J.M., et al., *Stack Pressure Considerations for Room-Temperature All-Solid-State Lithium Metal Batteries.* Advanced Energy Materials, 2019. **10**(1).

90. Ahmed, R.A., et al., *Pressure-induced interfacial contacts and the deformation in all solid-state Li-ion batteries.* Journal of Power Sources, 2022. **521**.

91. Lee, H.-J., et al., *Crack Healing Mechanism by Application of Stack Pressure to the Carbon-Based Composite Anode of an All-Solid-State Battery.* ACS Applied

Energy Materials, 2022. **5**(4): p. 5227-5235.

92. Hänsel, C., P.V. Kumar, and D. Kundu, *Stack Pressure Effect in Li3PS4 and Na3PS4 Based Alkali Metal Solid-State Cells: The Dramatic Implication of Interlayer Growth.* Chemistry of Materials, 2020. **32**(24): p. 10501-10510.

93. Xu, R., et al., *A Morphologically Stable Li/Electrolyte Interface for All-Solid-State Batteries Enabled by 3D-Micropatterned Garnet.* Adv Mater, 2021: p. e2104009.

94. Heine, J., et al., *Fluoroethylene Carbonate as Electrolyte Additive in Tetraethylene Glycol Dimethyl Ether Based Electrolytes for Application in Lithium Ion and Lithium Metal Batteries.* Journal of The Electrochemical Society, 2015. **162**(6): p. A1094-A1101.

95. Cheng, D., et al., *Unveiling the Stable Nature of the Solid Electrolyte Interphase between Lithium Metal and LiPON via Cryogenic Electron Microscopy.* Joule, 2020. **4**(11): p. 2484-2500.

96. Wenzel, S., et al., *Interfacial reactivity and interphase growth of argyrodite solid electrolytes at lithium metal electrodes.* Solid State Ionics, 2018. **318**: p. 102-112.

97. Porz, L., et al., *Mechanism of Lithium Metal Penetration through Inorganic Solid Electrolytes.* Advanced Energy Materials, 2017. **7**(20).

98. Yuan, C., et al., *Coupled crack propagation and dendrite growth in solid electrolyte of all-solid-state battery.* Nano Energy, 2021. **86**.

99. Zhao, Y., R. Wang, and E. Martínez-Pañeda, *A phase field electro-chemo-mechanical formulation for predicting void evolution at the Li–electrolyte interface in all-solid-state batteries.* Journal of the Mechanics and Physics of Solids, 2022. **167**.

100. Lewis, J.A., et al., *Linking void and interphase evolution to electrochemistry in solid-state batteries using operando X-ray tomography.* Nat Mater, 2021. **20**(4): p. 503-510.

101. Hao, S., et al., *Tracking lithium penetration in solid electrolytes in 3D by in-situ synchrotron X-ray computed tomography.* Nano Energy, 2021. **82**.

102. Velde, O.v.d., *A mechanical and Fractographic Research of Glass Biaxial Strength for Structural Purpose*. 2015, Delft University of Technology: Delft.

103. Griffith, A.A., *VI. The phenomena of rupture and flow in solids.* Philosophical Transactions of the Royal Society of London. Series A, Containing Papers of a Mathematical or Physical Character, 1997. **221**(582-593): p. 163-198.

104. Egboiyi, B. and T. Sain, *The Competing Effect of Initial Crack Depth Versus*

Chemical Strengthening Parameters on Apparent Fracture Toughness of Sodium Aluminosilicate Glass. 2020.

105. Kistler, S.S., *Stresses in Glass Produced by Nonuniform Exchange of Monovalent Ions.* Journal of the American Ceramic Society, 1962. **45**(2): p. 59-68.

106. Acloque, P. and J. Tochon, *Measurement of Mechanical Resistance of Glass after Reinforcement, pp 687–704 in Colloquium on Mechanical Strength of Glass and Ways of Improving It, Sept 25–29, 1961, Florence Italy.* 1962.

107. Lin, C., et al., *Modeling of ion exchange in glass considering large viscoelastic deformation and mechano–electrochemical coupling.* Journal of the American Ceramic Society, 2022. **105**(8): p. 5190-5202.

108. Jiang, L., et al., *Effect of residual stress on the fracture of chemically strengthened thin aluminosilicate glass.* Journal of Materials Science, 2016. **52**(3): p. 1405-1415.

109. Gomes, J.A.C., E.C. Barbano, and L. Misoguti, *Cross-section profile of the nonlinear refractive index of Gorilla Glass obtained by nonlinear ellipse rotation measurements.* Appl Opt, 2019. **58**(28): p. 7858-7861.

110. Sglavo, V.M., L. Larentis, and D.J. Green, *Flaw-Insensitive Ion-Exchanged Glass: I, Theoretical Aspects.* Journal of the American Ceramic Society, 2004. **84**(8): p. 1827-1831.

111. Sglavo, V.M. and D.J. Green, *Flaw-Insensitive Ion-Exchanged Glass: II, Production and Mechanical Performance.* Journal of the American Ceramic Society, 2004. **84**(8): p. 1832-1838.

112. RyanClaudeAndrews, G., PA, et al., *METHODS OF CHARACTERIZING ION - EXCHANGED CHEMICALLY STRENGTHENED GLASSES CONTAINING LITHIUM*, CORNING INCORPORATED and N.U. Corning, Editors. 2016, CORNING INCORPORATED, Corning, NY (US): United States.

113. Roger J. Araujo, H., N.Y., *STRENGTHENING GLASS BY ION EXCHANGE*. 1997, Corning Incorporated, Corning, N.Y.: United States.

114. Kohli, J.T., et al., *A Corning perspective on the future of technical glass in our evolving world.* International Journal of Applied Glass Science, 2022. **13**(3): p. 292-307.

115. Morris, D.J., S.B. Myers, and R.F. Cook, *Indentation crack initiation in ion-exchanged aluminosilicate glass.* Journal of Materials Science, 2004. **39**(7): p. 2399-2410.

116. Li, X., et al., *New insights into nanoindentation crack initiation in ion-exchanged*

sodium aluminosilicate glass. Journal of the American Ceramic Society, 2018. **101**(7): p. 2930-2940.

117. Green, D.J., R. Tandon, and V.M. Sglavo, *Crack Arrest and Multiple Cracking in Glass Through the Use of Designed Residual Stress Profiles.* Science, 1999. **283**(5406): p. 1295-1297.

118. Egboiyi, B., et al., *Mechanistic understanding of the fracture toughening in chemically strengthened glass—experiments and phase-field fracture modeling.* International Journal of Solids and Structures, 2022. **238**.

119. Sun, H. and R. Dugnani, *Predicting the flexural strength of chemically strengthened aluminosilicate glass plates with fractography.* Journal of the European Ceramic Society, 2022. **42**(8): p. 3603-3613.

120. Pugh, S.F., *The fracture of brittle materials.* British Journal of Applied Physics, 1967. **18**(2): p. 129-162.

121. Freiman, S.W. and J.J. Mecholsky Jr, *The fracture of brittle materials: testing and analysis*. 2019: John Wiley & Sons.

122. Richardson, C.L., et al., *An XFEM method for modeling geometrically elaborate crack propagation in brittle materials.* International Journal for Numerical Methods in Engineering, 2011. **88**(10): p. 1042-1065.

123. Rabczuk, T., *Computational Methods for Fracture in Brittle and Quasi-Brittle Solids: State-of-the-Art Review and Future Perspectives.* ISRN Applied Mathematics, 2013. **2013**: p. 1-38.

124. Bobaru, F. and G. Zhang, *Why do cracks branch? A peridynamic investigation of dynamic brittle fracture.* International Journal of Fracture, 2016. **196**(1-2): p. 59-98.

125. Rountree, C.L., et al., *Atomistic aspects of crack propagation in brittle materials: Multimillion atom molecular dynamics simulations.* Annual Review of Materials Research, 2002. **32**(1): p. 377-400.

126. Muralidharan, K., et al., *Molecular dynamics studies of brittle fracture in vitreous silica: Review and recent progress.* Journal of non-crystalline solids, 2005. **351**(18): p. 1532-1542.

127. Cui, C., R. Ma, and E. Martínez-Pañeda, *A phase field formulation for dissolution-driven stress corrosion cracking.* Journal of the Mechanics and Physics of Solids, 2021. **147**.

128. Jamie T. Westbrook, J.F.B., Tim A. Roe, Jum S. Kim, and T.O. Po-Hua Su, and

Suresh T. Gulati, *Strength Measurements of Thin AMLCD Panels_April.* 2021.

129. Forrester, A., A. Sobester, and A. Keane, *Engineering design via surrogate modelling: a practical guide*. 2008: John Wiley & Sons.

130. Bhosekar, A. and M. Ierapetritou, *Advances in surrogate based modeling, feasibility analysis, and optimization: A review.* Computers & Chemical Engineering, 2018. **108**: p. 250-267.

131. Samadian, D., I.B. Muhit, and N. Dawood, *Application of data-driven surrogate models in structural engineering: a literature review.* Archives of Computational Methods in Engineering, 2024: p. 1-50.

132. Wang, W., et al., *Causality-respecting adaptive refinement for pinns: Enabling precise interface evolution in phase field modeling.* arXiv preprint arXiv:2410.20212, 2024.

133. Raissi, M., P. Perdikaris, and G.E. Karniadakis, *Physics-informed neural networks: A deep learning framework for solving forward and inverse problems involving nonlinear partial differential equations.* Journal of Computational Physics, 2019. **378**: p. 686-707.

134. Cuomo, S., et al., *Scientific machine learning through physics–informed neural networks: Where we are and what's next.* Journal of Scientific Computing, 2022. **92**(3): p. 88.

135. Huang, S., et al., *Partial differential equations meet deep neural networks: A survey.* IEEE Transactions on Neural Networks and Learning Systems, 2025.

136. Lu, L., et al., *Learning nonlinear operators via DeepONet based on the universal approximation theorem of operators.* Nature machine intelligence, 2021. **3**(3): p. 218-229.

137. Goswami, S., et al., *Physics-informed deep neural operator networks*, in *Machine learning in modeling and simulation: methods and applications*. 2023, Springer. p. 219-254.

138. Fanaskov, V.S. and I.V. Oseledets. *Spectral neural operators*. in *Doklady Mathematics*. 2023. Springer.

139. Hao, Z., et al. *Gnot: A general neural operator transformer for operator learning*. in *International Conference on Machine Learning*. 2023. PMLR.

140. Lee, S. and Y. Shin, *On the training and generalization of deep operator networks.* SIAM Journal on Scientific Computing, 2024. **46**(4): p. C273-C296.

141. De Ryck, T. and S. Mishra, *Generic bounds on the approximation error for physics-*

informed (and) operator learning. Advances in Neural Information Processing Systems, 2022. **35**: p. 10945-10958.

142. Kovachki, N., S. Lanthaler, and S. Mishra, *On universal approximation and error bounds for Fourier neural operators.* Journal of Machine Learning Research, 2021. **22**(290): p. 1-76.

143. Michałowska, K., et al. *Neural operator learning for long-time integration in dynamical systems with recurrent neural networks*. in *2024 International Joint Conference on Neural Networks (IJCNN)*. 2024. IEEE.

144. Oommen, V., et al., *Rethinking materials simulations: Blending direct numerical simulations with neural operators.* npj Computational Materials, 2024. **10**(1): p. 145.

145. Navaneeth, N. and S. Chakraborty, *Koopman operator for time-dependent reliability analysis.* Probabilistic Engineering Mechanics, 2022. **70**: p. 103372.

146. Yin, M., et al., *Interfacing finite elements with deep neural operators for fast multiscale modeling of mechanics problems.* Comput Methods Appl Mech Eng, 2022. **402**.

147. Chan, T.F. and T.P. Mathew, *Domain decomposition algorithms.* Acta numerica, 1994. **3**: p. 61-143.

148. Smith, B.F., *Domain Decomposition Methods for Partial Differential Equations*, in *Parallel Numerical Algorithms*, D.E. Keyes, A. Sameh, and V. Venkatakrishnan, Editors. 1997, Springer Netherlands: Dordrecht. p. 225-243.

149. Dolean, V., P. Jolivet, and F. Nataf, *An introduction to domain decomposition methods: algorithms, theory, and parallel implementation*. 2015: SIAM.

150. Heinlein, A., et al., *Combining machine learning and domain decomposition methods for the solution of partial differential equations—a review.* GAMM-Mitteilungen, 2021. **44**(1): p. e202100001.

151. Snyder, W., I. Tezaur, and C. Wentland, *Domain decomposition-based coupling of physics-informed neural networks via the Schwarz alternating method.* arXiv preprint arXiv:2311.00224, 2023.

152. Farhat, C. and F.X. Roux, *A method of finite element tearing and interconnecting and its parallel solution algorithm.* International journal for numerical methods in engineering, 1991. **32**(6): p. 1205-1227.

153. Farhat, C., M. Lesoinne, and K. Pierson, *A scalable dual-primal domain decomposition method.* Numerical linear algebra with applications, 2000. **7**(7-8):

p. 687-714.

154. Dohrmann, C.R., *A preconditioner for substructuring based on constrained energy minimization.* SIAM Journal on Scientific Computing, 2003. **25**(1): p. 246-258.

155. Langer, U. and O. Steinbach, *Boundary element tearing and interconnecting methods.* Computing, 2003. **71**: p. 205-228.

156. Langer, U. and O. Steinbach, *Coupled boundary and finite element tearing and interconnecting methods*, in *Domain decomposition methods in science and engineering*. 2005, Springer. p. 83-97.

157. Mitusch, S.K., S.W. Funke, and M. Kuchta, *Hybrid FEM-NN models: Combining artificial neural networks with the finite element method.* Journal of Computational Physics, 2021. **446**: p. 110651.

158. Zhou, M. and G. Mei, *Transfer learning-based coupling of smoothed finite element method and physics-informed neural network for solving elastoplastic inverse problems.* Mathematics, 2023. **11**(11): p. 2529.

159. Thel, S., et al., *Introducing Finite Element Method Integrated Networks (FEMIN).* Computer Methods in Applied Mechanics and Engineering, 2024. **427**: p. 117073.

160. Margenberg, N., et al., *DNN-MG: A hybrid neural network/finite element method with applications to 3D simulations of the Navier–Stokes equations.* Computer Methods in Applied Mechanics and Engineering, 2024. **420**: p. 116692.

161. Pantidis, P. and M.E. Mobasher, *Integrated Finite Element Neural Network (I-FENN) for non-local continuum damage mechanics.* Computer Methods in Applied Mechanics and Engineering, 2023. **404**: p. 115766.

162. Morlet, A.C., N.J. Lybeck, and K.L. Bowers, *The Schwarz alternating sinc domain decomposition method.* Applied numerical mathematics, 1997. **25**(4): p. 461-483.

163. Mota, A., I. Tezaur, and C. Alleman, *The Schwarz alternating method in solid mechanics.* Computer Methods in Applied Mechanics and Engineering, 2017. **319**: p. 19-51.

164. Mota, A., I. Tezaur, and G. Phlipot, *The Schwarz alternating method for transient solid dynamics.* International Journal for Numerical Methods in Engineering, 2022. **123**(21): p. 5036-5071.

165. Fung, T., *Complex-time-step Newmark methods with controllable numerical dissipation.* International Journal for numerical methods in Engineering, 1998. **41**(1): p. 65-93.

166. Mohammadzadeh, B. and H.C. Noh, *Investigation into central-difference and Newmark's beta methods in measuring dynamic responses.* Advanced Materials Research, 2014. **831**: p. 95-99.

167. Lu, H.A. and H. Conrad, *Influence of an electric charge during quench aging of a low-carbon steel.* Applied Physics Letters, 1991. **59**(15): p. 1847-1849.

168. Liu, W. and J.Z. Cui, *The effect of electric field on the recrystallization of 2091 Al–Li alloy.* Journal of Materials Science Letters, 1997. **16**(16): p. 1400-1401.

169. Shou, W., et al., *Influence of electric field on microstructure and mechanical properties of an Al-Cu-Li alloy during ageing.* Materials & Design, 2016. **98**: p. 79-87.

170. Fu, S., et al., *Influence of electric field on the quenched-in vacancy and solute clustering during early stage ageing of Al-Cu alloy.* Journal of Materials Science & Technology, 2018. **34**(2): p. 335-343.

171. Hakim, V. and A. Karma, *Laws of crack motion and phase-field models of fracture.* Journal of the Mechanics and Physics of Solids, 2009. **57**(2): p. 342-368.

172. Lin, C., J. Wan, and H. Ruan, *Phase field modeling of Widmanstätten ferrite formation in steel.* Journal of Alloys and Compounds, 2018. **769**: p. 620-630.

173. Lin, C. and H. Ruan, *Phase-field modeling of scale roughening induced by outward growing oxide.* Materialia, 2019. **5**.

174. Wan, T.H. and F. Ciucci, *Electro-chemo-mechanical modeling of solid-state batteries.* Electrochimica Acta, 2020. **331**.

175. Zuo, P. and Y.P. Zhao, *A phase field model coupling lithium diffusion and stress evolution with crack propagation and application in lithium ion batteries.* Phys Chem Chem Phys, 2015. **17**(1): p. 287-97.

176. Marrocchelli, D., C. Chatzichristodoulou, and S.R. Bishop, *Defining chemical expansion: the choice of units for the stoichiometric expansion coefficient.* Physical Chemistry Chemical Physics, 2014. **16**(20): p. 9229-32.

177. Lin, C., H. Ruan, and S.-Q. Shi, *Mechanical–chemical coupling phase-field modeling for inhomogeneous oxidation of zirconium induced by stress–oxidation interaction.* npj Materials Degradation, 2020. **4**(1).

178. LePage, W.S., et al., *Lithium Mechanics: Roles of Strain Rate and Temperature and Implications for Lithium Metal Batteries.* Journal of The Electrochemical Society, 2019. **166**(2): p. A89-A97.

179. Masias, A., et al., *Elastic, plastic, and creep mechanical properties of lithium metal.* Journal of Materials Science, 2018. **54**(3): p. 2585-2600.

180. Anand, L. and S. Narayan, *An Elastic-Viscoplastic Model for Lithium.* Journal of The Electrochemical Society, 2019. **166**(6): p. A1092-A1095.

181. Chen, L., et al., *Modulation of dendritic patterns during electrodeposition: A nonlinear phase-field model.* Journal of Power Sources, 2015. **300**: p. 376-385.

182. Bazant, M.Z., *Theory of chemical kinetics and charge transfer based on nonequilibrium thermodynamics.* Acc Chem Res, 2013. **46**(5): p. 1144-60.

183. Wang, Y.U., *Computer modeling and simulation of solid-state sintering: A phase field approach.* Acta Materialia, 2006. **54**(4): p. 953-961.

184. Shi, R., et al., *Towards understanding particle rigid-body motion during solid-state sintering.* Journal of the European Ceramic Society, 2021. **41**(16): p. 211-231.

185. Cahn, J.W., *The kinetics of cellular segregation reactions.* Acta Metallurgica, 1959. **7**(1): p. 18-28.

186. Li, J., et al., *A multi-phase-field model of topological pattern formation during electrochemical dealloying of binary alloys.* Computational Materials Science, 2022. **203**.

187. Moelans, N., B. Blanpain, and P. Wollants, *A phase field model for the simulation of grain growth in materials containing finely dispersed incoherent second-phase particles.* Acta Materialia, 2005. **53**(6): p. 1771-1781.

188. Deng, Z., et al., *Data-Driven First-Principles Methods for the Study and Design of Alkali Superionic Conductors.* Chemistry of Materials, 2016. **29**(1): p. 281-288.

189. Hanghofer, I., et al., *Substitutional disorder: structure and ion dynamics of the argyrodites Li6PS5Cl, Li6PS5Br and Li6PS5I.* Physical Chemistry Chemical Physics, 2019. **21**(16): p. 8489-8507.

190. Deng, Z., et al., *Elastic Properties of Alkali Superionic Conductor Electrolytes from First Principles Calculations.* Journal of The Electrochemical Society, 2015. **163**(2): p. A67-A74.

191. Sargent, P.M. and M.F. Ashby, *Deformation mechanism maps for alkali metals.* Scripta Metallurgica, 1984. **18**(2): p. 145-150.

192. Zhou, L., et al., *Solvent-Engineered Design of Argyrodite Li6PS5X (X = Cl, Br, I) Solid Electrolytes with High Ionic Conductivity.* ACS Energy Letters, 2018. **4**(1): p. 265-270.

193. Goswami, S., C. Anitescu, and T. Rabczuk, *Adaptive fourth-order phase field analysis for brittle fracture.* Computer Methods in Applied Mechanics and Engineering, 2020. **361**.

194. Borden, M.J., et al., *A phase-field description of dynamic brittle fracture.* Computer Methods in Applied Mechanics and Engineering, 2012. **217-220**: p. 77-95.

195. Zhuang, X., et al., *On the hydraulic fracturing in naturally-layered porous media using the phase field method.* Engineering Geology, 2020. **266**.

196. Miehe, C., *Comparison of two algorithms for the computation of fourth-order isotropic tensor functions.* Computers & Structures, 1998. **66**(1): p. 37-43.

197. Karabulut, M., et al., *Mechanical and structural properties of phosphate glasses.* Journal of Non-Crystalline Solids, 2001. **288**(1-3): p. 8-17.

198. Rouxel, T., et al., *Poisson's ratio and the densification of glass under high pressure.* Phys Rev Lett, 2008. **100**(22): p. 225501.

199. İLERİSOY, Z. and B. ÇOLAK, *Discovery of Innovative Materials in Structural System Design: Glass Structures.* 2018.

200. Baratta, I.A., et al., *DOLFINx: the next generation FEniCS problem solving environment.* 2023.

201. Geuzaine, C. and J.F. Remacle, *Gmsh: A 3-D finite element mesh generator with built-in pre-and post-processing facilities.* International journal for numerical methods in engineering, 2009. **79**(11): p. 1309-1331.

202. Logg, A., K.-A. Mardal, and G. Wells, *Automated solution of differential equations by the finite element method: The FEniCS book*. Vol. 84. 2012: Springer Science & Business Media.

203. Fish, J. and T. Belytschko, *A first course in finite elements*. Vol. 1. 2007: Wiley New York.

204. Newmark, N.M., *A method of computation for structural dynamics.* Journal of the engineering mechanics division, 1959. **85**(3): p. 67-94.

205. Erlicher, S., L. Bonaventura, and O.S. Bursi, *The analysis of the generalized-α method for non-linear dynamic problems.* Computational mechanics, 2002. **28**(2): p. 83-104.

206. Cartwright, J.H. and O. Piro, *The dynamics of Runge–Kutta methods.* International Journal of Bifurcation and Chaos, 1992. **2**(03): p. 427-449.

207. Yu, Y., et al., *A partitioned coupling framework for peridynamics and classical theory: Analysis and simulations.* Computer Methods in Applied Mechanics and Engineering, 2018. **340**: p. 905-931.

208. Lions, P.-L. *On the Schwarz alternating method. I*. in *First international symposium on domain decomposition methods for partial differential equations*. 1988. Paris, France.

209. Henry, H. and H. Levine, *Dynamic instabilities of fracture under biaxial strain using a phase field model.* Phys Rev Lett, 2004. **93**(10): p. 105504.

210. Wu, C., et al., *Current status and future directions of all-solid-state batteries with lithium metal anodes, sulfide electrolytes, and layered transition metal oxide cathodes.* Nano Energy, 2021. **87**.

211. Seymour, I.D. and A. Aguadero, *Suppressing void formation in all-solid-state batteries: the role of interfacial adhesion on alkali metal vacancy transport.* Journal of Materials Chemistry A, 2021. **9**(35): p. 19901-19913.

212. Shi, S., et al., *Direct calculation of Li-ion transport in the solid electrolyte interphase.* J Am Chem Soc, 2012. **134**(37): p. 15476-87.

213. Landstorfer, M., S. Funken, and T. Jacob, *An advanced model framework for solid electrolyte intercalation batteries.* Phys Chem Chem Phys, 2011. **13**(28): p. 12817-25.

214. Hao, S., et al., *3D Imaging of Lithium Protrusions in Solid-State Lithium Batteries using X-Ray Computed Tomography.* Advanced Functional Materials, 2020. **31**(10).

215. Tu, Q., et al., *Electrodeposition and Mechanical Stability at Lithium-Solid Electrolyte Interface during Plating in Solid-State Batteries.* Cell Reports Physical Science, 2020. **1**(7).

216. Meyers, M.A. and K.K. Chawla, *Mechanical behavior of materials*. 2008: Cambridge university press.

217. Qi, Y., C. Ban, and S.J. Harris, *A New General Paradigm for Understanding and Preventing Li Metal Penetration through Solid Electrolytes.* Joule, 2020. **4**(12): p. 2599-2608.

218. Ko, J., et al., *Suppression of formation of lithium dendrite via surface modification by 2-D lithium phosphorous oxynitride as a highly stable anode for metal lithium batteries.* Journal of Alloys and Compounds, 2020. **845**.

219. Ye, L. and X. Li, *A dynamic stability design strategy for lithium metal solid state batteries.* Nature, 2021. **593**(7858): p. 218-222.

220. Jagad, H.D., et al., *Tradeoff between the Ion Exchange-Induced Residual Stress and Ion Transport in Solid Electrolytes.* Chemistry of Materials, 2022. **34**(19): p. 8694-8704.

221. Quinn, G.D., *Fracture toughness of ceramics by the Vickers indentation crack length method: a critical review.* Mechanical properties and performance of engineering ceramics II: Ceramic engineering and science proceedings, 2006. **27**: p. 45-62.

222. Meyer, W.H., *Polymer Electrolytes for Lithium-Ion Batteries.* Advanced Materials, 1998. **10**(6): p. 439-448.

223. Tang, Y., et al., *Electro-chemo-mechanics of lithium in solid state lithium metal batteries.* Energy & Environmental Science, 2021. **14**(2): p. 602-642.

224. Fleck, N.A. and J.W. Hutchinson, *A phenomenological theory for strain gradient effects in plasticity.* Journal of the Mechanics and Physics of Solids, 1993. **41**(12): p. 1825-1857.

225. Keshri, S.R., et al., *Elucidating the influence of structure and Ag+-Na+ ion-exchange on crack-resistance and ionic conductivity of Na3Al1.8Si1.65P1.8O12 glass electrolyte.* Acta Materialia, 2022. **227**.

226. Thomas, C., et al., *Stress engineering for crack and dendrite prevention in solid electrolytes via ion implantation.* Cell Reports Physical Science, 2025. **6**(4).

227. Yao, X., et al., *Xenon Ion Implantation Induced Surface Compressive Stress for Preventing Dendrite Penetration in Solid-State Electrolytes.* Small, 2022. **18**(23): p. e2108124.

228. Tandon, R. and S.J. Glass, *Controlling the Fragmentation Behavior of Stressed Glass*. Fracture Mechanics of Ceramics, ed. R.C. Bradt, et al. 2005, Boston, MA: Springer US. 77-91.

229. Kingma, D.P., *Adam: A method for stochastic optimization.* arXiv preprint arXiv:1412.6980, 2014.

230. Balay, S., et al., *PETSc/TAO users manual (Rev. 3.20)*. 2023, Argonne National Laboratory (ANL), Argonne, IL (United States).

231. Virtanen, P., et al., *SciPy 1.0: fundamental algorithms for scientific computing in Python.* Nature methods, 2020. **17**(3): p. 261-272.

232. Goswami, S., et al., *Transfer learning enhanced physics informed neural network for phase-field modeling of fracture.* Theoretical and Applied Fracture Mechanics, 2020. **106**.

233. Hakimzadeh, M., et al., *Phase-field finite deformation fracture with an effective energy for regularized crack face contact.* Journal of the Mechanics and Physics of Solids, 2022. **167**: p. 104994.

234. Hakimzadeh, M., et al., *Crack Face Contact Modeling is Essential to Predict Crack-Parallel Stresses.* Journal of Applied Mechanics, 2025. **92**(9).

235. Goswami, S., et al., *A physics-informed variational DeepONet for predicting crack path in quasi-brittle materials.* Computer Methods in Applied Mechanics and Engineering, 2022. **391**: p. 114587.

236. Jia, Y., et al., *An adaptive isogeometric analysis collocation method with a recovery-based error estimator.* Computer Methods in Applied Mechanics and Engineering, 2019. **345**: p. 52-74.

237. Goswami, S., C. Anitescu, and T. Rabczuk, *Adaptive fourth-order phase field analysis using deep energy minimization.* Theoretical and Applied Fracture Mechanics, 2020. **107**.

238. Hakimzadeh, M., et al., *Phase -Field Modeling of Fracture Under Compression and Confinement in Anisotropic Geomaterials.* International Journal for Numerical and Analytical Methods in Geomechanics, 2025. **49**(4): p. 1319-1335.

239. Krishnan, U.M., A. Gupta, and R. Chowdhury, *Adaptive phase-field modeling of brittle fracture using a robust combination of error-estimator and markers.* Engineering Fracture Mechanics, 2022. **274**: p. 108758.

240. Gupta, A., et al., *An adaptive mesh refinement algorithm for phase-field fracture models: Application to brittle, cohesive, and dynamic fracture.* Computer Methods in Applied Mechanics and Engineering, 2022. **399**: p. 115347.

241. Li, L., et al., *An auto-adaptive finite element analysis software for stiffened plate and shell structures.* Advances in Engineering Software, 1997. **28**(5): p. 285-291.

242. Pantidis, P., et al., *Integrated Finite Element Neural Network (IFENN) for Phase-Field Fracture with Minimal Input and Generalized Geometry-Load Handling.* arXiv preprint arXiv:2505.19566, 2025.

243. Ke, X., et al., *Towards rational mechanical design of inorganic solid electrolytes for all-solid-state lithium ion batteries.* Energy Storage Materials, 2020. **26**: p. 313-324.

244. Perez, N., *Linear-elastic fracture mechanics*, in *Fracture mechanics*. 2017, Springer. p. 79-130.